SAPIENZA
UNIVERSITÀ DI ROMA

Engineering of reconfigurable integrated photonics for quantum computation protocols

Scuola di Dottorato in Fisica
Dottorato di ricerca in fisca - XXXV Ciclo

Francesco Hoch
ID number 1895197

Advisor
Prof. Fabio Sciarrino

Academic Year 2022/2023

Thesis defended on 15-05-2023
in front of a Board of Examiners composed by:

Prof. Eugenio Del Re (chairman)
Prof. Andrea Fratalocchi
Prof. Emanuele Pelucchi
Prof. Claudio Conti
Prof. Fabio Sciarrino

Engineering of reconfigurable integrated photonics for quantum computation protocols
Sapienza University of Rome

This thesis has been typeset by LaTeX and the Sapthesis class.

Author's email: francesco.hoch@uniroma1.it

Contents

Scientific publications

Witnesses of coherence and dimension from multiphoton indistinguishability tests Taira Giordani, Chiara Esposito, Francesco Hoch, Gonzalo Carvacho, Daniel J. Brod, Ernesto F. Galvão, Nicolò Spagnolo, and Fabio Sciarrino Phys. Rev. Research 3, 023031, April 2021 [1].

Reconfigurable continuously-coupled 3d photonic circuit for boson sampling experiments. Francesco Hoch, Simone Piacentini, Taira Giordani, Zhen-Nan Tian, Mariagrazia Iuliano, Chiara Esposito, Anita Camillini, Gonzalo Carvacho, Francesco Ceccarelli, Nicolò Spagnolo, Andrea Crespi, Fabio Sciarrino, and Roberto Osellame. npj Quantum Information, 8(1), May 2022 [2]. (Chapter 7)

Characterization of multimode linear optical networks Francesco Hoch, Taira Giordani, Nicolò Spagnolo, Andrea Crespi, Roberto Osellame, Fabio Sciarrino. Adv. Photon. Nexus 2(1), 016007 (2023) [3]. (Chapter 4)

Experimental multiparameter quantum metrology in adaptive regime. Mauro Valeri, Valeria Cimini, Simone Piacentini, Francesco Ceccarelli, Emanuele Polino, Francesco Hoch, Gabriele Bizzarri, Giacomo Corrielli, Nicolò Spagnolo, Roberto Osellame, Fabio Sciarrino. Phys. Rev. Research 5, 013138, February 2023 [4]. (Chapter 11)

In print

Non-asymptotic Heisenberg scaling: experimental metrology for a wide resources range. Valeria Cimini, Emanuele Polino, Federico Belliardo, Francesco Hoch, Bruno Piccirillo, Nicolò Spagnolo, Vittorio Giovannetti, Fabio Sciarrino. arXiv:2110.02908 Oct 2021 [5]. (Chapter 11)

Integrated photonics in quantum technologies. Taira Giordani, Francesco Hoch, Gonzalo Carvacho, Nicolò Spagnolo and Fabio Sciarrino. Riv. del Nuovo Cim.

Preprint

Optimizing quantum-enhanced bayesian multiparameter estimation in noisy apparata Federico Belliardo, Valeria Cimini, Emanuele Polino, Francesco Hoch, Bruno Piccirillo, Nicolò Spagnolo, Vittorio Giovannetti, and Fabio Sciarrino. arXiv:2211.04747 Nov 2022 [6].

In preparation

Modular Quantum-to-Quantum Bernoulli Factory in a fully reconfigurable integrated photonic platform Francesco Hoch, Taira Giordani, Luca Castello, Gonzalo Carvacho, Nicolò Spagnolo, Roberto Osellame, Ernesto F. Galvão, and Fabio Sciarrino. (Chapter 9)

Conferences and schools

APS March Meeting 2021 March 2021
Poster contributions: Witnesses of coherence and dimension from multiphoton indistinguishability tests.

Cargese School of Quantum information and Quantum technology June 2021
Poster contributions: Witnesses of coherence and dimension from multiphoton indistinguishability tests.

Introduction

Quantum information is a branch of science that embraces different fields, from physics to engineering passing mathematics and computer science, and has the aim of investigating the limits of quantum theory and how can be used to engineer new technologies. In analogy to the classical counterpart, quantum information has been paired with quantum computation which aims, on the one hand, to understand how to study and simulate quantum theory through computers and on the other hand, to understand how quantum theory can be used to improve current computing technologies. In this context, it has already been theoretically demonstrated how a quantum computer, exploiting the superposition of states and entanglement, can solve problems that are currently too complex for a classical computer such as, for example, the factorization of a number into primes.

In this context, optics, and more specifically photonics, from the very beginning has appeared as one of the most suitable platforms for experimentally testing new theories and algorithms. Indeed, photons have many degrees of freedom that can be used to encode information, such as path, polarization, angular momentum and arrival time. Also, many of the devices and techniques needed to manipulate them are already well-known and relatively easy to acquire as they coincide in most cases with those used for classical optics. Also, due to the low interaction between the photons and the environment, they can be transmitted over long distances without losing the encoded information and substantially represent one of the best candidates as information carriers for quantum communication protocols. Furthermore, in the last decade, integrated optical circuits are becoming increasingly popular, allowing the realization of more complex and stable reconfigurable interferometers that can be used in a wide range of problems on both the computation and information sides. One of the most famous applications of optics and integrated photonics to quantum computation is the *Boson sampling* problem, which has been proposed as one of the candidates for proving quantum advantage. It uses indistinguishable photons and a reconfigurable optical integrated circuit to generate samples from a distribution that is computationally impossible for a classical computer. In recent years claims of quantum advantages based on the implementation of a Boson sampler have been made [7, 8] but the effective achievement of the quantum advantage is still a matter of debate.

This thesis work aims to study integrated photonics from two perspectives: on the other hand, the design of new photonic devices and, on the other, the development of new algorithms in which it can be used. One of the main objectives of integrated optics is to implement a reconfigurable universal interferometer, which is a device capable of reproducing a generic unitary transformation that can be

changed through external controllers. In the literature, there are some proven universal geometries [9] and experimental implementations of reconfigurable chips [10]; however these geometries have scalability problems for a high number of modes of the interferometer, in particular, the resulting interferometer is of significant size with a consequent increase in losses. In this thesis work, we theoretically and experimentally investigated the possibility of using three-dimensional geometries, already used previously for small interferometers [11], as a universal geometry with the possibility to build random unitary matrices distributed according to the invariant Haar distribution (that are the natural flat distribution on the space of unitary matrices) and the potential use of a chip with this type of geometry for the implementation of a Boson sampling experiment. We show the first implementation of a unitary matrix via a continuous-coupled three-dimensional reconfigurable photonic chip with 32 modes where the waveguides are arranged according to a triangular lattice and the reconfigurability is achieved by sixteen resistive heaters placed on the surface of the chip. With this device, we demonstrate the possibility to perform several Boson sampling experiments with three and four photons using different unitary matrices extracted from a distribution close to the haar-invariant one. Two new protocols were also developed and tested to characterize the unitary evolution implemented by the photonic chip. The first one is based on the use of classical light and second-order correlation measurements. This has several advantages over existing techniques as will be explained later in this thesis. The second one is specific to chips implementing a planar rectangular geometry first proposed by Clements et al. [9]. Despite their widespread use in the literature, a procedure for characterizing them has not yet been presented.

In addition to the integrated platforms, it is also necessary to develop the software counterpart. Indeed to have an effective quantum advantage is not sufficient to translate the algorithm in the quantum domain but sometimes it is necessary a completely new formulation of the problem. In this context, there are algorithms that do not have an immediate application but that solve problems sufficiently general to be useful as components of larger algorithms. Recently, a new routine called Bernoulli factory has been brought to attention. A classical Bernoulli factory, associated with a function $f(x)$, is an algorithm that accepts in input a series of independent variables distributed according to a Bernoulli distribution of parameter p unknown and generates a new sequence of random variables distributed according to a Bernoulli distribution of parameter $f(p)$. The existence criteria [12] and various algorithms to implement a classic Bernoulli factory [13–16] have been demonstrated in the literature. Later, first in an article published in 2015 by Dale et al. [17] and then in one of 2018 by Jiaqing et al. [18] two quantum extensions of the problem were proposed in which the input (in both works) and the output (only in the second work) are replaced with two-dimensional quantum states. The existence criteria [17–20] and some experimental implementations of specific functions [20–23] have been demonstrated in the literature. In this thesis, we completely characterize the computational complexity of the quantum-to-quantum Bernoulli factory problem providing the minimum number of qubits needed and the quantum circuitry required to implement the protocol, and also demonstrating that it is optimal in terms of probability of success. Moreover, since the previous theoretical works focused only on the qubit formalism, in this work we study and managed to demonstrate the

feasibility of the quantum Bernoulli factory in the linear optics formalism both in polarization and dual-rail encoding by finding modular interferometers that implement the basic operations needed to build a quantum Bernoulli factory with photons. We also experimentally implement the interferometers found so far in a reconfigurable six-mode interferometer showing its proper functioning and resilience to experimental noise. In addition to the quantum Bernoulli factory problem, we also study quantum metrology algorithms applied to integrated devices. The idea behind this type of algorithm is to exploit quantum mechanics to measure a physical quantity under consideration efficiently and more precisely in terms of variance. In particular, we focus on multi-parameter algorithms, i.e. algorithms in which more than one parameter is measured at the same time. To do this, we use a reconfigurable integrated photonic platform in which the quantity under consideration is a difference in phase between a set of waveguides and one taken as a reference. We theoretically analyze and experimentally implement an interferometer that simultaneously estimates three phases showing how the use of indistinguishable photons achieves higher performance compared to using single photon states or classical light.

This thesis was developed within the European project PHOQUSING [24] which has a dual purpose; on the one hand, the development of a photonic quantum sampling device based on a large reconfigurable interferometer with active feedback and state-of-the-art photon sources based on both quantum dot and parametric conversion and, on the other hand, the theoretical analysis of new quantum algorithms that can be implemented on this device.

The concepts and the results presented in this thesis are structured as follows: The first part provides the general theoretical tools necessary to understand the presented results. In particular, in the first chapter, we describe the primitive elements of quantum information such as qubits, entangled states, quantum circuits and an overview of computational complexity classes. In the second one, we introduce the second quantization formalism, necessary to describe the interference between indistinguishable photons, and some of the photon degrees of freedom in which information can be encoded, focusing on those used in the experiments described in this thesis. Finally, the third chapter provides the experimental background describing the general structure of a quantum information experiment using photons and the materials and technologies involved in implementing it.

In the second part, we describe two new methods developed during the thesis for the characterization of a linear optical interferometer. In the fourth chapter, we describe a black box approach, i.e. one that makes no assumptions about the structure of the interferometer, using classical light and second-order correlation measurements. The only methods already present in the literature that is insensitive to the phase noise present at the input and output of the interferometer use indistinguishable single photons [25]. Instead, our proposal maintains the same property by using a coherent light probe. This simplifies the characterization for apparatuses without quantum light sources. The fifth chapter describes a procedure for characterizing a universal interferometer with a geometry arranged in a Clements configuration [9]. Although such a geometry is widely used in recent years, no method has yet been presented in the literature for characterizing it that takes into account the possible imperfections present in an integrated chip implementing it.

In the third part, we present a 32-mode reconfigurable integrated circuit with a three-dimensional continuous-coupled structure for the realization of Boson sampling experiments. Specifically, in the sixth chapter we review the literature concerning the Boson sampling problem, and in the seventh, we describe the new chip and the experiments conducted to characterize and test the correct operation of the device.

In the fourth part, we present the Bernoulli factory problem and its quantum extensions. In the eighth chapter, we present a brief summary of the literature concerning the problem and then present the theoretical analysis of the problem by re-evaluating the result already present in the literature with a new technique that allows us to derive the computational complexity in terms of the minimum number of qubits required and the maximum success probability of the protocol. In addition, two new quantum variants of the Bernoulli factory problem called Multivariate quantum to quantum Bernoulli factory and Multifunctional quantum to quantum Bernoulli factory, respectively, are presented and analyzed. In the ninth chapter, we present the theoretical analysis and experimental implementation of a quantum-to-quantum Bernoulli factory photonics by going on to verify the correct operation of the proposed interferometers.

Finally, in the fifth and final part, the theory of quantum metrology and its application in two experiments developed during the doctoral program are presented. In the tenth chapter goes a summary of the literature concerning quantum metrology with special emphasis on techniques used for phase estimation. In the eleventh chapter, two experiments are presented. The first one is the simultaneous estimation of three phases in a photonic chip showing how the use of indistinguishable photons improves the error in the estimation compared to the single photon case. The second experiment concerns the measurement of the relative angle between two reference systems through the use of the orbital angular momentum of light going to show experimentally the overcoming of the classical precision limit and showing the validity of the results for a wide range of quantum resources used.

This thesis concludes with a brief summary of the results and possible perspectives on the development of the works presented.

Part I

Introduction to quantum information

Chapter 1

Quantum information and quantum computation

Quantum information theory is the field of physics that combines together information theory and quantum mechanics. Information theory has always implicitly used the fact that physical systems suitable for computation follow the rules of classical mechanics. Instead, quantum information theory assumes that the computing system follows the rules of quantum mechanics and it tries to understand what differences this change of paradigm brings. In the last two decades, we witnessed an increasing interest in this topic motivated by the benefits that quantum theory appears to bring to cryptography and computation [26]. In the scientific community, this idea of being able to increase the computing capacity with a quantum computer can be summarized in the concept of the *quantum advantage* [26, 27] which is used with two related but distinct meanings. The first one is the condition where there is an experimental demonstration that a quantum device can solve a particular problem faster compared to any classical computer. The second one is the condition in which the previous demonstration is performed with a universal quantum computer that is not specialized in solving that particular problem. In recent years claims of quantum advantages have been made [7, 8, 28, 29] but some of them have been successively disproved [30], therefore the effective achievement of the quantum advantage is still a matter of debate.

To better understand the theory of quantum information, in this chapter we present some of the fundamental concepts that will be useful for the rest of the thesis. In the first section, we will revise the principal aspects of quantum mechanic theory such as vector formalism, density matrix formalism and the concept of entanglement. In the next section, we will define the basic unit of quantum information called *qubit* and we describe some of its properties. In the third section, we will introduce the circuital formalism for quantum computation where a quantum algorithm is represented as a certain series of quantum gates acting on a group of qubits. In the last section, we will conclude with a brief revision of the computational complexity theory and the computational complexity classes to better frame the meaning of quantum advantage.

An important note is that this chapter only presents the concepts that are useful for the understanding of this PhD thesis, therefore this can not be considered an

exhaustive treatment of quantum information theory. For a more detailed description of the theory, please refer to the specific literature such as [26].

1.1 Quantum mechanics

In this section, we introduce the theory of quantum mechanics, in particular how to describe closed systems, their time evolution and how to measure them.

1.1.1 Vector formalism

The description of quantum mechanics using the vector formalism states that every physical system is represented by a complex vector $|\psi\rangle$ belonging to a Hilbert space $\mathcal{H}$. For historical reasons, this vector is called *wave function*. The dimension d of the Hilbert space necessary to describe the system under consideration is called the *dimension of the system*. For a closed system, the associated wave function $|\psi(t)\rangle$ evolves over time according to the Schrödinger equation:

$$i\hbar\frac{\mathrm{d}}{\mathrm{d}t}|\psi(t)\rangle = \hat{H}(t)\,|\psi(t)\rangle \tag{1.1}$$

where $\hbar$ is the reduced Planck constant, whose value is currently fixed by convention [31], and $\hat{H}(t)$ is a self-adjoint operator called *Hamiltonian* of the system. The relation between the states of the system at two different times t_1 and t_2 is given by a linear unitary transformation that does not depend on the initial state but only on the Hamiltonian and the two times considered

$$|\psi(t_2)\rangle = U(t_2, t_1)\,|\psi(t_1)\rangle \tag{1.2}$$

If the Hamiltonian $\hat{H}$ is time-independent, then the unitary transformation can be expressed as $U(t_2, t_1) = e^{-\frac{i}{\hbar}H(t_2-t_1)}$. If the system is open, i.e. can interact with an external environment, then the time evolution is no longer unitary. The Schrödinger equation is not valid anymore, and it is necessary to replace it with the so-called master equation [26].

Now that we have presented the description and the evolution of a physical system, we need to know how to measure it. At each measurable quantity, the quantum theory assigns a self-adjoint operator $\hat{O}$ acting on the Hilbert space of the system. The result of the measurement returns one of the eigenvalues of the operator and projects the wave function into the corresponding eigenstate of the operator. In formulas, if we define the eigenvectors of the operator as $\{|j\rangle\}_{j=1}^{d}$ with associated real eigenvalues $\{o_j\}_{j=1}^{d}$ we can write the observable as $\hat{O} = \sum_j o_j\,|j\rangle\langle j|$. We can also express the state of the system in the same basis as $|\psi\rangle = \sum_j s_j\,|j\rangle$, where $\{s_j\}_{j=1}^{d}$ are called the coefficient of the state associated to the considered base. Then, the probability to obtain the outcome o_k is given by the Born rule:

$$p_k = |\langle k|\psi\rangle|^2 = |s_k|^2 \tag{1.3}$$

Due to the normalization of the state vector, the Born rule returns a probability distribution over the outcome of the measure with $\sum_j p_j = 1$. The expectation value

of the physical observable $\hat{O}$ over the state $|\psi\rangle$ is

$$\left\langle \hat{O} \right\rangle = \sum_j p_j o_j = \sum_j o_j \langle \psi | j \rangle \langle j | \psi \rangle = \langle \psi | \hat{O} | \psi \rangle \tag{1.4}$$

and the standard deviation associated with the measure is

$$\Delta^2 \hat{O} = \left\langle \hat{O}^2 \right\rangle - \left\langle \hat{O} \right\rangle^2 \tag{1.5}$$

To conclude the section, it is useful to introduce one last concept. Given two observables $\hat{A}$ and $\hat{B}$ we say that they are *compatible* if their respective operators commute; i.e. $[\hat{A}, \hat{B}] \equiv \hat{A}\hat{B} - \hat{B}\hat{A} = 0$. This means that they can be diagonalized simultaneously and therefore they can be measured simultaneously ideally without uncertainty. Conversely, if the two operators do not commute $[\hat{A}, \hat{B}] \neq 0$ they are called *incompatible*. In this case, a common set of eigenstates for both operators do not exist, which means that they can not be simultaneously measured with unlimited precision. In particular, *the Schrödinger uncertainty relation* provides a quantitative limit to the simultaneous measurement accuracy of the two observables, via a lower bound on the product of the two observable uncertainties $\Delta\hat{A}\Delta\hat{B}$.

$$\Delta^2 \hat{A} \Delta^2 \hat{B} \geq \frac{1}{4} \left| \left\langle [\hat{A}, \hat{B}] \right\rangle \right|^2 + \frac{1}{4} \left| \left\langle \{\hat{A}, \hat{B}\} \right\rangle - \left\langle \hat{A} \right\rangle \left\langle \hat{B} \right\rangle \right|^2 \tag{1.6}$$

where $\{\hat{A}, \hat{B}\} \equiv \hat{A}\hat{B} + \hat{B}\hat{A}$. This inequality is equivalent to the *Heisenberg uncertainty principle* [32] with an additional term that makes the inequality more precise. It is important to notice that the additional term is also null in the case of compatible operators.

1.1.2 Density operator formalism

To introduce the density operator formalism, it is better to start with an example. We can suppose to have a source that generates particles that half of the times are in the state $|\psi_1\rangle$ and the remaining half in a different one $|\psi_2\rangle$. If we attempt to describe the state of a particle generated by the source just described, no matter how hard we try, we will never find a solution. Until now, we see that a quantum system can be described as a unitary complex vector in a Hilbert space, but this formalism is incomplete since it does not take into account possible ignorance about the system under consideration. To deal with this problem it is necessary to introduce a new way to describe a quantum system called *density operator formalism* or density matrix formalism. In this formalism, every quantum system is characterized by an operator ρ acting on a particular Hilbert space $\mathcal{H}$. Each vector $|\psi\rangle$ in the previous formalism is associated to a projector operator $\hat{P}_\psi$ that can be written as:

$$\rho = \hat{P}_\psi = |\psi\rangle\langle\psi| \tag{1.7}$$

Since there is a one-to-one relationship between the vectors in the Hilbert space and the projector operators on it, those operators are also called *pure states*. Conversely, a *Mixed state* is a convex combination of an ensemble of pure states and can be written as:

$$\rho = \sum_i p_i |\psi_i\rangle\langle\psi_i| \tag{1.8}$$

In this notation, the elements p_i represent the probability that the system described by the density matrix ρ is in the state $|\psi_i\rangle$. In general, a density operator ρ is a Hermitian semidefinite positive operator acting on the Hilbert space $\mathcal{H}$ with trace one, that in formulas is:

$$\rho^\dagger = \rho \qquad \forall\, |\psi\rangle \in \mathcal{H}\ \ \langle\psi|\,\rho\,|\psi\rangle \geq 0 \qquad Tr(\rho) = 1 \tag{1.9}$$

The Schrödinger equation for the density matrix can be written as

$$i\hbar \frac{\mathrm{d}}{\mathrm{d}t}\rho(t) = [H, \rho(t)] \tag{1.10}$$

and the evolution between the matrices at different times is

$$\rho(t_2) = U(t_2, t_1)\rho(t_1)U^\dagger(t_2, t_1) \tag{1.11}$$

where the unitary matrix $U(t_2, t_1)$ is the same as described in the previous formalism. To complete the description, we need to define the measurement. Given an observable $\hat{O}$ the expectation value over the state ρ is defined as

$$\left\langle \hat{O} \right\rangle = \mathrm{Tr}\Big(\hat{O}\rho\Big) \tag{1.12}$$

Moreover, writing the operator in the eigenbasis $\hat{O} = \sum_j o_j\, |j\rangle\langle j|$, the probability to obtain the outcome o_j is

$$p_j = \mathrm{Tr}\Big(\hat{P}_j\rho\Big) = \langle j|\rho|j\rangle \tag{1.13}$$

and the projection on the eigenstate is

$$\rho' = \frac{\hat{P}_j\rho\hat{P}_j}{\mathrm{Tr}\Big(\hat{P}_j\rho\Big)} \tag{1.14}$$

Now that we have defined what is a density matrix, we are going to see some related properties and definitions. The first important concept is the purity. We define a density matrix "pure" if it is associated with a pure state, this means that we can use the definition of projector operator to test the purity of a state, so a state is pure if and only if the equality $\rho^2 = \rho$ is satisfied. Moreover, we can quantify the degree of purity of a density operator as the quantity $\mathcal{P} = \mathrm{Tr}(\rho)^2$. For operators on a Hilbert space of dimension d, this quantity range from $1/d$ to 1 and it is equal to 1 only if the state is pure. The lower bound is reached for the state $\rho = \frac{1}{d}\mathbb{I}$.

The second important concept is coherence. To be clearer, we will start with an example considering the state $\rho_1 = \frac{1}{2}(|0\rangle\langle 0| + |1\rangle\langle 1|)$ and the state $\rho_2 = (\frac{|0\rangle+|1\rangle}{\sqrt{2}})(\frac{\langle 0|+\langle 1|}{\langle 2|})$. If we represent the associated matrices on the basis $|0/1\rangle$ then we have

$$\rho_1 = \frac{1}{2}\begin{pmatrix} 1 & 0 \\ 0 & 1 \end{pmatrix} \qquad \rho_2 = \frac{1}{2}\begin{pmatrix} 1 & 1 \\ 1 & 1 \end{pmatrix} \tag{1.15}$$

The measurement on the basis $|0/1\rangle$ returns the same 50 : 50 statistics for both states. Instead, if we perform a measurement on the $|\pm\rangle = \frac{|0\rangle\pm|1\rangle}{\sqrt{2}}$ basis, then the first state returns as previously a 50 : 50 statistics and the second one returns +

with probability 1. As we can see, the difference between the two states lies in the off-diagonal terms. The diagonal terms of the density matrix are called the *population* of the basis used to represent the matrix, they are the probabilities that a measure in the chosen basis returns the corresponding pure state. Instead, the off-diagonal terms are called the *coherence therms* and represent the coherence between the basis state used. Those terms are relevant only when a change of basis is performed as we saw in the example of the previous paragraph. It is important to notice that, due to the Hermitian property, always exists a basis even if not unique, such that the density matrix does not have the coherence terms. In this context, the state $\rho = \frac{1}{d}\mathbb{I}$ plays a particular role, it is called *totally mixed state* since it is the most mixed state and it does not present coherence therm in any basis.

As seen at the beginning, a mixed state can be created when a source generates states probabilistically extracted from an ensemble. This situation is not the only one where it is necessary to describe the state with a density matrix. This formalism is also useful to describe the state of a subsystem of a composite one. For example, when a system is composed of various degrees of freedom but only some of them are accessible or taken into account. For instance, given a joint state $|\psi_{AB}\rangle \in \mathcal{H}_A \otimes \mathcal{H}_B$, the state of the system A can be obtained by the partial trace over the space $\mathcal{H}_B$.

$$\rho_A = \mathrm{Tr}_B(|\psi_{AB}\rangle\langle\psi_{AB}|) \tag{1.16}$$

1.1.3 Composite system, entangled/separable states

We have seen how to describe a quantum system, now we see what happens when we combine two or more of them together. We suppose to have two systems A and B described respectively by the Hilbert spaces $\mathcal{H}_A$ and $\mathcal{H}_B$, obviously, there is a Hilbert space that describes the combined system and it is defined as the tensor product between the two original spaces $\mathcal{H}_{AB} = \mathcal{H}_A \otimes \mathcal{H}_B$. This means that the dimension of the combined system is the product of the dimensions of the single ones. Defined $\{|i\rangle\}_{i=1}^{d_A}$ and $\{|j\rangle\}_{j=1}^{d_B}$ respectively a basis for the system A and B a generic pure state $|\psi\rangle$ in the combined space can be written as

$$|\psi\rangle = \sum_{i,j} c_{i,j} |i\rangle \otimes |j\rangle \qquad c_{i,j} \in \mathbb{C} \qquad \sum_{i,j} |c_{i,j}|^2 = 1 \tag{1.17}$$

In this situation when more than one system are involved, new physical phenomena appear, in particular one of the most controversial features is called *Entanglement*. A pure quantum state $|\psi\rangle$ of a composite system is called *separable* if it can be written in the form

$$|\psi\rangle = |\psi_A\rangle \otimes |\psi_B\rangle \tag{1.18}$$

For the density matrix ρ the condition of separability is the existence of two sets of states $\{\rho_{Ai}\}$, $\{\rho_{Bi}\}$ and a set of probability $\{p_i\}$ such that the state can be written as

$$\rho = \sum_i p_i \rho_{Ai} \otimes \rho_{Bi} \tag{1.19}$$

A state that is not separable is called *entangled*. A pure state of a bipartite system is called *maximally entangled* if the reduced matrix for each subsystem is totally mixed.

Entanglement is one of the most discussed and controversial effects of quantum theory and it takes a fundamental role for some of the well-known quantum algorithms such as super dense coding [33], quantum teleportation [34] and particular protocols of quantum cryptography [35].

1.2 Qubit and Qudit

In classical information theory, the fundamental unit of information is the bit. It can be any physical quantity that takes two distinct values normally identified with the two logical states $\{0, 1\}$. In quantum information theory, the bit is replaced with its quantum counterpart called qubit which is a vector in a two-dimensional Hilbert space. In this space, we can identify a privileged basis called the *computational basis* whose components are normally indicated as $\{|0\rangle, |1\rangle\}$. As the notation suggests, those basis elements are associated with the corresponding classical logical states. A generic qubit state $|\psi\rangle$ can be written as a superposition of the two basis vectors

$$|\psi\rangle = \alpha\,|0\rangle + \beta\,|1\rangle \tag{1.20}$$

where $\alpha, \beta \in \mathbb{C}$ with the constraint $|\alpha|^2 + |\beta|^2 = 1$. This definition of qubit shows its substantial difference compared to the classical equivalent. Indeed, during a classical computation the bits always have a well-defined value. This is also true for the probabilistic algorithms since even if the value of some bits is not defined in advance, during the computation it is assigned to them. On the other hand, the qubit can be in a superposition state all the time. This property is at the basis of what is historically called *quantum parallelism*, i.e. the possibility of storing different data in the same state and processing them all at the same time due to the superposition princile [36]. However, the computational power of quantum parallelism is heavily mitigated by the quantum theory itself; in particular, the projection of the state due to a measure allows only one bit of information to be extracted from a qubit. This and other problems have limited the development of new quantum algorithms but on the other hand, they have led to the more in-depth development of quantum information theory to understand the real potential and limitations of quantum computation.

The expression of a generic qubit state in eq: (1.20) can be simplified, for example, the multiplication of a state for a phase does not change the physics of the system represented. The general qubit state $|\psi\rangle$ can be represented by two real parameters as in the form:

$$|\psi\rangle = \cos\frac{\theta}{2}\,|0\rangle + \sin\frac{\theta}{2}e^{i\phi}\,|1\rangle \tag{1.21}$$

with $\theta \in [0, \pi]$ and $\phi \in [0, 2\pi]$. This parameterization is one of the most suitable since it already takes state normalization into account and uses the minimum number of parameters necessary. Furthermore, it shows a profound connection between the Hilbert space of a qubit and the surface of a three-dimensional sphere. Using the parameters θ and ϕ as polar coordinates, it is possible to associate each qubit state to a point on the surface of the unit sphere and vice-versa. This representation of a two-dimensional Hilbert space is called *Bloch-sphere*.

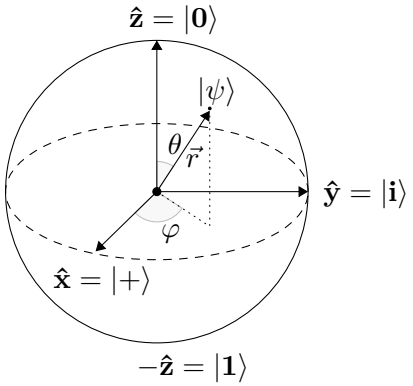

Figure 1.1. Block-sphere representation of a qubit's Hilbert space. The Bloch-sphere is a sphere of radius one that represents the Hilbert space of a Qubit. Each point on the surface of the sphere can be associated with a pure state in the Hilbert space and vice-versa. The points inside the sphere can be associated one-to-one with the mixed states of a qubit. The states at the intersection between the surface and the Cartesian axis are $|0/1\rangle$, $|\pm\rangle$ and $|\pm i\rangle$ that are respectively the eigenvalue of the Pauli matrices $\hat{Z}$, $\hat{X}$ and $\hat{Y}$.

Now we define three operators called *Pauli operators* whose matrix representations in the computational basis are:

$$\hat{X} = \begin{pmatrix} 0 & 1 \\ 1 & 0 \end{pmatrix} \qquad \hat{Y} = \begin{pmatrix} 0 & -i \\ i & 0 \end{pmatrix} \qquad \hat{Z} = \begin{pmatrix} 1 & 0 \\ 0 & -1 \end{pmatrix} \tag{1.22}$$

All the three operators have eigenvalue 1 and -1 with eigenvectors $|\pm\rangle = \frac{|0\rangle \pm |1\rangle}{2}$ for the $\hat{X}$-operator, $|\pm i\rangle = \frac{|0\rangle \pm i|1\rangle}{2}$ for the $\hat{Y}$-operator and $|0/1\rangle$ for the $\hat{Z}$-operator. Those three sets of states form a group of mutually unbiased basis, meaning that the scalar product between each couple of states in all the different basis is the same and it is equal to $\sqrt{2}/2$. Moreover, those states on the Bloch sphere are situated at the intersection between the surface and the Cartesian axis.

The Pauli matrices take an important role in the representation of the state of a qubit. Defining the vector of matrices $\vec{\sigma} = (\hat{X}, \hat{Y}, \hat{Z})^T$ a generic density matrix for a qubit can be expressed as

$$\rho_{\vec{r}} = \frac{\mathbb{I} + \vec{r} \cdot \vec{\sigma}}{2} \tag{1.23}$$

where $\vec{r}$ is a tridimensional vector with $|\vec{r}| \leq 1$. The purity of the state is related to the modulus of the vector $\vec{r}$ by the relation

$$\mathcal{P}(\rho_{\vec{r}}) = \frac{1 + |\vec{r}|^2}{2} \tag{1.24}$$

showing that a state is pure if $|\vec{r}| = 1$. In the Bloch sphere, the vector $\vec{r}$ represents the vector that connects the center of the sphere to the point representing the associated state. With this geometrical representation, we can see that all the pure states live on the surface of the sphere, while all the internal states are mixed and that at the center of the sphere there is the fully mixed state.

Since it will be useful in the following chapters, a different characterization is introduced where each qubit state is associated with a complex number $z \in \mathbb{C}$. The idea is to use the map induced by the stereographic projection that associates each point in the complex plane to a point on the surface of the unit sphere called the Riemann sphere [37]. By identifying the Riemann sphere with the Bloch sphere and applying the inverse transformation, we construct the map between the qubit states and the complex numbers. If the description made so far may seem complicated, in reality, the map is particularly simple to describe. Given a complex number $z \in \mathbb{C}$ the associated state is:

$$|z\rangle = \frac{z\,|0\rangle + |1\rangle}{\sqrt{1+|z|^2}} \tag{1.25}$$

the relation between the complex parameter and the polar coordinate is given by the formula:

$$z = \cot\left(\frac{\theta}{2}\right) e^{-i\phi} \tag{1.26}$$

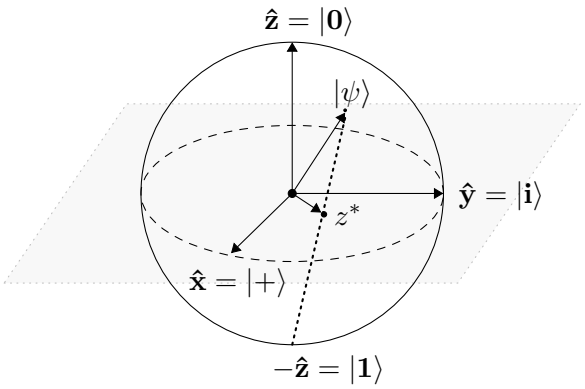

Figure 1.2. Complex representation of the qubit state Each qubit state can be represented by a complex number z. The idea is to use the map induced by the stereographic projection that for each point in the complex plane associates a point on the Riemann sphere. Reversing this relation is possible to associate each state on the Bloch Sphere with a complex number.

Before concluding the section, we introduce a generalization of the concept of qubit. As was done in classical information theory where the concept of trit was introduced, which is a physical system that can have three distinct values usually identified with $\{0, 1, 2\}$, also in quantum information theory was introduced the concept of *qudit* that is the generalization of the qubit for a system with dimension d. The general state of a qudit is defined as

$$|\psi\rangle = \sum_{i=1}^{d} \alpha_j\,|j\rangle \tag{1.27}$$

where $\alpha_j \in \mathbb{C}$ with the constraint $\sum_j |\alpha_j|^2 = 1$ and the set of states $\{|j\rangle\}_{j=1}^{d}$ is a generalization of the computational basis to the d-dimensional case. To describe the state of a qudit various parametrizations can be proposed, one is the generalization

of the parametrization with the complex number done previously for the qubit. A qudit can be associated with a tuple of $d-1$ complex number $(z_1, \ldots, z_{d-1})$ such that the state can be written as

$$|\psi\rangle = \frac{\sum_{j=0}^{d-1} z_j |j\rangle + |d\rangle}{\sqrt{1 + \sum_j |z_j|^2}} \tag{1.28}$$

The concept of qudit is important since it has been seen that in some cases it is more performing than the two-dimensional counterpart. In particular, in the literature, we can find quantum cryptographic and communication protocols that guarantee higher performances in terms of security and resilience to noise if implemented with qudits [38–43].

1.2.1 Random qubit state generation

In the following, we will briefly describe how to sample a random qubit. The first essential concept to understand is which distribution we consider uniform in the two-dimensional Hilbert space. Since the most general linear transformation in the Hilbert space is the unitary matrix we define a distribution uniform if it is invariant over all the possible unitary transformations. In order not to go into too much mathematical detail we can use the fact that a unitary transformation of the two-dimensional Hilbert space can be associated with a rotation of the Bloch sphere and vice versa. Therefore the uniform distribution of the space is exactly the uniform distribution on the Bloch sphere. Using the polar coordinates θ and ϕ, it is well known that sampling uniformly on the surface of the sphere is equivalent to sampling uniformly in the parameters $\phi \in [0, 2\pi]$ and $h = \cos(\theta) \in [-1, 1]$. So the uniform distribution of the qubit states can be written as

$$|\psi\rangle = \frac{\sqrt{1+h}\,|0\rangle + \sqrt{1-h}e^{i\phi}\,|1\rangle}{\sqrt{2}} \qquad (h, \phi) \in [-1, 1] \times [0, 2\pi) \text{ uniformly} \tag{1.29}$$

With this we can also write the distribution on the complex plane such that the associate distribution of state is uniform in the Hilbert space. In formulas, the distribution can be written as

$$z = \sqrt{\frac{1+h}{1-h}} e^{-i\phi} \qquad (h, \phi) \in [-1, 1] \times [0, 2\pi) \text{ uniformly} \tag{1.30}$$

1.2.2 Qubit entangled states

In the theory of quantum information, certain particular entangled states play an important role at theoretical and practical levels.

For a system of two qubits, the four maximally entangled states are

$$\left|\Phi^{\pm}\right\rangle = \frac{|0\rangle\,|0\rangle \pm |1\rangle\,|1\rangle}{\sqrt{2}} \qquad \left|\Psi^{\pm}\right\rangle = \frac{|0\rangle\,|1\rangle \pm |1\rangle\,|0\rangle}{\sqrt{2}} \tag{1.31}$$

Those states, called also Bell or EPR states, form a basis for the two-qubit space and possess the property that if the bases used for each of the two qubits coincide,

then the state coefficients remain the same. For those reasons, those states are at the basis of most quantum protocols involving entanglement.

Another well-known entangled state is the GHZ state [44]. This is a state of three qubits that can be seen as a generalization of the Bell state $|\Phi^+\rangle$ and it is written as

$$|GHZ\rangle = \frac{|000\rangle + |111\rangle}{\sqrt{2}} \tag{1.32}$$

This state is particularly peculiar and finds applications in quantum causality [44], quantum metrology [45] and quantum cryptography [46]. The natural generalization of the GHZ to N qubits is the state

$$|GHZN\rangle = \frac{|0\rangle^{\otimes N} + |1\rangle^{\otimes N}}{\sqrt{2}} \tag{1.33}$$

1.3 Quantum circuit

Now that we have defined what is the quantum unit of information we need to know how to manipulate it to perform a quantum algorithm.

In classical computation, components called logic gates are used to build every circuit implementing a logic function. There are 7 fundamental logic gates that can create any logic circuit, one is a one-bit gate and the other 6 are two-bit gates. Their names are: NOT, AND, NAND, OR, NOR, XOR and XNOR and they implement the logical functions suggested by their names. This set of gates is universal but redundant, indeed, it is possible to show that the only necessary gate is the NAND or the NOR, given that all the other gates can be built starting from it.

In analogy with the classic case, the quantum circuit model was created. The qubits are represented by wires that enter and exit quantum logic gates in order to implement a quantum algorithm [26]. For a quantum circuit, there are two substantial differences compared to the classic equivalent. The first one is that due to the no-cloning theorem [47] it is not possible to copy a qubit which means that it is not possible to divide a wire in two. The second difference is that all logic operations are unitary and therefore reversible. This implies that, unlike the classical logic gates, the quantum ones must have the same number of input and output qubits. As done for the classical case, it is possible to divide quantum gates into two classes, those that act on one qubit and those that operate on more than one.

1.3.1 Single-qubit gates

By defining the two vectors of the computational basis as

$$|0\rangle \equiv \begin{pmatrix} 1 \\ 0 \end{pmatrix} \qquad |1\rangle \equiv \begin{pmatrix} 0 \\ 1 \end{pmatrix} \tag{1.34}$$

We can represent any logic gates acting on a single qubit as a 2×2 unitary matrix $U \in SU(2)$ or equivalently as a rotation of the Bloch sphere. The generic single qubit gate can be expressed as:

$$U(\vec{n}, \xi) = e^{-i\frac{\xi}{2}\vec{n}\cdot\vec{\sigma}} = \cos\left(\frac{\xi}{2}\right)\mathbb{I} - i\sin\left(\frac{\xi}{2}\right)\vec{n}\cdot\vec{\sigma} \tag{1.35}$$

where $\vec{n}$ is the unit vector indicating the axis of the rotation of the Bloch sphere, ξ the angle of rotation and $\vec{\sigma}$ is the vector of Pauli matrices. Now that we have a representation of all the possible logical gates acting on a single qubit we can think if it is possible to reduce the number of different matrices type necessary to generate all the possible gates.

Using the associations between the gate and the rotation of the Bloch sphere we can use the well-known theory of tridimensional rotations to try to simplify the problem. In particular, the decomposition of the rotation with the Euler angle tells us that all we need are only two rotations around orthogonal axes. Defining the two matrices

$$R_z(\theta) = e^{-i\frac{\theta}{2}\hat{Z}} = \begin{pmatrix} e^{-i\frac{\theta}{2}} & 0 \\ 0 & e^{-i\frac{\theta}{2}} \end{pmatrix} \qquad R_y(\theta) = e^{-i\frac{\theta}{2}\hat{Y}} = \begin{pmatrix} \cos\frac{\theta}{2} & \sin\frac{\theta}{2} \\ -\sin\frac{\theta}{2} & \cos\frac{\theta}{2} \end{pmatrix} \tag{1.36}$$

then every gate can be expressed as

$$U(\alpha, \beta, \gamma) = R_z(\alpha) R_y(\beta) R_z(\gamma) \tag{1.37}$$

However, we are not completely satisfied by this decomposition since it uses two different matrices both controlled by a parameter. Introducing the Hadamard gate $\hat{H}$ defined as

$$\hat{H} = \frac{1}{\sqrt{2}} \begin{pmatrix} 1 & 1 \\ 1 & -1 \end{pmatrix} \tag{1.38}$$

we can use it associated with the rotation $R_z(\theta)$, sometimes called also the phase gate and indicated as $\hat{P}(\theta)$, to decompose the general gate as

$$U(\phi, \theta, \psi) = \hat{P}(\phi)\hat{H}\hat{P}(\theta)\hat{H}\hat{P}(\psi) \tag{1.39}$$

as we can see this decomposition uses only a single parametrized matrix but at the cost that we need to apply five gates instead of three.

1.3.2 Two-qubit Gates

Multi-qubit gates are operations that allow qubits to interact with each other, they are fundamental for the realization of more complex circuits and in particular for the creation of entanglement. In this section, we will focus only on two-qubit gates since it is possible to build all gates acting on more qubits starting from those.

Defining the computational basis for two-qubit as

$$|00\rangle \equiv \begin{pmatrix} 1 \\ 0 \\ 0 \\ 0 \end{pmatrix} \qquad |01\rangle \equiv \begin{pmatrix} 0 \\ 1 \\ 0 \\ 0 \end{pmatrix} \qquad |10\rangle \equiv \begin{pmatrix} 0 \\ 0 \\ 1 \\ 0 \end{pmatrix} \qquad |11\rangle \equiv \begin{pmatrix} 0 \\ 0 \\ 0 \\ 1 \end{pmatrix} \tag{1.40}$$

we can express all the two-qubit gates as 4×4 unitary matrices. Among all the possible gates there is a particular class that plays a significant role and that is the *control gates*. A controlled unitary gate or CU is a gate acting on two qubits called respectively control $|c\rangle$ and target $|t\rangle$. The gate applies a unitary transformation U

on the target qubit only if the control one is in the state $|1\rangle$. The associated matrix expression is

$$CU = \begin{pmatrix} 1 & 0 & 0 & 0 \\ 0 & 1 & 0 & 0 \\ 0 & 0 & u_{11} & u_{12} \\ 0 & 0 & u_{21} & u_{22} \end{pmatrix} \tag{1.41}$$

where u_{11}, u_{12}, u_{21} and u_{22} are the components of the unitary matrix U. Among the controlled gates, there is one called CNOT or CX that plays an important role since all the other controlled gates can be constructed from this one. The CNOT gate is the quantum equivalent of the XOR gate:

$$CNOT(|c\rangle\,|t\rangle) = |c\rangle\,|c \oplus t\rangle \tag{1.42}$$

where $\oplus$ is the sum modulus 2. The matrix representation of the CNOT is

$$CNOT = \begin{pmatrix} 1 & 0 & 0 & 0 \\ 0 & 1 & 0 & 0 \\ 0 & 0 & 0 & 1 \\ 0 & 0 & 1 & 0 \end{pmatrix} \tag{1.43}$$

Another extremely important two-bit gate is called SWAP and it exchanges the states of the two qubits in inputs, the matrix representation is

$$SWAP = \begin{pmatrix} 1 & 0 & 0 & 0 \\ 0 & 0 & 1 & 0 \\ 0 & 1 & 0 & 0 \\ 0 & 0 & 0 & 1 \end{pmatrix} \tag{1.44}$$

In many physics implementations, the qubits are arranged in a lattice where operations are allowed only between adjacent qubits. This particular gate enables us to move the state from one qubit to another allowing the appropriate positioning of the states to progress the computation.

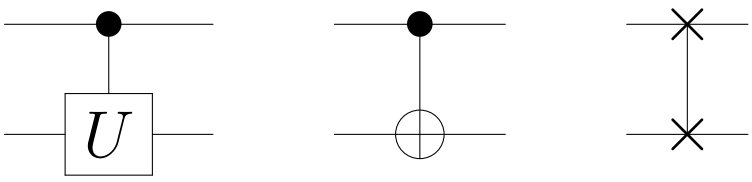

Figure 1.3. Circuit representation of some two-qubit gates. From left to right there is the representation of the CU gate, the CNOT and the SWAP. For the controlled gates, the upper wire is the control qubit and the lower wire is the target one.

Using the gates presented up to now let's see a simple quantum circuit that is of particular interest. In Fig. 1.4 it is represented a circuit that converts the computational basis in the Bell states basis, in particular maps the state $|00\rangle$ in the state $|\psi^+\rangle$. The circuit is composed of a Hadamard gate followed by a CNOT.

To do the inverse transformation it is simply necessary to use the mirrored circuit. These couple of circuits are very useful since allow to create and measure the Bell states that are at the base of some of the most important quantum protocols.

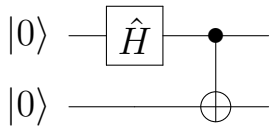

Figure 1.4. Circuit for the generation of Bell state. The circuit represented in the figure allows the creation of the Bell state $|\Phi^+\rangle$. A Hadamard gate is used to generate the superposed state $|+\rangle$ on the control qubit then a CNOT creates the entanglement between the two qubits.

1.3.3 Deferred Measurement Principle

In this section, we see a principle of quantum computing that will be useful in later chapters. The *Deferred Measurement Principle* asserts that a quantum circuit with intermediate measurement can be simulated by a quantum circuit with only measurements at the end with at most a linear overhead. Here we do not cover all the demonstration of the principle [26, 48] but we analyze two examples that show the idea behind the principle.

The first example is when the result of a measurement is used to control an operation on a different qubit, see Fig. 1.5. The idea is that if we replace the conditioned operation with an equivalent controlled unitary operation performed before the measurement the result is the same, which means that the output state and the probabilities of the events are the same for the two circuits.

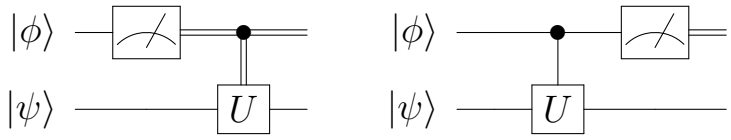

Figure 1.5. Commutation Between Measurement and quantum control. The two circuits depicted are equivalent, which means that all the output quantum states and the probability are the same

For the circuit in Fig. 1.6 the situation is a bit different. In this case, a qubit is measured and then the resulting state is used to continue the computation. The performed measurement may not commute with the quantum operations applied to the result, this means that we need a different strategy to be able to postpone the measurement. The idea is to replace the measurement with a CNOT gate having as control the original qubit and as target an ancillary qubit. This implies that measuring the ancilla or the original qubit is equivalent. At this point, it is possible to delay the measure of the ancilla at the end of the computation. In this way, the

result we will have is equivalent to those we would have obtained if we had made the intermediate measurement.

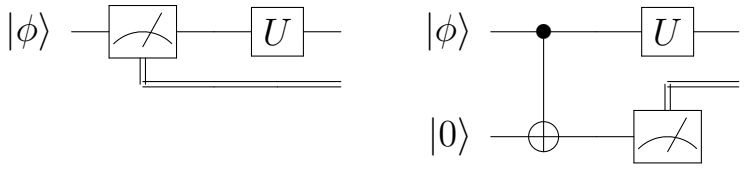

Figure 1.6. Replacement of a measure. In this case, a measure is replaced with a CNOT gate acting on an ancillary qubit. Since the two qubits became entangled and no operations are performed on the ancillary one, a measurement of the latter is equivalent to having performed the intermediate measurement at the position of the CNOT.

1.4 Fidelity between quantum states

In quantum information theory, a pivotal requirement is the possibility to quantify the distance between two quantum states [26]. This permits us to evaluate the agreement between an experiment and the theory. To quantify how much two states are similar there are some functions called *fidelities*. A function of two density matrices $F(\rho, \sigma)$ is a fidelity if it follow the properties below:

i *Symmetry*: $F(\rho, \sigma) = F(\sigma, \rho)$

ii *bounded value*: $0 \leq F(\rho, \sigma) \leq 1$

iii *Identity of indiscernible*: $F(\rho, \sigma) = 1 \Leftrightarrow \rho = \sigma$

iv *Invariance under unitary transformation*: $F(U\rho U^\dagger, U\sigma U^\dagger) = F(\rho, \sigma)$

v *Pure state fidelity*: $F(|\phi\rangle\langle\phi|, |\psi\rangle\langle\psi|) = |\langle\phi|\psi\rangle|^2$

The most common fidelity is the *Uhlmann's fidelity* described by the formula

$$F(\rho, \sigma) = \mathrm{Tr}\left(\sqrt{\sqrt{\rho}\sigma\sqrt{\rho}}\right)^2 \tag{1.45}$$

Furthermore, we would like to define a fidelity also for the unitary matrices so we can compare a physical implementation of a quantum circuit with the theoretical counterpart. The most common one is the *Hilbert-Smith inner product* and it is defined as

$$F(U, \tilde{U}) = \frac{1}{d}\sum_{i,j} U^*_{ij}\tilde{U}_{j,i} = \frac{1}{d}\,\mathrm{Tr}\left(U^*\tilde{U}\right) \tag{1.46}$$

where d is the dimension of the matrix. This fidelity is equivalent to considering the columns of the unitary transformation as a quantum state and computing the mean fidelity between the set of states of the two matrices.

1.5 Introduction to the computational complexity theory

In this last section, we will provide an overview of the computational complexity theory [49] that is necessary to understand the concept of quantum advantage. Intuitively, when we try to solve a problem with a computer, we realize that there are simpler problems and more difficult ones. The computational complexity theory is a branch of computability theory that formalize the concept of complexity of a problem by quantifying the resources needed to solve it through an algorithm using a particular model of computation. This quantification allows the grouping of computational problems into *classes of complexity*. The two types of resources primarily used for the classification are space and time: space is the amount of memory used during the execution of the algorithm needed to solve the problem; by time we mean the number of elementary operations performed by the program, such as accessing and writing memory, adding two numbers or comparing them. The set of problems for which we analyze the classes of complexity are the so-called decision problems, those are all the problems that can be posed as a yes-no question. The first class of complexity for the decisional problems is the class **P** of the problems that can be solved in polynomial time compared to the size of the input n that is the minimum number of bit required to describe the input. An example of **P** problem could be: "Given a list of n integers and an integer k, is there a number in the list greater than k?"; clearly the question can be solved in time linear in n since it is sufficient to go through the list and check all the numbers one by one. The next class of complexity **NP** is the class of problem that can be verified in polynomial time. For example, the following problem is in **NP**: Given a list of n integers and an integer k, is there a set of integers in the list that the sum is equal to k?"; So far no algorithms have been found that solves the problem in polynomial time but, if a solution is provided, then it is easy to check whether it is correct or not. It's straightforward to convince ourselves that $\mathbf{P} \subseteq \mathbf{NP}$ since to test a problem in **P** we just need to solve it. The equality or not between the two sets is still an open problem but most of the scientific community believes that they are distinct. To check whether the equality is valid or not, we have to look at the so-called **NP**-Hard and **NP**-complete problems. A problem is **NP**-Hard if every **NP** problem can be mapped to that problem in polynomial time. A **NP**-complete problem is a **NP**-Hard problem that belongs in the **NP** class, this implies that if one of these problems can be solved in polynomial time then the class **NP** and **P** coincide. Another class of complexity is the class of problem **coNP** that contains all the problems that are the complement of a **NP**, meaning that it is possible to certify the non-existence of a solution for the problem. A strong belief is that $\mathbf{NP} \neq \mathbf{coNP}$.

To do a step forward we introduce the concept of oracle. An oracle is a black box machine that can solve a certain class of decisional problems in a single operation. Obviously is only a theoretical machine but it is useful for the definition of certain classes of complexity. With the symbol $\mathbf{X}^{\mathbf{Y}}$ we define the class of problems that would be in class **X** if we had an oracle that solves problems in class **Y**. For example, the class $\mathbf{P}^{\mathbf{NP}}$ is the class of the problems that are polynomials in time if an oracle for the class **NP** exists.

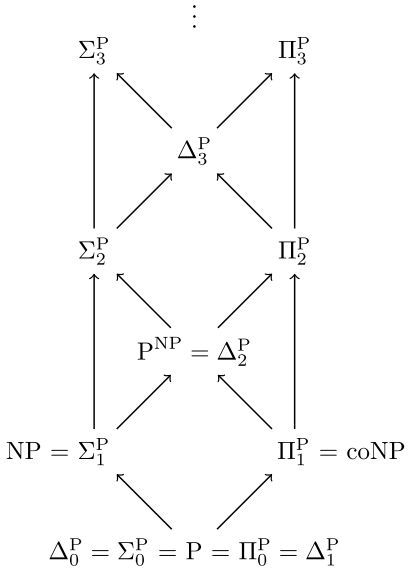

Figure 1.7. Polynomial hierarchy. Pictorial representation of the component of the polynomial hierarchy class **PH**. The arrows denote inclusion.

Now we have all the ingredients needed to define the polynomial hierarchy. Starting from the **P** class we can define the following classes:

- $\Delta_0^{\mathbf{P}} = \Sigma_0^{\mathbf{P}} = \Pi_0^{\mathbf{P}} = \mathbf{P}$
- $\Delta_{i+1}^{\mathbf{P}} = \mathbf{P}^{\Sigma_i^{\mathbf{P}}}$
- $\Sigma_{i+1}^{\mathbf{P}} = \mathbf{NP}^{\Sigma_i^{\mathbf{P}}}$
- $\Pi_{i+1}^{\mathbf{P}} = \mathbf{coNP}^{\Sigma_i^{\mathbf{P}}}$

these definitions create a hierarchy of classes depicted in Fig. 1.7 and the polynomial hierarchy class **PH** is defined as the union of all of these classes

$$\mathbf{PH} = \bigcup_i \Sigma_i^{\mathbf{P}} = \bigcup_i \Pi_i^{\mathbf{P}} = \bigcup_i \Delta_i^{\mathbf{P}} \tag{1.47}$$

and the following inclusion hold:

$$\Sigma_i^{\mathbf{P}} \subseteq \Delta_{i+1}^{\mathbf{P}} \subseteq \Sigma_{i+1}^{\mathbf{P}} \qquad \Pi_i^{\mathbf{P}} \subseteq \Delta_{i+1}^{\mathbf{P}} \subseteq \Pi_{i+1}^{\mathbf{P}} \tag{1.48}$$

Is strongly believed that the polynomial hierarchy does not collapse at any level meaning that all the inclusions in the hierarchy are proper inclusions.

All the complexity classes defined up to now have been defined considering only the possibility of using deterministic algorithms. If we consider the possibility of using probabilistic algorithms then we can define the complexity class **BPP** of the bounded-error probabilistic polynomial time problems. Those are the problems that can be solved by a polynomial probabilistic classical algorithm with a probability error of at most 1/3 for all instances. The relation between the **BPP** and those

previously defined is not fully understood, we only know that the following inclusion must be valid

$$\mathbf{BPP} \subseteq \Sigma_2^{\mathbf{P}} \cap \Pi_2^{\mathbf{P}} \tag{1.49}$$

The quantum analogous of the **BPP** class is called **BQP**. The relationship between this and the other previous classes is also not known. Surely the intersection between the **BQP** class and the **NP** class is not null due to the Shor algorithm [50] that solves in polynomial time the factorization problem that is a well-known **NP** problem. The other relation is the inclusion $\mathbf{BPP} \subseteq \mathbf{BQP}$ since a quantum computer can simulate a classical probabilistic algorithm. The inclusion is believed to be proper due to the Boson sampling problem. In the following chapters, we will deal with the problem in more detail. What we need to know at the moment is that if a problem is in **BQP** but at the same time it is also in **BPP** then the polynomial hierarchy collapses at the third level [27, 51] a situation conjectured extremely improbable.

Chapter 2

Quantum information with photons

The study of quantum information and quantum computation requires different physical systems to implement the experimental verification depending on the specific task and purpose. From the very first proposals, light and photons immediately imposed themselves as one of the most used systems to experimentally study the theory of quantum information. Indeed, photons are the ideal physical system to employ in a lot of scenarios due to their high mobility and low interaction with the environment. Also, there are different degrees of freedom that can be exploited to encode qubits or qudits such as polarization, phat, time bin and frequency. Moreover, there are several well-studied common techniques to generate, manipulate and detect the photons and their degrees of freedom [52].

In this chapter, we will introduce the second quantization formalism and the concept of photon. After that, we present the degrees of freedom of the photon used in this work and the mathematical description of the principal component act to manipulate those degrees of freedom. In the end, we present the multi-photon interference in a linear interferometer, with a particular focus on the Hong-Ou-Mandel effect.

2.1 Photons and Fock States

The dynamics of the electromagnetic field and light are described by Maxwell's equations. Even though those equations perfectly describe a huge amount of phenomena, there are still some that do not have explanations in the theory. With the formulation of quantum mechanics, the electromagnetic field can also be described in the theory using the second quantization formalism [53]. In this formalism, each mode of the field is associated with a harmonic oscillator and the *photon* is a single excitation of those oscillators. Therefore, all the phenomena are described in terms of the creation and annihilation operators of the harmonic oscillators. A generic state for the electromagnetic field lives in a Hilbert space called *Fock space*. A base for the space is formed by the so-called *Fock states*. Those states are characterized by a tuple of positive numbers $|n_1, \ldots, n_k\rangle$ describing the number of excitation (photons) for each mode of the electromagnetic field. Considering one single mode the

corresponding Fock state is represented by the number of photons on that particular mode $|n\rangle$. Then the annihilation $\hat{a}$ and creation $\hat{a}^\dagger$ operator on that particular mode act as

$$\hat{a}\,|n\rangle = \sqrt{n}\,|n-1\rangle \qquad \hat{a}^\dagger\,|n\rangle = \sqrt{n+1}\,|n+1\rangle \tag{2.1}$$

with those rules we can rewrite each Fock state in terms of creation operators as

$$|n_1,\ldots,n_k\rangle = \prod_{j=1}^{k} \frac{(\hat{a}^\dagger)^{n_j}}{\sqrt{n_j!}}\,|0\rangle \tag{2.2}$$

We can also define the number operator $\hat{n} = \hat{a}^\dagger\hat{a}$ where the Fock stats are the eigenvectors of the operator with eigenvalue the number of photons in that mode $\hat{n}\,|n\rangle = n\,|n\rangle$.

One last thing that we have to analyze is how the Fock states evolve under a unitary transformation that conserves the total number of photons. It is possible to show that those transformations can be associated with a unitary matrix acting on the creation operator. Meaning that the creator operators $\{\hat{b}_i^\dagger\}$ after the evolution can be expressed as a linear combination of the creation operators before evolution $\{\hat{a}_i^\dagger\}$ and the transformation matrix U have to be unitary.

$$\hat{b}_i^\dagger = \sum_j U_{ij}\hat{a}_j^\dagger \tag{2.3}$$

2.2 Gaussian states

In this section, we introduce a common family of states in quantum optics, named *Gaussian states* [54]. Those states are employed in the continuous variable theory of light which is not an argument discussed in this thesis, however, to understand a variant of the problem of boson sampling explained later in this chapter 6 we need those families of states. Also, they are useful to describe the state at the output state of nonlinear crystals commonly used as a source of single photons.

The first set of states that we describe is called *coherent states* $|\alpha\rangle$. They are the eigenstate of the annihilation operators and at each of them is possible to associate a complex number $\alpha \in \mathbb{C}$. The representation of the state on the Fock basis is

$$|\alpha\rangle = e^{-\frac{|\alpha|^2}{2}} \sum_{n=0}^{\infty} \frac{\alpha^n}{\sqrt{n!}}\,|n\rangle \tag{2.4}$$

Those particular states can be used to well describe the light generated by a laser source.

The second class of states that we mention is the *vacuum-squeezed states*. In those states we can recognize the single-mode squeezed state associated with the complex parameter $\zeta = \chi e^{i\phi}$ as

$$|SMSS\rangle = \sqrt{1-|\zeta|^2} \sum_{n=0}^{\infty} \zeta^n \frac{\sqrt{(2n)!}}{2^n n!}\,|2n\rangle \tag{2.5}$$

and the two-mode squeezed state as

$$|TMSS\rangle = \sqrt{1-|\zeta|^2} \sum_{n=0}^{\infty} \zeta^n\,|n,n\rangle \tag{2.6}$$

Both these states are used to describe most of the parametric single photon sources. In literature, the modulus χ of the complex parameter is called the *squeezing* of the state.

2.3 Photon qubits encoding

In this section, we will see some of the principal degrees of freedom to encode the information in a photon. We will focus in particular on the discrete degrees of freedom and how they can be manipulated.

2.3.1 Path encoding

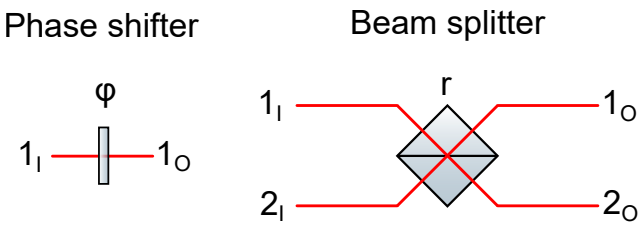

Figure 2.1. Phase shifter and beam splitter. Scheme symbols representing a phase shifter with apply a phase ϕ and a beam splitter with reflectance r.

One of the degrees of freedom of the photon to codify the information is the propagation direction [55] commonly referred as *path encoding*, if the number of modes is equal to two is also called *dual-rail encoding*. This encoding is particularly suitable for integrated photonics where a set of waveguides are used to carry the information [56] and can encode both qubits and qudits. The two key elements to manipulating the phat encoding are the *phase shifter* and the *beam splitter*.

Phase shifter

A phase shifter put a phase ϕ on an electromagnetic wave applied to it. For example, in the case of a two-mode system the unitary transformation represents the transformation performed by the phase shifter is:

$$U_{Ps} = \begin{pmatrix} 1 & 0 \\ 0 & e^{i\phi} \end{pmatrix} \tag{2.7}$$

the associated symbol is represented in Fig. 2.1

Beam splitter

A beam splitter is a component that has two inputs and two outputs and it is used to make interfere two electromagnetic fields or divide one into two different directions. In Fig. 2.1 is depicted one of the common symbols used to represent the component, and adopted in this work. In classical formalism or in the second

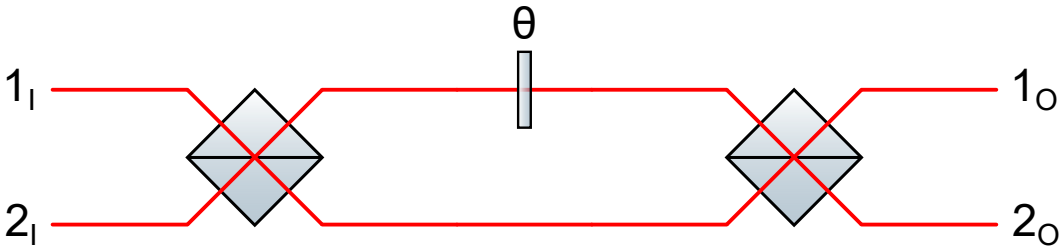

Figure 2.2. Mach-Zehnder interferometer. Scheme of a Mach-Zehnder interferometer composed of two balanced beam splitters in cascade and a phase shifter placed between them.

quantization formalism the most general unitary transformation associated with a beam splitter is

$$U_{BS} = \begin{pmatrix} r & t \\ t^* & -r^* \end{pmatrix} \tag{2.8}$$

where r and t are complex parameters that are called respectively reflectance and transmittance and must fulfill the equation $|r|^2 + |t|^2 = 1$. Commonly, the parameter used to describe a beam splitter is called *Reflectivity* $R = |r|^2$ and represents the ratio between the output intensity and the input intensity on the same port or the probability that a photon exits the same side as it entered. In most cases, the reflectivity of the beam splitter is a fixed parameter depending on the physical construction.

Among all the possible beam splitters a particular type plays a fundamental role. The *balanced beam splitter* or symmetric beam splitter is the one with reflectivity equal to one-half $R = 1/2$. Two equivalent unitary matrices are associated with the balanced beam splitter depending on the context.

$$U_H = \frac{1}{2}\begin{pmatrix} 1 & 1 \\ 1 & -1 \end{pmatrix} \qquad U_S = \frac{1}{2}\begin{pmatrix} 1 & i \\ i & 1 \end{pmatrix} \tag{2.9}$$

the first one is equivalent to a Hadamard transformation and the second one is called the symmetric transformation since if we swap both the inputs and outputs with each other the matrix remains the same. The only difference between them is some phases at the input and at the output.

Mach-Zehnder interferometer

The most simple application of beam splitters and phase shifters is the *Mach-Zehnder interferometer*. It is composed of two balanced beam splitters in cascade and a phase shifter placed between them (see Fig. 2.2). Using the symmetric matrix to represent the beam splitter the total unitary transformation is

$$U_{MZI}(\theta) = ie^{i\frac{\theta}{2}} \begin{pmatrix} \sin\left(\frac{\theta}{2}\right) & \cos\left(\frac{\theta}{2}\right) \\ \cos\left(\frac{\theta}{2}\right) & -\sin\left(\frac{\theta}{2}\right) \end{pmatrix} \tag{2.10}$$

we can notice that this expression is exactly like a beam splitter with reflectance equal to $r = \sin\left(\frac{\theta}{2}\right)$. This should not be surprising since it turns out to be the same

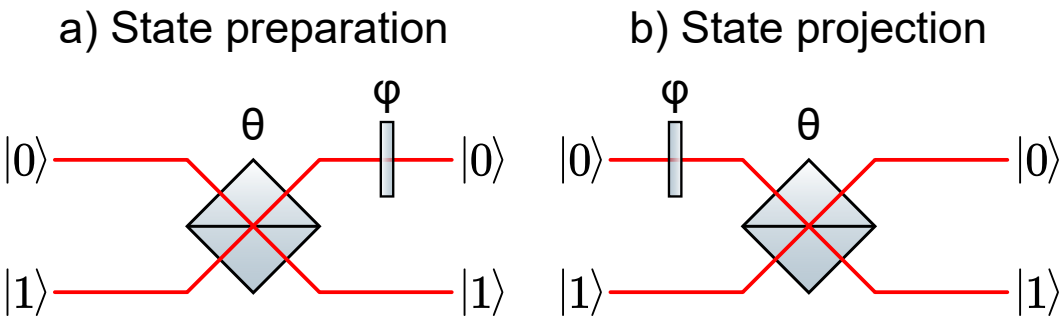

Figure 2.3. Dual-rail state preparation and projection In figure are represented the interferometer used for the state generation (a) and for the state projection (b); both are composed of a tunable beam splitter with an internal controllable phase followed, in the preparation case, or preceded, in the projection case, by a controllable phase shifter.

decomposition for qubits of two Hadamard gates with a phase gate in between and it turns out to have a useful practical application. Directly building a beam splitter with tunable reflectivity from a practical point of view is difficult, however, a Mach-Zehnder interferometer is easy to build, allowing us to still be able to implement a tunable beam splitter without too much effort at the price of a device of larger dimensions.

Dual-rail state preparation and projection

An application of a tunable beam splitter is the possibility to generate and project a dual rail state. For the generation of the state, we use a programmable beam splitter followed by a phase shifter (See Fig. 2.3 a). The implemented matrix $BS(\theta, \phi)$ is:

$$BS(\theta,\phi) = ie^{\frac{\theta}{2}} \begin{pmatrix} \sin\left(\frac{\theta}{2}\right)e^{i\phi} & \cos\left(\frac{\theta}{2}\right)e^{i\phi} \\ \cos\left(\frac{\theta}{2}\right) & -\sin\left(\frac{\theta}{2}\right) \end{pmatrix} \tag{2.11}$$

so if we put a photon in the upper arm of the interferometer, we generate the dual-rail state

$$|\theta,\phi\rangle = |0\rangle \sin\frac{\theta}{2}e^{i\phi} + |1\rangle \cos\frac{\theta}{2} \tag{2.12}$$

that is a generic qubit state.

To perform the projection it is necessary to use a slightly different apparatus, indeed we use a phase-shifter followed by a programmable beam splitter (See Fig. 2.3 b). The associated matrix is

$$BS'(\theta,\phi) = ie^{\frac{\theta}{2}} \begin{pmatrix} \sin\left(\frac{\theta}{2}\right)e^{i\phi} & \cos\left(\frac{\theta}{2}\right) \\ \cos\left(\frac{\theta}{2}\right)e^{i\phi} & -\sin\left(\frac{\theta}{2}\right) \end{pmatrix} \tag{2.13}$$

It is easy to see that applying this interferometer to a generic dual rail state and measuring the output probability is equivalent to measuring the projection of the input state compared to the state

$$|\theta,-\phi\rangle = |0\rangle \sin\frac{\theta}{2}e^{-i\phi} + |1\rangle \cos\frac{\theta}{2} \tag{2.14}$$

In this way, we have shown how to create and project on a generic dual-rail state.

Universal unitary transformation

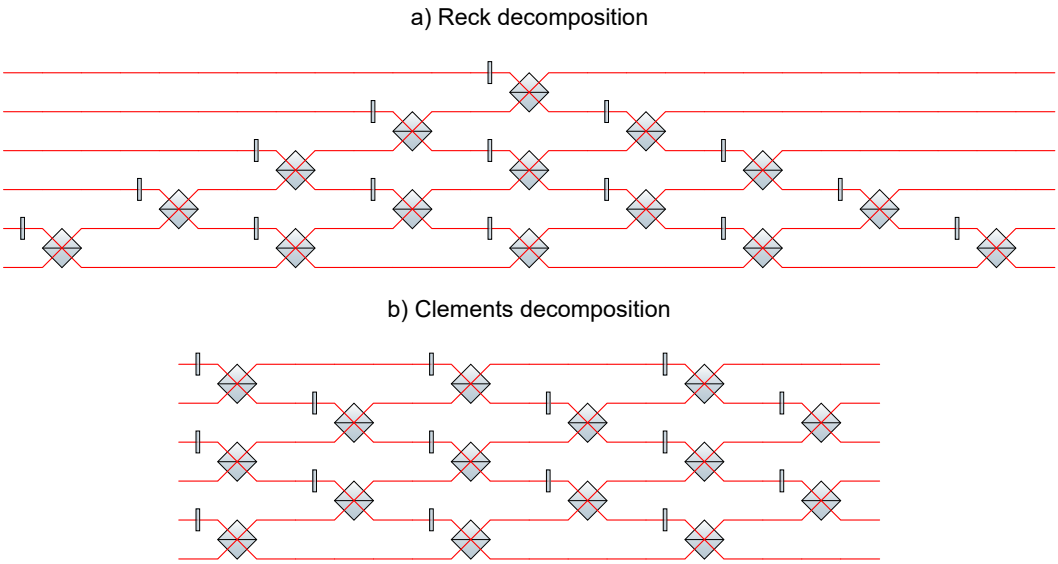

Figure 2.4. Universal interferometer. A general unitary transformation on N modes can be implemented by $\frac{N(N-1)}{2}$ reconfigurable beam splitters and phase shifters disposed on a triangular interferometer according to the Reck decomposition (a) or in a rectangular shape according to the Clements decomposition.

A different problem is how to generate an interferometer implementing a particular unitary transformation on a path-encoded state. Also, we can ask if a universal interferometer able to implement every possible unitary transformation on a given number of modes by changing some internal parameters exist or not. The first solution to the problem was proposed by Reck et al. [57] in 1994 where they show that a triangular interferometer can implement every unitary transformation (see Fig. 2.4 a). The idea is to show that every unitary matrix can be decomposed in a series of unitary transformations acting on a subspace of dimension two. Also, they add the restriction that the bidimensional matrices act only on adjacent modes. Since we already show that a Mach-Zehnder interferometer can implement every bidimensional unitary transformation then it is possible to implement every unitary transformation composing them. This decomposition presents some problems. Indeed, the scheme is not resistant to construction imperfections and losses in the material furthermore it is extremely asymmetrical and it presents a high optical depth (i.e. the maximum number of beams splitters crossed by one mode).

To solve the problems of the previous decomposition in 2016 Clements et al. [9] proposed a different scheme based on the same idea. This decomposition uses a rectangular interferometer as depicted in Fig. 2.4 b. The number of reconfigurable beam splitters is the same as the previous one but the optical depth is halved. Moreover, this interferometer is highly symmetrical meaning that the paths between each input and each output are the same. The disadvantage of this scheme is the high connectivity between the components meaning that if we want to add a new mode to the interferometer with the Reck decomposition is sufficient to add an additional layer of beam splitters at the end of the interferometer, instead, with

the Clements decomposition is not possible and it is necessary to rebuild the entire interferometer.

2.3.2 Polarization encoding

Another degree of freedom to codify the information in a photon and one of the most employed is the *polarization*. The polarization of an electromagnetic wave is the direction of oscillation of the electric field and can be associated with the spin angular momentum of the photon. The polarization of the photon lives in a Hilbert space of dimension two which makes it a natural degree of freedom to encode a qubit. Typically, the computational basis is associated with the horizontal/vertical basis $\{|H\rangle, |V\}\rangle$. As the name suggests, it is associated with the horizontal and vertical components of the electromagnetic field compared to a fixed reference frame. The other two basis are the diagonal basis $\{|D\rangle, |A\rangle\}$ or $\{|+\rangle, |-\rangle\}$. whit $|D/A\rangle = (|H\rangle \pm |V\rangle)/\sqrt{2}$, and the circular basis $\{|L\rangle, |R\rangle\}$, with $|L/R\rangle = (|H\rangle \pm i\,|V\rangle)/\sqrt{2}$. Like what we have done with the Block sphere, it is possible to associate every polarization to a point on a sphere called the *Poincaré sphere*.

Polarization is one of the most employed degrees of freedom due to the simplicity of its manipulation, in the following we see some common components used for that purpose.

Waveplates and Tunable phase shifter

The optical elements that allows the manipulation of the polarization are the *waveplates*. They are birefringent crystal plates cut such that an optical axis is parallel to the surface of the plate. Light passing through the waveplate in a perpendicular direction, compared to the surface, experiences different refractive indices depending on the polarization and therefore a difference in the optical length. This difference translates into a phase ϕ between the two polarizations and therefore to its change. Among the waveplates, there are two that play a particular role, those are called *Half waveplate* and *Quarter waveplate* respectively with a phase of $\phi_{HWP} = \pi$ and $\phi_{QWP} = \pi/2$.

Using the Jones calculus that defines the two polarizations horizontal end vertical as

$$|H\rangle = \begin{pmatrix} 1 \\ 0 \end{pmatrix} \qquad |V\rangle = \begin{pmatrix} 0 \\ 1 \end{pmatrix} \tag{2.15}$$

we can define the unitary matrices for the half waveplate as

$$U_{HWP} = e^{-i\frac{\pi}{2}} \begin{pmatrix} \cos(2\theta) & \sin(2\theta) \\ \sin(2\theta) & -\cos(2\theta) \end{pmatrix} \tag{2.16}$$

and for the quarter waveplate as

$$U_{QWP} = e^{-i\frac{\pi}{4}} \begin{pmatrix} \cos(\theta)^2 + i\sin(\theta)^2 & (1-i)\sin(\theta)\cos(\theta) \\ (1-i)\sin(\theta)\cos(\theta) & \sin(\theta)^2 + i\cos(\theta)^2 \end{pmatrix} \tag{2.17}$$

where θ is the angle between the axis of the waveplate and the horizontal direction.

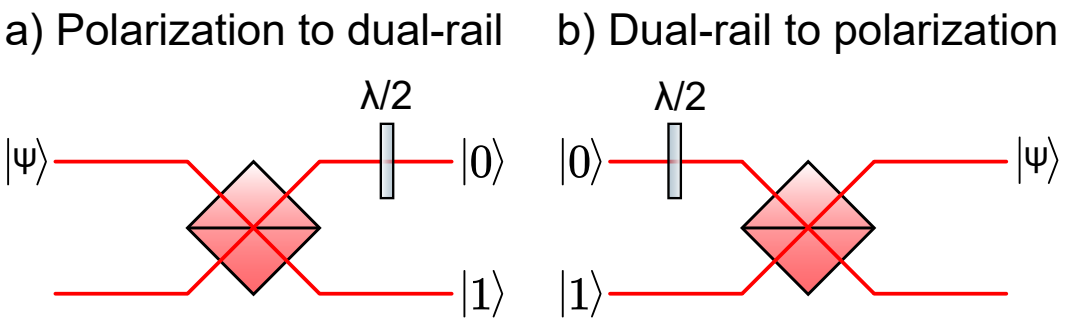

Figure 2.5. Polarization to dual-rail codification converter. The presented interferometers can be used to convert the polarization in the dual-rail codification and vice-versa. they are composed of a polarizing beam splitter followed or preceded by a half waveplate at an angle of 45°

One of the tunable versions of the waveplate is the *liquid crystal*. Like the other waveplates, they put a differential phase ϕ between the polarization aligned with the optical axis and the one perpendicular but with the difference that it can be controlled by an external electric field applied by a voltage source. If the axis of the liquid crystal is aligned with the horizontal direction, than its action is equivalent to a phase gate

$$U_{Lc} = \begin{pmatrix} e^{i\phi} & 0 \\ 0 & 1 \end{pmatrix} \tag{2.18}$$

Polarizing beam splitter and polarization to dual-rail conversion

A *polarizing beam splitter* is a device that changes the direction of propagation of a light beam depending on its polarization. The internal structure is similar to the one of a normal beam splitter but with the difference that the reflectivity depends on the incident polarization. The common choice is null reflectivity for the horizontal polarization and reflectivity equal to one for the vertical polarization. A polarizing beam splitter is extremely useful since combined with the waveplates permits to perform polarization measurement and the conversion between polarization and dual-rail encoding.

The interferometer to implement the conversion from the polarization to the dual-rail is composed of a polarizing beam splitter followed by a half waveplate on the upper arm (see Fig. 2.5 a). In formulas, we start from the polarization state

$$|\psi\rangle = (\alpha\,|H\rangle + \beta\,|V\rangle)\,|0\rangle \tag{2.19}$$

then we apply the polarizing beam splitter

$$U_{PBS}\,|\psi\rangle = \alpha\,|H\rangle\,|1\rangle + \beta\,|V\rangle\,|0\rangle \tag{2.20}$$

and finally we use the half waveplate on the upper harm to convert the vertical polarization to horizontal

$$U_{HWP0}U_{PBS}\,|\psi\rangle = \alpha\,|H\rangle\,|1\rangle + \beta\,|H\rangle\,|0\rangle = |H\rangle\,(\alpha\,|1\rangle + \beta\,|0\rangle) \tag{2.21}$$

To make the reverse conversion it is sufficient to apply the interferometer in the reverse order (see Fig. 2.5 b).

Polarization state preparation, projection and general unitary transformation

Once explained see how to manipulate the polarization we can think about how to prepare and project a polarization state and how to perform a generic unitary transformation on it.

In the previous chapter, we saw that to create a generic transformation on a qubit we need three rotations along two orthogonal axes. The quarter waveplate and the half waveplate are rotations of the Block sphere of respectively $\pi/2$ and π around an axis in the $\hat{x} - \hat{z}$ plane determined by the angle θ. Turns out that two quarter and one half waveplates are sufficient to generate all the possible unitary transformations. Normally the configuration used is the half waveplate sandwiched between the two quarters but all three possible orders are suitable as shown in [58].

For the state generation, we can rely on the previous result and use three waveplates to create a generic state from a horizontal state $|H\rangle$. It turn out that it is not the most efficient way to do it, in particular it is possible to show that only two waveplates are necessary to generate a generic state. The procedure consists in starting with a photon with horizontal polarization, a polarizing beam splitter can be used to ensure the condition, then a half waveplate followed by a quarter waveplate with opportune angles are applied to the photon to generate the final state. For the projection the reverse procedure can be used, i.e. a quarter waveplate followed by a half waveplate and a polarizing beam splitter to measure the state. Moreover, in principle the angles necessary to carry out the creation or projection of the state can be over all 2π, however it is possible to restrict the interval between $-\pi/4$ and $\pi/4$ for both.

2.3.3 Orbital angular momentum encoding

In paraxial approximation and cylindrical symmetry, the electric field of a laser can be described by the so-called Laguerre-Gauss modes, parametrized by two numbers $l \in \mathbb{Z}$ and $m \in \mathbb{N}_0$. We will limit ourselves to the case $m = 0$ (for the complete treatment, see specific texts [59]). The term with $l = 0$ is associated with a Gaussian beam that has a spherically shaped wavefront (i.e. the locus of constant phase points). The other terms are associated with phases that have helix-shaped wavefronts whose number of arms corresponds to the modulus of l and the direction of rotation to the sign. This helix-shaped causes the beam to have an intrinsic angular momentum called orbital angular momentum (OAM) proportional to l. Similarly, photons can have a quantized OAM given by $L = l\hbar$ [60].

The orbital angular momentum degree of freedom can be used to codify a qudit and it is of particular interest for various reasons. It is potentially unlimited, which makes it a good candidate for implementing quantum walks [61]. It has circular symmetry, therefore it is useful for long-distance communication, as it is possible to generate states that do not require alignment between the transmission and reception axes [62]. Finally, it is possible to manipulate it through devices called q-plates [60]. However, a practical method for measuring the orbital angular momentum has not yet been found.

q-plates

To manipulate the orbital angular momentum a particular kind of waveplate called *q-plates* is used. A q-plate enables the interaction between orbital angular momentum and polarization allowing the latter to be used as a means of manipulating orbital angular momentum. At each q-plate is associated a topological charge q that can take only semi-integer values. A circularly polarized beam passing through a q-plate gain or lose an amount of orbital angular momentum equal to twice the topological charge. The unitary action of the q-plate can be described as

$$\begin{aligned} U_q \left|l, L\right\rangle &= \cos\left(\frac{\delta}{2}\right)\left|l, L\right\rangle + \sin\left(\frac{\delta}{2}\right) e^{i2\alpha_0}\left|l+2q, R\right\rangle \\ U_q \left|l, R\right\rangle &= \cos\left(\frac{\delta}{2}\right)\left|l, R\right\rangle + \sin\left(\frac{\delta}{2}\right) e^{-i2\alpha_0}\left|l-2q, L\right\rangle \end{aligned} \tag{2.22}$$

where δ is called detuning, normally is set to $\delta = \pi$, and α_0 is a phase that depends on how the q-plate is aligned compared to the optical beam.

2.4 Photon interference

In this section, we revise the physics behind the multiphoton interference i.e. where more than one photon is injected in a linear interferometer.

2.4.1 Hong-Ou-Mandel effect

In quantum optics, the Hong-Ou-Mandel (HOM) effect is an interference effect that does not have any classical explanation. This effect is a simple method for comparing the states of two photons. The phenomenon was originally proposed to measure the delay between two photons by bringing the resolution down to the nanosecond [63]. More generally, this effect can be used to measure properties of a linear optical interferometer difficult to access with different measurements [25].

If at the input of a balanced beam splitter we put two indistinguishable photons, one for each harm $\left|1,1\right\rangle = a_1^\dagger a_2^\dagger \left|0\right\rangle$, then the output state is

$$\begin{aligned} \left|1_1, 1_2\right\rangle =& a_1^\dagger a_2^\dagger \left|0\right\rangle \\ \xrightarrow{U_{BS}} & \frac{1}{2}(a_1^\dagger + a_2^\dagger)(a_1^\dagger - a_2^\dagger)\left|0\right\rangle \\ =& \frac{1}{2}(a_1^\dagger a_1^\dagger - a_2^\dagger a_2^\dagger + a_1^\dagger a_2^\dagger - a_2^\dagger a_1^\dagger)\left|0\right\rangle \\ =& \frac{1}{\sqrt{2}}(\left|2,0\right\rangle - \left|0,2\right\rangle) \end{aligned} \tag{2.23}$$

It is possible to notice that the event where a photon came out for each output, called also *non-collisional term*, is suppressed due to the bosonic nature of the photons. If the photons are distinguishable then the interference effect disappears completely allowing the presence of the non-collisional therm. To detect the HOM effect, the coincidences, i.e. simultaneous detection of two detectors, between the photons of the two beam splitter outputs are measured (in this way the state $\left|1,1\right\rangle$ is measured). By varying the distinguishability of the two photons, for example by changing their

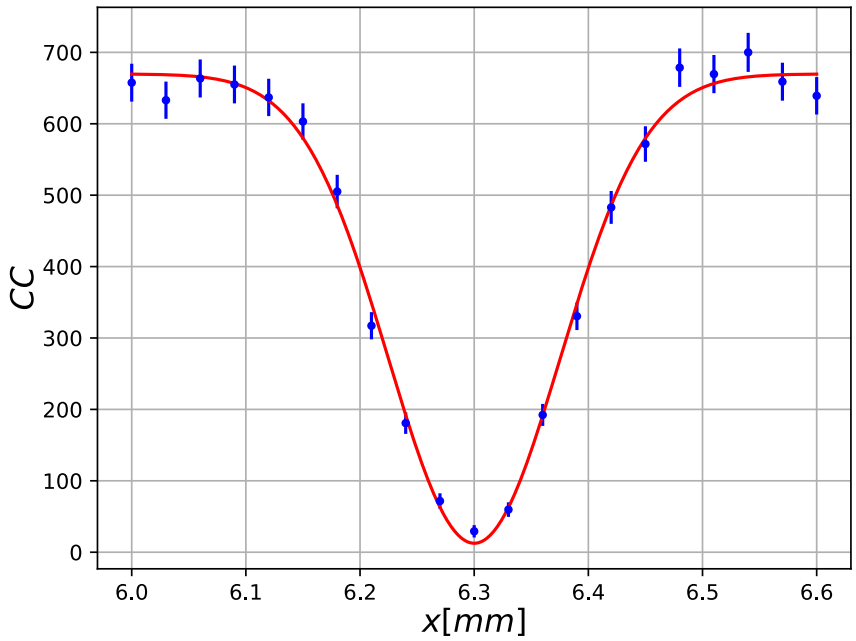

Figure 2.6. HOM dip. By varying the relative delay between two photons injected into a beam splitter, suppression in the coincidences due to the bosonic coalescence of the photons can be detected. The measured visibility is equal to $V = 0.98 \pm 0.02$

relative time delay, the so-called *HOM dip* can be traced (an example is shown in Figure 2.6).

Leaving aside the calculations (given in the Appendix A) the probability P_{nc} of measuring a coincidence is equal to

$$P_{nc} = 2RT(1 - |\langle\phi|\psi\rangle|^2) \tag{2.24}$$

where $|\phi\rangle$ and $|\psi\rangle$ are the states of the input photons and R and T are respectively the reflectivity and the transmissivity of the beam splitter.

A relevant parameter in the HOM effect is the visibility V (which gives a direct measure of the overlap between the two input states), defined as

$$V = 1 - \frac{P_{ncI}}{P_{ncD}} = \frac{2RT}{R^2 + T^2}|\langle\phi|\psi\rangle|^2 \tag{2.25}$$

where I and D stand for the probabilities in the case respectively of indistinguishable and distinguishable photons. Experimentally, instead of the probabilities, the ratio between the minimum and the maximum of the HOM dip can be use.

In the more general scenario of an interferometer implementing a unitary transformation U, when two photons are injected in the inputs h and k and the coincidence are detected at the outputs i and j the probability to detect a coincidence is

$$P_{ij}^{hk} = |U_{ih}|^2|U_{jk}|^2 + |U_{jh}|^2|U_{ik}|^2 + (U_{ih}U_{jk}U_{jh}^*U_{ik}^* + U_{jh}U_{ik}U_{ih}^*U_{jk}^*)|\langle\phi|\psi\rangle|^2 \tag{2.26}$$

and the corresponding visibility is

$$\mathcal{V}_{ij}^{hk} = -\frac{U_{ih}U_{jk}U_{jh}^*U_{ik}^* + U_{jh}U_{ik}U_{ih}^*U_{jk}^*}{|U_{ih}|^2|U_{jk}|^2 + |U_{jh}|^2|U_{ik}|^2}|\langle\phi|\psi\rangle|^2 \tag{2.27}$$

See Appendix A for the explicit calculation.

2.4.2 Multi-photons interference

In the previous section, we see what happens when two photons are injected into an interferometer giving rise to a new type of interference. Now we want to see what happens when more than two photons are put inside.

To understand the connection between the unitary transformation implemented by the linear interferometer and the quantum state at the output, we need to introduce a function called *permanent*. The permanent of a square matrix U of dimension n is defined as

$$Per(U) = \sum_{\sigma \in S_n} \prod_{j}^{n} U_{j\sigma(j)} \tag{2.28}$$

where S_n is the set of permutation of n elements. We can notice that the expression is quite similar to the determinant except that there is not the sign of the permutation.

If we define the matrices

$$U_{(h,k)\to(i,j)} = \begin{pmatrix} U_{ih} & U_{ik} \\ U_{jh} & U_{jk} \end{pmatrix} \tag{2.29}$$

we can notice that the expression of the probability for two photons in eq. 2.26 can be expressed as

$$P_{ij}^{hk} = \left| Per(U_{(h,k)\to(i,j)}) \right|^2 \tag{2.30}$$

This is not a coincidence and indeed, for the general case, we can construct the matrices $U_{s\to t}$, associated with the Fock states $|s\rangle = |s_1 \dots s_n\rangle$ and $|t\rangle = |t_1 \dots t_n\rangle$. This matrix has for columns s_1 copy of the first column of the original matrix U, s_2 copy of the second column and so on; and for rows the same procedure but with the state t. Then we can say that the probability of measuring the state t at the output of an interferometer when in input is placed the Fock state s is

$$P_{s\to t} = \frac{|Per(U_{s\to t})|^2}{\prod_i^n s_i! t_i!} \tag{2.31}$$

Intuitively, the formula is justified by the fact that the permanent is the coherent sum of all the possible configurations to assign each photon at the output with a distinct photon in the input. For a rigorous proof see [64].

For completeness, if the input photons are all distinguishable from each other then the probability became

$$P_{s\to t} = \frac{Per(|U_{s\to t}|^2)}{\prod_i^n s_i! t_i!} \tag{2.32}$$

Chapter 3

Photonic technology for Quantum information

Photons are one of the most common platforms used to implement and experimentally test quantum protocols. Indeed, they present various peculiar characteristics that make them particularly suitable for this purpose. Some of the best-known quantum protocols have been experimentally tested on photonic platforms, among which we can mention super dense coding, entanglement distillation [65,66], quantum state teleportation [67,68], entanglement swapping [69], quantum coin tossing [70] and others. In almost all the experiments done with photons, it is possible to recognize a structure composed of three parts, the generation, manipulation and detection of photons. This chapter analyses how these components are made experimentally and what technologies and physical principles are at their basis.

3.1 Single-photon sources

An ideal single-photon source should emit on-demand indistinguishable single photons in a defined spatial and temporal mode with the possibility of a high generation rate. Furthermore, the realization of the source should be sufficiently controllable so that it is possible to generate indistinguishable photons from different sources. In addition, there are also other types of sources studied in the literature that can generate states of more than one photon like the Bell states [71] or in a photon number superposition [72]. Despite a large number of applications in quantum technology, up to now a source with all those characteristics does not exist yet. Depending on the application and the experiment there are some sources that are more suitable than others. All the existing single-photon sources can be classified into two major categories: the probabilistic photon sources and the deterministic photon sources.

From the historical point of view, the first type of single-photon sources is the probabilistic ones that exploit the interaction between a non-linear crystal and a strong electromagnetic field called *pump*. This interaction spontaneously generates a pair of photons. The effect at the basis of this interaction is called spontaneous parametric down-conversion (SPDC). The SPDC sources are the most used method for the generation of the vacuum-squeezed state which forms the basis of

the continuous variable paradigm and exhibits non-classical properties of interest for the theory of quantum optics. Moreover, under the assumption of a small squeezing parameter the state can be approximated to the probabilistic generation of pairs of single photons. In this regime, using the post-selection operation, it is possible to generate single photons with a high degree of indistinguishability. Furthermore, with some precautions it is possible to use SPDC sources for the generation of pairs of photons in a maximally entangled state. The successful application of this type of source in numerous experiments in virtually all areas of quantum information and computation has motivated the engineering of various SPDC source configurations in both bulk and integrated optics [73–77]. The integrated sources are implemented by writing a waveguide in the non-linear material so that the generation of photons takes place directly in the waveguide and there is no need for subsequent coupling unlike bulk sources. In the context of integrated sources in addition to the SPDC effect, another nonlinear effect called spontaneous four-wave mixing (SFWM) is used. If the SPDC effect is a second-order effect, since a pump photon is converted into two photons, instead the SFWM effect is a third-order effect in which two photons of the pump are absorbed and converted into two photons. The advantage of the SFWM is that a greater number of materials have this effect. The disadvantage however is that being a process of higher order results in lower generation efficiency. To overcome this disadvantage longer waveguide, typically arranged in spirals, or ring resonator are used to increase the interaction length and the efficiency of the process [78–88]. Another advantage of integrated probabilistic sources is that the fabrication technique permits the realization of arrays of identical emitters [89–91]. Despite the large use of SPDC sources for quantum information experiments, their probabilistic nature prevents scaling the experiments to a higher number of photons. A possible solution to such an issue is the time-multiplexed technique which combines several probabilistic sources to increase the generation probability but up to now such a method is experimentally performed only in bulk optics [92].

The other type of single-photon source is the deterministic one. Those are composed of a quantum dot, a structure with atom-like properties, and a cavity around the dot that enhances the probability of emitting the photon in a determined spatial and frequency mode when the dot is exited with a pump pulse [93–97]. If the quantum dot is excited by a series of pulses with a period much longer than its lifetime, it will generate a train of identical single-photon states, but up to now the generation of indistinguishable photons from different sources is difficult. To overcome the problem a demultiplexing technique can be used to separate the photons of successive pulses in different spatial modes and then synchronized them to generate a multi-photon indistinguishable state. However, such an operation introduces additional losses to the apparatus that reduce the overall generation rate [98, 99]. These sources can also be used to generate couples of entangled photons [71] or states in a controllable superposition of vacuum and single-photon [72, 100].

Below, we analyze in detail the SPDC sources with bulk optics since they are the ones used in the experiments presented in this thesis. In particular, we present the classical and quantum explanation of the parametric down conversion phenomena and the principal characteristic of our single-photon sources used in the experiments presented in this thesis.

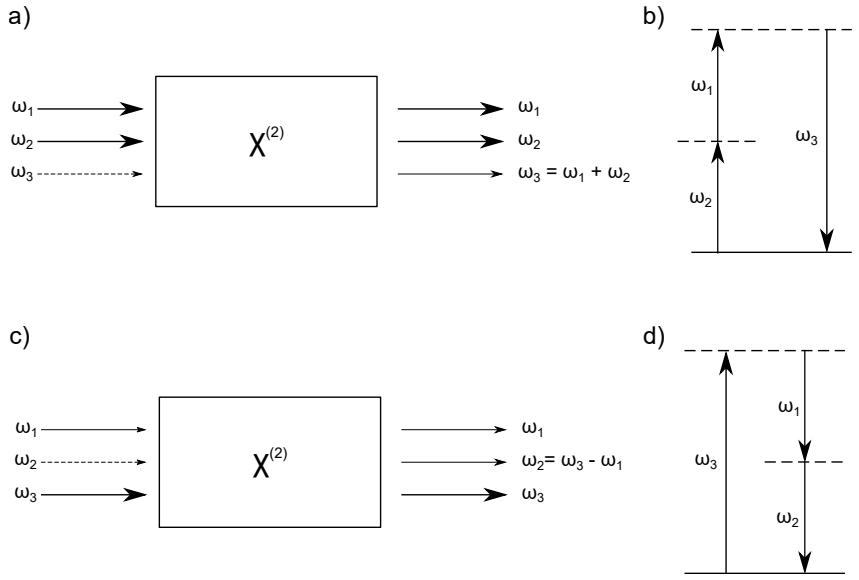

Figure 3.1. Non-linear optics effect. a) Schematic representation of the sum frequency generation effect, it occurs when two strong beams with frequency ω_1 and ω_2 impinge on a non-linear crystal and at the exit of the crystal, in addition to the two incident phases, there is also a third beam with a frequency which is the sum of the frequencies of the two incident beams. b) Energy conservation scheme for the sum frequency generation effect. c) Schematic representation of the optical parametric amplification effect, it occurs when a strong beam with frequency ω_3 and a weak beam with frequency ω_1 impinge on a non-linear crystal, at the output the weak field result amplified and there is a third beam with a frequency which is the difference of the frequencies of the two incident beams. d) Energy conservation scheme for the optical parametric amplification.

3.1.1 Spontaneous parametric down conversion

Optical parametric amplification

The spontaneous parametric down-conversion is a process that can be explained only with the tools of quantum optics theory. The classical analogous is called *optical parametric amplification* and consist of the amplification of an electric field at the frequency ω_s, historically called Signal, passing throw a non-linear crystal pumped by a second electric field called Pump with frequency ω_p. During this process, a third electric field called Idler is generated with a frequency that due to the energy conservation is $\omega_i = \omega_p - \omega_s$. To describe the phenomenon we start with the maxwell equations in the presence of non-linear media. The interaction of a material with a strong electromagnetic field induces a non-linear response of the latter. The material's response is completely described by the polarization vector $\vec{P}$ which is a function of the applied electric field $\vec{E}$. By expanding the polarization vector in Taylor expansion and truncating the series at the second order we can write $\vec{P} = \vec{P}^{(1)} + \vec{P}^{(2)}$ with

$$P_i^{(2)} = \epsilon_0 \sum_{j,k} \chi_{ijk}^{(2)} E_j E_k \tag{3.1}$$

where ϵ_0 is the vacuum dielectric constant, the subscripts $i, j, k \in \{x, y, z\}$ are the direction of the used basis and the tensor $\chi^{(2)}_{ijk}$ is the second order susceptibility of the material under consideration [101]. From this expression, it is possible to notice that if two monochromatic waves, respectively at the frequency ω_1 and $\omega_2 < \omega_1$, are made to interact with the non-linear material then two other monochromatic waves are created inside the material, the first at the frequency $\omega_1 + \omega_2$ and the second at the frequency $\omega_1 - \omega_2$. The generation of the first wave is called *sum frequency generation* and the second one is called *parametric amplification* or difference frequency generation. The two phenomena are closely related to each other since they can be viewed as the inverse of each other. To mathematically describe both phenomena we want to solve the wave equation in presence of the non-linear material

$$\nabla^2 \vec{E} - \frac{1}{c^2}\frac{\partial^2 \vec{E}}{\partial t^2} = \frac{1}{\epsilon_0 c^2}\frac{\partial^2 \vec{P}}{\partial t^2} \tag{3.2}$$

where c is the speed of the light in the vacuum. To simplify the calculation and show the salient points of the theory we make the assumption of monochromatic plane waves all with the same direction perpendicular to the interface of the non-linear material that we can consider lossless.

To solve the case of the sum frequency generation, we can assume that the fields E_1 and E_2 are much stronger than the field E_3 and that they are constant for the entire duration of the interaction. These assumptions are not restrictive since the value of the non-linear susceptibility is very small. Then we want to find a solution for the field E_3 in the form

$$E_3(z,t) = A_3(z)e^{i(k_3 z - \omega_3 t)} + c.c. \tag{3.3}$$

where $k_3 = n_3\omega_3/c$ and n_3 is the refractive index of the material at the frequency ω_3. Then the polarization vector can be written as

$$P_3(z,t) = \mathcal{P}_3 e^{i(k_3 z - \omega_3 t)} + c.c. \qquad \mathcal{P}_3 = 2\epsilon_0 \chi_{\text{eff}} E_1 E_2 \tag{3.4}$$

where χ_{eff} is the effective susceptibility, which summarizes the properties of the susceptibility and orientation of the material compared to the direction of the waves. Putting these expressions in the wave equation (3.2) we obtain

$$\frac{\partial^2 A_3}{\partial z^2} + 2ik_3\frac{\partial A_3}{\partial z} = -\frac{2\epsilon_0 \chi_{\text{eff}}\omega_3^2}{c^2} A_1 A_2 e^{i(k_1+k_2-k_3)z} \tag{3.5}$$

Using the slowly varying amplitude approximation that assumes that the change of intensity on a distance of a wavelength is negligible, i.e.

$$\left|\frac{\partial^2 A_3}{\partial z^2}\right| \ll \left|k_3\frac{\partial A_3}{\partial z}\right| \tag{3.6}$$

with this approximation the expression becames

$$\frac{\mathrm{d}A_3}{\mathrm{d}z} = \frac{i\epsilon_0 \chi_{\text{eff}}\omega_3}{n_3 c} A_1 A_2 e^{i(k_1+k_2-k_3)z} \tag{3.7}$$

Defining the quantity $\Delta k = k_1 + k_2 - k_3$ and assuming that at the input of the crystal the intensity of the sum electric field is null $E_3(0,t) = 0$, we can integrate the previous equation and calculate the intensity of the electromagnetic field as a function of the position z.

$$I_3 = \frac{2\chi_{\text{eff}}^2 \omega_3^2 z^2}{n_1 n_2 n_3 \epsilon_0 c^3} I_1 I_2 \text{sinc}^2\left(\frac{\Delta k z}{2}\right) \tag{3.8}$$

Just from this equation, we can see some of the important features of the non-linear process. As we can see for the same length of the non-linear material the maximum intensity of the generated field is reached when $\Delta k = 0$. This condition is called *phase matching* and turns out to be a crucial condition in all nonlinear processes. Also, the "Sinc" function reflects the phenomena of energy exchange between the two pump beams and the signal beam generated in the material. In fact, if the phase-matching condition is not satisfied, we can be seen how the intensity of the generated fields spatially oscillates showing this energy exchange. The phase-matching condition can be seen as a conservation of the total momentum of the fields and guarantees a constant flow of energy from the pump beams to the signal beam via a constructive interaction between them. The phase-matching condition is not a trivial condition to fulfil, for example in the collinear case under examination we can writhe the phase-matching condition as

$$\frac{n_1 \omega_1}{c} + \frac{n_2 \omega_2}{c} = \frac{n_3 \omega_3}{c} \tag{3.9}$$

also remembering that it must be valid the relation $\omega_1 + \omega_2 = \omega_3$. Almost all the materials in the lossless regime present a refractive index that increases with frequency meaning that the phase-matching condition can not be satisfied. As we will see later, in order to comply with the phase-matching condition and therefore to have an efficient generation, it is necessary to use birefringent materials.

Now we move to the parametric amplification effect which is the closest classical effect to SPDC. In this case, we have a strong field at frequency ω_3 and a very weak field at the frequency $\omega_1 < \omega_3$. Applying the same assumption of the sum frequency generation case that the electromagnetic field E_3 remains constant during all the interaction and using the same slowly varying amplitude approximation we can write the equations for the intensity of the signal at ω_1 and for the idler at $\omega_2 = \omega_3 - \omega_1$ as

$$\frac{\mathrm{d}A_1}{\mathrm{d}z} = \frac{i\epsilon_0 \chi_{\text{eff}} \omega_1}{n_1 c} A_3 A_2^* e^{i\Delta k z} \tag{3.10}$$

$$\frac{\mathrm{d}A_2}{\mathrm{d}z} = \frac{i\epsilon_0 \chi_{\text{eff}} \omega_2}{n_2 c} A_3 A_1^* e^{i\Delta k z} \tag{3.11}$$

$$\tag{3.12}$$

In the case of phase matching condition, $\Delta k = 0$, the equations turn out to be easy to solve and the solution is

$$\begin{aligned} A_1(z) &= A_1(0)\cosh(\alpha z) \\ A_2(z) &= i\sqrt{\frac{\omega_3 n_2}{\omega_2 n_3}} \frac{A_3}{|A_3|} A_1(0)^* \sinh(\alpha z) \end{aligned} \qquad \alpha = \frac{\chi_{\text{eff}}|A_3|}{c}\sqrt{\frac{\omega_2 \omega_3}{n_2 n_3}} \tag{3.13}$$

From that expression we can understand why this process is called parametric amplification, indeed the signal field is amplified by the non-linear process and as a side effect the idler signal is generated to conserve total energy. Furthermore, it is possible to note that for the process to take place it is necessary that at the entrance of the non-linear media there is an electromagnetic wave at the frequency ω_1 to be amplified. From this, we see how the theory of classical electromagnetism cannot explain the SPDC since it is a spontaneous process. In the next section, we will look at the quantum description of the nonlinear process and how SPDC occurs through interaction between the nonlinear crystal and the vacuum state, a concept completely absent in classical theory.

Description according to the quantum theory

To understand the SPDC process we start by writing the Hamiltonian of the non-linear crystal in the second quantization formalism [102]. In the following, the indices p, s and i are used to indicate the quantities connected respectively to the pump, signal and idler fields.

$$\hat{H}_{\text{SPDC}} = i\hbar\mathcal{K}(\hat{a_s}\hat{a_i}\hat{a_p}^\dagger e^{i\Delta\vec{k}\vec{r}-i\Delta\omega t} + \hat{a_s}^\dagger\hat{a_i}^\dagger\hat{a_p}e^{-i\Delta\vec{k}\vec{r}+i\Delta\omega t}) \qquad \mathcal{K} = \frac{\chi_{\text{eff}}}{3\epsilon_0 V}\sqrt{\frac{\omega_p\omega_s\omega_i}{2\epsilon_0 V}} \tag{3.14}$$

where $\Delta\omega = \omega_p - \omega_i - \omega_s$. The first term of the hamiltonian is related to the sum frequency generation phenomena since a photon of the signal and a photon of the idler are destroyed to create a photon with a frequency that is the sum of the two. The second term is related to the parametric amplification effect since a photon of the pump is destroyed to create a couple of photons one as a signal and one as an idler. The two processes are one the hermitian conjugate of the other which means that they can see as one the inverse process to the other. Also, this tells us that the two processes can not be separated and always compete with each other.

To explain the SPDC phenomena we solve the Schrödinger equation for an initial state with N_p photons in the pump and no photon in the signal or in the idler.

$$|\psi(t)\rangle = e^{\frac{1}{\hbar}\int_0^t \mathrm{d}t'\, \hat{H}_{\text{SPDC}}(t')}\,|N_p, 0_s, 0_i\rangle \tag{3.15}$$

Since the parameter $\mathcal{K}$ is very small, which reflects the fact that the SPDC process is very inefficient, it is reasonable to express the evolution operator in Taylor expansion and truncate it at the first order

$$|\psi(t)\rangle \sim \left(C_0 + \frac{C_1}{\hbar}\int_0^t \mathrm{d}t'\, \hat{H}_{\text{SPDC}}(t')\right)|N_p, 0_s, 0_i\rangle \tag{3.16}$$

if the interaction time t is sufficiently long then the only remaining therm of the integral is the one that conserves the energy, i.e. $\Delta\omega = 0$, meaning that we can express the final state as

$$|\psi(t)\rangle = C_0\,|N_p, 0_s, 0_i\rangle + C_1\mathcal{K}e^{-i\Delta\vec{k}\vec{r}}\,|N_p - 1, 1_s, 1_i\rangle \tag{3.17}$$

To compare this expression with the one found in the previous section we need to compute the square modules of the wave function. The term $e^{-i\Delta\vec{k}\vec{r}}$ generate

the same sinc function dependence for the phase matching condition found for the classical derivation. On the other hand, compared to the classical phenomena, we can see that the intensity of the signal and idler field are linear in the pump intensity I_p. Indeed, such property arises from the fact that the intensity of the pump is proportional to the number of photons $|N_p\rangle$. Since the generation probability is proportional to $\mathcal{K}^2$ and $C_1 \ll C_0$ the efficiency of SPDC is very low. The increase of the pump intensity I_p could be a solution but in this way, we can not neglect the higher contribution in the Taylor expansion. It is possible to show that the complete state generated by an SPDC source is a two-mode vacuum-squeezed state which tends to be a classical state for a high value of the squeezing parameter. To bypass the problem the solution adopted in most of the experiments of quantum information is the post-selection in the measurement stage. Since the signal and the idler photon are generated contemporaneously, to herald the generation of the photons is sufficient for the detection of two simultaneous events in the measurement stage. In this way, we discard the vacuum state $|0_s, 0_i\rangle$. Also, accidental coincidences due to the dark count or multi-pair emission can be kept under control by a proper choice of the coincidence time window and eventually during measurement results processing.

3.1.2 SPDC phase matching condition

In the previous section, we saw that the phase-matching condition is a pivotal condition to maximize the efficiency of all the non-linear processes both in the classical and quantum regimes. We have also seen how it is not trivial to be able to satisfy this condition. For example, for the collinear case (Eq. (3.9)) we have seen how it is difficult to satisfy this condition with a transparent isotropic material. Since we are interested in the generation of indistinguishable photons in the following we will focus on the case where the signal and idler photons have the same frequency $\omega_s = \omega_i = \omega_p/2$. Since finding a dispersive material that presents the condition $n(\omega) = n(2\omega)$ is complicated, to solve the problem we resort to the use of birefringent materials which have a different refractive index depending on the polarization. With the birefringent materials, it is possible to reach the phase-matching condition due to the fact that the pump field and the photons can be affected by different dispersion curves. The birefringent materials can be divided into *uniaxial materials* if it has two distinct refractive indexes or *biaxial materials* if it has three distinct refractive indexes. The two most common non-linear birefringent materials used to make single-photon sources are Beta-Barium Borate (BBO) and Potassium titanyl phosphate (KTP) for which the dispersion curves, i.e. the dependence of the refractive indexes as a function of the frequency, are well known.

The SPDC sources can be classified according to the polarization of the emitted photons compared to the pump polarization. In this sense, we can identify three different configurations

- *type-0*: when the polarization of the two photons emitted is the same and is parallel to that of the pump.
- *type-I*: when the polarization of the two photons emitted is the same and is perpendicular to that of the pump.

- *type-II*: when the polarization of the two emitted photons are perpendicular to each other.

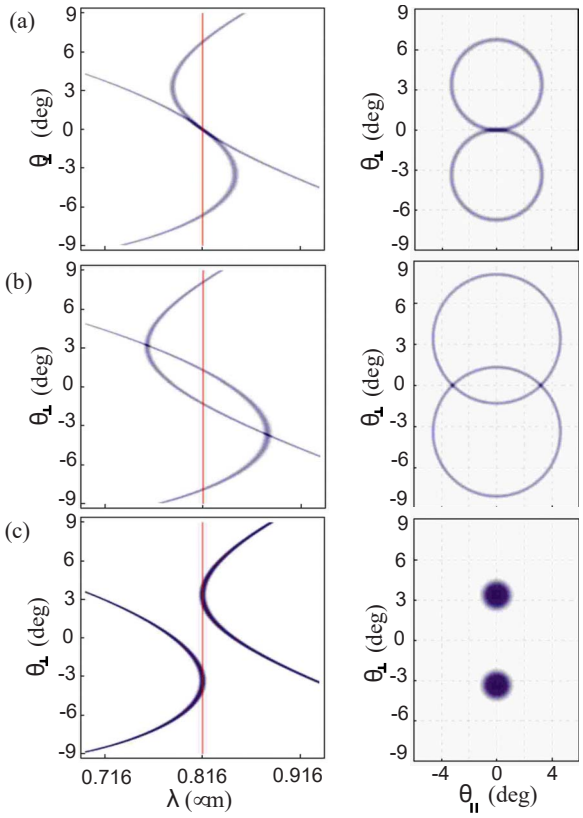

Figure 3.2. Phase-matching conditions for a type-II SPDC. Tuning curve for a BBO crystal pumped at the wavelength of $\lambda_p = 408nm$ and with the selected photon wavelength at $\lambda_s = 826nm$ (red line). a) Collinear emission that appends when for the selected wavelength the two curves are tangent. b) Non-collinear emission for the generation of entangled states, in this configuration the two cones intersect each other and the generated state at the intersection is an entangled state in polarization. c) Beam-like emission that happens when the tuning curve is tangent to the red line in two points. In those points, the photons are emitted in a Gaussian beam that is suitable for coupling in single-mode fibers. The figure is taken from Ref. [103]

Until now only the scalar version of the phase-matching condition has been considered, in general we can consider that the generated photons are not collinear with the pump. Below we analyse the main geometries in the case of type-II emissions. Finding a general solution for the phase-matching condition is not a trivial task and normally only numerical solutions can be found [104]. The result of the calculation is the so-called tuning curve that represents the emission angle θ of the photon, referred to the pump direction, as a function of the wavelength. Some examples of tuning curves are represented if Fig. 3.2 [103]. For a BBO crystal in the type-II emission, the phase matching condition predicts that the photons are generated along two cones in space and considering the relative position of these two cones it is possible to distinguish three different configurations of interest. The first one (see Fig. 3.2 a) is the collinear configuration where the two cones are tangent to each other, this

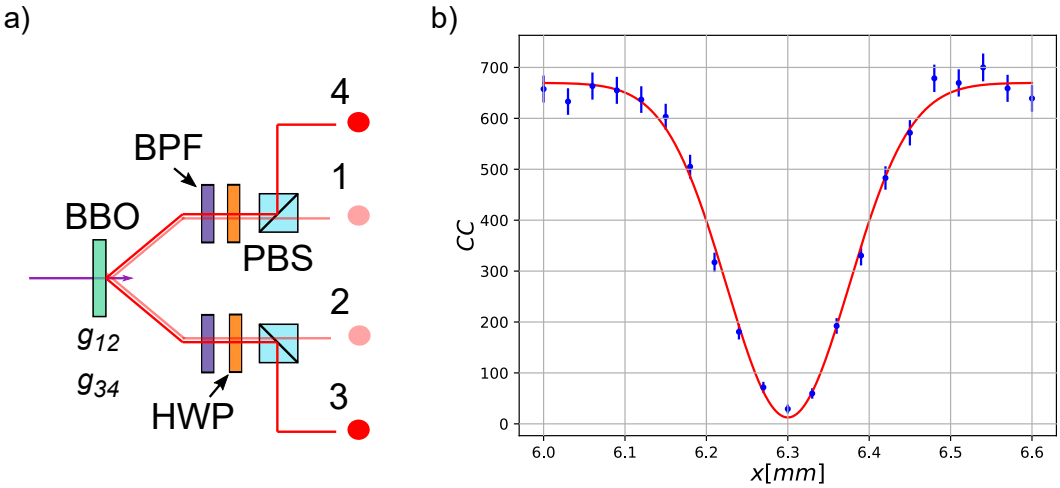

Figure 3.3. Source structure and indistinguishability. a) The source is split in two independent double pairs emissions characterized by two nonlinear gains g_{ij}. Each source generates photons in a pair of optical modes. Legend: BB0 - Beta-Barium-Borate crystal; BPF - Band Pass Filter; HWP - Half wave plate; PBS - Polarizing Beam-splitter. b) HOM dip for photons belonging to the same pair, the errors are estimated by considering the Poissonian uncertainties. From the fit (in red) we measure a visibility of $V = 0.98(2)$.

configuration is similar to the scalar one since in the tangential point the signal and the idler photons came out from the same direction. The second configuration is when the two cones intersect (see Fig. 3.2 b). In this configuration if we collect the photon generated at the intersection since we cannot know which photon is emitted by which cone the generated state is entangled in polarization. The third configuration is called beam-like emission (see Fig. 3.2 b) and is the configuration where the two cone collapse in two spots. Since the spatial profile of this spots is Gaussian this configuration is optimal for high coupling efficiency in single-mode fibre [105].

3.1.3 SPDC sources

Now that the basic principles of the SPDC sources are understood, we proceed to describe the single-photon sources that we are going to use in the experiments of this thesis. The source is a BBO crystal pumped with a pulsed laser at the wavelength of $\lambda_p = 392.5nm$ with a power sufficient to be in a two-pair emission regime. The photon pairs are emitted at the wavelength of $\lambda_s = 785nm$ in the configuration where the two cones intersect and the collection is performed along the intersection. To increase the indistinguishability the generated photons are filtered through a narrow band-pass filter with a window of $3nm$ and centred at the wavelength of the photons. Then a half-wave plate and a polarizing beam splitter are used to separate the photons in four different modes according to the polarization of the photons (see Fig. 3.3 a). With this configuration, we can perform experiments with 2, 3 and 4 indistinguishable photons. Due to the correlation between the polarization if we detect a couple of photons they can come out only in the configurations $(1, 2)$ or $(3, 4)$ and since we do not stabilize any phase we can consider that the two sources

are independent. The state generated by each one of the two sources can be written as

$$\rho_{ij} = \frac{1}{1-g_{ij}}(|00\rangle\langle 00| + g_{ij}|11\rangle\langle 11| + {g_{ij}}^2|22\rangle\langle 22| + \dots) \tag{3.18}$$

where g_ij is the probability to generate a couple of photons in the mode $(i,j) \in \{(1,2),(3,4)\}$. The overall state generated by the sources can be described as $\rho = \rho_{12} \otimes \rho_{12}$. Post-selecting on the measure of a four-fold coincidence, i.e. the contemporaneous generation of four photons we can describe the state as

$$\rho^{4-\text{photon}} = \frac{1}{g_{12}^2 + g_{34}^2 + g_{12}g_{34}}\left(g_{12}g_{34}|1111\rangle\langle 1111| + g_{12}^2|2002\rangle\langle 2002| + g_{34}^2|0220\rangle\langle 0220|\right) \tag{3.19}$$

where we have described the state on the Fock basis described by the occupation numbers in the order $|n_4, n_1, n_2, n_3\rangle$. Which can be simplified by taking into account that $g_{12} = g_{34}$

$$\rho^{4-\text{photon}} = \frac{1}{3}\left(|1111\rangle\langle 1111| + |2002\rangle\langle 2002| + |0220\rangle\langle 0220|\right) \tag{3.20}$$

From this expression, it is immediately noticeable that in addition to the generation of a photon per mode, two other "spurious" configurations are generated. In some cases, it is possible to use post-selection techniques to eliminate the contributions due to the two "spurious" terms. However, in general, it is necessary to take them into account during the data analysis.

To test the indistinguishability of the photons generated by the source we perform a HOM measurement between each couple of photons. To perform the measurements the two photons are made to interact in a fiber beam splitter with the precaution that the polarization is identical for the two photons. At this point, we change the relative length between the paths, and thus the relative delay between the photons, and measure the number of coincidences. In Fig. 3.3 b is represented one of the HOM dips used for the analysis of the sources. For this type of source, the measured visibility for photons belonging to the same pair is around $0.95 \div 1$ and for photons of different couples is around $0.8 \div 0.95$. This difference can be explained by the fact that the photons of the same pair are temporally correlated meaning that they are always generated at the same time, therefore those of a different pair, even if generated by the same impulse, have a fluctuation in the relative generation time which decreases the visibility.

3.2 Evolution

After the generation of the photons the next is the evolution stage, I.e. an interferometer that implements the quantum protocol of interest. The literature presents a very large variety of interferometers depending on the experiment and the application to be pursued. Below we will focus only on linear interferometers, i.e. composed only of linear components. With regard to non-linear interferometers, please refer to the specific literature [109].

To implement a linear interferometer various platforms have been proposed depending on the degree of freedom used and the required characteristics. In Fig. 3.4

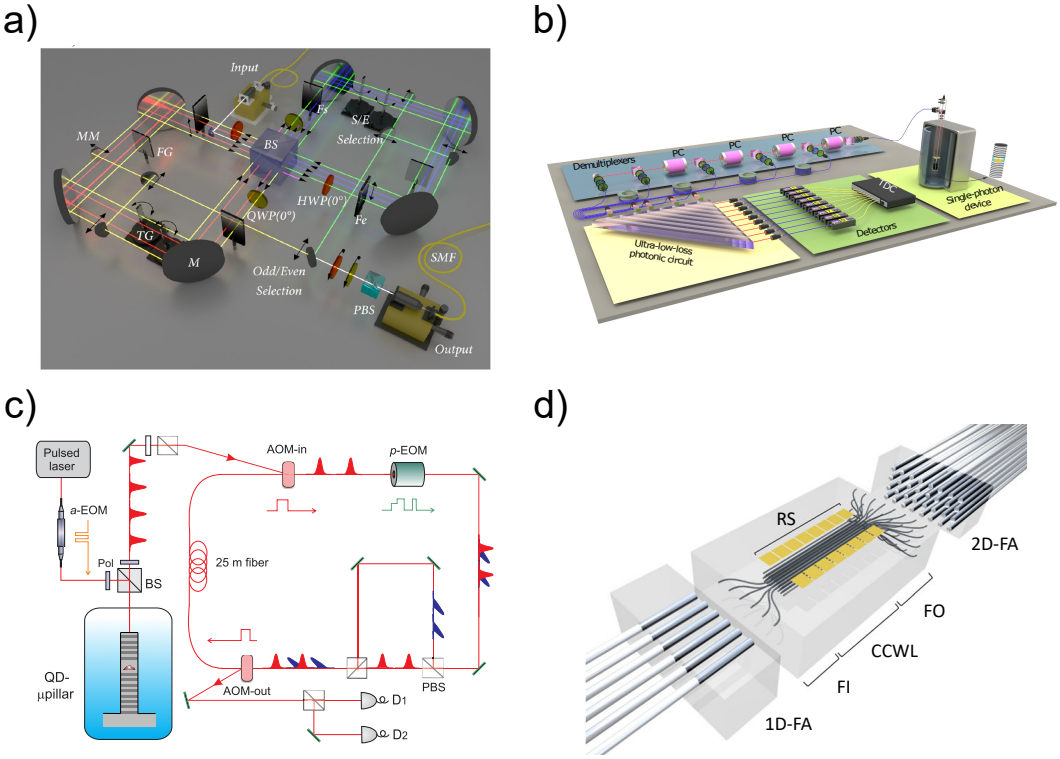

Figure 3.4. Photonic platform. a) Bulk-optics interferometer implementation, is composed of bulk components, i.e. components of macroscopic dimension, and represents the first type of interferometer implemented and remains one of the principal methods since present lower losses compared to other implementations. (figure from Ref. [106]) b) Micro-optics interferometer implementation, these interferometers are built of several fused-quartz trapezoids, covered with differently reflecting optical coatings, stacked together. (figure from Ref. [107]) c) Fiber-loop interferometer implementation, uses time bin codification and fast optical components to route the photon along paths of different lengths to make different time bins interact with each other. (figure from Ref. [108]) d) Integrated interferometer implementation. This implementation employs a series of waveguides which interact appropriately with each other through the effect of evanescent waves to create a generic linear interferometer. (figure from Ref. [2])

are represented four of the most common platforms for the implementation of a linear optical interferometer. The first implementation is with the bulk-optics component, for obvious reasons historically it is the first typology of platform used for the implementation of the interferometers and still today results in one of the most used. The main advantages of the bulk-optics platform are the easy availability of the components and the low losses that can be obtained. The main disadvantages are the lack of system stability and the necessity to realign the equipment from time to time. Furthermore, the scalability of the interferometers is impractical since the physical dimensions of the system tend to grow rapidly as the number of interferometer modes to be implemented increases. The second platform is called micro-optics and consists of a series of fused quartz trapezoids covered with differently reflecting optical coatings and glued together [107,110]. The advantages of this implementation are the low losses equal to the bulk implementation and greater stability. However, it has the enormous disadvantage that at present there are no methods to make the device reconfigurable. This implies that if one wants to modify the transformation implemented by the interferometer it is necessary to replace the device itself and realign the entire apparatus from scratch. The third platform used to implement linear interferometers is called fibre-loop [108]. This implementation uses time bin encoding and is particularly suitable for single-photon sources based on quantum dots. It consists of a loop implemented with bulk or fiber optics in which photons are spun. Through optical switches, it is possible to route the photons on a path of different lengths in order to make the photons interact in different time bins. The main advantage of this implementation is the need for a relatively small number of optical components even for implementations of interferometers with a high number of modes. The main disadvantage of this platform is the need to use high-speed optical components in order to be able to implement the necessary optical switches and a sufficiently fast and precise control system which allows the changing of the configuration of the switches at each pulse. This condition is necessary in order to implement a generic transformation. Finally, in order to be able to stay in reasonable frequency regimes for the control electronics it is necessary that the period between the pulses is sufficiently high implying a not indifferent lengthening of the length differences between the various optical paths which turn into the need to use more long optical fibers.

The last implementation is the integrated platforms which in recent years is becoming one of the most promising platforms for quantum optics experiments. The main methods for integrating optical elements into photonic chips involve the fabrication of optical waveguides. In this context, there is no unique and well-established technology since depending on the material and the fabrication process there are different properties that may or may not be implemented. For example, some of those properties are the level of miniaturization, the operating wavelength, the sensitivity to the polarization of light and the possibility to integrate also the sources and the detector of the photons. Since the integration technique for electronic circuits is based on silicon materials it is natural to think of methods based on similar technology for the integration of photonic devices, this construction technique is called Silicon-on-insulator and uses silicon [111] and silicon nitride [112] to integrate the waveguides. These materials have the advantage of having a high degree of miniaturization and the possibility of integrating both photon sources

and detectors. However, compared to other materials, they have higher losses. Many recent experiments exploit silicon circuits [87, 89–91, 113–119] and silicon nitride circuit [84, 85, 120, 121] in the various fields of quantum information. Other proposed materials for the construction of the waveguides are Lithium niobate, Gallium arsenide and Indium phosphide present large electro-optical properties that allow for fast operations on the photons [122–126]. The most used material for the construction of photonic chips, and historically the first one used, is fused silica (SiO_2) since it displays transparency of a wide range of wavelengths from visible to infrared and high coupling efficiency with fibers. Also, depending on the fabrication process, silica waveguides can display low propagation losses and birefringence. The first fabrication method used for the construction of silica waveguides is called silica-on-silicon. The fabrication process consists of the deposition of a layer of undoped silica, which is the core material of the waveguides, on a substrate of Silicon. Then the layer is patterned via standard optical lithography techniques and covered by a second layer of doped silica. This platform is the first used for the implementation of quantum and reconfigurable photonic circuits [127–131] but the further development of this technology has been limited by problems intrinsic to the constructive method. To try to solve the problems of the prior technique a different one has been developed and is called UV-writing. The silica waveguides are fabricated by focusing a strong laser pulse in a photosensitive doped silica layer placed between two layers of undoped silica. The waveguides are then etched translating the sample with respect to the laser beam [132]. This technique simplifies the fabrication process since do not require a mask for the lithography process and also allows tridimensional geometry. With this technique, the possibility of implementing integrated interferometers [133–135] and sources of quantum light [79, 136–139] have been shown, however to date a device that has both components simultaneously has not yet been created. A different laser-writing technique is the femtosecond laser writing [140]. This fabrication technique is based on the non-linear absorption of strong laser pulses focused on the silica sample. The absorption creates a permanent change in the refractive index of the material localized in the focalization point. A waveguide is directly written in the sample by translating the focal point at a constant speed. The very low birefringence of the material and the possibility to control the shape of the cross-section of the waveguides allow the realisation of chips that are polarization insensitive [141–143] as well as components to manipulate the polarization like polarizing beam splitter and waveplates [144, 145]. The possibility of creating three-dimensional geometries makes the technique more flexible than others. Indeed, with the femtosecond-laser-wiring, the possibility of implementing discrete interferometers both in a planar [142, 146–148] and in three-dimensional [149–151] configuration and also continuously coupled interferometers [152–156] has been demonstrated. Furthermore, the possibility of making the device reprogrammable through the use of thermo-optic effects has been demonstrated [2, 10, 99, 157, 158].

For the experiments presented in this thesis, we use photonic chips both in the planar and tridimensional geometry. The chips were fabricated by femtosecond laser writing in a boro-aluminosilicate glass substrate (EAGLE XG, Corning) extending on an area of $75 \times 12 mm^2$. The laser source (PHAROS, Light Conversion), operating at a wavelength of $1030 nm$, was configured to produce pulses with a duration of $178 fs$ and energy equal to $290 nJ$ at a repetition rate of $1 MHz$. The laser was focused with

a $20\times$ ($NA = 0.5$) water-immersion objective, while the substrate was translated at $20mm/s$. To ensure efficient reconfigurability, the circuit was inscribed at $30\mu m$ from the surface. After a thermal annealing step [159], single-mode waveguides operating at $785nm$ with a $1/e^2$ mode diameter of $4.5\mu m$ were obtained. Heaters were fabricated by depositing gold on the chip surface and patterning the electrical circuit with the process reported in [160] to create resists with length $3mm$ and resistance $70 \div 100\Omega$ on the surface of the chip. To guarantee proper heat dissipation, the device was mounted on an aluminium heat sink.

3.3 Detection

In an experiment after the evolution stage, we need to detect the photons in order to perform the needed measure. Photodetectors are devices that generate a macroscopic electric signal when stimulated by one or more photons. Detecting photons with a high probability and reliability represents a pivotal requirement. The photon detectors can be classified into two categories the threshold detectors and the photon-number resolved detectors. The threshold detectors generate an electrical impulse when at least one photon hit the detector. Instead, the photon-number resolved detectors in addition to detecting the presence of photons also provide their number. The threshold detectors category includes single-photon avalanche photodiodes (SPAD) made of Indium gallium arsenide [161, 162] or Germanium on silicon [163, 164], also there are detector based on negative feedback avalanche diodes [18, 165, 166], quantum dots [167], artificial Λ-type three-level systems [168], up-conversion detectors [169–173] and superconducting nanowires [174–185]. Instead, the principal technologies for the photon-number resolved detectors are transition-edge sensors [186–189], organic field-effect transistors [190], parallel superconducting nanowire single-photon detectors [191, 192]. It is also possible to implement a probabilistic version of the photon-number resolved detectors from the threshold ones using multiplexing techniques [193, 194]. As has been done for the previous components, also for single photon detectors in the literature there are various attempts to integrate them into integrated photonic devices. The principal materials used are Lithium niobate [195], Gallium arsenide [196, 197] and silicon [198, 199].

In our laboratory, we use the Exelitas SPAD detectors since they present a high efficiency at our working wavelength and do not require special precautions to be used such as cryogenic temperatures.

Part II

New protocols for optical circuits characterization

Chapter 4

General approach to the characterization of optical networks

In the previous chapters, we presented linear optical circuits and their mathematical description through the unitary operator U. An important stage for any experiment is the reconstruction of such operations. Several relevant aspects connected to optical networks have been identified in the literature. They range from engineering the optical setup for the implementation of a given unitary matrix to the identification of universal architectures that can perform any transformation [9, 57]. In this chapter, we focus on the characterization problem of a linear optical circuit which requires a systematic procedure to test its operation, or more in general, to reconstruct the unitary matrix implemented by the network. For example, interferometers based on a bulk optic implementation can be typically decomposed in elementary units that can be addressed and characterized separately. In certain cases, it is not possible to separate the various components of a linear optical circuit, e.g. in the case of integrated optics. This involves finding characterization procedures that analyze the linear network as a single element Several techniques have been developed to achieve full characterization of integrated photonic devices by exploiting different degrees of knowledge of the network's internal structure and various measurement approaches with classical or quantum light. These algorithms can be divided into two main groups. The first one is called *black box approach* and exploits only the information provided by the measurements, without assumptions on the internal structure of the optical network. The second one is the *white box approach*, which exploits knowledge of the optical network structure together with the information obtained from a set of appropriately chosen measurements. White box approaches usually make use of an optimization algorithm to estimate the parameters of the given architecture [200, 201]. It is clear that this family of reconstruction algorithms strongly depends on the knowledge of the relation between the optical component parameters and the matrix elements, and thus requires accurate modeling of the system including noise processes. On the contrary, black box approaches aim at characterizing a multimode linear optical interferometer without using any information about its structure. They are very useful when the structure

is inaccessible, untrusted or too complex to be modelled [2]. A black-box method for linear optical circuits was proposed in Ref. [25] and subsequently refined in Ref. [202]. The authors presented an analytical algorithm to reconstruct the elements of the unitary matrix U from quantum light measurement, via single- and two-photon experiments. The algorithm is advantageous since it permits to retrieval the matrix U even in the presence of losses and optical phase instabilities due to, for example, fiber connections in the input and output stages. However, such a method requires quantum light input states and the accuracy is limited by noisy experimental data. In fact, the result of this reconstruction method is typically employed as a starting point for further numerical optimization to improve the stability of the solution. An alternative method exploits only classical field intensities measurements [203]. The moduli of the matrix elements are measured from the field intensities distribution in the output modes, while, the complex phases are estimated by a measurement of the interference fringes between two coherent beams. The two procedures for the moduli and the phases estimations are independent and they can be mapped directly onto the unitary matrix without the need to apply any further optimization algorithms [200, 203]. With this approach, a crucial requirement for a correct phase measurement is to perform the phase scan in times much shorter than the typical timescale of phase fluctuations of the system. In addition, it cannot be used in the presence of mode-dependent losses in the collection stages. Other black-box algorithms based on coherent light measurements always require high phase stability during the scan in the input and output sections [204–206], thus making them not viable for optical setups with in-fiber connections, which are nevertheless typical for integrated photonic devices. The last class we mention is machine-learning algorithms [207, 208] that need large sets of data to learn the correct transformation. Very recently, Kuzmin et al. [209] simulated the application of a supervised-learning strategy for the calibration of a reconfigurable interferometer and experienced an unfavorable scaling of the training set size with the number of modes in the black box scenario.

In this chapter, we propose a new black box approach that aims at solving some open issues mentioned in the past algorithms. The goal is to provide a methodology to identify separately mode-dependent losses and matrix elements of U via coherent light measurements. In particular, we first present two algorithms to estimate the amount of loss imbalance in the injection and collection stages of a linear optical interferometer and consequently characterize the moduli of the elements of the unitary matrix. Then, we move to the problem of measuring the phases of the unitary matrix elements. Previous algorithms [25, 202] exploited second-order quantum optical correlations such as the Hong-Ou-Mandel effect [63], or the first-order classical correlations in Mach–Zehnder like interferometric structures [203]. Since there are mathematical analogies between classical and quantum second-order correlations [210], we propose to replace such quantities with the second-order correlations of classical light in a Hanbury-Brown&Twiss like experiment [211]. This approach combines some advantages of both the previous methods, i.e. the use of classical light [203] and the independence from losses and optical phase instabilities, like the methods that employ as a probe pair of indistinguishable photons [25, 202]. Moreover, we show that the proposed classical second-order measurements depend only on the matrix phases and not on the moduli as for the quantum correlations.

This allows for completely independent estimations of the phases, input/output losses and the moduli of the unitary matrix. From an experimental point of view, this is an important improvement that reduces the propagation of the error along the characterization process. Thus, this method can be applied in a general scenario and can be effective for different experimental platforms, ranging from bulk to integrated and in-fiber optical setups. Some results of this chapter are published in the following work:

Characterization of multimode linear optical networks Francesco Hoch, Taira Giordani, Nicolò Spagnolo, Andrea Crespi, Roberto Osellame, Fabio Sciarrino. Adv. Photon. Nexus 2(1), 016007 (2023) [3]

4.1 Overview on black-box linear optical circuits reconstruction

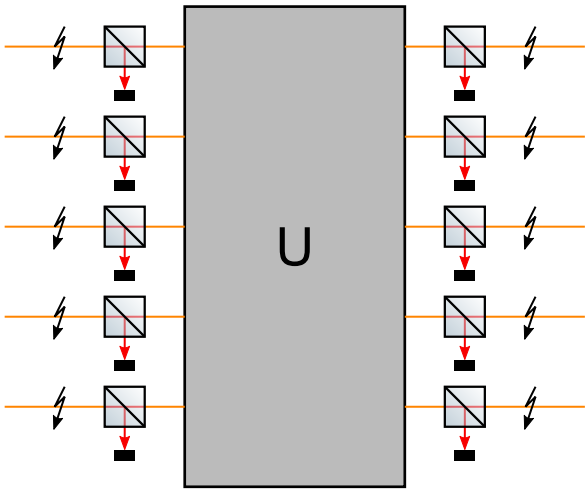

Figure 4.1. multimode linear interferometer. The multimode interferometer model considered in this chapter. It consists of the ideal optical circuit described by the unitary transformation U plus layers of mode-dependent losses at the input and at the output (represented by beam splitters in the figure), and phase instabilities (represented by sparks). Output losses take into account also possible differences in the detection efficiencies among the modes.

Any ideal linear optical interferometer can be represented by a unitary matrix U, acting on the annihilation operators of the electromagnetic field of the input (a_j) and output (b_i) modes as follows

$$b_i = \sum_j U_{ij} a_j \tag{4.1}$$

where U_{ij} are the elements of the unitary matrix. The same relation holds for classical states of light, replacing the operators a_i and b_i with the complex field E_i in Eq. (4.1). In other words, the elements of the unitary matrix U_{ij} completely characterize the field amplitudes propagation through a multimode optical network.

In general, the set of optical modes i may represent any degree of freedom of light, such as polarization, path, time of arrival and frequency.

Optical losses deviate the interferometer operation from unitarity. To take into account the losses we consider biased insertion losses in input and output, and balanced internal losses which are known to commute with the unitary matrix [212]. This assumption is not the most general since it considers the optical transformation U without any internal unbalances among the modes, but most of the photonic circuits are designed in such a way that losses are practically unbiased along the evolution. Then, our model of losses can find applications in many scenarios. We model losses as in Fig. 4.1 with a set of beam splitters placed on the input and output modes. We further consider the presence of unknown (and possibly unstable) phase terms on these modes. The device is thus described by a matrix $T = \mathcal{D}_1 U \mathcal{D}_2$, where $\mathcal{D}_1$ and $\mathcal{D}_2$ are diagonal matrices that account for such losses and additional phases. The matrix elements of the unitary part are expressed as $U_{ij} = \tau_{ij} e^{i\phi_{ij}}$, where τ_{ij} and ϕ_{ij} are the matrix moduli and phases respectively. In what follows, we briefly analyze the two most general algorithms in the literature to reconstruct the matrix U. The first algorithm exploits quantum light [25] and the second one is based on coherent light measurements [203].

If one employs measurements with Fock states at the input of the interferometer and photon-number-resolving detection at the output, the results will be insensitive to the (unstable) phase terms at the input and at the output. This means that the matrix U and all the matrices U' in the form $U' = F_1 U F_2$, where F_1 and F_2 are a unitary diagonal matrix, are equivalent. Another invariance property of these measurements carried out with Fock states is that the outcomes do not change with respect to the conjugate operation $U' = U^*$. Given these equivalence relations, it is not necessary to reconstruct the actual unitary matrix implemented by the interferometer but only a representative element of its class of equivalence. This is commonly defined by choosing a matrix with real-valued elements in the first row and first column ($\phi_{0i} = 0$ and $\phi_{i0} = 0$) together with the condition that the element U_{11} has positive phase ($\phi_{11} > 0$). In Ref. [25], the authors presented an algorithm to reconstruct the value of moduli and phases of the representative unitary matrix elements via single-photon intensity and two-photon measurements, the latter via the visibility $\mathcal{V}$ of Hong-Ou-Mandel (HOM) interference [63]. Labelling the input modes of the two photons as h, k, and the output ones as i, j, as defined in chapter 2, the visibility is

$$\mathcal{V}_{ij}^{hk} = -\frac{2\tau_{jk}\tau_{ih}\tau_{ik}\tau_{jh}}{\tau_{jk}^2\tau_{ih}^2 + \tau_{ik}^2\tau_{jh}^2} \cos\left(\phi_{jk} + \phi_{ih} - \phi_{ik} - \phi_{jh}\right) \tag{4.2}$$

The important thing about visibility $\mathcal{V}$ is the cosine dependence from the phases of the unitary transformation. Moreover, this quantity does not change in the presence of mode-dependent losses in both the preparation and measurement stages, and thus its estimation gives direct access to the matrix elements. By measuring these quantities it is possible to define a system of equations and to retrieve an analytical solution to the problem, as shown in [25, 202]. One of the main constraints of such an approach is the requirement of measurements with quantum light.

The other method proposed in Ref. [203], based on classical intensity measurements, requires phase stability within the measurement time to estimate matrix

phases since these values are extracted from first-order correlation functions. This means that in such a measurement scheme the equivalence between U and U' does not hold. Additionally, the correct estimation of matrix element moduli, which in this approach is performed independently of the phase estimations, is spoiled by the presence of output mode-dependent losses.

4.2 Algorithm for reconstruction of linear interferometers

In this section, we propose a different black-box approach based on the same assumption of the model presented in the previous section that uses as a probe only coherent light. This method permits to estimate of the matrix moduli and the losses imbalances without needing to know the phases. In particular, it presents a quantity similar to the visibility $\mathcal{V}$ that does not depend on the moduli of the matrix making it completely independent from their measure.

4.2.1 Reconstruction of moduli and losses

We start our investigation with the estimation of the matrix elements moduli τ_{ij}. The τ_{ij}^2 coefficients represent the probability to find a single photon in output mode j given an input mode i or, alternatively, the fraction of classical field intensity in the mode j. This observation allows defining a probability matrix $P_{ij} = \tau_{ij}^2$. The main task is to estimate such a matrix when mode-dependent losses are present in the preparation and collection stages. Let us define M as the matrix obtained from single-mode intensity measurements, estimated experimentally via single-photon input states or by injecting laser light in a single mode. Following the model presented in Fig. 4.1, the actually measured matrix M can be expressed as follows

$$M = D_1 P D_2 \tag{4.3}$$

where D_1 and D_2 are diagonal matrices that describe the unbalanced losses in input and output modes. The task then requires reconstructing the probability matrix P and the input and output losses matrices D_1 and D_2 starting from the measured matrix M. To this end, we introduce two approaches that can be used to estimate D_1 and D_2 up to a multiplicative factor and, consequently, the matrix P under very few assumptions on the measured matrix M.

Sinkhorn's decomposition-based algorithm.

A first approach to reconstruct the matrices P, D_1 and D_2 is obtained starting from the observation that the probability matrix P is a doubly stochastic matrix, i.e. the matrix has non-negative entries and the sum of each row and each column is equal to one. It is thus possible to apply Sinkhorn's theorem and the matrix scaling algorithm on this system [213, 214]. Indeed, a matrix with non-negative elements such as M admits a Sinkhorn's decomposition if it is diagonally equivalent to a doubly stochastic matrix, i.e. can be written in the form $D_1 P D_2$ where D_1 and D_2 are diagonal matrices and P is a doubly stochastic matrix. This decomposition

exactly represents the solution to our problem (see Eq. (4.3)). Sinkhorn's theorem and subsequent extensions [213] guarantee that this solution exists and it is unique. The theorem gives us also an important warning since the algorithm is sensitive to the position of the zero elements of the measured matrix M. This means that an incorrect attribution of zero-valued elements in M, due to experimental errors or limited measurement sensitivity, could make the matrix impossible to decompose with the Sinkhorn's theorem.

Finding Sinkhorn's decomposition for a non-negative matrix M is a special case of the matrix scaling problem that has applications in a large variety of fields. In our case, defining $X = D_1^{-1}$ and $Y = D_2^{-1}$, we can write $P = XMY$ and using the property that P have to be doubly stochastic, we obtain the following system of equations

$$\begin{cases} XMY\vec{e} = \vec{e} \\ YM^T X\vec{e} = \vec{e} \end{cases} \tag{4.4}$$

where $\vec{e}$ is the vector with all the components equal to 1.

In the literature, different algorithms have been proposed to solve Eq. (4.4). Here, we present a specific choice among the possible algorithms (see Ref. [215] for a review of the possible approaches). The chosen algorithm allows the recovery of all three matrices in Eq. (4.3). The idea is to rearrange Eq. (4.4) in terms of vectors $\vec{x}$ and $\vec{y}$ which are the diagonal elements of X and Y. Formally, they can be expressed as $\vec{x} = X\vec{e}$ and $\vec{y} = Y\vec{e}$. By defining the inversion of a vector as the inversion component-by-component, $\vec{x}^{-1} = (x_1^{-1}, x_2^{-1}, \ldots, x_N^{-1})$, we find that:

$$\begin{cases} \vec{x} = (M\vec{y})^{-1} \\ \vec{y} = (M^T\vec{x})^{-1} \end{cases} \tag{4.5}$$

The iterative algorithm solves the following system of equations for the vectors $\vec{x}$ and $\vec{y}$. The algorithm start with an initial guess $\vec{y} = \vec{e}$, then iteratively applies the two equations of the system in Eq.(4.5) as:

$$\begin{aligned} \vec{y}^{(0)} &= \vec{e} \\ &\cdots \\ \vec{x}^{(n)} &= (M\vec{y}^{(n-1)})^{-1} \\ \vec{y}^{(n)} &= (M^T\vec{x}^{(n)})^{-1} \end{aligned} \tag{4.6}$$

The algorithm proceeds until the deviations from 1 of the sum of the column elements, and of the sum of the row, are smaller than a threshold error ϵ. In particular, the columns of the matrix $P^{(n)} = X^{(n)}MY^{(n)}$ after n iterations will be, by definition, always normalized, i.e. $(P^{(n)})^T\vec{e} = \vec{e}$. Then, the algorithm checks if the sums of the rows are close to 1, which can be expressed as

$$\max_i |(P^{(n)}\vec{e})_i - 1| < \epsilon \tag{4.7}$$

The algorithm stops when such a condition is satisfied. The latter can be expressed in the following equivalent form, used during the iterations, that is computationally less complex

$$\max_i |x_i^{(n)}(x_i^{(n+1)})^{-1} - 1| < \epsilon \tag{4.8}$$

At this point, the algorithm returns the two vectors $\vec{x}$ and $\vec{y}$, and consequently the two diagonal matrices X and Y. Then, we can retrieve the probability matrix $P = XMY$ and the two losses matrices as $D_1 = X^{-1}$ and $D_2 = Y^{-1}$.

Variance-minimization based algorithm.

In the derivation of the previous algorithm to solve Eq. (4.3) we have implicitly assumed to have measured the field intensity distribution for any combination of outputs j for any input i. In the following method, we define an alternative procedure that can be applied when only a subset of the inputs are available while requiring the capability of reconfiguring the linear optical network.

Let us then consider an interferometer in which it is possible to change the probability matrix P without affecting the input and output losses D_2 and D_1, and to measure all the output configurations only for a subset of input modes. We first consider the scenario in which the light source, a single photon or a laser beam, is injected only in mode i. In absence of unbalanced losses, the outcome $\vec{M}$ of such intensity measurements is proportional to the vector $\vec{\mathcal{P}}$, (the i-th column of the matrix P) and represents a discrete probability distribution which depends from a set of parameters $\vec{\theta}$ describing the optical circuit settings. By taking into account the presence of unbalanced losses $\vec{D}$ (D_1 in the general case), the components M_j of the vector $\vec{M}$ are

$$M_j(\vec{\theta}) = I\mathcal{P}_j(\vec{\theta})D_j \tag{4.9}$$

where I is the intensity attenuated by the input loss. Since we are injecting light in the same mode for all measurements, this factor can be included in $\vec{D}$.

The separation of the probability from the losses in Eq. (4.9) can be done starting from the following observation. Let us define the quantity $S(\vec{\alpha}, \vec{\theta})$ as the weighted sum of the components of $\vec{M}$:

$$S(\vec{\alpha}, \vec{\theta}) = \sum_j \alpha_j M_j(\vec{\theta}) \tag{4.10}$$

If the vector of the weights $\vec{\alpha}$ is proportional to the element-wise inverse of the losses vector $\vec{D}$, the quantity S does not vary with the control parameter $\vec{\theta}$. In fact, when $\vec{\alpha} = \beta\vec{D}^{-1}$, where β is a global factor, we have:

$$S(\beta\vec{D}^{-1}, \vec{\theta}) = \beta \sum_j D_j^{-1} M_j(\vec{\theta}) = \beta \sum_j D_j^{-1} D_j \, \mathcal{P}_j(\vec{\theta}) = \beta \tag{4.11}$$

In general, $S(\vec{\alpha}, \vec{\theta})$ changes with the controls parameters $\vec{\theta}$. Then, the idea is to find the weight vector $\vec{\alpha}$ such that $S(\vec{\alpha}, \vec{\theta})$ is constant when the controls parameters $\vec{\theta}$ vary. This vector can be obtained by minimizing the variance of $S(\vec{\alpha}, \vec{\theta})$ with respect to $\vec{\alpha}$. The variance $\xi^2(\vec{\alpha})$ can be estimated on a sufficiently large set of settings of the parameters $\{\vec{\theta_i}\}$ as

$$\xi^2(\vec{\alpha}) = \frac{\sum_{i=0}^{n-1} S(\vec{\alpha}, \vec{\theta_i})^2}{n} - \left(\frac{\sum_{i=0}^{n-1} S(\vec{\alpha}, \vec{\theta_i})}{n} \right)^2 \tag{4.12}$$

where n is the number of different settings $\{\vec{\theta_i}\}$, and consequently represent the size of the measurement outcome vector $\{\vec{M}(\vec{\theta_i})\}$. This minimization is equivalent to a

quadratic optimization problem. To solve such a task, let us call $\mathcal{M}_{ij} = [\vec{M}(\vec{\theta}_i)]_j$ the matrix in which each row contains the output intensities distribution for a particular configuration of the chip then we define the following positive semi-definite matrix Q as

$$Q_{hk} = \frac{1}{n}\sum_{i=0}^{n-1}\mathcal{M}_{ih}\mathcal{M}_{ik} - \frac{1}{n^2}\sum_{i=0}^{n-1}\sum_{j=0}^{n-1}\mathcal{M}_{ih}\mathcal{M}_{jk} \tag{4.13}$$

Then our problem can be rewritten, in terms of the matrix Q, as

$$\xi^2(\vec{\alpha}) = \sum_i \sum_j Q_{ij}\alpha_i\alpha_j \tag{4.14}$$

The minimization of Eq. (4.14) has as trivial solution $\vec{\alpha} = \vec{0}$ (the vector with all null components) and another one that is the eigenvector of Q corresponding to a null eigenvalue. The latter solution corresponds exactly to the element-wise inverse of the losses vector $\vec{\alpha} = \vec{D}^{-1}$. In the presence of noisy experimental data, the solution is the eigenvector of Q corresponding to the lowest eigenvalue. Alternatively, the non-trivial solution can be found by an ordinary numerical minimization approach of Eq. (4.14). This can be fulfilled by setting a normalization constraint $\vec{N}\cdot\vec{\alpha} = 1$ for some normalization vector $\vec{N}$, since losses can be estimated with this procedure up to a multiplicative factor common to all the modes.

The method can be generalized to the scenario in which one is interested in reconstructing a sub-matrix of P. Then, it is possible to reconstruct even the relative losses between the different measured input modes. Here, we suppose to have a set of output vectors $\{\vec{M}_i\}_k$ for each input $k \in K$ and compute the variance function $\xi_k^2(\vec{\alpha})$ and the associated matrix $Q^{(k)}$. At this point we minimize the sum of all variances with the same constraints of the previous derivation:

$$\sum_{k\in K}\xi_k^2(\vec{\alpha}) = \sum_i\sum_j\sum_{k\in K} Q_{ij}^{(k)}\alpha_i\alpha_j \tag{4.15}$$

After the minimization, it is possible to recover the input losses from the value of the sum function associated with each input as follows

$$\frac{(\vec{D}_2)_k}{(\vec{D}_2)_{k'}} = \frac{\frac{1}{n}\sum_{i=0}^{n-1}\sum_j \alpha_j\mathcal{M}_{ij}^{(k)}}{\frac{1}{m}\sum_{i=0}^{m-1}\sum_j \alpha_j\mathcal{M}_{ij}^{(k')}} \tag{4.16}$$

4.2.2 Reconstruction of the internal phases with classical light.

Here we propose a procedure to estimate the complex phases of the matrix elements ϕ_{ij}. The methods reported in Ref. [25, 202] employs the visibility of the Hong-Ou-Mandel (HOM) effect described in Eq. (4.2) for this task, by sending a two-photon input state whose indistinguishability is tuned during the experiment. In this chapter, we propose an analogous quantity that can be measured by intensity cross-correlation at the output of the linear network with classical light. The measurement scheme is presented in Fig. 4.2. The laser source is split and sent into the network in modes (h, k). The additional phases φ_1 and φ_2 account for phase instabilities in the optical paths between the sources and the interferometer. We can define the

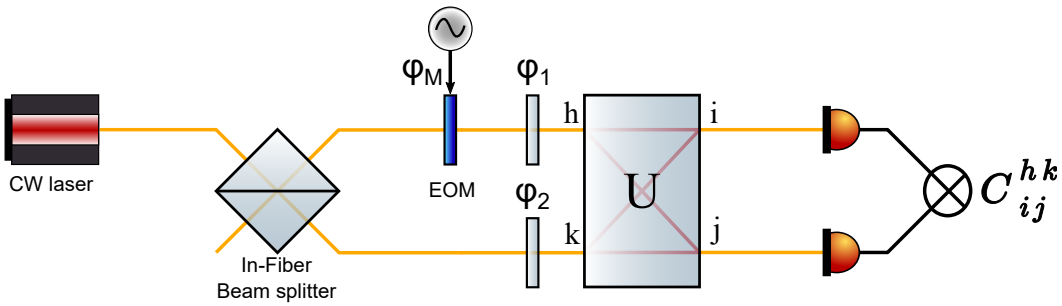

Figure 4.2. Scheme for the measurement of second-order cross-correlations C_{ij}^{hk} with coherent light emitted by a continuous wave laser (CW). The latter is coupled in single-mode fiber and split into two beams by an in-fiber beam splitter. The two beams enter the interferometer in modes h, k. The phase modulation φ_M performed by a liquid crystal compensates the fiber phase fluctuations $\varphi = \varphi_1 - \varphi_2$ to satisfy the conditions in Eq. (4.28).

cross-correlation σ_{ij}^{hk} between the output modes (i, j) when the two beams enter from modes (h, k) as

$$\sigma_{ij}^{hk} = \langle (I_i - \langle I_i \rangle)(I_j - \langle I_j \rangle) \rangle = \langle I_i I_j \rangle - \langle I_i \rangle \langle I_j \rangle \tag{4.17}$$

where I_i and I_j are the field intensities in the corresponding output modes, while $\langle \cdot \rangle$ is the time average. We define also the self-correlation σ_{ii}^{hk} of the intensity fluctuation as

$$\sigma_{ii}^{hk} = \langle (I_i - \langle I_i \rangle)^2 \rangle = \langle I_i^2 \rangle - \langle I_i \rangle^2 \tag{4.18}$$

Finally, we can define the normalized cross-correlation C_{ij}^{hk} as

$$C_{ij}^{hk} = \frac{\sigma_{ij}^{hk}}{\sqrt{\sigma_{ii}^{hk} \sigma_{jj}^{hk}}} \tag{4.19}$$

Using the hypotheses that (i) the external phase fluctuations $\varphi = \varphi_1 - \varphi_2$ have zero time average, and (ii) the input laser intensity is constant, we want to show that the normalized cross-correlation can de used to substitute the HOM visibility for the characterization of the phase.

Starting from Figure 4.2, we consider two laser beams at the input of the interferometer. The input fields are described as:

$$\tilde{E}_h = \tilde{E}_1 e^{i\varphi_1(t)} \tag{4.20}$$

$$\tilde{E}_k = \tilde{E}_2 e^{i\varphi_2(t)} \tag{4.21}$$

where $\phi_1(t)$ and $\phi_2(t)$ are the phases introduced via propagation in optical fibers, and by all the other possible optical delays in the apparatus. After propagation through the interferometer, the electric fields on the output modes read:

$$\begin{aligned} \tilde{E}_i &= U_{ih} \tilde{E}_h + U_{ik} \tilde{E}_k \\ \tilde{E}_j &= U_{jh} \tilde{E}_h + U_{jk} \tilde{E}_k \end{aligned} \tag{4.22}$$

Then, the output intensity of light is measured via two photodiodes:

$$\begin{aligned} I_i &= \tilde{E}_i \tilde{E}_i^* = I_1 \tau_{ih}^2 + I_2 \tau_{ik}^2 + \tilde{E}_1 \tilde{E}_2^* U_{ih} U_{ik}^* + \tilde{E}_1^* \tilde{E}_2 U_{ih}^* U_{ik} \\ I_j &= \tilde{E}_j \tilde{E}_j^* = I_1 \tau_{jh}^2 + I_2 \tau_{jk}^2 + \tilde{E}_1 \tilde{E}_2^* U_{jh} U_{jk}^* + \tilde{E}_1^* \tilde{E}_2 U_{jh}^* U_{jk} \end{aligned} \tag{4.23}$$

If we suppose that the intensity of the input lasers I_1 and I_2 are constant and that $\langle \tilde{E}_1 \tilde{E}_2^* \rangle = 0$ (that in our scenario is equivalent to $\langle e^{\imath(\varphi_1 - \varphi_2)} \rangle = 0$), we can calculate the residual as:

$$\begin{aligned} I_i - \langle I_i \rangle &= \tilde{E}_1 \tilde{E}_2^* U_{ih} U_{ik}^* + \tilde{E}_1^* \tilde{E}_2 U_{ih}^* U_{ik} \\ I_j - \langle I_j \rangle &= \tilde{E}_1 \tilde{E}_2^* U_{jh} U_{jk}^* + \tilde{E}_1^* \tilde{E}_2 U_{jh}^* U_{jk} \end{aligned} \tag{4.24}$$

At this point we can calculate the cross-correlation σ_{ij}^{hk} between the output modes (i, j) when the two beams enter from modes (h, k), and the self-correlation σ_{ii}^{hk} of the intensity fluctuation as:

$$\begin{aligned} \sigma_{ij}^{hk} &= \langle (I_i - \langle I_i \rangle)(I_j - \langle I_j \rangle) \rangle \\ \sigma_{ii}^{hk} &= \langle (I_i - \langle I_i \rangle)^2 \rangle \end{aligned} \tag{4.25}$$

Let us know define a parameter $\gamma = \langle \tilde{E}_1 \tilde{E}_2^* \tilde{E}_1^* \tilde{E}_2 \rangle / (I_1 I_2)$, related to the first order correlation functions of the two beams that it is in turn related to the visibility of the interference fringes. In addition, we assume that the fields satisfy the following hypothesis $\langle (\tilde{E}_1 \tilde{E}_2^*)^2 \rangle = 0$, which is equivalent to the condition $\langle e^{\imath 2(\varphi_1 - \varphi_2)} \rangle = 0$. Under these assumptions, the cross-correlations can be calculated as:

$$\begin{aligned} \sigma_{ij}^{hk} &= \gamma I_1 I_2 (U_{ih} U_{ik}^* U_{jh}^* U_{jk} + U_{ih}^* U_{ik} U_{jh} U_{jk}^*) \\ \sigma_{ii}^{hk} &= 2\gamma I_1 I_2 |U_{ih}|^2 |U_{ik}|^2 \\ \sigma_{jj}^{hk} &= 2\gamma I_1 I_2 |U_{jh}|^2 |U_{jk}|^2 \end{aligned} \tag{4.26}$$

Finally, by calculating the normalized cross-correlation C_{ij}^{hk} we obtain the equation:

$$C_{ij}^{hk} = \frac{\sigma_{ij}^{hk}}{\sqrt{\sigma_{ii}^{hk} \sigma_{jj}^{hk}}} = \frac{(U_{ih} U_{ik}^* U_{jh}^* U_{jk} + U_{ih}^* U_{ik} U_{jh} U_{jk}^*)}{2|U_{ih}||U_{ik}||U_{jh}||U_{jk}|} = \cos(\phi_{ih} - \phi_{ik} - \phi_{jh} + \phi_{jk}) \tag{4.27}$$

Note that this quantity only depends on the phase of the matrix elements. Similarly to HOM visibility in two-photon experiments, the set $\{C_{ij}^{hk}\}$ does not depend on the input and output losses. Additionally, and at variance with HOM visibility, $\{C_{ij}^{hk}\}$ does not depend also on the moduli $\{\tau_{i,j}\}$ of the matrix elements, thus permitting an independent estimation of the phases. The derivation of Eq. (4.27) is performed under a specific assumption on the external optical phase fluctuations at the input. More specifically, we require that

$$\langle e^{\imath\varphi} \rangle = 0 \qquad \langle e^{2\imath\varphi} \rangle = 0 \tag{4.28}$$

In general, mechanical and thermal phase fluctuations do not satisfy these conditions. These equations can be satisfied by adding a phase modulator in one of the two input paths. In this scenario, the external phase contribution can be expressed as

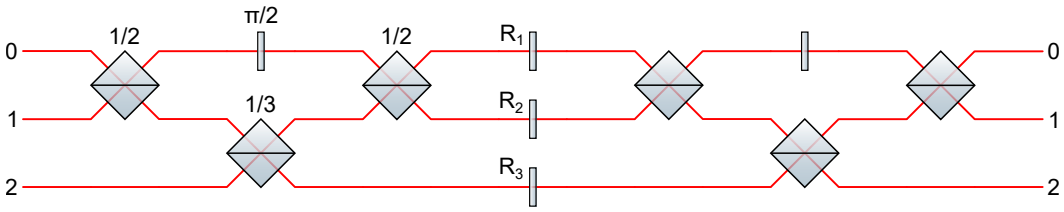

Figure 4.3. The 3-mode integrated chip employed to test the reconstruction algorithm. It is composed of a sequence of two tritter structures. Each tritter comprises three beam-splitters, whose reflectivity is reported in the figure, and a phase-shift equal to $\pi/2$. Between the two tritters there are three heaters $\{R_1, R_2, R_3\}$ that dynamically control the optical phases between the two structures via the thermo-optic effect.

$\varphi = \varphi_M + \varphi_T$, where φ_M is the modulated phase and φ_T is the one modified by thermal and mechanical noise. Since the two contributions are uncorrelated, we can write $\langle e^{\imath\varphi}\rangle = \langle e^{\imath\varphi_M}\rangle\langle e^{\imath\varphi_T}\rangle$. Controlling the phase modulation such that $\langle e^{\imath\varphi_M}\rangle = 0$ and $\langle e^{2\imath\varphi_M}\rangle = 0$, for example by adding white noise with appropriate amplitude or by a discrete set of phases, the conditions of Eq. (4.28) can be satisfied.

4.2.3 Complete algorithm

Given the methods defined above, we can summarize the complete procedure to reconstruct the matrix U as follows

1. Perform field intensity measurements in the output of the circuit. Apply the Sinkhorn-based algorithm to retrieve the complete set of moduli for the matrix elements ($\{\tau_{i,j}\}$) or the variance minimization approach to estimate a specific subset.

2. Perform cross-correlation measurements in pairs of the output of the circuit. Solve the system of equations for the set $\{C_{ij}^{hk}\}$ to extract the complex phases of the unitary matrix.

Note that point 2 has some similarities to the procedure proposed in Refs. [25, 202] with HOM visibilities. In particular, this approach could require a further minimization step on a larger set of $\{C_{ij}^{hk}\}$ with respect to the minimum ensemble needed to solve the system. Nonetheless, it is worth noting that in our case we do not require (i) the use of indistinguishable single-photon states and (ii) the measurements of $\{C_{ij}^{hk}\}$ give us directly the information about the phases without requiring the knowledge of the matrix moduli. In fact, in our algorithm points 1 and 2 are independent, as for the previous methods with coherent probe light [203, 206], but having the additional features of permitting the estimation of losses. Furthermore, it can be applied in any scenario with phase instabilities.

4.3 Experimental verification in a reconfigurable integrated circuit

We tested the complete algorithm described in the previous section in a 3-mode reconfigurable optical circuit. The waveguides of the device were fabricated in a

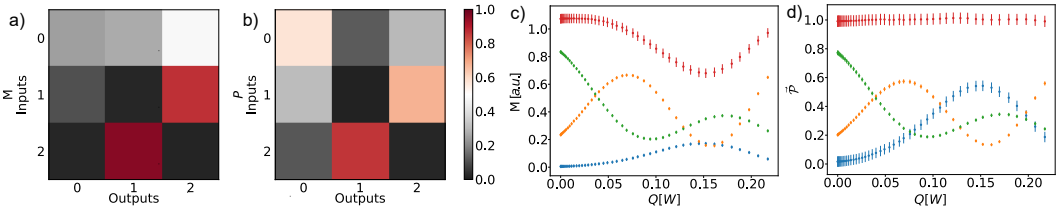

Figure 4.4. Losses and moduli estimation. We show the results of the Sinhkorn- and variance minimisation-based algorithms. First, we compare the matrix of the field intensities M (panel a) with the matrix P after the application of the Sinkhorn's algorithm (panel b). In figure c) we report the output intensity distribution at the three output ports when the laser is injected in the first input for different values of the electrical powers dissipated in the resistor R_1. Red points correspond to the sum of the three intensities in the outputs (blue: output port 0, orange: output port 1, green: output port 2). In figure d), we report the distribution $\vec{\mathcal{P}}$ and the sum after the application of the variance minimization algorithm. The error bars reported in c) correspond to the precision of the field intensity measurements performed by a power meter. They are propagated to estimate the error of the sum. In figure d) the error bars are the result of a Monte Carlo approach applied to the reconstruction algorithm.

glass sample via the femtosecond laser-writing technique [140]. The structure is composed of a sequence of two tritters, a circuit that generalizes the beam-splitter over three modes [157, 216] (see also Fig. 4.3). Between the two tritters the presence of three resistive heaters permits to change the unitary transformation performed by the circuit via the thermo-optic effect. The measurements were performed with a continuous wave laser at the wavelength of $\lambda = 785nm$. The laser is routed in different input modes via a fiber switch connected to a fiber array that injects light into the input port of the interferometer. The field intensity distribution in the 3 output ports was recorded via a CCD camera.

Our first experimental test regards the two algorithms described above, to retrieve the losses vectors and moduli of the matrix elements. In Fig 4.4 a) and b) we report the results for the application of Sinkhorn's decomposition method. In particular, in panel a) we report the measured field intensity M for a particular configuration of the chip, normalized to the column total intensity. Here we inserted on-purpose additional losses by placing an attenuation filter on the output mode 0, to test the performances of the approach. In Fig 4.4 b) we report the probability matrix P after the applications of the Sinkhorn algorithm. We measured the moduli of a set of N different transformations U, each of them in two loss conditions, namely by inserting and removing the attenuation filter in mode 0. Defining the fidelity as $F = (1/3 \sum_{i,j=0}^{2} \sqrt{P_{ij} P'_{ij}})^2$, the average classical Similarity between the two reconstructed distributions in the two losses configurations for a given U via the Sinkhorn method is $\bar{F} = 0.9999 \pm 0.0001$ ($F_{\min} = 0.9997$). The average was estimated on the set of the N pairs of matrices. This confirms that the method works properly in different mode-dependent loss configurations, and retrieves as expected always the same moduli $|\tau_{i,j}|^2$ associated with the transformation U.

We then move to test the second algorithm based on variance minimization. In Fig. 4.4 c) we report the measured field intensity in the three outputs of the interferometer for different dissipated powers in one heater, thus corresponding

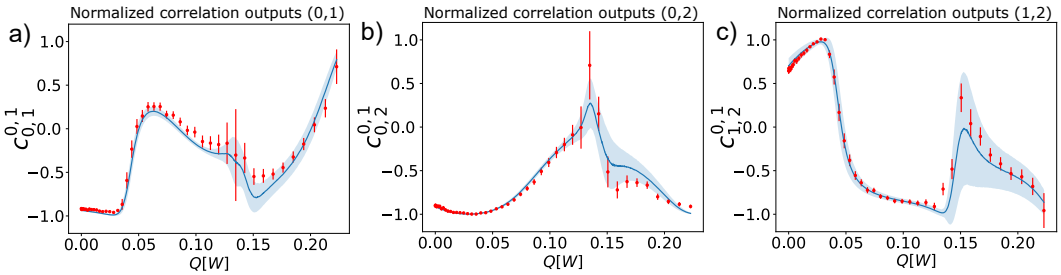

Figure 4.5. Cross-correlation measurements. In this figure we report the measurement of the normalized cross-correlations C_{ij}^{hk} for different pairs of outputs, entering from $(h,k) = (0,1)$. In particular in a) we measure the pair $(0,1)$, in b) the pair $(0,2)$ and in c) the pair $(1,2)$. In red we report the experimental correlations for different configurations of the dissipated electrical power in the heater R_1. In blue the predictions according to the results of a white-box fit that makes use of the structure of the interferometer and the previous measurements of the matrix moduli. The two independent estimations are in good agreement within one standard deviation of the experimental error.

to different evolutions U, when the signal is injected in input 0. We also report the sum (red curve) of the three intensities for each tested configuration for U. We observe that such a sum is not constant, as one would expect if the output losses were balanced. In d) we report the same curves after applying the variance minimization algorithm, showing that the application of the algorithm makes the sum constant with respect to changes in the internal transformation. We repeat the same procedure of the previous paragraph by tuning the output mode-dependent losses, showing the capability of retrieving the correct moduli values. The average fidelity, among the same set of N internal operations, between the reconstructed distributions in the two different conditions of losses after the application of the algorithm is $\bar{F} = 0.9996 \pm 0.0002$ ($F_{\min} = 0.9990$). As a further confirmation, we compared the distributions, corresponding to the same optical circuit settings, retrieved by the application of the two algorithms. The mean fidelity between the reconstructed matrix with the two methods is $\bar{F} = 0.999 \pm 0.001$ ($F_{\min} = 0.992$), thus confirming the effectiveness of both algorithms.

Finally, we tested the measurement of the cross-correlations defined in Eq. (4.19) for the phase reconstruction. Since the phase fluctuations of the fibers do not fulfil the conditions of Eq. (4.28), we placed a liquid crystal in one arm before the first input of the photonic chip. For the phase modulation, we used a discrete set of phases instead of a continuous one. In particular we employed the set $\{0, 2\pi/3, 4\pi/3\}$. After recording the temporal fluctuations of the output field intensities, we calculated the normalized cross-correlations for various configurations of the interferometer (red dot in Fig. 4.5). These measurements are compared with the predictions made by an independent characterization of the device via a white-box algorithm, used as a reference to test our approach. By this alternative method, which exploits the structure of the two tritters, the moduli and the phases of the matrix are retrieved directly from the field intensity distributions of the previous paragraph. It follows that, in this white-box approach used as a reference, the cosines of the internal phases are the result of a numerical optimization between the parameters of the optical circuit, which is designed according to the structure in Fig. 4.3, and

the measurements of the $\vec{P}$ distributions. The blue curve in Fig. 4.5) represents the prediction of such an optimization. We observe that the direct measurement of cross correlation via the proposed approach with classical light, and the same quantities retrieved via the white-box method, are compatible with the experimental error, with a normalized $\chi^2 = 1.09$. As a final comparison, we compute the fidelity between the second column of the matrix retrieved via our black-box algorithm (bb) U_{i1}^{bb} and the column of the white-box approach (wb) U_{i1}^{wb}. We choose the second column of the matrix since it presents non-trivial phases, namely $\phi_{i1} \neq 0$ for $i > 0$. Indeed, the first row and column are imposed to be real vectors because of the equivalence between U and $U' = F_1 U F_2$ with F_1 and F_2 unitary diagonal matrices. The fidelity defined here as $\mathcal{F} = |\sum_{i=0}^{2} U_{i1}^{\mathrm{bb}} (U_{i1}^{\mathrm{wb}})^*|^2$, i.e the overlap between pure single-photon states described by the second column of U, has been estimated for each configuration of the dissipated power in R_1 as reported in Fig. 4.5. The average fidelity is $\bar{\mathcal{F}} = 0.999 \pm 0.001$ ($\mathcal{F}_{\mathrm{min}} = 0.994$).

4.4 Conclusive remarks

In this chapter, we proposed a new algorithm for the characterization of a linear optical network. In particular, we have shown the possibility to reconstruct the moduli of the unitary matrix element by field intensity measurements, in the presence of unbalanced losses at the input and output ports. This is in contrast to the previous black-box algorithms [25, 202] that can reconstruct the moduli of the matrix only after phase measurements via HOM visibility and by imposing the constraint to have a unitary matrix. We also propose a new method to characterize the internal matrix phases based on intensity correlations of coherent light beams at the outputs of the linear network. These measurement methods do not require knowledge of the matrix moduli and of input/output losses. These approaches enable the possibility to characterize separately the moduli and the phases of the unitary matrix implemented by the optical network, with a reliable and independent approach. We experimentally test the effectiveness of the complete algorithm by applying it to a three-mode reconfigurable integrated optical circuit. We compared the results of our algorithm with the predictions of an independent reconstruction based on the knowledge of the internal structure of the circuit showing a very good agreement between the two reconstructions.

Statement of Work

The work presented in this chapter was published in Hoch et. al. Adv. Photon. Nexus 2(1), 016007 (2023) [3]. The theoretical results presented, the design of the experimental apparatus and the data analysis were carried out by myself with suggestions from T. Giordani. The photonic chip used was realized in the laboratories of Professor R. Osellame with the help of A. Crespi.

Chapter 5

Clements scheme characterization

In the previous chapter, we analyzed the characterization problem using the so-called Black Box approach meaning that the characterization is performed without the knowledge of the internal structure of the interferometer under consideration. This approach finds applications in many contexts since it is very general. However, it is not always the best solution, especially in terms of computational cost. Furthermore, it does not provide direct information regarding the relationship between the matrix elements U_{ij} and the external control parameters. A practical example in which a completely black-box algorithm is not the optimal strategy is a reconfigurable integrated circuit. A crucial requirement in this kind of experiment is to have a precise algorithm that tells how to program the circuit to realize a given transformation. An alternative approach to the problem of characterization is to exploit some knowledge of the internal structure of the optical network. There are two possible strategies. The first method involves using targeted measures and an analytical procedure, while the second method uses redundant measures and global minimization of the model parameters. The first method offers more control over the model but is not as robust to experimental errors, while the second method is more resilient to errors but may be computationally expensive and prone to getting stuck in local minima, which can lead to an incorrect characterization of the physical system.

In this chapter, we described a technique for the characterization of a six-mode reconfigurable interferometer in a plana rectangular geometry, proposed by Clements et al. [9], using femtosecond laser writing and thermal-optic controls [10]. This technique uses a hybrid approach, incorporating analytical formulas as much as possible, but instead of using targeted measures, the data is obtained from redundant measurements. A minimization algorithm is then applied to this data in order to obtain the correct characterization of the interferometer. The proposed approach tries to balance the trade-off between computational complexity and robustness to experimental errors.

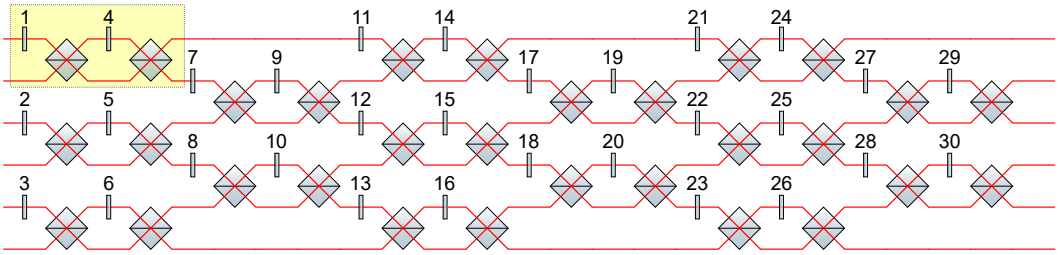

Figure 5.1. Chip Structure. The Figure shows the structure of the chip considered in this chapter. It is a six-mode interferometer with a Clements structure where the reconfigurable beam splitters are replaced with balanced Mach-Zehnder's interferometers. Each rectangle represents the position of resistive heaters placed on the surface of the chip. All the beam splitters represented are unbiased. In yellow is highlighted the unitary cell that composes one of the variable beam splitters with the heater 4 controlling the reflectivity and the heater 1 the external phase.

5.1 Description of the interferometer and conventions

The considered chip has 6 optical modes and the internal structure follows the Clements decomposition [9] where the variable beam splitters are replaced with Mach-Zehnder interferometers as depicted in Fig. 5.1. The rectangles are resistive heaters placed on the surface of the optical chip. The heaters are used to control the phase of the chip via the thermo-optic effect, which exploits the change in the refractive index of the material due to the change in temperature. In the following, we refer to the heaters according to the number reported in Fig. 5.1.

We divide the heaters into two sets called respectively *internal* and *external* heaters. The internal heaters are the ones that control the internal phase of the variable beam splitter and are used to control the reflectivity of the associated variable beam splitters. They are $4, 5, 6, 9, 10, 14, 15, 16, 19, 20, 24, 25, 26, 29, 30$. Instead, the external heaters are the ones between different variable beam splitters and control the phases between a layer of reconfigurable beam splitters and the next one. They are $1, 2, 3, 7, 8, 11, 12, 13, 17, 18, 21, 22, 23, 27, 28$.

5.1.1 Mach-Zehnder interferometer conventions

Since in literature exist various conventions to describe a Mach-Zehnder interferometer, in this section we review the one that we choose to follow in order to ensure consistency in the characterization.

As we see in chapter 2, a variable beam splitter can be implemented by using two balanced beam splitters with a phase between them. In our case, due to the thermal cross-talk which means that a heater changes not only the phase of the waveguide on which it is placed but also the adjacent ones, we must consider that the phases are present on both internal branches of the interferometer. We describe the two balanced beam splitters constituting the interferometer with the balanced matrix since they are physically implemented with directional couplers which possess the same symmetries. This implies that the matrix describing the action of the variable

beam splitter is

$$U_{VBS} = e^{i\frac{\xi+\psi}{2}} \begin{pmatrix} \sin\left(\frac{\xi-\psi}{2}\right) & \cos\left(\frac{\xi-\psi}{2}\right) \\ \cos\left(\frac{\xi-\psi}{2}\right) & -\sin\left(\frac{\xi-\psi}{2}\right) \end{pmatrix} \tag{5.1}$$

where ξ is the phase on the upper arm and ψ is the phase in the lower one. Since both phases are controlled by the same heater we can not change them separately. It follows that the reflectivity of the variable beam splitter depends on the difference between these two phases. We rename such a phase θ. This choice change also how we describe the global phase ϕ. Since depend on the sum of the two phases, this does not have any relation with the phase θ. Then, the unitary matrix is

$$U_{VBS} = e^{i\frac{\phi}{2}} \begin{pmatrix} \sin\left(\frac{\theta}{2}\right) & \cos\left(\frac{\theta}{2}\right) \\ \cos\left(\frac{\theta}{2}\right) & -\sin\left(\frac{\theta}{2}\right) \end{pmatrix} \tag{5.2}$$

where both θ and ϕ are phases controlled with the power of the internal heater.

During the characterization, we also create Mach-Zehnder interferometers with the variable beam splitters of the chip. If we program the two variable beam spitters as balanced ones by putting $\theta = \pi/2$, This changes the matrix that describes the overall interferometer compared to the one used for the variable beam splitter. In this case, the matrix is

$$U_{MZI} = e^{i\frac{\xi+\psi}{2}} \begin{pmatrix} \cos\left(\frac{\xi-\psi}{2}\right) & i\sin\left(\frac{\xi-\psi}{2}\right) \\ i\sin\left(\frac{\xi-\psi}{2}\right) & \cos\left(\frac{\xi-\psi}{2}\right) \end{pmatrix} \tag{5.3}$$

also where ξ and ψ are respectively the phases on the upper and lower arm of the interferometer. It is important to take into account those changes in the matrix otherwise characterization errors are introduced that are difficult to detect.

5.2 Resistor characterization

The first parts to characterize are the response features of the resistive heaters. As we saw previously, the phase depends on the local temperature of the material that is proportional to the power dissipated in the heater. If the heater is a linear resistor then there is no need to characterize it, since the power is proportional to the square of the current that flows in the resistor then we can directly characterize the relation between the square of the current and the phase induced in the circuit. However, a measurement to check the actual linearity of the heater is normally carried out.

In Fig. 5.2 a is represented the current-voltage characteristic of a heater of the chip and a comparison with a linear model retrieved from the first point in the low current regime. In the figure is evident a deviation from the Ohm law for a high value of the current. There are various possible ways to handle non-linear behavior. The simplest is to use a Taylor expansion and employ a polynomial to fit the current-voltage characteristics. We can restrict the expansion only on the odd component since due to the construction materials there is no physical reason to suppose that the resistor has an asymmetric behavior to the reverse of the current

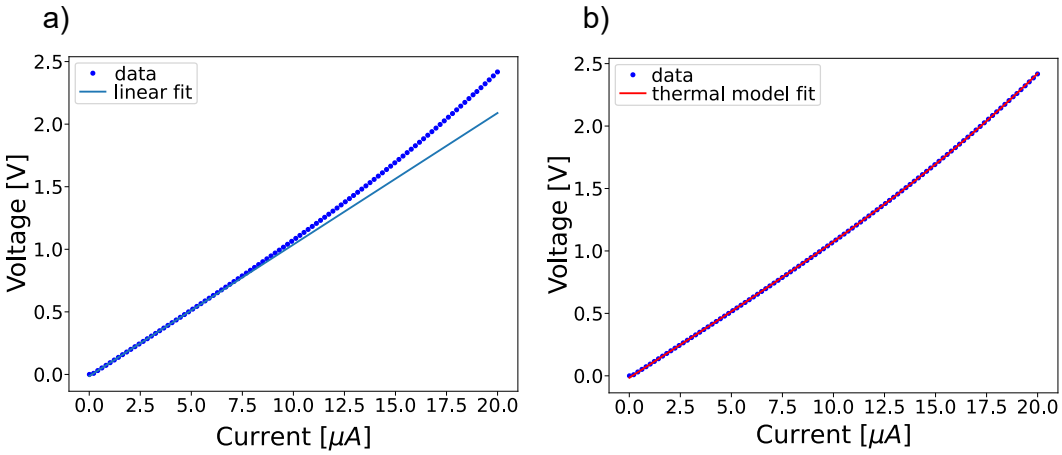

Figure 5.2. Resistive heater current-voltage characteristic. In a) is represented the current-voltage characteristics of one of the resistive heaters of the chip compared with a linear fit performed only on the first part of the curve representing the resistive behavior for low currents. In b) is represented the same curve fitted with a thermal model that takes into account the change of resistivity of the materials in function of the temperature.

flow. While this method works quite well it does not explain why such non-linear behavior occurs in a metal resistor. To try to explain the phenomenon we use a model based on the fact that the resistance increases linearly with the resistor's temperature. In formula is

$$R(T) = R_0(1 + \alpha\Delta T) \tag{5.4}$$

Where R_0 is the resistance at room temperature, ΔT is the temperature difference between the resistor and the environment and α is the thermal coefficient of the resistor. We can also say that there is a thermal resistance R_{th} between the resistor and the environment so the dissipated power P towards the environment is

$$P = R_{th}\Delta T \tag{5.5}$$

so putting everything together, with the additional consideration that we control the resistor with constant current, at the equilibrium we can write

$$RI^2 = R_{th}\Delta T = \frac{R_{th}}{\alpha}\left(\frac{R}{R_0} - 1\right) \quad \Rightarrow \quad R = \frac{R_0}{1 - \frac{\alpha R_0}{R_{\text{th}}} I^2} \tag{5.6}$$

So the equation for the current-voltage characteristics is

$$V(I) = RI = \frac{R_0 I}{1 - \gamma I^2} \tag{5.7}$$

where we define $\gamma = \frac{\alpha R_0}{R_{\text{th}}}$. This model fits quite well with the experimental data (see Fig 5.2 b) and help us to understand the phenomena behind the chip. Moreover, this model has the advantage to be quite easy to invert and enables us to calculate the current needed to dissipate a certain amount of power in the resistor. This allows us

to control the chip in a simple way since its phases depend linearly on the power dissipated in the heaters. The equations are

$$P = \frac{R_0 I^2}{1 - \gamma I^2} \qquad I = \sqrt{\frac{P}{R_0 + \gamma P}} \tag{5.8}$$

To be sure that this characterization holds when more than one resistor is turned on we need to check that the interaction between the resistors is negligible. The electrical interaction that can occur due to the common ground is already handled due to the current control that prevents any flow of current from one resistor to another. Furthermore, if the voltage of the ground changes the dissipated power in the resistor does not change since depend only on the current that flows throw. To check if there are thermal interactions between the resistances, we measure the change in the resistance of one resistor when a second one nearby is turned on. We do not see measurable modifications meaning that the thermal interactions between the resistors are negligible.

5.3 Phases characterization

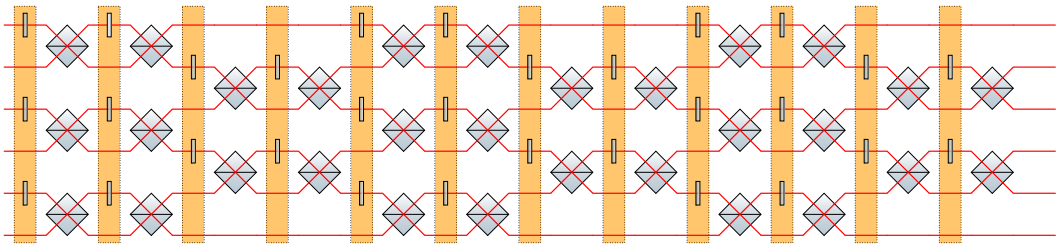

Figure 5.3. Thermal crosstalks. Schematic representation of the crosstalk present in the chip. Each heater induces a phase change in the intersection between the waveguides and the orange rectangle to which the heater belongs.

The next step is to characterize the relationship between the power dissipated in the heaters on the surface of the chip and the phase inside. We assume that there is a linear relationship between the refractive index of the material and the local temperature of the chip, which implies that the phase applied by a waveguide is also proportional to the temperature and therefore to the power dissipated by a heater. Since the waveguides are embedded under the surface of the chip, the heat generated by the heater does not interact only with the waveguide on which it is positioned but also with those nearby. If two or more heaters are switched on at the same time, since we assume the linear relationship, the superposition principle will apply and thus the phase in a waveguide will be the sum of the phases induced by the individual heaters. Due to this thermal crosstalk, the characterization and control of the phases is not trivial. Taking into account the geometry of the chip, we can assume that the crosstalk is only in the vertical direction as represented in Fig. 5.3 since the distance between different columns is orders of magnitude higher compared to the distance of the waveguides.

The characterization is performed under the assumption that no superposition states are put in the input and no interferometric measurements are performed

at the output. This means that the phases at the input and at the output are not considered. The characterization procedure can be divided into three different steps. In the first one, we characterize the internal heaters. In the second step, we characterize the external heaters. In the third one, we characterize the phase induced by the Mach-Zehnder interferometers.

5.3.1 Internal phase characterization

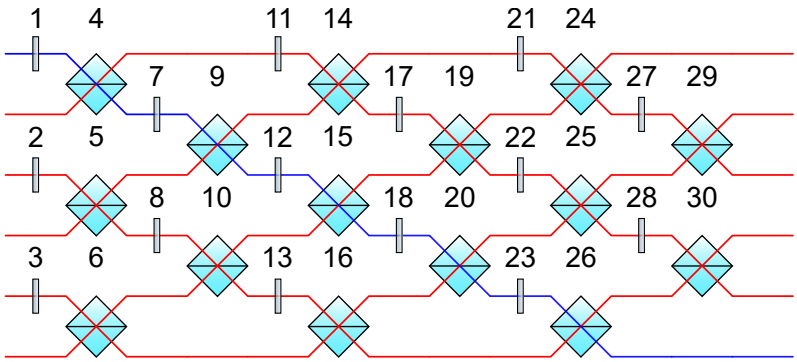

Figure 5.4. Non-interferometric path. In the figure is represented a non-interferometric path, i.e. a path between a particular input and a particular output that is unique. This means that the fraction of light passing through is affected only by the beam splitters reflectivity along the path and not by the phase in between. Each beam splitter in the figure represents a variable beam splitter in the chip.

The first step to represent the interferometer is the characterization of the internal phases and the related crosstalk. We have to find a procedure that "isolates" the single variable beam splitter and excludes interference effects since we have no information on the phase of the chip. The idea is to use so-called *non-interferometric paths*, i.e. a path between a particular input and a particular output that is unique. This means that the fraction of light passing through is affected only by the beam splitters reflectivity along the path and not the phase in between. In Fig. 5.4 in blue is represented one non-interferometric path, this one allows the characterization of the variable beam splitter associated with the heaters 4, 9, 15, 20 and 26.

Now, we show as an example the procedure for the characterization of the heater 4. The procedure is the same for the other internal heaters of the path, i.e. heaters 9,15, 20 and 26. As seen above, the internal phase has a linear dependency on the local chip temperature and therefore with the power dissipated in the neighbouring heaters. Therefore, we can write the dependence as

$$\theta_4 = \alpha_{4,4}P_4 + \alpha_{4,5}P_5 + \alpha_{4,6}P_6 + \theta_{0,4} \tag{5.9}$$

where $\alpha_{4,i}$ is the proportionality coefficient between the power dissipated in the heater i and the change of phase 4 and $\theta_{0,4}$ is the initial phase when all the heaters are turned off. The intensity measured at the output of the chip following the non-interferometric path is

$$I_O = I\gamma\cos^2(\theta_4) = I\gamma\frac{1+\cos(\theta_4)}{2} \tag{5.10}$$

with I the input intensity and γ the damping coefficient that takes into account the reflectivities of all the other variable beam splitters along the path. For our chip, we saw that γ is not null but if it is not the case then we can apply a current to heaters 9, 15, 20 and 26 to change their reflectivity so that they are not null.

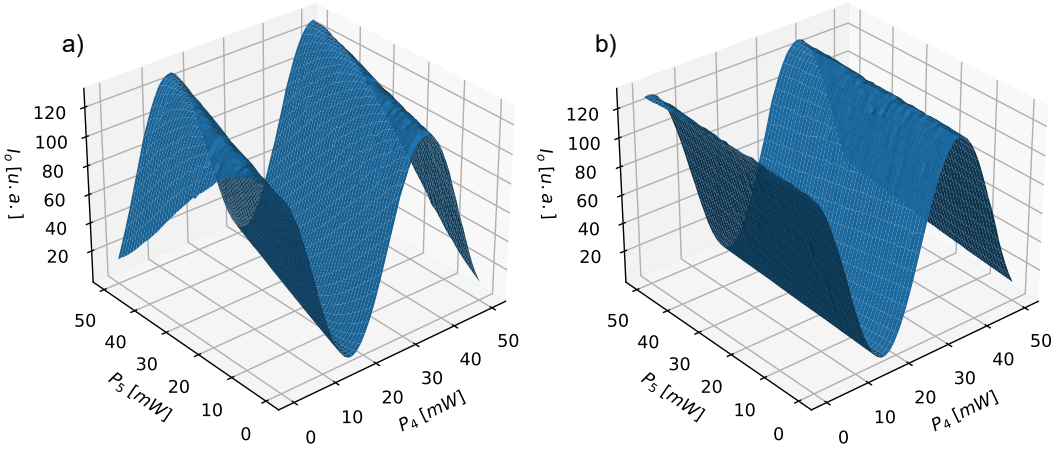

Figure 5.5. In the figure are represented the output intensity of the chip used for the calibration of the variable beam splitter corresponding to the heaters 4 when heaters 4 and 5 are changed in a) and for the heaters 4 and 6 in b)

Since the variable beam splitter under consideration is primarily controlled by heater 4 and for cross-talk by 5 and 6, we measure the output intensity when the couple of heaters $4-5$ and $4-6$ are changed contemporaneously and the corresponding curves are recorded as in Fig. 5.5. Then we perform a global flit with the least squares methods on both the curve since the parameters $I\gamma$, $\alpha_{4,4}$ and $\theta_{0,4}$ are in common. With this fit, we characterize all the necessary parameters of the variable beam splitter.

Using the first non-interferometric path, we characterize five beam splitters associated with the heaters 4, 9, 15, 20 and 26. The second one is the symmetric, which instead of going from top to bottom, goes from bottom to top. This second path allows the characterization of four more variable beam splitters associated with the heaters 6, 10, 19 and 24.

To continue with the characterization, we want to follow the same procedure. However, due to the lack of other non-interferometric pathways, it is necessary to change the methodology a little. The idea is to use the Variable beam splitters already characterize to create new non-interferometric paths.

For example, using the Fig. 5.6 as a reference, programming the beam splitter 4 marked in yellow (that we characterized previously) with $\theta_4 = \pi$ (which corresponds to reflectivity 1) then the blue path marked in the figure became a non-interferometric one. This new path allows us to characterize the beam splitters associated with the heaters 14, 25 and 30. The symmetric one, which is created by programming the beam splitter 6, allows the characterization of the variable beam splitters 16 and 29. The last beam splitter (5) is characterized by controlling the interferometer 24 and using the diagonal path that connects this interferometer with the beam splitter 5. In general, all the non-interferometric paths follow the diagonal of the chip and to

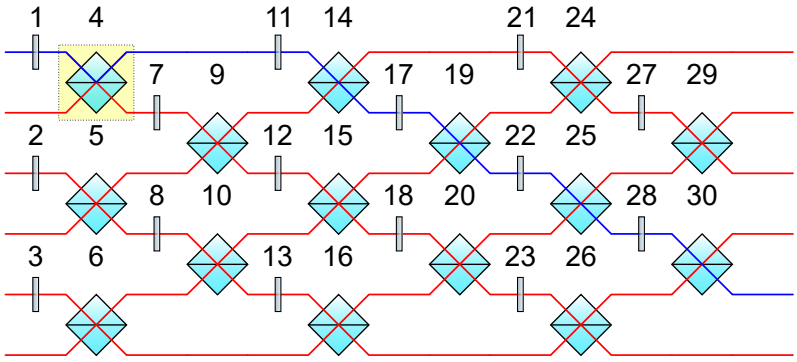

Figure 5.6. Non-interferometric path 2. In order to continue the characterization, new non-interferometric paths need to be created and the idea is to use the variable beam splitters already characterized to achieve this. For example, programming the beam splitter 4 marked in yellow (that we characterized previously) with $\theta_4 = \pi$, which corresponds to reflectivity 1, then the blue path marked in the figure becomes a non-interferometric path.

create new ones is sufficient to control the variable beam splitters on the first or the last row of the global interferometer. With this procedure, we characterize all the internal phases of the photonic chip.

Internal phase control

We characterized the relationship between the dissipated powers in the photonic chip and the internal phases. Now, we see how to perform the inverse relation, i.e. how to set the powers to apply a certain phase in the chip.

The idea is to group the data collected during the characterization into matrices each describing a column of Mach-Zehnder interferometers. For example, the first column is described by the equation

$$\begin{pmatrix}\theta_4\\ \theta_5\\ \theta_6\end{pmatrix} = \begin{pmatrix}\alpha_{4,4} & \alpha_{4,5} & \alpha_{4,6}\\ \alpha_{5,4} & \alpha_{5,5} & \alpha_{5,6}\\ \alpha_{6,4} & \alpha_{6,5} & \alpha_{6,6}\end{pmatrix}\begin{pmatrix}P_4\\ P_5\\ P_6\end{pmatrix} + \begin{pmatrix}\theta_{0,4}\\ \theta_{0,5}\\ \theta_{0,6}\end{pmatrix} \quad \Rightarrow \quad \vec{\theta} = A\vec{P} + \vec{\theta}_0 \tag{5.11}$$

To obtain the powers from the angles it is sufficient to invert the previous equation as

$$\vec{P} = A^{-1}(\vec{\theta} - \vec{\theta}_0) \tag{5.12}$$

This equation sometimes returns negative power that can not be applied to our chip. To solve the issue, we can use the periodicity of the angle and add or subtract 2π to increase the powers. One strategy that can be followed is adding 2π in random places until the issue is solved, but can be computationally expensive and impractical. We decide to follow a more systematic procedure that uses some property of the matrix A^{-1}. For how we construct the matrix A, we can say that all the diagonal therm are positive and are at least an order of magnitude greater compared to the off-diagonal ones. The same property belongs also to the inverse matrix A^{-1}. With this consideration, we can follow the simple rule that if a power P_i is negative, we add a 2π to the relative angle θ_i and then recalculate the powers. We proceed

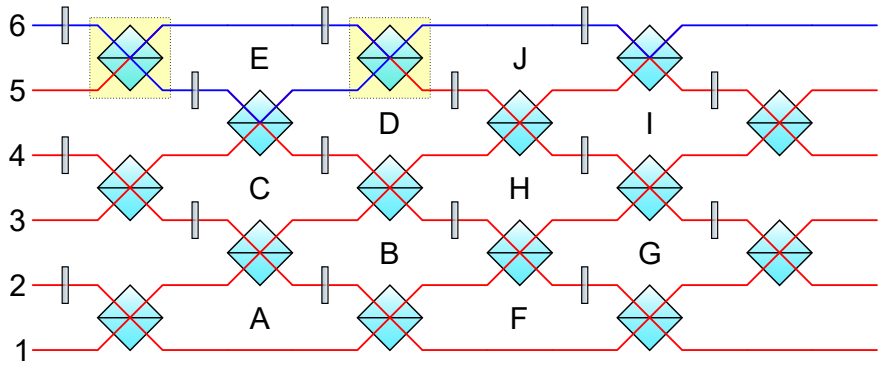

Figure 5.7. Mach-Zehnder interferometers for external phase. In blue is represented a Mach-Zehnder interferometer created by programming the two marked beam splitters as balanced ($R = 1/2$) and setting the reflectivity of all other beam splitters to 1. That particular interferometer is called with the letter E. The other Mach-Zehnder interferometers are created by putting all the variable beam splitters reflectivities equal to 1, except the one just before the labelling letter and the one after that are both programmed with reflectivity equal to 1/2. As represented, we enumerate the mode of the interferometer from the bottom to the top.

iteratively until all the powers are positive. For a generic matrix this approach does not work, however since the diagonal term is positive the power of this value always increases until become positive. Moreover, given that the off-diagonal terms are smaller in magnitude than those on the diagonal during the iterations if an element is corrected to become positive it cannot become negative in the next iteration, guaranteeing convergence.

It is necessary to be careful that the algorithm does not increase too much the power since the heaters also have a maximum power that can be dissipated without damage. For our chip, we have not found any combination of angles which causes an increase of the powers higher than the maximum for the heaters.

5.3.2 External phase characterization

The second step is the characterization of the external phases. To do it, we need to create some Mach-Zehnder interferometers with the variable beam splitters. In Fig. 5.7 is marked in blue one of the Mach-Zehnder interferometers used, is composed of two balanced beam spitters (marked in yellow) and all the others are programmed with reflectivity equal to 1.

In the following, we describe how to characterize the heater 11 all the others follow the same procedure except for 7, 8, 27 and 28 which have a slightly different characterization procedures which we will discuss later.

As done previously, we want to find the linear relation between the power dissipated in the heaters and the phase applied to the six waveguides, taking into account also the crosstalks. we refer the phases to a reference that we chose to place on waveguide 1 meaning that we assume that the phase on waveguide 1 is always

null. In formulas, we can write

$$\begin{gathered} \phi_{1,11} = 0 \qquad \phi_{2,11} = \alpha_{2,11} P_{11} \qquad \phi_{3,11} = \alpha_{3,11} P_{11} \\ \phi_{4,11} = \alpha_{4,11} P_{11} \qquad \phi_{5,11} = \alpha_{5,11} P_{11} \qquad \phi_{6,11} = \alpha_{6,11} P_{11} \end{gathered} \tag{5.13}$$

where $\phi_{i,11}$ is the phase induced by the heater 11 on the waveguide i and $\alpha_{i,11}$ is the proportionality coefficient between the phase and the power dissipated in the heater. For the characterization, we use all and only the Mach-Zehnder interferometers affected by the action of the heater under consideration. For the heater 11 they are the ones marked with the letters A. B, C, D, E. For each Mach-Zehnder, we record the output intensity as a function of the power dissipated in the heater and we fit the curve to measure the frequency $\beta_{m,11}$ of the oscillation (where m mark the corresponding interferometer under consideration). The frequency of each Mach-Zehnder is the difference of the proportional coefficient α of the two waveguides affected by the interferometer. In equations can be expressed as

$$\begin{gathered} \beta_{A,11} = \alpha_{2,11} \qquad \beta_{B,11} = \alpha_{3,11} - \alpha_{2,11} \qquad \beta_{C,11} = \alpha_{4,11} - \alpha_{3,11} \\ \beta_{D,11} = \alpha_{5,11} - \alpha_{4,11} \qquad \beta_{E,11} = \alpha_{6,11} - \alpha_{5,11} \end{gathered} \tag{5.14}$$

and by inverting the equations the coefficients α can be derived from the frequencies β, obtained by the fits, as

$$\begin{aligned} \alpha_{2,11} &= \beta_{A,11} \\ \alpha_{3,11} &= \beta_{A,11} + \beta_{B,11} \\ \alpha_{4,11} &= \beta_{A,11} + \beta_{B,11} + \beta_{C,11} \\ \alpha_{5,11} &= \beta_{A,11} + \beta_{B,11} + \beta_{C,11} + \beta_{D,11} \\ \alpha_{6,11} &= \beta_{A,11} + \beta_{B,11} + \beta_{C,11} + \beta_{D,11} + \beta_{E,11} \end{aligned} \tag{5.15}$$

As we say for the heater 7 and 8 the situation is a bit different since they interact with only three Mach-Zehnder interferometers (A, C and E) instead of the five for all the other heaters. The two missing equations are due to the fact that we can not characterize the initial and final phases of the chip and this gives some freedom on the heater characterization. Using this property, we can assume that the phase of the waveguide 1, 4 and 6 are null. For example, for the heater 7 gives the system of equations

$$\begin{gathered} \phi_{1,7} = 0 \qquad \phi_{2,7} = \alpha_{2,7} P_7 \qquad \phi_{3,11} = \alpha_{3,7} P_7 \\ \phi_{4,7} = 0 \qquad \phi_{5,11} = \alpha_{5,7} P_7 \qquad \phi_{6,7} = 0 \end{gathered} \tag{5.16}$$

Similar reasoning is valid for the heaters 27 and 28 where we can consider null the phase on the mode 1, 2, 4 and 6. With those equations, we have the complete characterization of the external phase.

Since the cross talks are not so big and consequently also the β frequencies in the fits they do not allow seeing a complete oscillation in the scans of the power dissipated in the heaters. To increase the precision of the measurements, some precautions can be taken during data acquisition and in the execution methods of the fits. The first possibility is to use the measurement method as before but instead of doing the fits separately they are grouped together when where there are parameters in common and make a global fit for each group where these parameters

are forced to be equal. Groupings are made by Mach-Zehnder interferometer, i.e. all the measurements made on the same Mach-Zehnder with different heaters are all fitted together. This choice is due to the fact that the input intensity and the initial phase are common to all the measurements. For example Fig. 5.8 represent all the curves measured for the interferometer E when respectively the heater 7, 8, 11, 12 and 13 are changed. In red is the fitted curve with the common parameter forced to be equal.

Another possibility is to refine the measures further and proceed as we did for the internal phases. Instead of measuring a curve for each heater, we control two heaters simultaneously and measure the resulting surface. The idea is to use a heater that has a high effect on the Mach-Zehnder interferometer under consideration (as an example for the Mach-Zehnder E could be the heater 11 or 7) and measure the surface generated by this particular heater coupled with all the others that interact with the interferometer under consideration. This method is more precise than the previous one since instead of directly measuring the cross-talk we measure how it changes the curve of a heater placed directly in the Mach-Zehnder. however, it requires many more measurements than the previous methods proposed meaning more required time.

5.3.3 Characterization of the beam splitter and the initial phases

The final step is the characterization of the phases introduced by the variable beam splitters and the initial phases when all the heaters of the chip are turned off. In the following, we explain how to characterize the phases of the variable beam splitter for the heater 9. The characterization of the others heaters follows the same procedure.

The idea is similar to the one used previously for the external phases. As we see in Eq. (5.2) each variable beam splitter put a phase to the two waveguides on which it is applied. We can writhe the linear relation between the phases of the six modes and the power dissipated in the heater 9 as

$$\begin{aligned} \phi_{1,11} = 0 \qquad & \phi_{2,11} = \phi_{3,11} = \alpha_{2,11} P_{11} \\ \phi_{4,11} = \phi_{5,11} = \alpha_{4,11} P_{11} \qquad & \phi_{6,11} = \alpha_{6,11} P_{11} \end{aligned} \tag{5.17}$$

For the characterization, we need to use the three Mach-Zehnders A, C and E. The procedure is similar to the one used previously but with the exception that the heaters on the same column of the heater under exam are turned off. At this point, we change the power dissipated in the heater 9 and for each value, we made a scan with one of the external heaters which acts directly on the Mach-Zehnder (as an example for the Mach-Zehnder E we can use the heater 11 or 7). Fig. 5.9 a shows some of the curves for the Mach-Zehnder E when the scan is performed with the resistor 11 and varying the power dissipated in the heater 9. all those curves are fitted with the function

$$I_O = I \frac{1 + V \cos(\beta_{E,11} P_{11} + \phi_E)}{2} \tag{5.18}$$

where V is called visibility of the fringes and ϕ_E is the phase that gives us the information of the phase applied by the variable Beam splitter. In Fig. 5.9 b and c

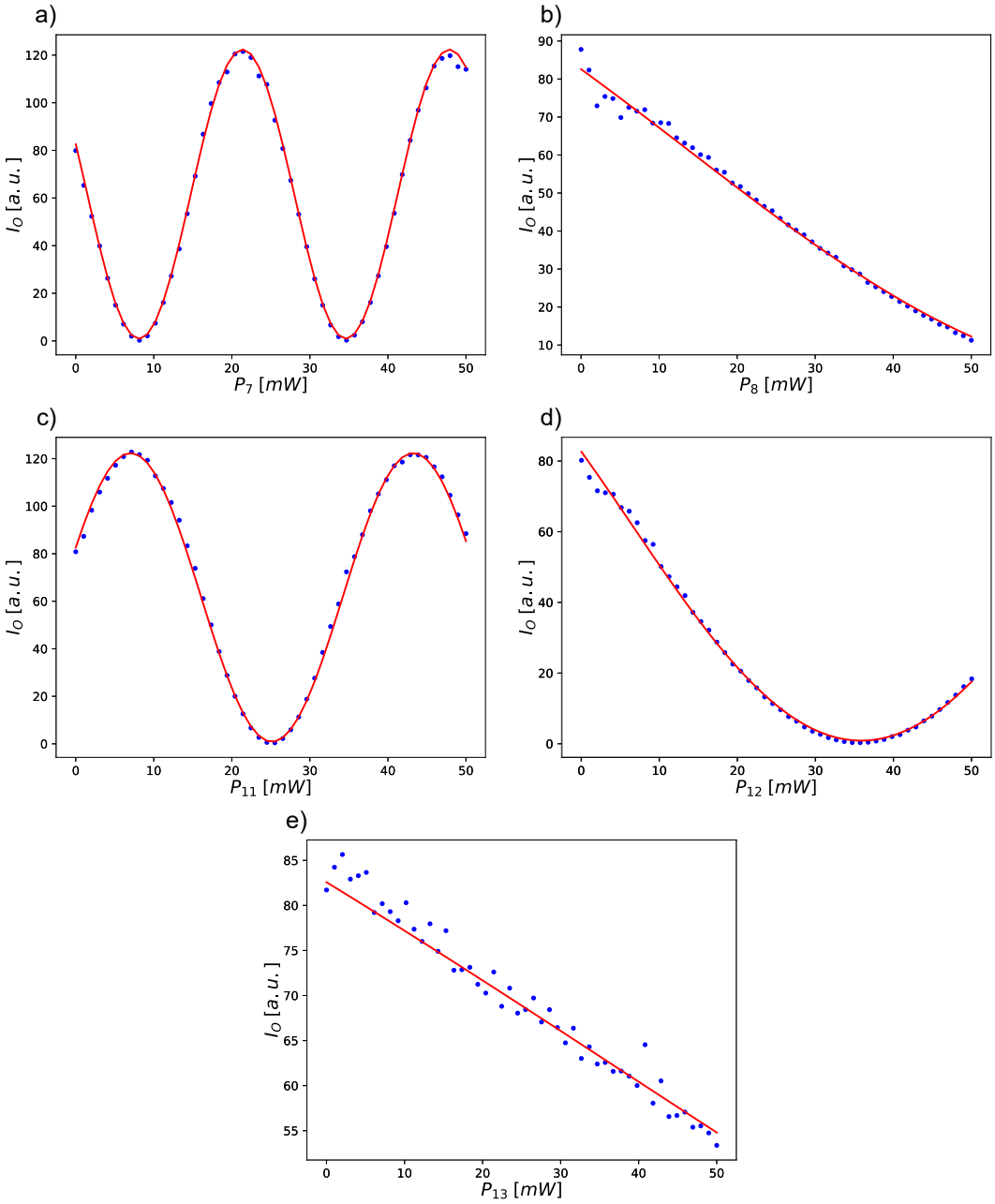

Figure 5.8. In the figures in blue are presented the output intensity measured for the Mach-Zehnder interferometer E when respectively the heaters 7, 8, 11, 12 and 13 are controlled separately. In red are represented the fit curves where the common parameter of the input intensity and the starting angle, i.e. the angle when no power is applied, are forced to be equal for all the curves.

are plotted respectively the visibility and the phase ϕ_E as a function of the power dissipated in the heater 9. The visibility of the Mach-Zehnder nullifies when the reflectivity of the internal beam splitter is zero. We can see that in correspondence to that point, the phase ϕ_E makes a jump of π. This can be explained by the fact that the reflectance of the internal variable beam splitter changes sign and this can be seen as a jump of π in the phase.

Fitting the curve for the phase ϕ_E as a function of the dissipated power in 9 with a linear dependence (since all the phases are linear in the dissipated power in the heaters) and taking into account the π jumps, we can derive the proportional coefficient β of the interferometer as the slope of the line. Performing the same procedure for all the three Mach-Zehnder interferometers A, B and E we can measure the tree coefficient β that are related to the coefficient α by the equations

$$\begin{aligned} \beta_{A,9} &= \alpha_{2,9} \\ \beta_{C,9} &= \alpha_{4,9} - \alpha_{2,9} \\ \beta_{E,9} &= \alpha_{6,9} - \alpha_{4,9} \end{aligned} \tag{5.19}$$

and inverting the equation we can derive all the proportional coefficient

$$\begin{aligned} \alpha_{2,9} &= \beta_{A,9} \\ \alpha_{4,9} &= \beta_{A,9} + \beta_{C,9} \\ \alpha_{6,9} &= \beta_{A,9} + \beta_{C,9} + \beta_{E,9} \end{aligned} \tag{5.20}$$

the intercept coefficient C derived from the fit of the curve of the phase ϕ_E gives us information on the initial phase of the interferometer when all the heaters are turned off. Due to the symmetry of the global interferometer, we can assume that the initial phases are present only in correspondence with the external heaters except for the heaters 11 and 21 for which we can assume that they have a null initial phase. We can notice that in each interferometer there are one or two initial phases, so to reconstruct them from the intercept coefficient C of the interferometers we proceed by diagonals. Following the diagonal $A - B - H - I$ we can writhe the equations for the initial phase ϕ_0 as

$$\begin{aligned} C_A &= \phi_{0,13} \\ C_B &= \phi_{0,18} - \phi_{0,13} \\ C_H &= \phi_{0,22} - \phi_{0,18} \\ C_I &= \phi_{0,27} - \phi_{0,12} \end{aligned} \tag{5.21}$$

so inverting the system we have

$$\begin{aligned} \phi_{0,13} &= C_A \\ \phi_{0,18} &= C_A + C_B \\ \phi_{0,22} &= C_A + C_B + C_H \\ \phi_{0,27} &= C_A + C_B + C_H + C_I \end{aligned} \tag{5.22}$$

the same procedure can be applied to the other diagonals $F - G$ and $J - D - C$ and derive all the initial phases. In this way, we completely characterize all the components of the photonic chip.

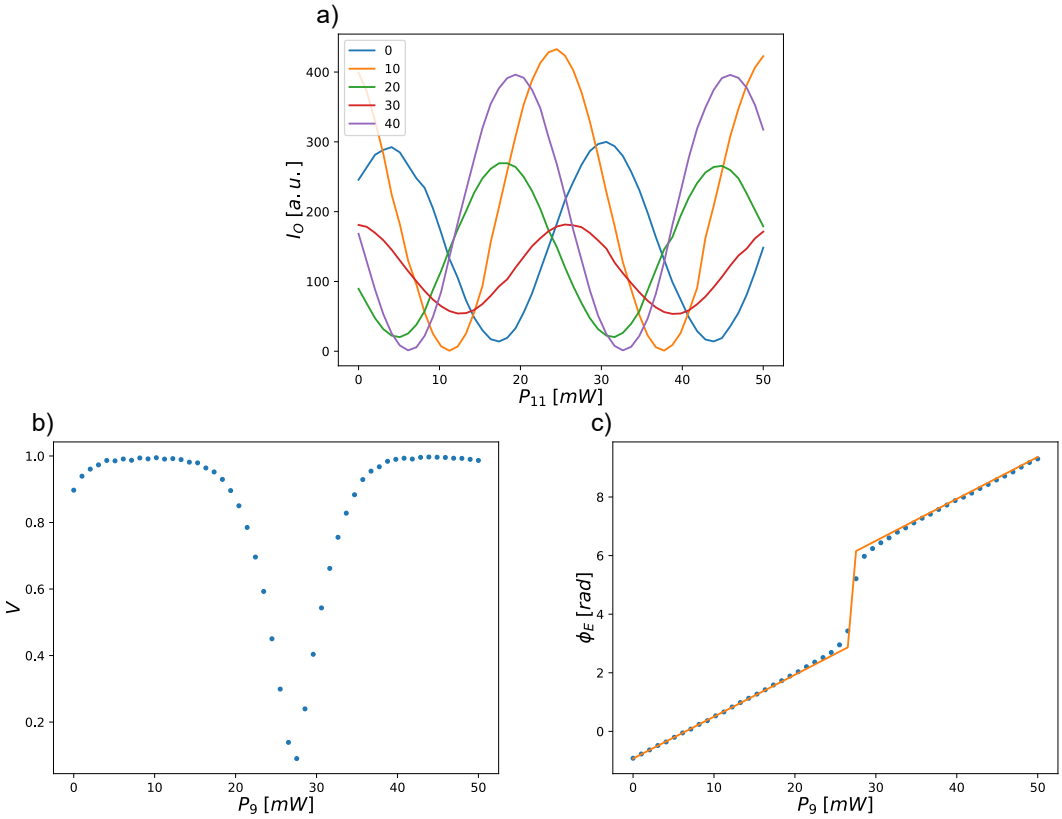

Figure 5.9. Characterization of the beam splitter phase In figure a) are represented some of the scans performed on the Mach-Zehnder interferometer E with the heater 11 when the power n the heater 9 are changed. All those curved are fitted and the visibility and the initial phase as a function of the power dissipated in the heater 9 are plotted respectively in b) and c). In c) in orange is plotted also the fit of the experimental data. It is important to notice that the jump in phase corresponds exactly where the visibility vanishes.

5.4 Conclusive remarks

In this chapter, we present a complete procedure to characterize a six-mode photonic chip with Clements Geometry. This kind of chip represents a milestone in the reconfigurable photonic chip but, in the literature, there are no clear methods for the characterization of this type of chip. Moreover, there is large technological research to be able to increase the number of modes without affecting the reconfigurability of the device [120, 121]. The proposed procedure is used to characterize a device used in chapter 9 to experimentally test the feasibility of a quantum protocol called the Quantum Bernoulli factory. Furthermore, the whole characterization method can be generalized easily to chips with a high number of modes, always taking into account that they must respect the used hypothesis on the structure of the cross-talks and the linearity of the phases as a function of the local temperature of the chip.

Statement of Work

The theoretical results presented, the design of the experimental apparatus and the data analysis were carried out by myself. The photonic chip used was realized in the laboratories of Professor R. Osellame with the help of A. Crespi.

Part III

New integrated photonic platform for bosons sampling

Chapter 6

Boson sampling

A large-scale universal quantum computer requires a significant technological leap forward. Many laboratories are developing technologies to manipulate large quantities of quantum physical objects individually but, to date, no satisfactory solutions have been identified. However, many experiments have opened the way to an intermediate possibility to show the potentialities of quantum computing in simpler systems. A quantum computer will make it possible to perform calculations and simulations currently impossible for a classical computer. Also, there are proposals to disprove the extended Church-Turing thesis (ECCT), that assert that a probabilistic Turing machine can efficiently simulate any realistic model of computation, with non-universal devices now within our reach [27]. If we assume that quantum mechanics can correctly describe the behavior of an arbitrarily large system, then the ECCT is effectively false; but given that ECCT concerns many different fields, from physics to computer science and by extension also to mathematics, the theory of quantum mechanics must be supported with solid experimental evidence. In this context, the *Boson Sampling* problem represents a valid model of quantum computation capable of providing evidence against ECCT, although it is not a universal computational model.

In this chapter, we will present the Boson sampling problem and some of its variants, such as the scattershot Boson sampling [217] and the Gaussian Boson sampling [218], explaining in detail the peculiarities that distinguish the various versions. Next, the computational complexity of the problem is analyzed by reviewing the demonstration proposed by Aaronson and Arkhipov with particular attention to the conjectures on which it is based [51]. Subsequently, some of the classical algorithms used to simulate the problem are briefly presented. They are of special interest in order to understand what scale the quantum experiment must reach in order to be considered intractable by a classical computer, and what experimental imperfections affect its computational complexity. Furthermore, in order to be able to perform a Boson sampling experiment correctly, it is not enough to make measurements on a Boson process, but it is also necessary to validate the data to confirm that the entire experiment has been carried out correctly. It is not possible to directly verify that the samples obtained were measured from a distribution of indistinguishable bosons, on the contrary, it must be ruled out that they were not obtained from classically simulated distributions. With this in mind, we will analyze

the main validation techniques in the literature to understand which principles they are based on and which distributions they exclude. Finally, we will present the state of the art of experimental realizations of a Boson sampler.

6.1 Versions of Boson sampling problem

6.1.1 Canonical Boson sampling

In 2011, Aaronson and Arkhipov introduced the concept of Boson sampling in their work entitled "he computational complexity of linear optics" [51]. Given a passive linear interferometer of size m implementing a unitary operator $\hat{U}$, and given a Fock state at n photons entering the interferometer, the *Boson sampling problem* aims to sample the outcome distribution of the events. The idea behind Boson sampling can be traced back to the machine invented by Sir Francis Galton (hence its name) to show the central limit theorem. Galton's machine consists of a table in which pegs are planted vertically in the shape of a quincunx (that is, like the representation of the number 5 on the dice). From above, balls are dropped which, by hitting the pegs, move to the right or left randomly. At the base of the machine, there are collectors in which the fallen balls accumulate. Similarly, a photon placed in a linear interferometer when it meets a beam splitter can travel in both directions with the peculiarity of being able to do so simultaneously and establish interference phenomena. These properties, combined with the bosonic nature of the photons, imply that inserting more photons into the interferometer at the same time completely changes the output distribution, which does not occur in the Galton machine.

The first experimental implementations of Boson sampling experiments were performed with probabilistic photon sources [216,219–224]. It soon became clear that this type of source constituted a problem with the scalability to a greater number of photons, therefore two ways were envisaged either to change the type of source, a path that was impracticable at the time or to adapt the problem to make it compatible with the type of source without however renouncing the computational complexity. The main variants proposed over time are the *Scattershot Boson sampling* and the *Gaussian Boson sampling*.

6.1.2 Scattershot Boson sampling

First proposed in Ref. [217] the scattershot Boson sampling differs from the original version in that the input Fock state is not fixed but is randomly extracted. Indeed, the idea is that, instead of trying to overcome the probabilistic nature of the source, to use it to our advantage. The implementation is to use k probabilistic heralded single-photon sources at the input of the interferometer and use the heralding photons to measure which state is presented at the input. This setting generates randomly

$$n_k = \binom{k}{n} \tag{6.1}$$

possible inputs states and if the number of sources has the same order of magnitude as the number of modes of the interferometer $k \simeq m \geq n^2$ then the complexity of

the input states becomes exponetial. Moreover, the computational complexity of this problem is the same as the original one since changing the input state does not spoil the complexity of the task but there is an increase in the generation rate due to the increase in the possible input state accepted.

6.1.3 Gaussian Boson sampling

The Gaussian Boson sampling is a variant of the conventional Boson sampling where the input states instead of being Fock states are Gaussian states [218], usually the protocol is implemented within input single-mode squeezed states. This change in the input state implies that the number of photons at the input is not defined, which means that sampled events also do not have a defined number of photons. The complexity of the Gaussian boson sampling is related to the computation of a function called Hafnian. It has been proven that computing the Hafnian is hard as computing the permanent [218]. The hafnian function is connected to the problem of finding perfect matchings of a graph [225] that is shown to be an **NP**-complete problem [226] this could open the way for applications of the boson sampling problem beyond the demonstration of quantum advantage.

6.1.4 Others variants

To fully understand when the complexity of the Boson sampling problem arises and to study other solutions to the problems of the canonical version, in addition to scattershot and Gaussian Boson sampling, other variants have been proposed in the literature. One of the first variations proposed is the possibility of replacing the Fock states with the photon-added and photon-subtracted states [227, 228] like the Gaussian Boson sampling those states present a complexity transition to the classical simulability depending on the mean number of photon present in the states. Another proposal in the literature is the *superposition Boson sampling* [229]. This variant instead of using Gaussian states use superpositions of vacuum and single-photon states. This type of state is interesting given that a suitably excited quantum dot naturally generates them [72] and maintains the requirement to have at most one photon per input mode as in the canonical version. Other variants, instead of changing the input state, modifies the structure with which the evolution of the photons is done. In this category, we can find the *membosonsampling* [230] and the *non-linear Boson sampling* [231]. The membosonsampling uses the same strategy as canonical Boson sampling but with the addition that some of the outputs of the interferometer are connected to some of the inputs of the interferometer with a delay line that matches the repetition rate of the input photons. This arrangement adds memory to the system and therefore a certain degree of complexity. Instead, the non-linear Boson sampling to increase system complexity uses the single-mode non-linear phase shift gates, which are gates that apply a phase depending on the number of photons that pass through and the associated operator is $\tilde{U}_{nlp} = e^{-i\hat{n}^2\phi}$. Those gates are placed between two unitary interferometers to create global evolution. The non-linearities are interesting since it can be shown that each gate can be simulated by a linear interferometer using ancillary photons and post-selection. This analogue shows how introducing nonlinearity is similar to using a larger interferometer and a

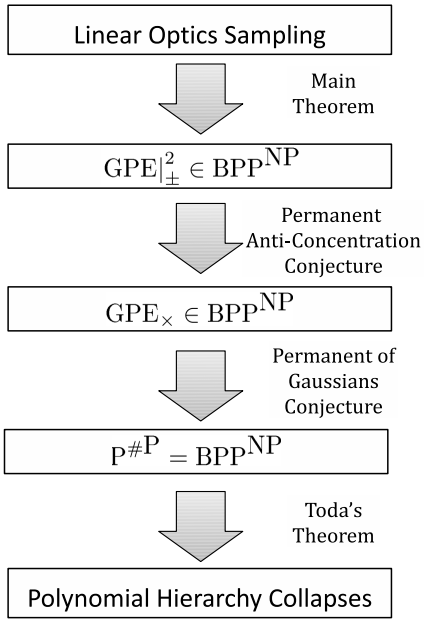

Figure 6.1. Summary of the complexity proof of the Boson sampling problem. Aaronson and Arkhipov show that does not exist a classical algorithm that samples from the Boson sampling distribution in polynomial time with a bounded error does not exist. To do so, they prove that if such an algorithm exists then the calculation of the permanent of a matrix with complex entry distributed according to a Gaussian distribution is a problem in $\mathbf{BPP}^{\mathbf{NP}}$. But since the calculation of those permanent is also a $\#P$-hard problem this implies that $\mathbf{BPP}^{\mathbf{NP}} = \mathbf{P}^{\#\,\mathbf{P}}$. Using Toda's theorem [232], that entails the collapse of the polynomial hierarchy at the third level. Since the collapse is conjectured impossible at any level this implies that does not exist a classical algorithm for the simulation of Boson sampling. Image from [51]

.

higher number of photons.

6.2 Boson sampling complexity

Now we want to analyze the classical complexity of the Boson sampling problem. Classically, the complexity of the problem seems related to the computation of the transition probability seen in the previous section (Eq. 2.31). In particular, it is well known that the computation of the permanent of a complex matrix is a $\#\mathbf{P}$-hard problem [1] [233]. The best-known classical algorithm to compute the permanent of a matrix of dimension n is the Ryser algorithm and has complexity $\mathcal{O}(n2^n)$ [234]. Turn out that the computation of the permanent of a matrix is a hard problem also for a quantum computer [235]. It is important to notice that the Boson sampling problem is not the reconstruction of the distribution but a generation of a sample from it. So, we can think if exist the possibility to generate a sample from a distribution $\mathcal{D}'$ close to the original one $\mathcal{D}$ where the total variation distance between the two distributions

[1] The $\#\mathbf{P}$ complexity class is the class related to the $\mathbf{NP}$ complexity class where instead of asking if exist a solution we ask the number of solutions for a particular question.

is at most ϵ ($\|\mathcal{D} - \mathcal{D}'\| = \frac{1}{2}\sum_i |\mathcal{D}_i - \mathcal{D}'_i| \leq \epsilon$). If such an algorithm exists then, using the Stockmeyer algorithm [236], it is possible to solve a # **P**-hard problem in $\mathbf{BPP}^{\mathbf{NP}}$, that belongs at most to the third level of the polynomial hierarchy. Then due to the Toda theorem [232] this implies the collapse of the polynomial hierarchy to the third level, an event that is conjectured very unlucky. This implies that does not exist any classical algorithm that can solve the Boson sampling problem even in the approximated case.

6.3 Classical simulation algorithms

As we saw previously, in their article Aaronson and Arkhipov [51], in addition to presenting the Boson Sampling problem, provided a convincing argument that shows how any classical simulation algorithm requires exponential times in the number of photons n. Nevertheless, it is important to find the best classical simulation algorithm. This allows to establish the objectives to be achieved in order to experimentally demonstrate a computational advantage in using quantum devices. On the other hand, being able to simulate interferometers of small dimensions allows us to characterize how the inevitable experimental imperfections (for example the partial distinguishability of the photons or the losses) invalidate the computational potential of the model.

6.3.1 Classical simulation algorithms

The brute-force approach for the simulation of Boson Sampling involves calculating the probability associated with each input-output configuration. The most efficient algorithm known to compute the permanent is Ryser's algorithm [237] which has complexity $O(n2^n)$, so the total complexity is more than exponential. By counting for n photons placed in an interferometer with $m = kn$ ways, the order of magnitude of the probabilities to be calculated is $O(n^{-1}(ek)^{2n})$ so the total complexity is $O((2e^2k^2)^n)$. Since the brute-force approach is computationally expensive, alternative algorithms for sampling the Boson Sampling distribution have been proposed. A first approach is based on the well-known Rejection-sampling algorithm [238]: an output state is sampled from an easy-to-calculate distribution (for example the uniform one) and to decide whether to accept or reject the event, the probability that this event will be generated (in our case by calculating the permanent associated with the event). If the maximum event that can be generated is known and not too large, this approach returns an exact sampling at an acceptable computational cost. If the maximum event that can be generated is not known, there will be an approximate sampling and, if it is too large, there will be too high a computational cost given by the multitude of rejected events. Another algorithm is a variant of the Markov chain Monte Carlo method, known as Metropolis–Hastings algorithm [239]. The basic idea is to construct a Markov chain with a stationary distribution equal to that of Boson Sampling. To improve the performance of this approach, it is necessary to choose an initial distribution that is not too distant from the final one and that is efficient to calculate. Neville et al. [238] proposed to use as an initial distribution the one corresponding to distinguishable photons. More sophisticated algorithms have been proposed to solve the problem. One out

of all showed a complexity equal to $O(n2^n)$ [240]. On the basis of those studies on the calculation of the permanent of large matrices, it is believed that the Boson Sampling problem is difficult to simulate for a number of photons higher than 60. With the progress of supercomputers, this number is questioned by some parts of the scientific community, but it is a good reference point.

Similar simulation algorithms have also been proposed for Gaussian Boson sampling, always showing exponential complexity in the number of photons measured. In particular, let us mention the algorithm proposed by Quesada et al. [241], which has a computational complexity of $O(n^3 2^n)$, and the one of Björklund [242] with a complexity of $O(n^5 2^n)$.

6.3.2 Classical simulability

An important problem is to understand how much the imperfections of the experimental apparatus invalidate the computational complexity of Boson Sampling and, above all, under what conditions classical computation becomes efficient. The first and most relevant imperfection is the photon loss in the apparatus which can be described in two ways. The first way, more commonly used in the literature, involves replacing the losses with beam-splitters that have a certain probability of sending the photons in unmeasured ways [243]. The second way is to modify the calculation of the probability to take into account a specific number of photons lost and then average over all possible losses [212]. It has been shown that the complexity of Boson Sampling is not affected if the number of photons lost is constant [244], on the contrary it can be classically simulated if $O(\sqrt{n})$ photons remain due to losses [212]. This estimate would worsen enormously if, in addition to the losses, the dark counts of the detectors were taken into account [243]. Another imperfection widely analyzed in the literature is the partial distinguishability of the input photons. In the original paper, Aaronson and Arkhipov showed how Boson Sampling becomes classically solvable using totally distinguishable photons [51]. It is interesting to notice how the probability always depends on a permanent but since it is of a real matrix it can be approximated in polynomial time. Intermediate regimes of distinguishability have been considered in the literature and, depending on the conditions in which one arises, it is possible to maintain or completely lose the computational complexity. The effect of Gaussian noise on the output of the interferometer is also analyzed in the literature [245]. It has recently been shown how a noisy quantum circuit can be efficiently simulated with a tensor network [246]. While this approach was designed specifically for quantum circuits, it could be adapted for other systems as well, including Boson sampling.

6.4 Validation problem

Boson sampling is a problem whose solution is not efficiently verifiable. However, it is important to find a method to be able to validate the result. Any experiment that wants to show a quantum advantage must necessarily be accompanied by an appropriate verification that the device is working as expected and is not sampling from classically computable distributions. The first experiments of Boson Sampling used a direct comparison between the sampled distribution and the theoretical one

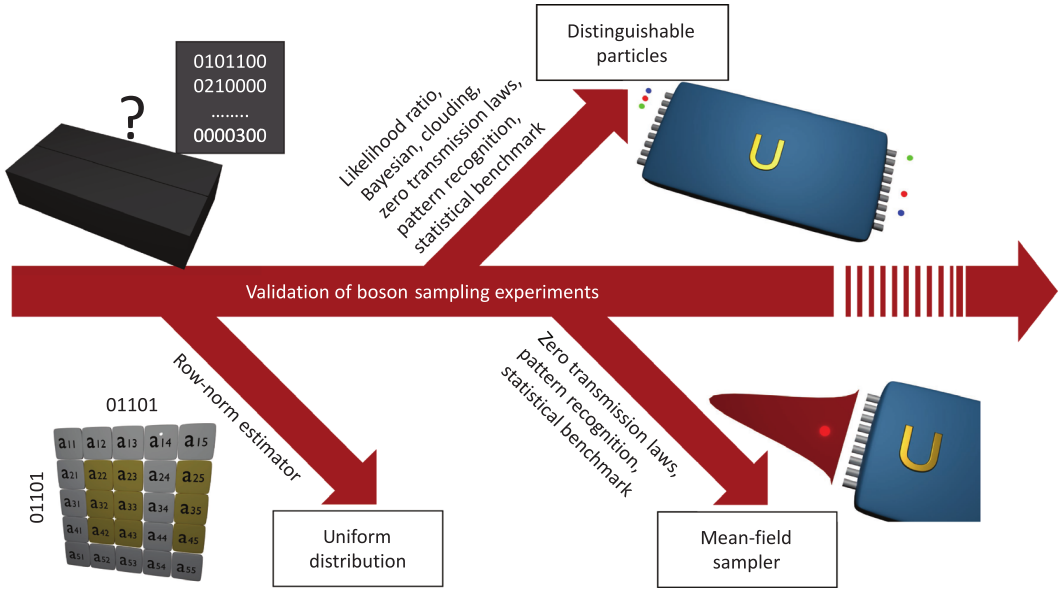

Figure 6.2. Experimental methods for the validation of Boson Sampling. A sequence of tests is progressively applied to rule out different scenarios. Image from [247].

calculated through classical algorithms [219–222]. Obviously such an approach cannot be applied to large-scale experiments, so it is necessary to find alternative ways. Subsequently, three alternative models to Boson Sampling that can be efficiently calculated and the related validation techniques used to discriminate them are presented.

6.4.1 Uniform distribution

The uniform distribution was proposed by Gogolin et al. [248] to challenge Boson Sampling as a valid method against the extended Church Turing thesis. Shortly thereafter Aaronson and Arkhipov presented an efficient method (called Row-norm Estimator) to discriminate a sampling from a uniform distribution from a Boson Sampling [249]. The idea behind this method is to calculate the quantity

$$P = \left(\frac{m}{n}\right)^n \prod_{i=0}^{n} \sum_{j=0}^{n} |U_{s\to t}|_{ij}^2 \tag{6.2}$$

where n is the number of photons, m is the number of interferometer modes and $|U_{s\to t}|_{ij}^2$ is the probability matrix used for the probabilities calculation of the multi-photon interference. It is demonstrated how the quantity P is related to the probability that the sample was obtained from Boson Sampling [249]. In particular if $P > 1$ then it is asserted that the distribution was obtained from Boson Sampling. The algorithm has a success probability of $1 - O(\delta)$ if $m > n^{5.1}/\delta$. Since an interferometer of this size is not feasible in practice, the multi-sampling algorithm is applied and the majority result is used. The article by Spagnolo et al. [216] is shown, through numerical simulations, how the size of the sample necessary to have a probability of success of 95% decreases exponentially with the number of modes m of the interferometer.

6.4.2 Distinguishable photons

A second classically calculable distribution is obtained from the same interferometer used for Boson sampling but by injecting distinguishable [216, 250, 251] photons. Although the distinguishable photons generate non-trivial probability distributions, various methods are found in the literature to distinguish these distributions from those of Boson Sampling. The first proposal made by Spagnolo et al. [216], applied to an interferometer with $m = 13$ modes and $n = 3$ input photons, uses a variant of the likelihood test. In this type of test, the ratio between the likelihood of the two models (distinguishable or indistinguishable photons) is calculated. From this ratio a discrimination parameter D is calculated: if $D > 0$ then it is affirmed that the sampling was generated by Boson Sampling otherwise it is rejected (See the next chapter for an application). This method requires calculating the permanent of the samples, without the need to calculate the full distribution.

To try to solve the issue of the computational complexity of validation other techniques have been proposed. Recently a new technique based on the binned photon-number distributions seems promising [252]. The idea behind this technique is to replace the Boson sampling distribution measured at the chip output with a coarse-grained version that can be easily simulated but still allow the ideal distribution generated by indistinguishable photons to be distinguished from other distributions. To generate the coarse-grained distribution, the authors propose to group the outputs into subsets and count how many photons end up in each set. In the paper, they show how by choosing an appropriate number of subsets it is possible to construct a distribution with the desired properties and that it is simulable not only in the ideal case but also when accounting for imperfections such as losses and partial distinguishability of photons. Finally, this protocol shows similar properties to other validation techniques, e.g. based on suppression laws [253], but in a more general scenario.

6.4.3 Mean field states

In 2014 Tichy et al. [254] proposed an alternative distribution to the previous ones from which to sample to simulate Boson Sampling which passes many of the tests proposed to distinguish previous distributions. The idea is to replace the input Fock$|1, \ldots, 1\rangle$ state with a mean-field state $|\psi\rangle^{\otimes n}$ with

$$|\psi\rangle = \frac{1}{\sqrt{n}} \sum_{r=0}^{n} e^{i\theta_r} a_r^\dagger |0\rangle \tag{6.3}$$

where n is the number of populated modes and θ_r are random phases.

The first proposal to distinguish this type of state is to use the so-called zero transmission Laws [255]: for particular unitary matrices it is easy to show, for symmetry reasons, that certain states cannot be generated at the output in the case of photons indistinguishable. Other methods have been devised for use on a general-purpose interferometer. A first class of validation texts is based on pattern recognition algorithms [256]: they compare two different samples and determine whether they were generated from the same distribution or not. Another method is based on particular statistical "signatures" of quantum interference [257] using

advanced techniques of statistical physics and stochastic matrix theory. Also, over time, additional methods have been proposed [258–260].

6.5 State of the art

The table 6.1 shows the main Boson sampling experiments in the literature in chronological order. Note how 3 photons are always used in the first experiments. This is due to the type of source used. In order to have indistinguishable photons early proposals used SPDC pumped so as to generate four-photon states of which one was used as an eralder for the other 3 photons. To overcome this limitation in recent years, alternative sources, for example Quantum Dot, are exploited. In terms of strategies used two particularly notable ones are that of He et al. in 2017 [108] (which exploits time-bin coding instead of space one, providing a viable alternative platform) and that of Paesani et al. in 2019 [115] (first group to integrate the source and interferometer on a single chip). Instead, going to see the number of maximum photons detected three items stand out over the others they are those of Wang et al. [261], Zhong et al. [262] and Madsen et al. [8] respectively with 20, 76, and 216 photons detected. They represent the first attempts to implement the Boson sampling experiment in a classically non-simulable regime. Although the results of the experiments are particularly promising there is still a debate about the actual achievement of quantum supremacy and thus the falsification of ECTT.

Year	First author	Ref.	n	m	Sources	Platform	Detector
2012	Broome	[219]	3	6	SPDC	FBS	SPAD
	Spring	[220]	3	6	SPDC	SoS	SPAD
2013	Spagnolo	[216]	3	5	SPDC	ULW	SPAD
	Tillmann	[221]	3	5	SPDC	Si	SPAD
	Crespi	[222]	3	5	SPDC	FLW	SPAD
2014	Spagnolo	[223]	3	5	SPDC	FLW	SPAD
	Carolan	[224]	3	9	SPDC	SiN	SPAD
			4	21	SPDC	SiON	SPAD
2015	Bentivegna	[251]	3	9/13	SPDC	FLW	SPAD
	Carolan	[263]	6	6	SPDC	SoS	SPAD
	Tillmann	[264]	3	5	SPDC	FLW	SPAD
2016	Crespi	[265]	2	8	SPDC	FLW	SPAD
2017	Loredo	[266]	3	6	QD	FBS	SPAD
	He	[108]	4	8	QD	FL	SNSPD
	Wang	[267]	5	9	QD	AMO	SPAD
2018	Viggianiello	[268]	2	8	SPDC	FLW	SPDC
	Wang	[110]	5	16	QD	AMO	SNSPD
	Zhong	[105]	5	12	SPDC	AMO	SNSPD
2019	Paesani	[115]	4	12	SFWM	SoS	SNSPD
	Zhong	[269]	5	12	SPDC	AMO	SNSPD
	Taballione	[270]	2	8	SPDC	SiON	SNSPD
	Wang	[261]	20	60	QD	AMO	SNSPD
2020	Zhong	[262]	76	100	SPDC	AMO	SPAD
2021	Arrazola	[85]	8	8	MR	SiON	TES
2022	Hoch	[2]	4	32	SPDC	FLW	SPAD
	Madsen	[8]	216	219	OPO	FL	SNSPD

Table 6.1. Bibliography of Boson sampling experiments. In this table are listed the most relevant Boson sampling experiment, ordered by year of publication. For each experiment is listed the first author, the maximum number of photons detected n, the number of mode m of the linear interferometer, the type of sources used for the experiment, The technology involved in the implementation of the linear interferometer and the type of detector employed. **Legend**: SPDC - Spontaneous parametric down-conversion, QD - Quantum dot, SFWM - Spontaneous four-wave mixing, MR - Microring resonator, OPO - Optical parametric oscillator, FBS - On fiber Beam splitter, SoS - Silica on silicon, ULW - UV laser writing, Si - Silicon, FLW - Femtosecond laser writing, SiN - Silicon nitride, SiON - Silica nitride, FL - Fiber loop, AMO - Assembled micro-optics, SPAD - Single-photon avalanche photodiode, SNSPD - Single-photon superconducting nanowire, TES - Transition-edge sensor.

Chapter 7

3D photonic circuit for boson sampling experiments

Since it was first proposed by Feynman and Benioff [271] many efforts have been made to demonstrate the possibility of building a computer based on the laws of quantum mechanics [272]. Despite this, the construction of a universal quantum computer with higher performances or at least comparable to those of a classical computer is far from being achieved.

In order to reach the so-called quantum supremacy, i.e. the existence of a universal quantum computer with significantly higher performance than any classical computer, an intermediate milestone to be reached is the demonstration of the existence of a quantum device that can solve a particular problem with performance superior to any classical computer.

The Boson sampling problem [51, 247] was proposed as a candidate to reach this intermediate milestone with intermediate-scale quantum devices and to this day it remains one of the most feasible and pursued problems for this purpose. The problem is well studied from a theoretical and practical point of view characterizing the level of experimental imperfection that can be accepted in a quantum machine without this entailing a loss of computational advantage compared to a classical computer [238, 240]. Furthermore, variants of the problem have been proposed to try to adapt the problem to currently available technologies [217, 218, 251]. A crucial technological requirement to fulfil a boson sampler is the possibility to implement a large-scale interferometer that is highly reconfigurable and has low losses. Reconfigurability is not an essential request but is extremely useful since allows us to test the Haar distribution of the unitary evolution [51, 273] implemented using a single device. Moreover, the possibility to have programmable devices paves the way for applications other than just demonstrating the quantum advantage [85]. The low losses instead is a pivotal request to not spoil the quantum process and reduce the computational complexity to a classical simulable level [274, 275]. Up to now, in the literature there is no experiment showing both those requirements, from one side there are bulk optics that present low losses but no reconfigurability [261, 262, 276] and, on the other side, there are integrated optics based on universal geometries [9, 57] that permit full reconfigurability but still require technological improvement to reduce the losses. In the follow we present a different approach to the

problem by adopting a reconfigurable continuous-coupled 3D photonic circuit. This architecture uses the capability of femtosecond laser-writing to write "easily" the waveguides in tree dimensions [140,277]. The optical circuit is composed of thirty-two continuously coupled waveguides arranged in a triangular lattice. Such geometry has a significant advantage in terms of the number of modes and losses compared to previous ones. Moreover, these devices possess sixteen resistors on the surface allowing a high degree of reconfigurability, in contrast to other devices with the same geometry [278,279]. The reconfigurability of the device is certified by an analysis of the unitary transformations reachable and confronted with the Haar distribution. To test the devices we perform and validate a Boson sampling experiment with three and four photons for various unitary transformations implemented by the optical chip. All the results presented in this chapter represent the findings of the work:

Reconfigurable continuously-coupled 3d photonic circuit for boson sampling experiments. Francesco Hoch, Simone Piacentini, Taira Giordani, Zhen-Nan Tian, Mariagrazia Iuliano, Chiara Esposito, Anita Camillini, Gonzalo Carvacho, Francesco Ceccarelli, Nicolò Spagnolo, Andrea Crespi, Fabio Sciarrino, and Roberto Osellame. npj Quantum Information, 8(1), May 2022 [2].

7.1 Reconfigurable integrated 3D photonic chip

This chapter present a reconfigurable integrated photonic platform with a tridimensional geometry for the realization of Bosons sampling experiments. It has been shown that this platform is suitable for the main versions of Boson sampling such as the standard problem, Scattershot Bosons sampling and Gaussian Boson sampling (see Fig 7.1 a-b-c). At the state of the art, integrated optics circuits are one of the most promising platforms to implement large reconfigurable interferometers. In Fig 7.1 d are represented the two principal geometry used to implement a photonic chip. The first scheme (on the left) decomposes the unitary transformation implemented by an optical network in simple optical units. In this framework, the optical network is composed of beam splitters and phase shifters respectively parametrize by the reflectivity S_{ij} and the phase ϕ_i. In the reconfigurable circuit, electro-optic or Kerr effects are exploited to change locally the refractive index of the waveguides enabling the local change of the optical phases of the circuit. Despite the fact that this type of geometry is adopted in a large number of experiments [85,222,263,267,270], scaling the circuit to a larger number of modes remains challenging in terms of the size and losses of the physical devices. The second geometry (on the right) exploits the continuous coupling between the waveguides and is one that we used in our experiment. In particular, the waveguides are arranged in a three-dimensional array according to a particular lattice. This architecture allows an advantage over other previously proposed devices in terms of compactness and losses. As represented in Fig. 7.1 e and Fig. 7.2 b our circuit consists of 32 waveguides arranged in a triangular lattice, fabricated via femtosecond laser-writing in a borosilicate glass substrate [140,280]. To add more randomness to the system the distance between the waveguides is changed along the evolution direction z. To do this we introduced a random perturbation of the position of the guides compared to the unperturbed lattice. This modulation is reflected in a change in the coupling coefficients c_{ij}

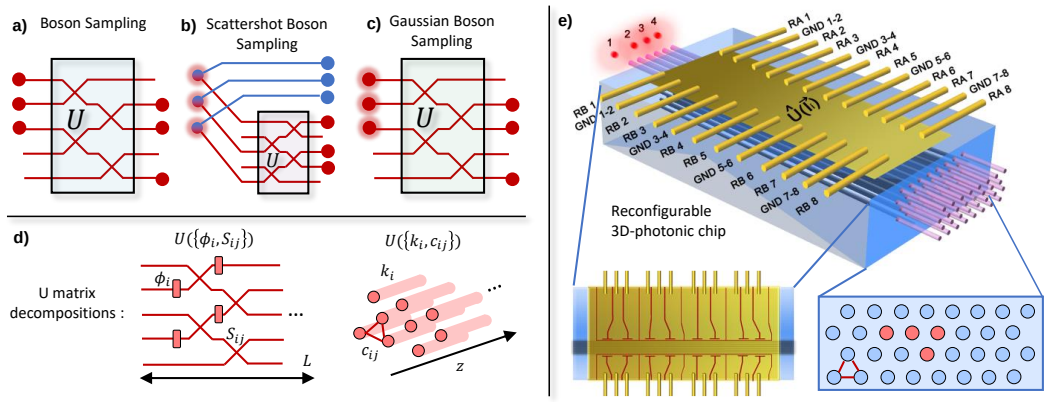

Figure 7.1. Boson Sampling in a 3D continuous-coupling integrated device. a) Boson Sampling (BS) and the most recent variants, **b)** Scattershot Boson Sampling (SBS) and **c)** Gaussian Boson Sampling GBS). The corresponding computational problems require sampling from the output distribution using different input quantum states of light, such as Fock states in BS, two-mode squeezed vacuum states in SBS and single-mode squeezed vacuum states in GBS. The common element among the schemes is the optical random circuit, described by the unitary evolution U. **d)** The most widely adopted decomposition of the operator U is via a network of beam splitters, with splitting ratios S_{ij}, and phase-shifts ϕ_i (left); an alternative implementation exploits continuous-coupling by evanescent waves among waveguides (right) depending on the coupling coefficients c_{ij} and the propagation constants k_i, where both may vary along the direction z. **e)** Overview of the reconfigurable 3D integrated photonic chip, realized through the femtosecond laser writing technique. The device is composed of 32 optical modes arranged in a triangular lattice, as shown in the inset reporting the transverse section of the sample. In red we have highlighted the input modes employed in the 3- and 4-photon experiments. The transformation U is controlled by the 16 resistors fabricated on top of the glass sample. The second inset shows the top view of the electrical circuits that control the currents I_i applied to the resistors.

along the chip and breaks the symmetries of the unperturbed circuit which could make the device unsuitable for boson sampling. The reconfigurability of the devices is introduced via sixteen resistive heaters placed in two groups of eight resistors along the propagation length on either side of the coupling region. The resistors are engraved in a gold film deposition placed above the glass substrate whit the same femtosecond laser used to write the waveguides. An external power supply is used to control the currents that flow in the resistors and therefore the power dissipated in them due to the Joule effect. With this method, a thermal gradient is induced in the substrate and, via a thermo-optic effect, a local change in the refractive index of the waveguides [10,281]. Those changes modulate the propagation constant k_i of the waveguides and therefore the overall unitary transformation U implemented by the devices. With this, we demonstrate that it is possible to apply the phase-shifting technology based on thermo-optic effects also in the continuous-coupled three-dimensional scenario but not a punctual control of the characteristic parameters.

7.1.1 Experimental apparatus

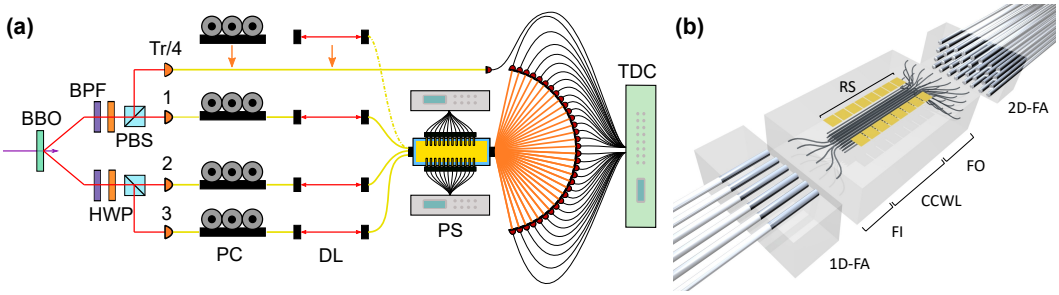

Figure 7.2. Scheme of the experimental apparatus. a) A parametric down-conversion process in a Beta-Barium Borate crystal generates one- and two-pair photon states. Generation in the single-pair regime is employed for the unitary reconstruction procedures, while 3- and 4-photon states are employed for experiments in the Boson Sampling framework. Photons are prepared in their polarization and temporal degrees of freedom before coupling in the input single-mode fiber array. After evolution, photons are finally detected via a set of 32 single-photon avalanche photodiodes connected to a 32-channel time-to-digital converter for the reconstruction of the coincidence pattern. **b)** Schematic of the in- and out-coupling of the single photons with the 3D photonic circuit: one- and two-dimensional fibre arrays connect to the fan-in and fan-out sections of the circuit. **Legend:** BBO - beta-barium borate crystal, BPF - band-pass filter, HWP - half-wave plate, PBS - polarizing beam splitter, PC - polarization controller, DL - delay line, PS - power supply, TDC - time-to-digital converter, 1D-/2D-FA - one-/two-dimensional fiber array, FI - fan-in, FO - fan-out, CCWL - continuously-coupled waveguide lattice, RS - resistors.

In Fig. 7.2 a we illustrate the experimental apparatus employed during the experiment to benchmark the photonic chip and to perform the three and four photons boson sampling experiment. We exploit one- and two-pair photon emission in a Type-II spontaneous parametric down-conversion (SPDC) sources composed of a beta-barium borate (BBO) crystal operating at the wavelength of $785nm$. The first stage of the apparatus includes all the optical components to generate the state resource to perform sampling with either indistinguishable or distinguishable photons. Photon spectra are filtered through a $3nm$ band-pass filter. Then, photons are split into four different spatial modes according to the polarization via half-wave plates and polarizing beam splitters and coupled into single-mode fibers. Photons are controlled in polarization and in time-of-arrival by polarization controllers and delay lines respectively, in order to tune their degree of indistinguishability. Then, they are injected into the reconfigurable integrated chip via an array of six single-mode fibers that have been aligned and glued to the device. A fan-in waveguide section leads the photons to selected inputs of the waveguide array, as depicted in Fig. 7.2. After the evolution in the integrated device, a fan-out waveguide section leads the photons to a 8×4 rectangular multimode fiber array that matches the fan-out geometry. It is worth noting that the two-dimensional fiber array further helps the compactness of the device by greatly reducing the length of the fan-out section. The detection stage includes thirty-tow single-photon avalanche photo-diodes. We have developed a custom software that simultaneously controls the delay lines, the power supply and the 32-channel time-to-digital converter module to record two- and four-fold

coincidences. This implies full control over the unitary transformation implemented in the circuit, the switching between indistinguishable and distinguishable photons, and the recording and processing of the data samples.

7.2 Results

In this section, we illustrate the principal findings of our article. In the first part, we test the reconfigurability of the devices by sampling various submatrices implemented by the devices and testing how those are far from the Haar distribution. In the second part, we test the devices by performing and validating a bosons sampling experiment with three and four photons with various configurations of the currents in the photonic chip.

7.2.1 Unitary matrix sampling and reconstruction

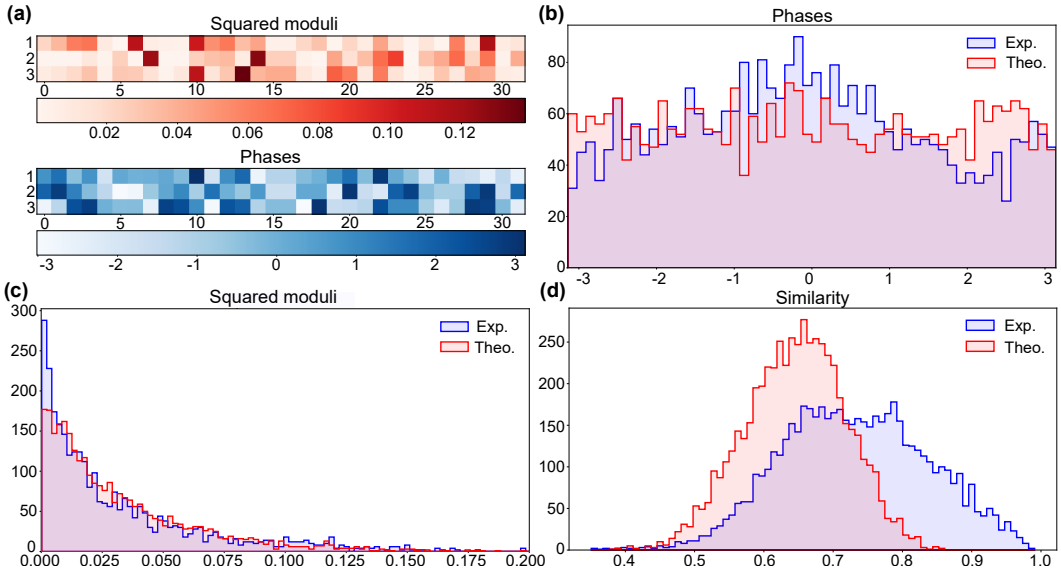

Figure 7.3. Experimental reconstruction of the $[3\times32]$ sub-matrix and comparison with the Haar-random matrices. (a) Experimental reconstruction of the squared moduli ρ_{ij}^2 (red) and phases θ_{ij} (blue) for three input ports of the reconfigurable photonic chip, highlighted by the labels in the figure. The chip is set on a random configuration of currents. Each input port represents a row of the unitary transformation applied to the input state. **(b)-(c)** Comparison of the phases and the squared moduli frequency distribution respectively, between 15 experimentally reconstructed sub-matrix (blue) and 15 $[3 \times 32]$ sub-matrix sampled from the Haar-random unitaries (red). **(d)** Distribution of the similarity between the squared moduli of two columns of different sub-matrix. We repeated the measurement for $\sim$ 200 different configurations of the currents in the chip. In red it is shown the theoretical similarity distribution obtained by sampling columns distributed according to the Haar measure. The overlap between the two histograms is 62.4% of the total area.

The control of the unitary transformation implemented by the photonic chip is performed by applying specific currents to the resistor on the surface of the devices.

To verify the classes of matrices U that can be implemented by the device due to its reconfigurability, we have reconstructed a large number of different evolutions, each corresponding to a different setting for the currents in the resistors. Thus, a crucial ingredient was the adoption of a fast and efficient reconstruction algorithm. Additionally, efficient and fast reconstruction of the unitary transformations is a fundamental step also for benchmarking and validating the three- and four-photon experiments described in the next section. We made use of an adapted version of the method reported in [25]. The latter envisages the measurements of two-photon Hong-Ou-Mandel (HOM) dips resulting from pairs of photons injected in different combinations of input ports. In our case, we restricted the measurements to two of the possible input pair combinations for the reconstruction of 3×32 sub-matrix and to only three pairs in the case of 4×32 sub-matrix. From each input pair, we analyzed 496 HOM dips, namely all the possible non-redundant pairs obtained by the combination of the 32 output ports. From these measurements, we have extracted the information about the moduli ρ_{ij} and the phases θ_{ij} of the sub-matrix elements expressed as $U_{ij} = \rho_{ij} e^{i\theta_{ij}}$. In Fig. 7.3 a we have reported an example regarding the 96 squared moduli and phases of one of the 15 different reconstructed 3×32 sub-matrices. Our next step was to prove that the random unitaries, sampled by changing the currents' configuration in the circuit, were drawn from a distribution as close as possible to the Haar measure. This requirement is fundamental to ensure the hardness of BS. To this aim, we compared the distributions of phases and moduli of the 15 sub-matrix measured in the experiment with the one retrieved from likewise Haar-random extracted unitary matrices (Fig. 7.3 b-c). In both cases, we have obtained a good agreement between the two distributions but we can notice that there are slight discrepancies between the experimental and theoretical distributions. So we decided to perform some simulations to identify the experimental imperfections that generate such deviations from the expected distributions. The histogram of the squared moduli in Fig. 7.3 b is more peaked towards zero than the theoretical one. This is likely due to errors in the estimation of input and output losses. To support this hypothesis, we performed a numerical simulation in which an error of at most 10% on the estimated values of the losses was inserted in the Haar random matrices. The results are shown in Fig. 7.4 a. The green distribution that displays losses is in good agreement with the experimental one. For what concerns Fig. 7.3 c, we observe a slight concentration around zero in the experimental phase distribution. In this case, such discrepancy can be attributed to residual correlations between the phases of the neighboring waveguides and to the reconstruction method of unitary matrices. To study this aspect we have performed a second numerical simulation that exploits a simplified model of our device. We consider the case in which the first neighboring couplings are static along z and the whole surface is uniformly heated. This produces a linear gradient of the temperature at different depths in the sample, which in turn generates correlated changes in the propagation constants and thus in the matrix phases. Note that this condition is quite far from the experiment in which each heater has been controlled independently. The red curve in Fig. 7.4 b corresponds to the resulting phase distribution. Interestingly, this distribution is completely flat as for the case of Haar random matrices. This highlights the fact that a flat distribution of the unitary matrix phases alone is not sufficient proof for the sampling from the Haar distribution. The green histogram, on the other hand,

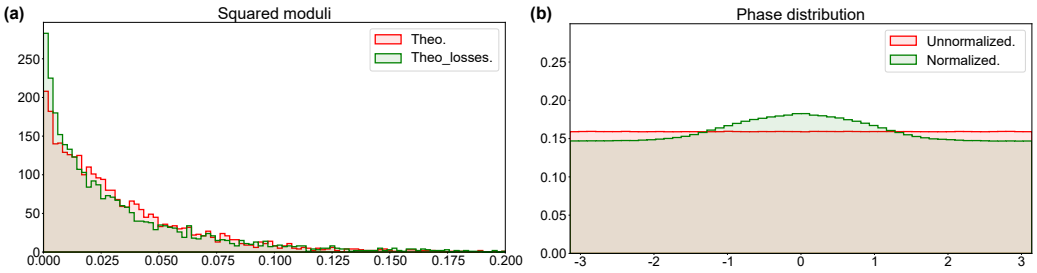

Figure 7.4. Discrepancy from the Haar random matrices distributions. (a) Comparison between the squared-moduli distributions of 15 [3×32] ideal sub-matrices from Haar-random-extracted unitary transformations (red) and the same sub-matrices with randomly modulated insertion losses in the input and output stages (green). The lossy case reproduces the experimental distribution reported in Fig. 3b in the main text. (b) Numerical simulation of the sub-matrix phase distributions in the presence of correlations due to uniform heating of device surface. In red the resulting phases distribution and in green the same phases expressed by using the phases of the first column and row as reference. In this second case, the distribution is not flat.

corresponds to the same ensemble of matrices, multiplied both at left and at right by diagonal matrices of unit-valued complex elements (equivalent to phase shifters placed at the inputs and outputs of the device), in such a way that the phases of the first columns and rows are set to zero. The latter zero-valued phases were not included in the histogram distribution. Such a scenario reproduces what we did in the reconstruction algorithm of the experimental matrix; in fact, the measured HOM visibilities are not sensitive to the input and output individual phases and this allows us to set them to 0 in the corresponding first row and column of the matrix. This procedure generates a slight concentration of the phases in zero, as shown in Fig. 7.4 b.

As a second benchmark of the device, we measured 200 columns of different unitaries and calculated the similarities between the distributions given by the squared moduli of each column. The measurements were performed by sending one photon in the device and measuring it at the output in coincidence with his correlated one in a two-photon experiment. The unitaries have been generated by uniform sampling of the electrical power dissipated in the resistors. Also in this analysis, we find a good agreement with expectations, signified by the overlap with the histogram of the similarities calculated from the columns of Haar-random matrices shown in Fig. 7.3 d. The latter result represents one of the first investigations on the level of randomness that can be reached in this continuously-coupled waveguide architecture by changing only the propagation constants via the thermo-optic effect. The similarity to the Haar-random distribution could be improved by engineering the sampling strategy of the dissipated powers, which here have been extracted from a uniform distribution. Note that, in the discrete-decomposition schemes [9, 57] there exist algorithms to set the optical circuit to sample from the Haar distribution. However, the phase shift values and beam splitter reflectivity do not display trivial distributions [282, 283] which in turn require complex settings of the external control circuit. More precisely, by increasing the dimension of the matrix, the parameter distributions tend to be more and more peaked. For example, the uniform sampling

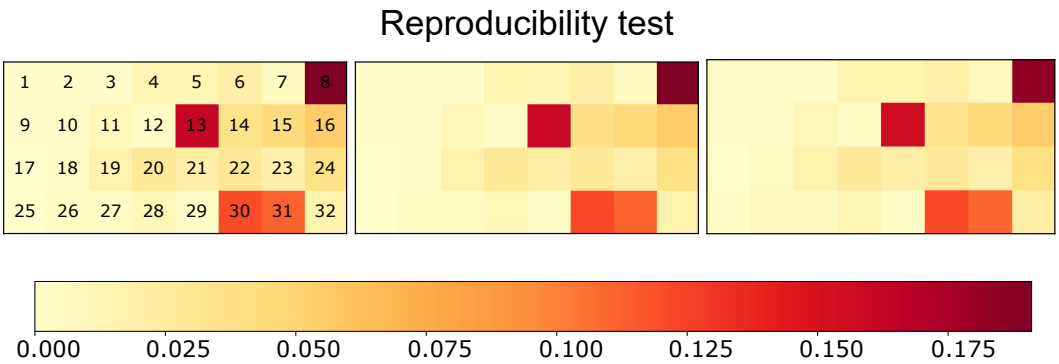

Figure 7.5. Reproducibility of the implemented transformations. We report the intensity patterns of the output modes for a fixed circuit configuration when a single heralded photon is injected in one input port. The average similarity between two of the three maps is 99.8%. The enumeration on the left map denotes the respective output mode's intensity. The other two maps follow the same enumeration.

of the dissipated electrical powers employed is far from the correct sampling to generate random Haar matrices in discrete optical circuits. An exhaustive and conclusive answer regarding the possibility to extract matrices from a distribution closer to the Haar measure with a continuously-coupled waveguide architecture needs further studies both from a theoretical and experimental point of view.

As a final test, we check the stability of the devices over a long period of time. We injected a single heralded photon in a fixed input port of the chip, and we collected the output intensities of the 32 modes. Thus, we obtained the squared moduli of a single column of the implemented unitary. We repeated the measurement three times a few days apart from each other, preserving the same setting for the applied currents. In Fig. 7.5 we report the measured output distributions. We quantified the reproducibility through the similarity between the three patterns, whose average is 99.8%.

7.2.2 Boson sampling experiment

After the characterization of the device we proceed to perform three- and four-photon experiments in the Boson Sampling framework with our integrated system. The four-photon state from double-pair emission generated by the source can be written as a statistical mixture of three Fock states $\rho^{\text{in}} \sim \alpha \left|1111\right\rangle \left\langle 1111\right| + \beta \left|2002\right\rangle \left\langle 2002\right| + \gamma \left|0220\right\rangle \left\langle 0220\right|$, by expressing the density matrix in the occupation number of the four modes and neglecting the higher order of multi-pair emission. In reality, the sources generate a coherent superposition of the three states but since we do not stabilize either the phase of the pump laser or the phases of the paths after generation the final state is reduced to a statistical mixture. To inject a 3-photon $\left|111\right\rangle$ input state, one of the four output modes of the source is directly measured and thus acts as a trigger. To this end, we have discarded one output mode of the chip, due to the requirement of using one detector for the trigger photon. Four-fold coincidences between the trigger photon and three output modes are then recorded, providing the output samples. In the four-photon experiment, we have sampled from the entire ρ^{in} by directly connecting the four output modes of the source to the

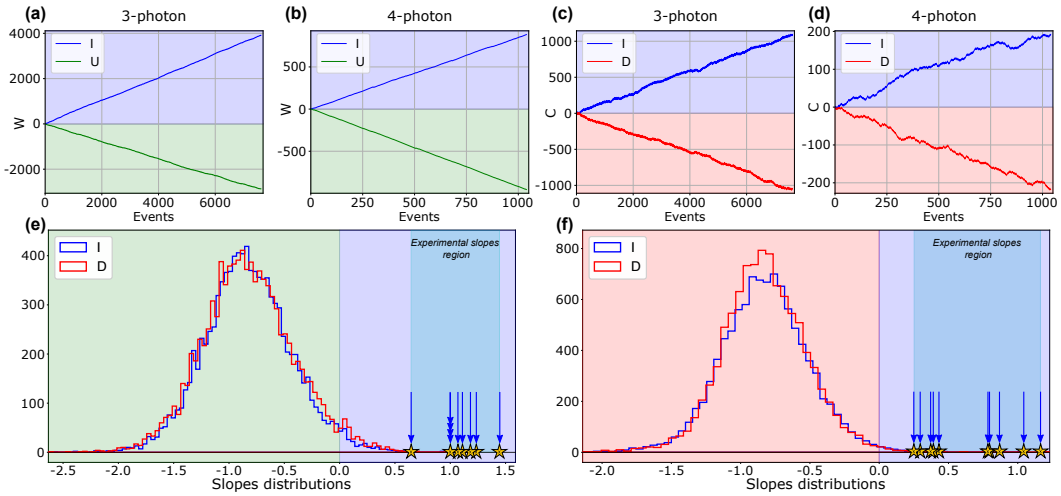

Figure 7.6. Boson Sampling data. Validation of the 3-photon (blue points in **(a)**) and 4-photon (blue points in **(b)**) Boson Sampling experiments against the uniform sampler hypothesis (green point in **a-b**). **(c-d)** Validation against the distinguishable photons sampler of 3- and 4-photon events. The test is applied using the same reconstructed sub-matrix in **(a)** and **(b)**. The distinguishable samples (red points) were collected by adjusting the relative time delay between the input photons. **(e)** Histograms of simulated 3-photon slopes for counter W (normalized to the slopes of distinguishable particles data) in the case of validation against the uniform sampler using a randomly extracted U transformation, i.e. U matrices that do not match the actual operation implemented in the circuit. The obtained slopes of the 10 different 3-photon BS experiments are highlighted by the arrows (and by the corresponding stars). The experimental points were validated with the reconstructed sub-matrix retrieved from the two-photon reconstruction. All the experimental slope values are in the positive range and far from the histogram average, thus showing the correct validation of the performed experiment. In **(f)**, we performed the same analysis for the validation against the distinguishable photons hypothesis.

integrated device (see Fig. 7.2 a). In this case, we have sampled from all the output ports of the device. For all reported experiments, our measurements are restricted to collision-free events. Such choice does not affect significantly the outcomes of the experiment since the configurations with more than one photon per mode display very low probabilities in the regime where the number of photons is much smaller compared to the number of the optical modes [216]. Let us now illustrate the analysis of the experimental samples collected in three- and Four-photon Boson sampling routines. In this context, the problem of data validation is pivotal to assessing the correctness of the sampling process, especially in the regime in which it is not possible to reproduce the output of the experiment with classical resources. In the past years, several tests have been developed to rule out classical models, such as the uniform and distinguishable particle samplers, that could reproduce some features of the boson sampling output distribution [223, 224, 256, 257, 265, 268, 284–286]. In Fig. 7.6 a-b we report one instance of the validation of a three- and four-photon boson sampling experiment against the uniform distribution test [284], assuming the input states described above for the two scenarios. We also employ the same data to validate the experiment against the distinguishable particles hypothesis [223]

(see appendix B). In both tests, each event collected in the experiment increases or decreases a counter, W for the case of a uniform sampler and C for the distinguishable particle sampler, according to a likelihood ratio test. Positive slopes are the signatures of the successful validation of the data. These kinds of hypothesis tests require good modeling of the system, including the knowledge of the input state and of the unitary transformation applied to the state. The latter has been reconstructed through two-photon measurements and exploiting the reconstruction algorithm discussed above. We have performed ten different three-photon Bosons sampling and three different four-photon with likewise configurations of the optical circuit. All the data were successfully validated against the two hypotheses. In Fig. 7.6 e-f we underline the sensitivity of these validation tests to the reconstruction of the matrix representing the optical circuit. The histograms report the distribution of the slopes normalized to that of distinguishable particles when the unitary is chosen randomly and does not coincide with the actual transformation performed in the circuit. We note that, in absence of correspondence between the unitary transformation related to the data and the one related to the likelihood ratio computations, these tests assign the data to the negative hypothesis independently from the particle statistics. In the same figure, we report the experimental slopes describing the set of ten different three-photon Boson sampling validated in this work using the unitary matrices reconstructed via our algorithm. The experimental points (stars in the Fig. 7.6 e-f) are distant more than three standard deviations compared to the average of the histograms, representing validations with random unitaries that do not correspond to the circuit from which the samples were generated as described above. Such additional results reinforce the successful validation of the performed experiments and benchmark the reconstruction accuracy of the optical circuit showing a high degree of control of the platform.

7.3 Conclusive remarks

In this chapter, we report on the implementation of a novel integrated photonic platform with a compact geometry based on a tridimensional continuous-coupled structure. Moreover, we show also the possibility to achieve a high degree of reconfigurability via a set of heaters controlled by external current sources. The tridimensional structure takes advantage of the femtosecond-writing technique and enables the possibility to increase the number of optical modes. We demonstrate that our device possesses a high degree of reconfigurability and that can cover a large amount of the space of unitary transformation with a distribution near the Haar one fulfilling the randomness hypothesis at the base of Boson sampling. Furthermore, we test the devices with a three- and four-photon experiment showing the possibility to use such a platform for a larger-scale Boson sampling experiment. Indeed, the fabrication technique is suitable to interface the devices with various types of single-photon sources such as the quantum dot [93, 287, 288] or integrated parametric sources [74] allowing to reduced coupling losses at the device interface which is now the major source. Furthermore, it is possible to duplicate or quadruple the number of modes of the device without too much effort since the limiting factors of such geometry are not the coupling region but the fan-in and fan-out regions. The

capability of implementing a compact reconfigurable photonic processor is useful for implementing other applications beyond the mere implementation of a Boson sampling experiment.

Statement of Work

The work presented in this chapter was published in Hoch et. al. npj Quantum Information, 8(1), May 2022 [2]. The realization of the experimental apparatus and data taking was carried out by myself, T. Giordani and C. Esposito. The characterization of the chip was carried out by the undersigned with the help of A. Camillini and M. Iuliano. The data analysis of the Boson sampling experiment was carried out by myself with the help of M. Iuliano. The photonic chip used was realized in the laboratories of Professor R. Osellame with the help of A. Crespi and Z. Tian.

Part IV

Bernoulli factory problem

Chapter 8

Quantum Bernoulli factory problem

Given the intrinsically probabilistic nature of quantum mechanics, it is logical to think that quantum computing is an excellent candidate to build algorithms able to generate and manipulate randomness. In this chapter, we will analyze a recently proposed quantum extension of an originally classical problem called Bernoulli Factory [18]. In the first part of this chapter, we revise the literature regarding the Bernoulli factory problem and its quantum extension. Next, the main results of this chapter are presented, where the quantum to quantum Bernoulli factory problem is studied. In particular, we start with the characterization of the set of simulable functions. In contrast to the demonstration in the literature that exploits the field properties of the set, in ours a constructive approach is applied by defining the quantum circuits that can be associated with a Bernoulli factory and then, using this result, we characterize the set of simulable functions. Subsequently, we will fully characterize the computational complexity of the problem in terms of used resources and success probability. Finally, we will propose two variants of the original problem and, as done for the original one, we will analyze their complexity.

8.1 Bernoulli factory problem

Some examples are best suited to introduce the Bernoulli factory problem. Let us imagine being in possession of a classical coin that we suspect does not produce equilibrated results. The coin produces heads with a probability p unknown to us. We would want the coin to be unbiased in order to use it for a fair coin flip, is there a method to obtain an equilibrated result? A method attributed to Von-Neumann [289] solves this problem in a simple way: flip the coin twice, if the results are different take the result of the second flip, if they are identical repeat the double flip (See Fig 8.1). Each of the two outputs occurs with probability $p(1-p)$ so they are equally likely. This technique does not work in the extreme case where the coin is entirely biased and produces heads with a probability of 0 or 1. For all the other cases, the technique transforms the initial biased coin into an equilibrated one. Another example is given the same coin with unknown bias p, we can ask if it is possible to construct another biased coin with probability p^2. The procedure is similar to the

previous one: flip the coin twice, if the result is both heads then the result is head, otherwise, the result is tail. The Bernoulli factory problem is the extension of the previous problem for a generic function $f(p)$.

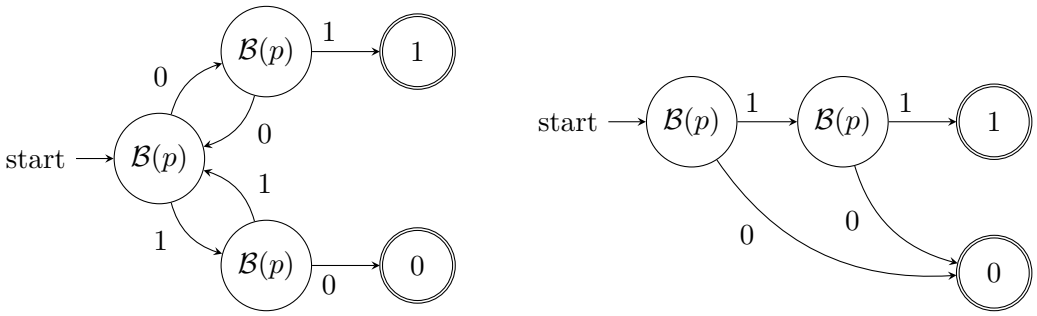

Figure 8.1. Finite state machine for the Von-Neumann algorithm and for the construction p^2 function. The figure shows the schematic representation of the Von-Neumann algorithm (on the Left) and the algorithm to implement the function $f(p) = p^2$ (on the Right). Starting from the start position for each encountered circle we flip the input coin and then we follow the harrow labeled with the toss result. The algorithm ends when it reached one of the final states marked with 0 or 1. The label of the final state is the result of the algorithm.

8.1.1 Definition

To formally define what is a Bernoulli factory first is necessary to define what is a Bernoulli distribution $\mathcal{B}(p)$. A *Bernoulli distribution* of parameter p is the discrete distribution that returns 1 with probability p and 0 with probability $1 - p$.

$$\mathcal{B}(p) = \begin{cases} 1 & \text{whit probability } p \\ 0 & \text{whit probability } 1-p \end{cases} \tag{8.1}$$

A *Bernoulli factory*, associated with a function $f : \mathcal{D} \subseteq [0,1] \to [0,1]$, is an algorithm that samples from a Bernoulli distribution with unknown bias p and returns 0 or 1 with a probability $f(p)$. Formally, a Bernoulli factory is an algorithm that defines a function $G_f : \{0,1\}^\infty \to \{0,1\}$ from the infinite string of bits to a single bit such that

$$G_f(\mathcal{B}(p)) = \mathcal{B}(f(p)) \tag{8.2}$$

This means that if we apply the function to a string sampled from a Bernoulli distribution with bias p, we obtain the same result as we sample from a Bernoulli distribution with bias $f(p)$. In the definition, there are two essential points. The first one is that the function G is independent of the parameter p, this property is related to our ignorance of the parameter as shown in the example presented in the introduction of the chapter. The second one is the exactness of the simulation, this point is important not only from a theoretical point of view since it prevents the possibility of estimating the parameter p with certain accuracy and then simulate the target Bernoulli distribution with the estimated parameter, but also from a practical point of view since the Bernoulli factory is meant to be a routine for larger algorithms. In those algorithms, also a small error in the routine can quickly grow up and become intractable.

8.1.2 Existence and complexity

Now that we have defined what a Bernoulli factory is, the first natural question one can ask is if exist a Bernoulli factory for every function. Unfortunately, the answer is negative. We define a function *simulable* if exist an associated Bernoulli factory. In Ref. [12] Keane and O'Brien demonstrate a theorem that provides a necessary and sufficient condition for a function to be simulable. In particular, they show that $f : \mathcal{D} \subseteq [0,1] \to [0,1]$ is simulable if it is constant, or if is continuous and satisfies the following condition

$$\exists n \geq 1 | \forall p \in \mathcal{D} \quad \min(f(p), 1 - f(p)) \geq \min(p^n, (1-p)^n) \tag{8.3}$$

An essential point that can be deduced from the theorem is that not only the function itself is important but also the domain of definition. For example, the function $f(p) = 2p : [0, 1/2] \to [0, 1]$ known as "probability amplification" is not simulable; but if we restrict the domain for which this function is defined $f_\epsilon(p) = 2p : [0, 1/2 - \varepsilon] \to [0, 1]$ for $\varepsilon > 0$ then the function became simulable.

The theorem stated above gives us a simple criterion for deducing whether a function is simulable or not; in the demonstration, the authors also provided a method to construct a Bernoulli factory from the associated function, but the resulting algorithm is indeed infeasible on a practical level since the number of samples needed for the simulation is unbounded. This leaves open the question on how to construct a Bernoulli factory and if it is possible to bound the number of samples necessary to simulate it. In the literature it is possible to find several manuscripts that show how to construct a Bernoulli factory for specific sets of functions [15, 290, 291], providing bounds on the number of samples necessary to perform the simulation [292, 293] and for some they also show that are optimal [14, 16, 294]. For more details, refer to the specific literature [295].

8.1.3 Variants

In the last years, variations on the original problem have been proposed; here we list some of them explaining similarities and differences from the original problem.

Multiple-Output Bernoulli Factory [295] The difference between this version and the original Bernoulli factory is that this version of the algorithm returns more than one sample at a time. Obviously, any single-output Bernoulli factory can be used to produce more samples by running it multiple times. The idea behind these algorithms is that for some functions, it may be more efficient to produce multiple samples at the same time compared to producing the samples one by one.

Multiparameter Bernoulli Factories [296] This version of the problem extends the notion of Bernoulli factory to multiparameter functions. More specifically a multiparameter Bernoulli Factory associated with a function $f(p_1, \dots p_n) : \mathcal{K} \subseteq [0,1]^n \to [0,1]$, is an algorithm that takes as input the samples from n independent Bernoulli distribution $\mathcal{B}(p_i)$, respectively with bias p_i, and return a sample from a Bernoulli distribution of bias $f(p_1, \dots p_n)$.

Dice enterprise and multidimensional distribution [290, 297] The third variant that we revise follows a similar path to the previous one. The idea is to change the input and the output from samples of Bernoulli distributions to samples

from distributions of higher dimensions. We define a *dice enterprise*, associated to a n-dimensional tuple of functions $(f_1(p_1,\ldots,p_m),\ldots,f_n(p_1,\ldots,p_m))$ with the constraint $\sum_i f_i(p_1,\ldots,p_m) = 1$ if $\sum_j p_j = 1$, is an algorithm that given a m-dimensional distribution described by the tuple $(p_1,\ldots,p_m)$, return a n-dimensional distribution described by the tuple $(f_1(p_1,\ldots,p_m),\ldots,f_n(p_1,\ldots,p_m))$. For example, in Ref. [290] was shown an algorithm to simulate a Poisson distribution with a mean equal to the bias of a Bernoulli distribution placed at the input.

8.2 Quantum extensions

Now that we understand what is a Bernoulli factory and its possible variants, we proceed to discuss how to extend the problem using the quantum theory and which consequences it entails. One may ask why try to translate the problem into quantum language, and the answer is that the Bernoulli factory problem has several properties that make it interesting to approach from a quantum perspective Sampling problems and, more generally, randomness manipulation problems are of particular interest in the literature on quantum information since tasks of this type have been proposed to show the quantum advantage with technologies that are currently available or achievable in the short term. Indeed, in recent years, the quantum advantage has been shown experimentally with this type of problem [7, 8, 28, 29]. At this point, it is necessary to understand how the problem can be transposed into quantum formalism.

8.2.1 Quantum resources

To understand how to translate the Bernoulli factory problem into quantum formalism, we must analyze what are the main components of the problem. A Bernoulli factory can be divided into three parts: the input distribution, the algorithm and the output distribution. The algorithm must necessarily be quantum since, even if the input and the output are quantum distributions, without a quantum algorithm there are no opportunities to exploit the possible advantage of quantum mechanics. To translate the input and the output distribution into quantum formalism we can go through various paths, in the following we describe three possibilities:

Coin

The first possibility is to rewrite the classical coin into the quantum formalism, in this sense a Bernoulli distribution can be seen as a mixed state ρ_p diagonal in the computational base

$$\rho_p = p\,|0\rangle\langle 0| + (1-p)\,|1\rangle\langle 1| \tag{8.4}$$

Quoin/Qubit

The second possibility is to use a coherent state to encode the Bernoulli distribution. We define the quantum coin, or quoin, parametrized by $p \in [0,1]$ as a qubit in the state

$$|C_p\rangle = \sqrt{p}\,|0\rangle + \sqrt{1-p}\,|1\rangle \tag{8.5}$$

It is direct to notice that if we measure a quoin with parameter p on the computational basis the result is equivalent to a sample from a Bernoulli distribution with the same parameter p. To perform a step forward, we can also think to extend the input state to all the possible qubits. It is essential to find a suitable parametrization of the qubits such that we can define a function of the parameters. The first parametrization that we can think of is the spherical coordinate parametrization, due to the map between the qubit space and the Bloch sphere, but we propose a different parametrization more suitable for our purpose, as will become clearer later. We define a qubit parametrized by a complex number $z \in \mathbb{C}$ as

$$|z\rangle = \frac{z\,|0\rangle + |1\rangle}{\sqrt{1 + |z|^2}} \tag{8.6}$$

This parametrization is related to the stereographic projection of the Bloch sphere on the complex plane, so to cover all the possible qubits it is necessary to add to the complex plane the point at infinity. Following the same idea, we can also define a parametrization for a qudit of dimension n with a $(n-1)$-dimensional vector of complex parameters $\vec{z} \in \mathbb{C}^{n-1}$ as

$$|\vec{z}\rangle = \frac{\sum_{i=1}^{n-1} z_i\,|i\rangle + |n\rangle}{\sqrt{1 + \sum_{i=1}^{n-1} |z_i|^2}} \tag{8.7}$$

Oracle

The third possibility considered is that instead of providing the Bernoulli factory with distribution or a quantum state as an input, we consider a unitary operator that can be used to generate the state, we call this operator the oracle associated with the state. The oracle for a quoin is the operator

$$C_p = \begin{pmatrix} \sqrt{p} & \sqrt{1-p} \\ -\sqrt{1-p} & \sqrt{p} \end{pmatrix} \tag{8.8}$$

instead, for the qubit, we consider the oracle in the form

$$Q_z = \frac{1}{\sqrt{1 + |z|^2}} \begin{pmatrix} z & -1 \\ 1 & z^* \end{pmatrix} \tag{8.9}$$

We can see that for both of them if we apply the oracle to the state $|0\rangle$ we obtain respectively the quoin and the qubit associated.

8.2.2 Bernoulli factory types

Now that we have briefly revised some quantum extensions of classical probability distributions, we can define different kinds of Bernoulli factories according to the type of input and output. The classification according to the type of distribution in input and output can be considered the primary one since other classifications, e.g.

Name	Abbreviation	Input	Output	First mention
Classical to Classical Bernoulli Factory	**CCBF**	Coin	Coin	[12]
Quantum to Classical Bernoulli Factory	**QCBF**	Quoin/Qubit	Coin	[17]
Quantum to Quantum Bernoulli Factory	**QQBF**	Quoin/Qubit	Quoin/Qubit	[18]
Oracle to Classical Bernoulli Factory	**OCBF**	Oracle	Coin	[298]
Oracle to Quantum Bernoulli Factory	**OQBF**	Oracle	Quoin/Qubit	[298]

Table 8.1. Bernoulli factories presented in the literature. This classification is based on the type of distribution in input and output; other classifications can be considered; for example, based on which operations are permitted for the evolution of the state or on the number of resources required, but to define what is a resource or which operation can be permitted depends on the input and output distributions making the presented classification one of the main ones.

according to computational complexity or the type of operations allowed, are not well defined without knowing what type of quantum distribution they are acting upon. In Table 8.1 are summarized the main types of Bernoulli factories in the literature.

Classical to Classical Bernoulli Factory

This type of Bernoulli factory has in input and output the classical Bernoulli distribution, making it exactly the canonical Bernoulli factory problem described in the previous paragraph. The different nomenclature was later given to distinguish the original problem from the various quantum versions below.

Quantum to Classical Bernoulli Factory

First proposed by Dale et al. in [17], this Bernoulli factory is the first quantum extension of the classical one. In particular, the problem considers the possibility to have at the input of the algorithm quoins (qubits) of parameter p (z), and at the output that returns a series of bits distributed according to a Bernoulli distribution of parameter $f(p)$ ($f(z)$). In Ref. [17] and [19] they completely cartelize the class of functions simulable by a quantum to classical Bernoulli factory, showing that the class of simulable functions by a Classical to Classical Bernoulli Factory is strictly contained in the set of function simulable by a Quantum to Classical Bernoulli Factory. They also show that the only necessary quantum operation is the change of basis of the measure before applying a classical algorithm to the obtained result. Experimental implementation of the quantum to classical Bernoulli factory was performed with superconductive qubits [21] and also with bulk photonics [22] showing that for particular functions there is an advantage in terms of computational resources used (sample from the quoin/coins) of the quantum version compared the classical counterpart. The problem of the complexity, i.e. characterizing the required number of quoin to simulate a given function, is an open problem and also if there is always an advantage in the quantum version or not. In this contest, can be noticed that it is not possible to have a more efficient Classical to Classical

Bernoulli Factory than the Quantum to Classical counterpart. Indeed, if we measure a quoin of parameter p we have a random bit distributed according to a Bernoulli distribution with the same bias so if we use the result of the quoin measure as an input for a Classical to Classical Bernoulli factory we obtain a Quantum to Classical Bernoulli factory with the same complexity. Except for this straightforward result Some others regarding the complexity of the problem are provided by Yoder [298] in particular they provided a lower bound on the required number of samples to simulate a given function showing also the existence of functions that saturates the bound.

Quantum to Quantum Bernoulli Factory

First proposed by Yoder [298] and Dale [19] in an embryonic form, a Quantum to Quantum Bernoulli Factory accepts at the input a set of identical quoins/qubits and returns a quoin/qubit. They provided some conditions on the set of functions simulable by a Quantum to quantum Bernoulli factory but a complete characterization was missing. Subsequent results were presented by Jiang et al. in Ref. [18] formalizing the Quantum to Quantum Bernoulli Factory and completely characterizing the set of simulable functions for the case of quoin both in input and output. Some attempts to experimentally implement a Quantum to Quantum Bernoulli Factory are presented in Ref. [23] and also in Ref. [20] but both the attempt have a conceptual problem in the implementation of a general Quantum to Quantum Bernoulli Factory. The next section will take a closer look at some of the problems of this version, in particular the computational complexity of the problem (i.e. the number of qubits required to implement a particular function) and the success probability of the protocol.

Oracle to Classical Bernoulli Factory and Oracle to Quantum Bernoulli Factory

The last two versions that we will present are the Oracle to Classical Bernoulli Factory and the Oracle to Quantum Bernoulli Factory. Proposed in Ref. [298] these problems are the least studied among those proposed in this section. In the work, they provide a characterization of the set of functions simulable by an Oracle to Classical Bernoulli Factory in the restricted case of one qubit and the only quantum operations allowed beyond the oracle are all diagonal in the computational basis. Even in this particularly restricted scenario, the set of simulable functions is not trivial. They also show a lower bound for the complexity of the Oracle to Classical, important to notice is that this did not give any information on the required number of qubits since in this scenario the complexity is related to how many times is used the oracle like in the quantum metrology scenario (see chapter 10). The principal open problem for these variants of the Quantum Bernoulli factory is the complete characterization of the set of simulable functions since other questions like the complexity of a function are meaningless if we can not say if exist an Oracle Bernoulli factory that implements that function.

8.3 Quantum to Quantum Bernoulli factory

In this section, we analyze in detail the Quantum to Quantum Bernoulli factory (QQBF) problem answering some open questions present in the literature. We start by characterizing the set of functions that can be simulated, something that is already present in the literature but using a different approach that not only allows us to check whether a function is simulable or not but also provides a systematic algorithm for constructing a quantum circuit that implements the function. Furthermore, it is shown how the circuit found uses the minimum number of qubits possible and has the highest probability of success, thus characterizing the computational complexity of the problem. Finally, we want to propose and study some variants of the original problem, for example going to change the type of input distributions but not their quantum nature.

In Ref [18] Jiang et al. characterize the set of simulable functions for a QQBF in the case that the inputs are quoins $|C_p\rangle$. They show that the output qubit $|z_f = f(p)\rangle$ is simulable if the function $f(p)$ belongs to the complex field generated by the function $\sqrt{\frac{p}{1-p}}$. This condition is equivalent to saying that the function $f(p)$ is in the form:

$$f(p) = \frac{g_1(p)}{g_2(p)} + \frac{g_3(p)}{g_4(p)}\sqrt{\frac{p}{1-p}} \tag{8.10}$$

where $g_1(p)$, $g_2(p)$, $g_3(p)$ and $g_4(p)$ are complex polynomials in p of arbitrary degree. Although this demonstration provides a fairly simple criterion for testing whether a function is simulable or not, it does not provide any information on how to construct a quantum circuit that implements the function.

8.3.1 Set of simulable functions, complexity and implementation

In the following, we completely characterize the Quantum to Quantum Bernoulli factory problem where we consider a generic qubit state in input and output. In particular, we provide a simple characterization of the set of simulable functions. Furthermore, for each simulable function, we construct a quantum circuit implementing the associated quantum Bernoulli factory showing that uses the minimum number of qubits possible and that is the most efficient in terms of success probability.

Generic Circuit

The first step in the demonstration is to show that every circuit implementing a Quantum to Quantum Bernoulli factory can be mapped into a circuit in the form of Figure 8.2. Since the hidden information in a Bernoulli factory circuit is provided only by the unknown state $|z\rangle$ we can divide the circuit into three principal components. First, the input state is composed of n copies of the state $|z\rangle$ and some ancillary qubits in known pure states. Then, a series of definite unitary evolution and, finally, a measurement is performed such that at the end remain only a qubit that carries the output state. Using the deferred measurement principle [26, 48] we can postpone all the measurements at the end of the circuit eventually adding some ancillary qubits, in this way we have only one known global unitary evolution between

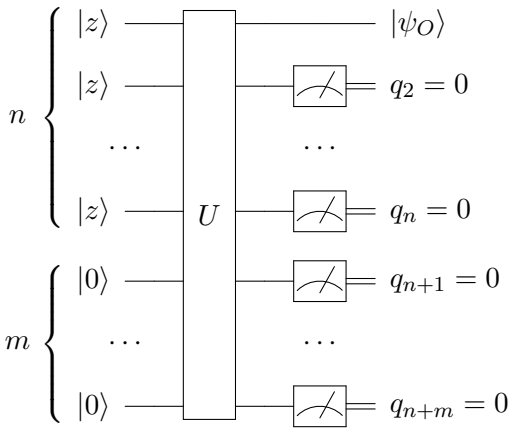

Figure 8.2. Quantum Bernoulli factory general circuit The circuit takes in input n qubit in the state $|z\rangle$ and m ancillary qubits in the state $|0\rangle$, making the resulting state evolve through a unitary evolution U and then apply a measure to all the qubits in the computational basis except the first one that carries the output state of the Bernoulli factory; the output $|\psi_O\rangle$ state is accepted if all the measures $q_2 \dots q_{n+m}$ return the result 0. We can say that this circuit is the most general one since every circuit implementing a Quantum to Quantum Bernoulli factory can be mapped into one in the presented form with the same output state and the same success probability.

the initial state and the measurement. Furthermore, without loss of generality, we can assume that all ancillary qubits are in the state $|0\rangle$ since any other state can be generated by applying a unitary transformation which can be reabsorbed in the global unitary transformation. With a similar argument, we can say that all the measures are performed on the computational basis and that the accepted result is when all the measures return 0.

Superset of simulable functions and lower bound on the required number of qubits.

Using the previous result we can provide a superset of the simulable functions, i.e. a set that contains the set of simulable functions, and also a lower bound on the required number of qubits to simulate a given function. Starting from the circuit in Fig 8.2, first we write the input state just before the unitary evolution:

$$|\psi_I\rangle = |0\rangle^{\otimes m} \otimes \left(\frac{z|0\rangle + |1\rangle}{\sqrt{1+|z|^2}}\right)^{\otimes n} = \left(\frac{1}{1+|z|^2}\right)^{\frac{n}{2}} \sum_{j=0}^{n} z^j \sqrt{\binom{n}{j}} |0\rangle^{\otimes m} \otimes \left|s_j^n\right\rangle \quad (8.11)$$

where $\left|s_j^n\right\rangle$ is the total symmetric state on n qubits with j zeros. It is important to notice that the coefficients composing the state are monomial in z and span all the powers from 0 to n. Since the unitary evolution is linear we can say that all the coefficients of the state after the evolution and before the measure are a linear

combination of the coefficients of the input state. This consideration demonstrates that all the coefficients of the state written in the computational basis are polynomial in z with the degree at most n. At this point we apply the measurements, since all are performed on the computational basis the result is to select some coefficients of the state without changing it; so the output state is in the form

$$|\psi_O\rangle = \frac{P(z)\,|0\rangle + Q(z)\,|z\rangle}{\sqrt{|P(z)|^2 + |Q(z)|^2}} = \frac{\frac{P(z)}{Q(z)}\,|0\rangle + |1\rangle}{\sqrt{\left|\frac{P(z)}{Q(z)}\right|^2 + 1}} = \left|g(z) = \frac{P(z)}{Q(z)}\right\rangle \tag{8.12}$$

where $P(z)$ and $Q(z)$ are polynomials in z. We show that the space of simulable function S is a subset of the set of polynomials Cartesian product itself $S \subseteq \mathcal{P}(\mathbb{C}) \times \mathcal{P}(\mathbb{C})$. Furthermore, we have shown that the functions implementable by a circuit with n copies of the state $|z\rangle$ as input are ratios of polynomials both of degree at most n. This result allows us to have a lower bound on the minimum number of qubits required to implement a given function indeed is necessary at least a number of qubits equal to the greater between the degrees of the two polynomials composing the function $n \geq \max\{deg(P), deg(Q)\}$.

Set of simulable functions, required number of qubits and associated unitary transformations

Now that we found a bound for the set of simulable functions and the required number of bits the goal is to prove that those bounds are tight. To do it, for each tuple $(P(z), Q(z)) \in \mathcal{P}(\mathbb{C}) \times \mathcal{P}(\mathbb{C})$ we construct a circuit implementing a Bernoulli factory with an associated function $g(z) = P(z)/Q(z)$ that use a number of qubits n equal to the lower bound $n = \max\{deg(P), deg(Q)\}$. First, we describe the state at the output of the circuit in Fig 8.2

$$|\psi_O\rangle = \frac{|0\rangle\,\langle 0|^{\otimes n-1} \otimes \langle 0|\,U\,|\psi_I\rangle + |1\rangle\,\langle 0|^{\otimes n-1} \otimes \langle 1|\,U\,|\psi_I\rangle}{\sqrt{\left|\langle 0|^{\otimes n-1} \otimes \langle 0|\,U\,|\psi_I\rangle\right|^2 + \left|\langle 0|^{\otimes n-1} \otimes \langle 1|\,U\,|\psi_I\rangle\right|^2}} \tag{8.13}$$

If we describe the first two rows of the unitary matrix with two covectors $\langle v_0|$ and $\langle v_1|$ we can simplify the previous expression as:

$$|\psi_O\rangle = \frac{|0\rangle\,\langle v_0|\psi_I\rangle + |1\rangle\,\langle v_1|\psi_I\rangle}{\sqrt{|\langle v_0|\psi_I\rangle|^2 + |\langle v_1|\psi_I\rangle|^2}} \tag{8.14}$$

Since we want to implement a Bernoulli factory with the associated function $g(z) = P(z)/Q(z)$, we impose the following equality

$$\langle v_0|\psi_I\rangle = K * P(z) \quad \langle v_1|\psi_I\rangle = K * Q(z) \tag{8.15}$$

for some real non-null proportional factor K. Defining $P(z) = \sum p_j z^j$, $Q(z) = \sum q_j z^j$, and using the property that the monomials with different power are linearly independent we can rewrite the precedent equations in the form

$$\left\langle v_0 \middle| s_j^n \right\rangle = K\frac{p_j}{\sqrt{\binom{n}{j}}} \quad \left\langle v_1 \middle| s_j^n \right\rangle = K\frac{q_j}{\sqrt{\binom{n}{j}}} \tag{8.16}$$

using the fact that the vector $\left|s_j^n\right\rangle$ are orthogonal to each other we can write the two vectors $|v_0\rangle$ and $|v_1\rangle$ in the general form

$$|v_0\rangle = \sum_{j=0}^{n} K \frac{p_j^*}{\sqrt{\binom{n}{j}}} \left|s_j^n\right\rangle + Kx\,|\theta_0\rangle \qquad |v_1\rangle = \sum_{j=0}^{n} K \frac{q_j^*}{\sqrt{\binom{n}{j}}} \left|s_j^n\right\rangle + Ky\,|\theta_0\rangle + Kw\,|\theta_1\rangle \tag{8.17}$$

where $|\theta_0\rangle$ and $|\theta_1\rangle$ are two vectors orthogonal to each other and to all vectors $\left|s_j^n\right\rangle$; and x, y, w are free parameters. Without loss of generality, we can assume that x and w are real positive parameters since the eventual phases can be reabsorbed by a redefinition of the vectors $|\theta_0\rangle$ and $|\theta_1\rangle$. Now we have to impose that the covector associated with the vector $|v_0\rangle$ and $|v_1\rangle$ are proper rows of a unitary transformation, so we have to impose that the two vectors are orthonormal which in formulas are

$$\begin{aligned} \langle v_0|v_0\rangle = 1 \quad & \sum_{j=0}^{n} \frac{|p_j|^2}{\binom{n}{j}} + |x|^2 = 1/K^2 \\ \langle v_1|v_1\rangle = 1 \quad & \sum_{j=0}^{n} \frac{|q_j|^2}{\binom{n}{j}} + |y|^2 + |w|^2 = 1/K^2 \\ \langle v_0|v_1\rangle = 0 \quad & x^* y = -\sum_{j=0}^{n} \frac{p_j q_j^*}{\binom{n}{j}} \end{aligned} \tag{8.18}$$

since there are four variables but only three equations we decide to solve the system as a function of the free parameter w. Defining ϕ the phase of the coefficient $\sum_{j=0}^{n} p_j q_j^*$ we can solve the system of equation as

$$\begin{aligned} x &= \frac{1}{\sqrt{2}} \sqrt{\sqrt{\left(|w|^2 + \sum_{j=0}^{n}\left(\frac{|q_j|^2}{\binom{n}{j}} - \frac{|p_j|^2}{\binom{n}{j}}\right)\right)^2 + 4\left|\sum_{j=0}^{n} \frac{p_j q_j^*}{\binom{n}{j}}\right|^2} + |w|^2 + \sum_{j=0}^{n}\left(\frac{|q_j|^2}{\binom{n}{j}} - \frac{|p_j|^2}{\binom{n}{j}}\right)} \\ y &= \frac{-e^{i\phi}}{\sqrt{2}} \sqrt{\sqrt{\left(|w|^2 + \sum_{j=0}^{n}\left(\frac{|q_j|^2}{\binom{n}{j}} - \frac{|p_j|^2}{\binom{n}{j}}\right)\right)^2 + 4\left|\sum_{j=0}^{n} \frac{p_j q_j^*}{\binom{n}{j}}\right|^2} - |w|^2 - \sum_{j=0}^{n}\left(\frac{|q_j|^2}{\binom{n}{j}} - \frac{|p_j|^2}{\binom{n}{j}}\right)} \\ K &= \frac{\sqrt{2}}{\sqrt{\left(|w|^2 + \sum_{j=0}^{n}\left(\frac{|q_j|^2}{\binom{n}{j}} - \frac{|p_j|^2}{\binom{n}{j}}\right)\right)^2 + 4\left|\sum_{j=0}^{n} \frac{p_j q_j^*}{\binom{n}{j}}\right|^2} + |w|^2 + \sum_{j=0}^{n}\left(\frac{|q_j|^2}{\binom{n}{j}} + \frac{|p_j|^2}{\binom{n}{j}}\right)} \end{aligned} \tag{8.19}$$

It is possible to notice that the solution exists for every combination of the polynomials' coefficients and for every value of w so to reduce the number of required basis vectors we put $w = 0$ making the vector $|\theta_1\rangle$ unnecessary.

With those parameters we can construct the orthonormal vectors $\left|v_{0/1}\right\rangle$ and by completing it to an orthonormal basis we can construct the corresponding unitary matrix U. The only remaining open issue is the possibility of finding a vector $|\theta_0\rangle$ that is orthogonal to all the vectors $|s_i^n\rangle$. Without the necessity to use ancillary qubits to increase the Hilbert space dimension. A Hilbert space generated by n qubit has dimension 2^n and the vectors $|s_i^n\rangle$ are $n+1$, so if $2^n - n - 1 > 0$ then there is at

least a vector that can be used for $|\theta_0\rangle$ without the necessity to use ancillary qubits. The inequality is true for $n \geq 2$ so only for functions composed of polynomials of degree one or less are necessary to use an ancillary qubit, in the other cases the required number of qubits is equal to the lower bound $\max\{deg(P), deg(Q)\}$.

Success probability

To complete the investigation on the Quantum to Quantum Bernoulli factory we analyse the success probability of the quantum circuit to generate the correct output state. The operator describing the final measurement in the circuit in Fig 8.2 is $E = |0\rangle\langle 0|^{\otimes n-1} \otimes \mathbb{1}$, so the corresponding success probability is

$$P_O = tr(EU\,|\psi_I\rangle\langle\psi_I|\,U^\dagger) = |\langle v_0|\psi_I\rangle|^2 + |\langle v_1|\psi_I\rangle|^2 \tag{8.20}$$

and using the expression obtained previously we can write

$$P_O = \frac{2\left(\left|\sum_{j=0}^n p_j z^j\right|^2 + \left|\sum_{j=0}^n q_j z^j\right|^2\right)}{\left(1+|z|^2\right)^n \left[\sqrt{\left(|w|^2 + \sum_{j=0}^n \left(\frac{|q_j|^2}{\binom{n}{j}} - \frac{|p_j|^2}{\binom{n}{j}}\right)\right)^2 + 4\left|\sum_{j=0}^n \frac{p_j q_j^*}{\binom{n}{j}}\right|^2} + |w|^2 + \sum_{j=0}^n \left(\frac{|q_j|^2}{\binom{n}{j}} + \frac{|p_j|^2}{\binom{n}{j}}\right)\right]} \tag{8.21}$$

first of all, we want to find the best probability of success for the same number of exploited qubits. We try to maximize the success probability as a function of $|w|^2$ since it is the only free parameter. With some calculation we can see that the success probability P_O is always a decreasing function in $|w|^2$ independently to the other parameters, so the maximum probability is reached for $|w|^2 = 0$ showing that the previous construction of the vectors $\left|v_{0/1}\right\rangle$ is not only the best in terms of basis vector used but also has the higher success probability. Hence the best success probability P_n for a given number of qubits n is

$$P_n = \frac{2\left(\left|\sum_{j=0}^n p_j z^j\right|^2 + \left|\sum_{j=0}^n q_j z^j\right|^2\right)}{\left(1+|z|^2\right)^n \left[\sqrt{\left(\sum_{j=0}^n \left(\frac{|q_j|^2}{\binom{n}{j}} - \frac{|p_j|^2}{\binom{n}{j}}\right)\right)^2 + 4\left|\sum_{j=0}^n \frac{p_j q_j^*}{\binom{n}{j}}\right|^2} + \sum_{j=0}^n \left(\frac{|q_j|^2}{\binom{n}{j}} + \frac{|p_j|^2}{\binom{n}{j}}\right)\right]} \tag{8.22}$$

The next step is to find the best success probability varying the number of qubits but this question is ill-posed since the comparison between the probabilities associated with a different number of qubits depends on the state therefore is necessary to know the probability distribution of the states that can be presented to the circuit. For example, we can consider the function $g(z) = 2z^2 + z$; if we assume that all the qubit states have the same probability to be presented to the circuit then the mean success probability is (see the appendix C for the explicit calculation):

$$< P_n >= \frac{n^2+7}{(n-1)n(n+1)\max\{1, \frac{n+7}{n(n-1)}\}} \qquad \begin{aligned} < P_2 > &= \frac{11}{27} = 0.407 \\ < P_3 > &= \frac{2}{5} = 0.400 \\ < P_4 > &= \frac{23}{60} = 0.383 \end{aligned} \tag{8.23}$$

where n is the number of qubits used by the circuit. It is possible to notice that in this case is not convenient to increase the number of qubits. Instead, if we consider that only the equatorial state (state in the form $(e^{i\phi}|0\rangle + |1\rangle)/\sqrt{2}$) can be presented with uniform probability then the mean success probability is:

$$< P_n >= \frac{6}{2^n \max\{1, \frac{n+7}{n(n-1)}\}} \qquad \begin{aligned} < P_2 > &= \frac{1}{3} = 0.333 \\ < P_3 > &= \frac{9}{20} = 0.450 \\ < P_4 > &= \frac{3}{8} = 0.375 \end{aligned} \tag{8.24}$$

In this case, is convenient to increase the number of qubits used compared to the strictly necessary ones.

With that consideration, we have completed the characterization of the Quantum to Quantum Bernoulli facotry problem. In particular, we have characterized the set of simulable functions by showing the most general possible circuit implementing a Bernoulli factory. In addition, a systematic procedure for constructing the quantum circuit related to a particular function was presented showing how the circuit is the most efficient in terms of qubits used and success probability.

8.3.2 Multivariate Quantum to Quantum Bernoulli factory

In the following, we present an extension of the Quantum to Quantum Bernoulli Factory problem taking into account the possibility to have more than one "hidden" state at the input of the circuit. This means that instead of having a state $|z\rangle$ we suppose to have a set of different states $\{|z_1\rangle, \dots |z_k\rangle\}$. Also, the function became a multivariate one $g(z_1, \dots z_k)$. We decided to baptize this new variant of the problem *Multivariate Quantum to Quantum Bernoulli factory* and we can try to characterize all the salient aspects of this new version as done previously for the original problem.

Following similar reasoning as used in the original problem, the more general circuit implementing the Multivariate Quantum to Quantum Bernoulli factory is the one presented in Fig. 8.3.

Continuing with the previous reasoning, it is plain to see that the constructible function $g(z_1, \dots z_k)$ is a subset of the set of functions $P(z_1, \dots z_k)/Q(z_1, \dots z_k)$ where $P(z_1, \dots z_k)$ and $Q(z_1, \dots z_k)$ are polynomials in all the variables $z_1, \dots z_k$.

Moreover, adapting the previous construction method, it is possible to show that for every function in the form $P(z_1, \dots z_k)/Q(z_1, \dots z_k)$ it is possible to construct a quantum circuit implementing the associated Multivariate Bernoulli factory. In addition, one can make the circuit use the minimum number of qubits for each variable that corresponds to the lower bound $n_j = \max\{deg_j(P), deg_j(Q)\}$, where $deg_j(P)$ is the degree of the polynomial P respect the variable z_j, and without the necessity of ancillary. The only exception in the possibility of not using ancillary qubits is when polynomials have degree 1 in all variables, in such a situation an ancillary qubit is needed.

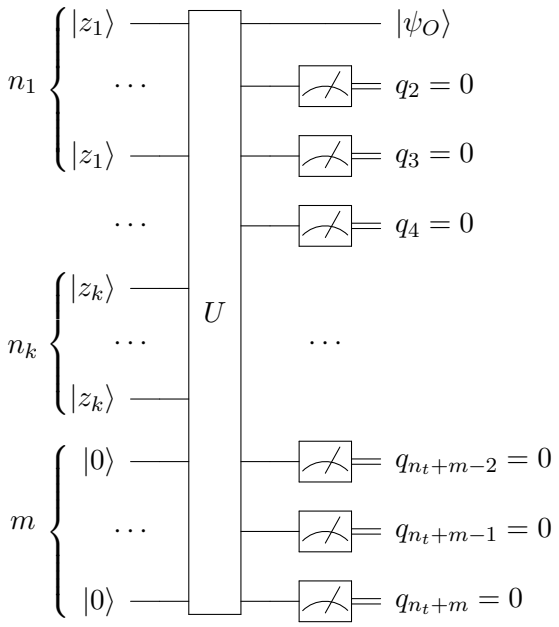

Figure 8.3. Multivariate Quantum to Quantum Bernoulli factory general circuit The circuit takes in input n_k qubits in the state $|z_k\rangle$ for a total of n_t and m ancillary qubits in the state $|0\rangle$. The state evolves through a unitary evolution U and then a measure in the computational basis is applied to all the qubits except the first one that carries the output state of the Bernoulli factory; the output $|\psi_O\rangle$ state is accepted if all the measures $q_2 \dots q_{n_t+m}$ return the result 0. This circuit can be considered the most general one since any other circuit implementing a Multivariate Quantum to Quantum Bernoulli factory can be mapped into one in the presented form with the same output state and the same success probability.

8.3.3 Multifunctional Quantum to Quantum Bernoulli factory

The idea for this second extension started from the consideration that the Quantum to Quantum Bernoulli factory is intrinsically probabilistic, i.e. that is necessary to post-select particular events to implement the desired output function. Extending the consideration, we can say that the Bernoulli factory implements a different function for each result of the measurement. Those considerations lead to the definition of a second extension of the Quantum to Quantum Bernoulli factory problem where we examine the possibility of implementing more than one function at the same time.

We define a *Multifunctional Quantum to Quantum Bernoulli factory* associated with a tuple of functions $(g_0, \dots g_k)$ a Quantum to Quantum Bernoulli factory implementing the functions $g_0, \dots g_k$ depending on the output of the measure. Below we consider only the simplest case of two functions but the analysis made can also be extended to the case involving more functions. From considerations similar

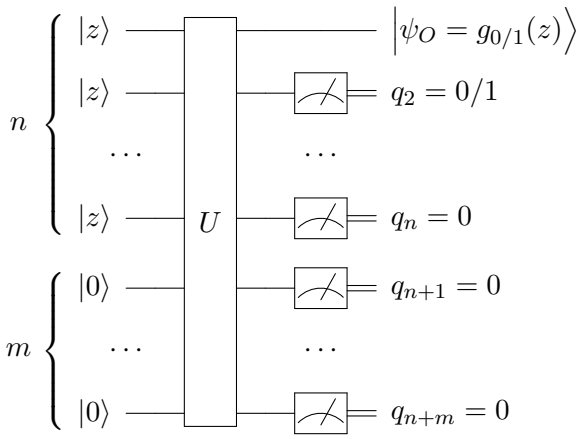

Figure 8.4. Multifunctional Quantum Bernoulli factory general circuit The circuit takes in input n qubit in the state $|z\rangle$ and m ancillary qubits in the state $|0\rangle$, making the resulting state evolve through a unitary evolution U and then a measure in the computational basis is applied to all the qubits except for the first one that carries the output state of the Bernoulli factory; the output $|\psi_O\rangle$ state is accepted if all the measures $q_3 \dots q_{n+m}$ return the result 0. The difference from the previous version is that if the measure q_2 returns 0 the circuit implements the function $g_0(z)$ if returns 1 the circuit implements the function $g_1(z)$. We can say that this circuit is the most general one since every circuit implementing a Multifunctional Quantum to Quantum Bernoulli factory can be mapped into one in the presented form with the same output state and the same success probability.

to those used for the base problem that all the hidden information is only in the input states, we can say that the most general quantum circuit implementing a Multifunctional Quantum to Quantum Bernoulli factory for two functions is the one depicted in Figure 8.4. The circuit is identical to the one implementing the Quantum to Quantum Bernoulli factory with the difference that the measure of the second qubit q_2 tells us if the circuit implements the function $g_0(z)$ or the function $g_1(z)$.

Given two simulable functions is always possible to construct a Multifunctional Quantum to Quantum Bernoulli factory. However, the success probabilities of individual functions will almost always turn out to be lower than the relative probabilities that the functions would have if they were implemented individually. With this consideration in mind, we want to propose a slightly different definition; in particular, we want to give a hierarchy to the functions, which means that we want to prioritize the success probability of some functions over others. In this context, we say that a function $g_1(z)$ is *compatible* with a function $g_0(z)$ if it is possible to implement a Multifunctional Quantum to Quantum Bernoulli factory where the success probability of the function $g_0(z)$ it is the same as when is implemented alone. To understand why we suggest this notion of compatibility we can take into consideration the following context: We suppose that to implement a particular

algorithm is necessary to perform two different Quantum Bernoulli factories with the same input states and respectively implement the functions $g_0(z)$ and $g_1(z)$. If the function $g_1(z)$ is compatible with the function $g_0(z)$ we can implement a Multivariate Quantum to Quantum Bernoulli factory without changing the success probability of the function $g_0(z)$ but with the addition that if the circuit returns a sample from the function $g_1(z)$ we can memorize the output state to be used in a second moment when is needed increasing the overall efficiency of the algorithm.

Defining $g_0(z) = P(z)/Q(z)$ and $g_1(z) = R(z)/S(z)$, the condition of compatibility of $g_1(z)$ respect $g_0(z)$ is equivalent to the following conditions:

$$\sum_j \left(\frac{p_j^*}{x} - \frac{q_j^*}{y}\right)\frac{r_j}{\binom{n}{j}} = 0 \qquad \sum_j \left(\frac{p_j^*}{x} - \frac{q_j^*}{y}\right)\frac{s_j}{\binom{n}{j}} = 0 \tag{8.25}$$

where p_j, q_j, r_j, s_j are the coefficients respectively of the polynomials $P(z)$, $Q(z)$, $R(z)$, $S(z)$ and x and y are the value defined by the equations Eq.(8.19) with $w = 0$. To prove the statement we want to show that if the two conditions are not satisfied then does not exist a unitary transformation implementing the circuit in Fig. 8.4.

Similar to the procedure used in Eq. (8.13)-(8.14), we call the first four rows of the unitary transformation as the covectors $\langle v_0|$, $\langle v_1|$, $\langle v_2|$ and $\langle v_3|$. The first two rows are fixed by the fact that we want the success probability of the function $g_0(z)$ does not to change compared to when it is implemented alone, so they are:

$$|v_0\rangle = \sum_{j=0}^{n} K\frac{p_j^*}{\sqrt{\binom{n}{j}}}\left|s_j^n\right\rangle + Kx\,|\theta_0\rangle \qquad |v_1\rangle = \sum_{j=0}^{n} K\frac{q_j^*}{\sqrt{\binom{n}{j}}}\left|s_j^n\right\rangle + Ky\,|\theta_0\rangle \tag{8.26}$$

where x, y and K are expressed in Eq. (8.19) with $w = 0$. The other two vectors can be expressed in the general form

$$\begin{aligned} |v_2\rangle &= \sum_{j=0}^{n} H\frac{r_j^*}{\sqrt{\binom{n}{j}}}\left|s_j^n\right\rangle + Ha_1\,|\theta_0\rangle + Ha_2\,|\theta_1\rangle \\ |v_3\rangle &= \sum_{j=0}^{n} H\frac{s_j^*}{\sqrt{\binom{n}{j}}}\left|s_j^n\right\rangle + Ha_3\,|\theta_0\rangle + Ha_4\,|\theta_1\rangle + Ha_5\,|\theta_2\rangle \end{aligned} \tag{8.27}$$

where H is the normalization factor and a_1, a_2, a_3, a_4 and a_5 are free parameters. To ensure that the four vectors represent four rows of a unitary transformation they must be orthonormal between each other, then in formulas:

$$\begin{gathered} \langle v_0|v_1\rangle = 0 \qquad \langle v_0|v_0\rangle = 1 \qquad \langle v_1|v_1\rangle = 1 \\ \langle v_0|v_2\rangle = 0 \qquad \langle v_1|v_2\rangle = 0 \qquad \langle v_0|v_3\rangle = 0 \qquad \langle v_1|v_3\rangle = 0 \\ \langle v_2|v_3\rangle = 0 \qquad \langle v_2|v_2\rangle = 1 \qquad \langle v_3|v_3\rangle = 1 \end{gathered} \tag{8.28}$$

The first three conditions are already satisfied. The next four are the critical ones since there are four equations and two free parameters. Exlicitating the first two conditions we obtain:

$$\langle v_0|v_2\rangle = 0 \Rightarrow \sum_j \frac{p_j r_j^*}{\binom{n}{j}} + x^* a_1 = 0 \qquad \langle v_1|v_2\rangle = 0 \Rightarrow \sum_j \frac{q_j r_j^*}{\binom{n}{j}} + y^* a_1 = 0 \tag{8.29}$$

But in order to exist a parameter a_1 that solves both the equations it is necessary that the first equation in Eq. (8.25) is satisfied; the other constraint descends from the second pair of conditions. If the Eq. (8.25) is satisfied then is possible to derive the value of a_1 and a_3. The last three conditions in Eq. (8.28) allow us to always derive the parameters a_2, a_4 and H; furthermore fixing the free parameter $a_5 = 0$ we can reach the maximum probability. With this, we have the first four rows of the unitary matrix U and completing to an orthonormal basis we can construct the circuit implementing the desired Multifunctional Quantum to Quantum Bernoulli factory.

In this way, we prove the necessity and sufficiency of the conditions in Eq. (8.25) to test if a function $g_1(z)$ is compatible with a function $g_0(z)$. Also, we explicitly construct a quantum circuit that implements the most efficient Multifunctional Quantum to Quantum Bernoulli factory associated with the functions.

8.4 Oracular to Quantum Bernoulli factory

In this last section, we present some results regarding the Oracular to Quantum Bernoulli factory problem [298]. In particular, we present the characterization of the set of simulable functions and also we provide an upper and a lower bound on the complexity of the problem.

First of all, let's recap the essential idea behind this particular type of Quantum Bernoulli factory. An Oracular to Quantum Bernoulli factory differs from a Quantum to Quantum Bernoulli factory since the hidden complex parameter $z \in \mathbb{C}$ is not encoded in a qubit but in an operator called *Oracle*. The oracle takes the form

$$\hat{Q}_z = \frac{1}{\sqrt{1+|z|^2}} \begin{pmatrix} z & -1 \\ 1 & z^* \end{pmatrix} \tag{8.30}$$

To characterize the set $\mathcal{S}$ of simulable factions by an Oracular to Quantum Bernoulli factory we provide a particular set of functions $\mathcal{M}$ and by showing the double inclusion we prove the equality between the two sets. First, we start to show that the set $\mathcal{M}$ of functions $g(z) = P(z, z^*)/Q(z, z^*)$, where $P(x, y)$ and $Q(x, y)$ are complex polynomials in two variable, is a subset of the simulable functions $\mathcal{S}$. We can use the oracle to generate qubits in the state $|z\rangle$ and $|z^*\rangle$ since $\hat{Q}_z |0\rangle = |z\rangle$ and $i\hat{Y}\hat{Q}_z |0\rangle = |z^*\rangle$. Then we use those qubits as inputs to a Multivariate Quantum to Quantum Bernoulli Factory to simulate a function exactly in the form $P(z, z^*)/Q(z, z^*)$. Now we want to demonstrate that the set of simulable functions $\mathcal{S}$ is a subset of $\mathcal{M}$. Defining $\mathcal{S}_n$ the set of functions simulable with n calls of the Oracle, then $\mathcal{S} = \bigcup_n \mathcal{S}_n$. If we show that $\forall n \mathcal{S}_n \subseteq \mathcal{M}$ then $\mathcal{S} \subseteq \mathcal{M}$. To demonstrate the statement we use the induction on n. The base case is simple; $\mathcal{S}_0 \subseteq \mathcal{M}$ is true since $\mathcal{S}_0$ is the set of the constant functions. Then the induction step, $\mathcal{S}_n \subseteq \mathcal{M}$ imply $\mathcal{S}_{n+1} \subseteq \mathcal{M}$. The demonstration uses the fact that just before measuring to obtain the final qubit the general state is in the form $|\psi\rangle = N \sum_j k_j(z, z^*) |j\rangle$ where $|j\rangle$ is a basis of a particular Hilbert space and $k_j(z, z^*)$ are polynomials in z and z^* of at most degree n and N is the normalization of the state. Now we can do three operations: adding a qubit but this does not change the polynomial nature

nor the degree of the coefficients $k_j(z, z^*)$. Applying a unitary transformation, but as in the previous case, the operation combines linearly the coefficients but does not change the polynomial nature nor the degree of the coefficients. Applying the oracle; like the unitary transformation case combines linearly the coefficients with the addition that they can also be multiplied by the coefficient z or z^* increasing the degree by one and translating it in the set $\mathcal{S}_{n+1}$. Finally, we can measure on the computational basis, this operation selects some of the components without changing them. Since none of these operations allows us to leave the set $\mathcal{M}$ if you start from $\mathcal{S}_n$, we demonstrate that $\mathcal{S} \subseteq \mathcal{M}$. Using the double inclusion we demonstrate that $\mathcal{S} = \mathcal{M}$.

Defining the complexity n of an Oracular to Quantum Bernoulli factory as the number of oracle calls we can provide some bound on it. Using the fact demonstrated previously, we can say that the minimum complexity n_m of an Oracular to Quantum Bernoulli factory implementing a function $g(z) = P(z, z^*)/Q(z, z^*)$ follow the bounds:

$$max\{n_z, n_{z^*}\} \leq n_m \leq n_z + n_{z^*} \tag{8.31}$$

where $n_z = \max\{deg_z(P), deg_z(Q)\}$ and $n_{z^*} = \max\{deg_{z^*}(P), deg_{z^*}(Q)\}$.

Some final considerations on the problem to mark the main differences of this version compared to the Quantum to Quantum one also in the light of the proofs made so far. The first one is that in therm of simulable functions the Oracle to Quantum Bernoulli factory is more powerful compared to the Quantum to Quantum Bernoulli factory, this advantage is given only by the definition of the oracle since gives access to the conjugate variable z^* that is not reachable with algebraic operation on the variable z. The second consideration is the complexity that is calculated on the number of times that the circuit gets access to the hidden variable. For the Oracular version, this is the number of times that the Oracular operator is interrogated but this does not tell any information on how much qubit is needed to implement the function. This means that also for the function that can be simulated by a Quantum to Quantum Bernoulli factory the number of Qubits required could be less for the Oracular to Quantum version compared to the Quantum to Quantum one, bringing advantage in terms of resources used but not in terms of complexity that have to be the same for the two version.

8.5 Conclusive Remarks

In this chapter, we have presented and analyzed the Quantum to Quantum Bernoulli factory problem from a theoretical point of view. We have demonstrated through a different approach the characterization of the set of simulable functions that have been found by the authors Jing et al. [18]. In contrast to the previous demonstration that exploits the field structure of the set, in this work we have used a constructive approach that allows us not only to characterize the set but also to analyse the computational complexity of the problem in terms of the qubits used and the probability of success of the protocol. In the first part of the demonstration, we have shown how any quantum circuit implementing a QQBF can be mapped to a canonical form shown in Fig. 8.2. Using those results, we provided a superset of the set of simulable functions and a lower bound on the number of qubits necessary

for a possible circuit to implement a given function. Finally, we have shown that the superset coincides with the set and that the bound on the number of qubits is tight by explicitly constructing, for each function in the superset, a quantum circuit using the minimum number of qubits provided by the bound. Also, for the proposed circuits, the success probability of the protocol is the maximum possible.

In addition to the analysis of the QQBF problem, two new variants called respectively Multivariate QQBF and Multifunctional QQBF were proposed and analysed. At the end, some remarks were made on the Oracular to Quantum Bernoulli factory problem providing bounds on the computational complexity of the problem and how it can be traced back to a Multivariate QQBF problem.

Statement of Work

All the results presented in the chapter, if not explicitly referred to the current literature, are my own work.

Chapter 9

Photonic Quantum to quantum Bernoulli factory

In the previous chapter, we described the Bernoulli factory problem and various quantum extensions. In particular, we analyse in detail the Quantum to quantum version, where both the input and the output of the algorithm are quantum states. We demonstrate various aspects of the computational complexity of the algorithm and propose some variants of the standard problem. All the demonstrations provided are based on the circuital model which is not a suitable computational paradigm to describe the action of a photonic interferometer. The question that we can ask is if the same characterization provided in the previous chapter remains valid also when the qubit input state is encoded in some degree of freedom of a photon and the manipulation is performed via linear optics. There are in literature previous attempts to implement a photonic Quantum to Quantum Bernoulli factory [20, 23] but, as we will later explain, both have theoretical problems that prevent the implementation of a general function. The important requirement for a correct implementation of a Bernoulli factory and that is missing in the proposed experiments is the lack of knowledge of the input states.

In this chapter, we present three interferometers that combined can implement every possible photonic Quantum to Quantum Bernoulli factory. In particular, we present two sets of interferometers for both polarization and dual-rail encoding. We characterize the action of the interferometers and how the action change with the indistinguishability of the input photons. We also experimentally implement the interferometers, using an integrated photonic platform, showing the effectiveness of the interferometers and the possibility to compose them. All the results presented in this chapter represent the results of an article in preparation and a pending patent.

9.1 Theory

In the previous chapter, we characterize the set of functions for which it is possible to implement the associated Quantum to Quantum Bernoulli factory by showing the general circuit and constructively characterizing which function can implement. In Ref. [18] Jiang et al. use a completely different approach to characterize the set of simulable functions, their idea is to prove that the set possesses a field structure

that is equivalent to our finding that the function has to be the ratio between two co-prime complex polynomials. This different characterization opens the way to a different strategy to characterize the set of simulable functions of a Photonic Quantum Bernoulli factory. If we prove that it is possible to construct three linear interferometers that implement the field operations then the set of simulable functions by a photonic Quantum to Quantum Bernoulli factory is equivalent to the set proven with the circuital formalism. The three operations that we need to implement are the sum, the product and the multiplicative inverse between states. The action of the operation on a generic state in the parameterization with complex numbers can be described in the following form:

- Sum: $|z_1\rangle |z_2\rangle \to |z_1 + z_2\rangle$
- Product: $|z_1\rangle |z_2\rangle \to |z_1 z_2\rangle$
- Inversion $|z\rangle \to |1/z\rangle$

In the following, we present and analyze the interferometers implementing the operations for bot polarization and dual-rail codification.

9.1.1 Implementation through polarization encoding

The polarization is the first degree of freedom that we propose since it is easy to manipulate and transmit, the downside is that it is difficult to work within an integrated device making it less appealing when the interferometer increase in dimension.

Inversion

The simplest operation to implement is the multiplicative inverse. To do it we swap $|H\rangle$ and $|V\rangle$.

$$|z\rangle = \frac{z|H\rangle + |V\rangle}{\sqrt{1+|z|^2}} \xrightarrow{\text{swap}} \frac{|H\rangle + z|V\rangle}{\sqrt{1+|z|^2}} = \frac{\frac{1}{z}|H\rangle + |V\rangle}{\sqrt{1+\left|\frac{1}{z}\right|^2}} = \left|\frac{1}{z}\right\rangle \tag{9.1}$$

This operation can be easily performed by exploiting a half wave-plate rotated by an angle of $\pi/4$ to the horizontal direction (See Fig. 9.1 a)

Product

The interferometer of Fig. 9.1 b can implement the product's operation between the state functions.

$$|z_1\rangle, |z_2\rangle \xrightarrow{\text{prod}} |z_1 z_2\rangle \tag{9.2}$$

Two photons will be making interact via a polarizing beam splitter. Working in post-selection we accept only the events in which the two photons exit from different outputs. After that, we apply a half-wave plate rotated by an angle of $\pi/8$ to the horizontal direction and we measure the polarization of the second photon; if the polarization is V(+ output) the output state is the product ($|z_1 z_2\rangle$) if the polarization

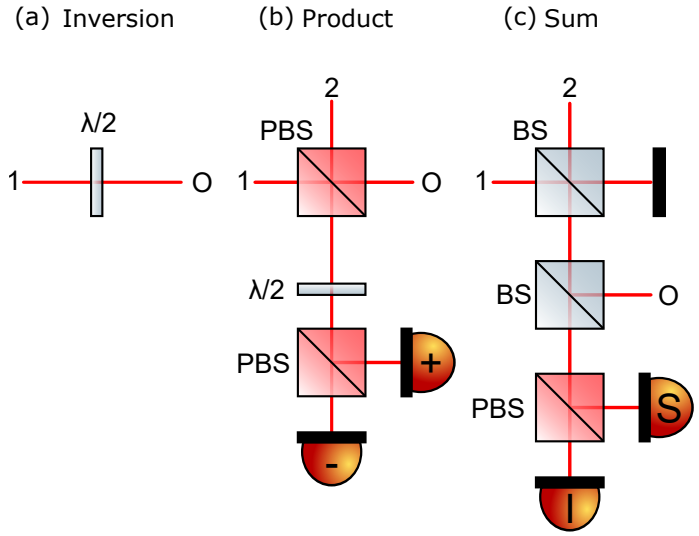

Figure 9.1. Building blocks for the polarization implementation. Interferometers that implement the basic operations to build a generic photonic quantum-to-quantum Bernoulli factory with polarization-encoded qubits. The inputs of the interferometers are labelled by numbers 1 and 2 and the outputs are labelled as O. **a) Inversion** Inversion is performed by mapping a half-wave plate with the axis at an angle of $\pi/4$ to the horizontal axis. **b) Product** product is performed by making two photons interact in a polarizing beam splitter and post-selecting the events where one photon came out for each port. Then on one of the outputs, a half-wave plate with the axis at an angle of $\pi/8$ to the horizontal axis is applied followed by a measure in the computational axis. Depending on the result of the measure the other photon is in the product or in the anti-product state. **c) Addition** Addition is performed by making two photons interact in a Beam splitter and post-selecting the events where the two photons came out from the same port. Then a second beam splitter is applied to separate the photons and one is measured. Depending on the result of the measure the other photon is in the sum or harmonic means state.

is H ($-$ output) the output state is the anti-product ($|-z_1 z_2\rangle$). Since the experiment is performed under post-selection conditions there is a success probability to perform the operation. The success probability of the product P_+ and of the anti-product P_- are

$$P_+ = P_- = \frac{1 + |z_1|^2 |z_2|^2}{2(1 + |z_1|^2)(1 + |z_2|^2)} \tag{9.3}$$

The probability of success is within the $[0, 0.5]$ and is not null everywhere except for the pair of states $(|0\rangle, |\infty\rangle)$ and $(|\infty\rangle, |0\rangle)$. These pairs have an associated complex value for which the product operation returns an indeterminate form.

In principle is also possible to recover the anti-product output by applying a π phase controlled by the "$-$ output" in order to correct the state by changing the phase.

Sum

The interferometer of Fig. 9.1-c is able to implement the operation of arithmetic mean between the state functions.

$$|z_1\rangle, |z_2\rangle \xrightarrow{\text{sum}} \left|\frac{z_1+z_2}{2}\right\rangle \tag{9.4}$$

Two photons enter into a beam splitter (BS), one for each input port. Working in post-selection we accept only the event in which the two photons exit from the same output. After that, we apply a second BS with the purpose of separating the two photons in different paths and we measure the polarization of one of the photons; if the polarization is V (S output) the output state is the arithmetic mean ($\left|\frac{z_1+z_2}{2}\right\rangle$) or if the polarization is H (I output) the output state is the harmonic mean ($\left|\frac{2z_1z_2}{z_1+z_2}\right\rangle$). The probability of the arithmetic mean P_S is

$$P_S = \frac{\left|\frac{z_1+z_2}{2}\right|^2 + 1}{4(1+|z_1|^2)(1+|z_2|^2)} \tag{9.5}$$

and probability of the harmonic mean P_I is

$$P_I = \frac{|z_1+z_2|^2 + |2z_1z_2|^2}{16(1+|z_1|^2)(1+|z_2|^2)} \tag{9.6}$$

Both the success probabilities within the range $[0, 0.25]$ and are not null everywhere except for the states $(|\infty\rangle, |\infty\rangle)$ and $(|0\rangle, |0\rangle)$ at the "S output" and "I output" respectively. These pairs have an associated complex value for which the arithmetic mean and the harmonic mean operations return an indeterminate form.

Partial distinguishability of the two photons

One of the experimental errors that can affect the interferometers is the partial distinguishability of the photons. If the two photons have other hidden degrees of freedom that we can not control then the two photons become partially distinguishable and the operations implemented by the interferometers are not perfect. It is possible to quantify the fidelity between the output mixed state and the expected state depending on the overlap V between the two photonic states. For this analysis, the inversion operation is not considered since is a single photon operation. For the interferometer implementing the product, the output density matrix and the fidelity between the output state compared to the indistinguishable case are:

- Product :

$$\rho_o = \begin{pmatrix} |z_1z_2|^2 & z_1z_2V \\ z_1^*z_2^*V & 1 \end{pmatrix} \frac{1}{1+|z_1z_2|^2} \qquad F = 1 - \frac{2|z_1z_2|^2}{(1+|z_1z_2|^2)^2}(1-V) \tag{9.7}$$

- Anti-product :

$$\rho_o = \begin{pmatrix} |z_1z_2|^2 & -z_1z_2V \\ -z_1^*z_2^*V & 1 \end{pmatrix} \frac{1}{1+|z_1z_2|^2} \qquad F = 1 - \frac{2|z_1z_2|^2}{(1+|z_1z_2|^2)^2}(1-V) \tag{9.8}$$

For the interferometer implementing the sum operation, the output density matrix and the fidelity compared to the indistinguishable case are:

- arithmetic mean:

$$\rho_o = \frac{\begin{pmatrix} |z_1+z_2|^2-(z_1z_2^*+z_1^*z_2)(1-V) & (1+V)(z_1+z_2) \\ (1+V)(z_1^*+z_2^*) & 2(1+V) \end{pmatrix}}{|z_1+z_2|^2-(z_1z_2^*+z_1^*z_2)(1-V)+2(1+V)} \tag{9.9}$$

$$F = 1-\frac{2|z_1-z_2|^2}{\Big[|z_1+z_2|^2-(z_1z_2^*+z_1^*z_2)(1-V)+2(1+V)\Big](|z_1+z_2|^2+4)}(1-V) \tag{9.10}$$

- Harmonic mean:

$$\rho_o = \frac{\begin{pmatrix} 2(1+V)|z_1z_2|^2 & (1+V)z_1z_2(z_1^*+z_2^*) \\ (1+V)z_1^*z_2^*(z_1+z_2) & |z_1+z_2|^2-(z_1z_2^*+z_1^*z_2)(1-V) \end{pmatrix}}{|z_1+z_2|^2-(z_1z_2^*+z_1^*z_2)(1-V)+2(1+V)|z_1z|^2} \tag{9.11}$$

$$F = 1-\frac{2|z_1-z_2|^2|z_1z_2|^2}{\Big[|z_1+z_2|^2-(z_1z_2^*+z_1^*z_2)(1-V)+2(1+V)|z_1z_2|^2\Big](|z_1+z_2|^2+4|z_1z_2|^2)}(1-V) \tag{9.12}$$

9.1.2 Implementation through dual-rail encoding

The second degree of freedom considered in this chapter is the dual-rail codification. This degree of freedom is particularly suitable when using integrated optics, making it easier to implement larger interferometers. However, it has the problem of being difficult to transmit but as we seen in precedence (See Ch. 2) it is quite easy to convert the dual rail codification in the polarization codification and vice-versa solving also this issue.

Inversion

To implement the multiplicative inverse we can use the same idea presented in the previous section. Practically the operation is implemented by exchanging the waveguides in the interferometer (See Fig. 9.2-a).

Product

The interferometer of Fig. 9.2-b is able to implement the product operation between two state functions. Two photons are inserted in the interferometer, where the waveguides representing respectively the states $|1\rangle_1$ and $|0\rangle_2$ of the two dual-rail qubits are taken to a balanced beam splitter, with measurement of the output. The final state of the remaining two waveguides, after compensating a $\pi/2$ relative phase

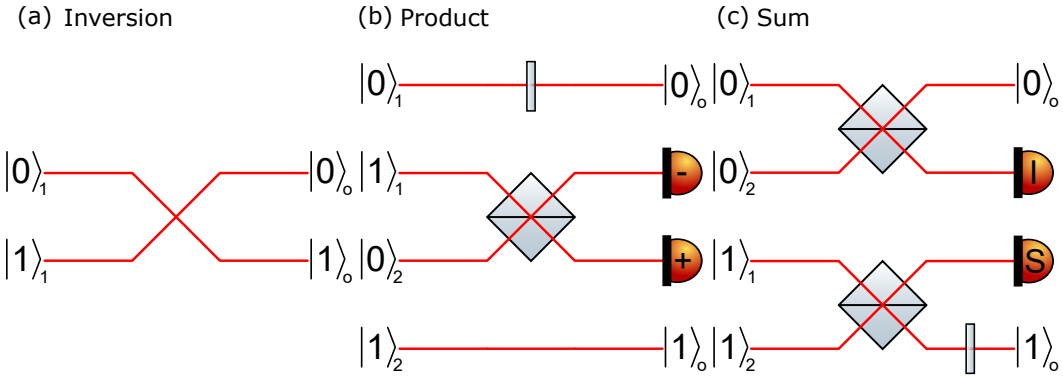

Figure 9.2. Building blocks for the dual-rail implementation. Interferometers that implement the basic operations to build a generic quantum-to-quantum Bernoulli factory with dual-rail encoded qubits. The inputs of the interferometers are labelled by numbers 1 and 2 and the outputs are labelled as O. **a) Inversion** is performed by swapping the dual-rail waveguides. **b) Product** is performed by sending one waveguide from each dual rail qubit ($|1\rangle_1$ and $|0\rangle_2$) into a balanced beam splitter, measuring the outgoing modes. Upon detection of a single photon, the output state is the product of the two input states except for a global phase. **c) Addition** is implemented by directing the waveguides representing the same state of the two qubits to equally unbalanced beam splitters, measuring one output mode for each beam splitter. If only one photon is detected, and this is found in the "S" detector, the output state is the sum of the input states (up to a global phase).

between them, and conditioned on the presence of a single photon in one of the two outputs of the beam-splitter, is:

$$|z_1 z_2\rangle_o = \frac{\pm z_1 z_2 |0\rangle_o + |1\rangle_o}{\sqrt{1 + |z_1 z_2|^2}} \tag{9.13}$$

where the $+/-$ sign depends on which detector clicks. Since the experiment is performed under post-selection, the probability of the product P_+ and anti-product P_- are given by:

$$P_+ = P_- = \frac{1 + |z_1|^2 |z_2|^2}{2(1 + |z_1|^2)(1 + |z_2|^2)}$$

The probability of success is within the range $[0, 0.5]$ and is not null everywhere except for the pair of states $(|0\rangle, |\infty\rangle)$ and $(|\infty\rangle, |0\rangle)$. These pairs have an associated complex value for which the product operation returns an indeterminate form.

Sum

The interferometer of Fig. 9.2-c is able to implement the sum operation between two state functions. Two photons are inserted in the interferometer and two identical beam splitters are used to couple the pairs of waveguides representing the same state ($|0\rangle_1$ with $|0\rangle_2$ and $|1\rangle_1$ with $|1\rangle_2$). After the mixing process, one output port of each beam-splitter is measured. Conditioned to the detection of only one photon at the "S output", the sum operation is performed and the state after compensation

of a relative phase is:

$$|S\rangle_o = \frac{(z_1 + z_2)\frac{\sqrt{RT}}{R-T}|0\rangle_o + |1\rangle_o}{c} \tag{9.14}$$

where R and T are the reflectivity and transmissivity of the beam splitters and c is the normalization factor. Conversely, if the photon is detected on the "I output", the harmonic mean operation is performed and the corresponding state is:

$$|I\rangle_o = \frac{-\frac{z_1 z_2}{z_1+z_2}\frac{R-T}{\sqrt{RT}}|0\rangle_o + |1\rangle_o}{c} \tag{9.15}$$

The numerical multiplicative factor can be chosen in $\mathbb{R}$, and can be set to 1 when the reflectivity of both beam splitters is $R = \frac{5+\sqrt{5}}{10}$. The probability of a single photon detected at S is:

$$P_S = \frac{|z_1 + z_2|^2 R(1-R) + (2R-1)^2}{(1+|z_1|^2)(1+|z_2|^2)} \tag{9.16}$$

while the probability of a single photon detected at P is:

$$P_I = \frac{|z_1 + z_2|^2 R(1-R) + |z_1 z_2|^2 (2R-1)^2}{(1+|z_1|^2)(1+|z_2|^2)} \tag{9.17}$$

The success probability is not null everywhere except for the states $(|\infty\rangle, |\infty\rangle)$ and $(|0\rangle, |0\rangle)$ at the "S output" and "I output" respectively. These pairs have an associated complex value for which the sum and the harmonic mean operations return an indeterminate form.

If we use the value of reflectivity $R = \frac{5+\sqrt{5}}{10}$ that erases the numerical multiplicative factor then the probabilities are

$$P_S = \frac{|z_1 + z_2|^2 + 1}{5(1+|z_1|^2)(1+|z_2|^2)} \qquad P_I = \frac{|z_1 + z_2|^2 + |z_1 z_2|^2}{5(1+|z_1|^2)(1+|z_2|^2)} \tag{9.18}$$

Partial distinguishability of the two photons

As done for the previous set we characterize the interferometers when partially distinguishable photons are presented at the inputs. For the interferometer implementing the product, the output density matrix and the fidelity between the output state compared to the indistinguishable case are:

- Product :

$$\rho_o = \begin{pmatrix} |z_1 z_2|^2 & z_1 z_2 V \\ z_1^* z_2^* V & 1 \end{pmatrix} \frac{1}{1+|z_1 z_2|^2} \qquad F = 1 - \frac{2|z_1 z_2|^2}{(1+|z_1 z_2|^2)^2}(1-V) \tag{9.19}$$

- Anti-product :

$$\rho_o = \begin{pmatrix} |z_1 z_2|^2 & -z_1 z_2 V \\ -z_1^* z_2^* V & 1 \end{pmatrix} \frac{1}{1+|z_1 z_2|^2} \qquad F = 1 - \frac{2|z_1 z_2|^2}{(1+|z_1 z_2|^2)^2}(1-V) \tag{9.20}$$

For the interferometer implementing the sum operation the output density matrix and the fidelity compared to the indistinguishable case are:

- Sum:

$$\rho_S = \frac{\begin{pmatrix} RT|z_1+z_2|^2 - RT(z_1z_2^* + z_1^*z_2)(1-C_I) & \sqrt{RT}(R-T)(z_1+z_2) + \sqrt{RT}(Tz_2 - Rz_1)(1-C_I) \\ \sqrt{RT}(R-T)(z_1^*+z_2^*) + \sqrt{RT}(Tz_2^* - Rz_1^*)(1-C_I) & (R-T)^2 + 2RT(1-C_I) \end{pmatrix}}{RT|z_1+z_2|^2 + (R-T)^2 + RT(2 - z_1z_2^* - z_1^*z_2)(1-C_I)} \tag{9.21}$$

$$F_s = 1 - \frac{2RT|Rz_1+Tz_2|^2}{\left[RT|z_1+z_2|^2 + (R-T)^2 + RT(2 - z_1z_2^* - z_1^*z_2)(1-C_I)\right]\left[RT|z_1+z_2|^2 + (R-T)^2\right]}(1-C_I) \tag{9.22}$$

- Harmonic mean:

$$\rho_I = \frac{\begin{pmatrix} |z_1z_2|^2(R-T)^2 + |z_1z_2|^2 2RT(1-C_I) & \sqrt{RT}(T-R)(|z_1|^2z_2 + z_1|z_2|^2) + \sqrt{RT}(R|z_1|^2z_2 - Tz_1|z_2|^2)(1-C_I) \\ \sqrt{RT}(T-R)(|z_1|^2z_2^* + z_1^*|z_2|^2) + \sqrt{RT}(R|z_1|^2z_2^* - Tz_1^*|z_2|^2)(1-C_I) & RT|z_1+z_2|^2 - RT(z_1z_2^* + z_1^*z_2)(1-C_I) \end{pmatrix}}{|z_1z_2|^2(R-T)^2 + RT|z_1+z_2|^2 + RT(2|z_1z_2|^2 - z_1z_2^* - z_1^*z_2)(1-C_I)} \tag{9.23}$$

$$F_I = 1 - \frac{2RT|Rz_1+Tz_2|^2|z_1z_2|^2}{\left[|z_1z_2|^2(R-T)^2 + RT|z_1+z_2|^2 + RT(2|z_1z_2|^2 - z_1z_2^* - z_1^*z_2)(1-C_I)\right]\left[|z_1z_2|^2(R-T)^2 + RT|z_1+z_2|^2\right]}(1-C_I) \tag{9.24}$$

9.2 Previous experimental implementations

In the literature, there are two previous attempts to implement a photonic Quantum to Quantum Bernoulli factory performed by Zhan et al. [23] and Liu et al. [20]. Both works follow the same procedure as ours by proposing three interferometers that implement the operations of a field on quantum states, however for different reasons, both have theoretical problems that prevent the implementation of a general function.

For the codification of the two qubits at the input of the operation, Zhan et al. [23] use the polarization for one qubit and the dual-rail for the second. Then a set of waveplate and Calcite Beam Displacers are used to perform the operations. At the end of the operation, the resulting qubit is encoded in the polarization of the outgoing photon. Problems arise when we want to concatenate the operations. They propose to apply a calcite beam Displacers to convert the polarization to the dual-rail encoding and then use a set of waveplates to restore the polarization qubit to its starting state. However, in order to programme the waveplates, it is necessary to know the desired state and this goes against the Bernoulli factory's assumption of ignorance of the input state. This problem affects the possibility of concatenating the interferometers and therefore the possibility of constructing functions more complex than the basic operations.

In the experimental realization of Liu et al. [20] exploited entangled photons for the generation of the building blocks. Each photon generated by the entangled source feeds a displaced Sagnac interferometer and the input state is constructed with a series of waveplates. This implementation presents the same problem as the

previous one of having to know the input state in order to programme the waveplates appropriately. Furthermore, the article does not specify at all how the operations can be concatenated.

9.3 Experimental apparatus

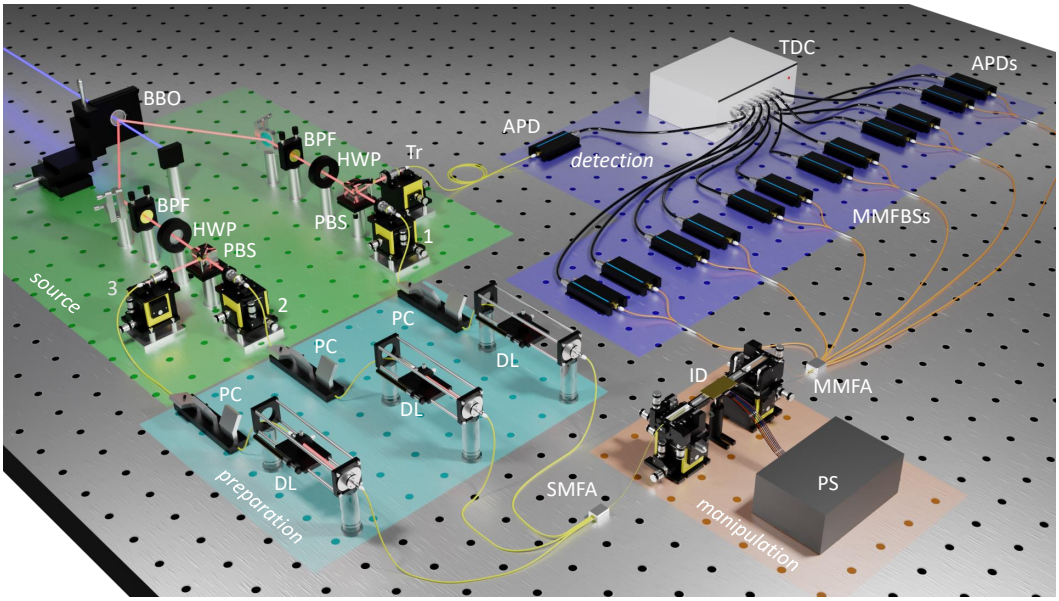

Figure 9.3. Scheme of the experimental apparatus. One and two pairs of photons are generated in a Beta Barium Borate crystal (BBO). The photons are filtered with a band-pass Filter (BPF) and divided into four different spatial modes using half wave-plates (HWP) and polarizing beam splitters (PBS). After coupling the photons in four single-mode fibers, the polarization and the time-arrival of the photons are compensated via Polarization controllers (PC) and delay lines (DL) so that the photons are made indistinguishable. Three of the four photons are injected into the chip, while the remaining one is used as a trigger (Tr). Each output of the chip is connected to an approximate number-resolving detector, consisting of six in-fiber beam splitters (MMFBS) and two single-photon avalanche-photodiode detectors (APD) for each MMFBS. All the detectors are connected to a time-to-digital converter for the reconstruction of the output probability. **Legend:** BBO - beta-barium borate crystal, BPF - band-pass filter, HWP - half-wave plate, PBS - polarizing beam splitter, PC - polarization controller, DL - delay line, PS - power supply, ID- integrated photonic circuit, MMFBS - multimode fiber beam splitter, APD - Single-photon avalanche diode detector, TDC - time-to-digital converter.

To experimentally implement and certify the correctness of our Bernoulli factory, we have employed the setup depicted in Fig. 9.3. In the preparation stage, we generate two pairs of photons which are deterministically separated in four different paths by using half-wave plates and polarizing beam splitters before coupling into single-mode fibers. One photon is detected by an avalanche photodiode hence acting as a trigger. The other three photons are sent through different paths, each of them composed of a polarization controller and a delay line to make them indistinguishable

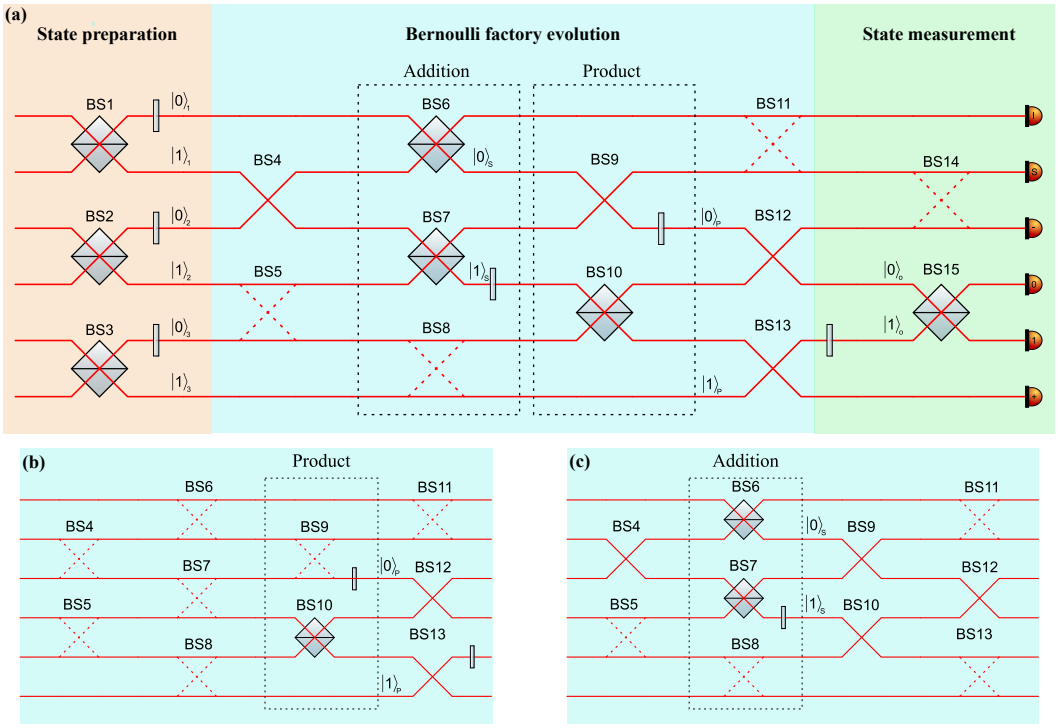

Figure 9.4. Circuital representation of the chip implementing a complete Bernoulli factory and the product/addition building blocks. In **(a)** is depicted the concatenation of the state preparation, the Bernoulli factory evolution and the state tomography. Beamsplitter BS5, BS8, BS11 and BS14 are represented with dotted lines since their reflectivity are set to 1; the reflectivity of beam splitters BS4, BS9, BS12, BS13 are set to 0 while BS6, BS7 and BS10 reflectivity are tuned opportunely to implement the desired operation. BS1, BS2, BS3 and BS15 are controlled during the experiment to generate the input state and reconstruct the output state. In **(b)** we represent only the internal evolution for the characterization of the product, while in **(c)** we depict the configuration for the characterization of the addition building block.

in the polarization and time-arrival degrees of freedom. The photons are then injected into the integrated photonic device, which is a six-mode fully reconfigurable chip able to: 1) prepare the input states, 2) implement a complete set of building block operations for the Bernoulli Factory and 3) perform state tomography and/or fidelity measurement. In the following, we explain each process within the integrated device. In Fig. 9.4 we have depicted a detailed construction of the chip, where it is possible to identify the three main stages.

State preparation: In the state preparation stage, six different paths are mixed in pairs by using three different beam splitters (BS). For each BS a phase shifter is placed in one of the two output ports. This configuration allows the preparation of a generic input state in dual-rail encoding (See Ch. 2).

Bernoulli factory evolution: In the second stage of the device, the reflectivity of the beam splitters and the phase shifters are appropriately tuned to implement the desired operation. In particular, the scheme of Fig. 9.4 a represents the implementation of an addition followed by a product operation, while panels b and c represent the optical elements required for the implementation of each operation individually.

Note that the addition operation is similar but not equal to the one represented in Fig. 9.2 c, since the first two waveguides are exchanged. This change is inserted to reduce the number of layers required for the concatenation of two operations and is implemented by replacing the reflectivity of BS6 with its complement, thus making BS6 and BS7 complementary.

State measurement: The final stage performs the necessary operations to characterize the output state. The system can be employed to perform both state tomography and direct measurement of the fidelity with respect to a target state. Tomography is composed of a series of operations allowing the correct identification of the state. In particular, the output probabilities are measured for three different projective measurements made on mutually orthogonal bases to reconstruct the output state. If one is only interested in the fidelity with respect to a target state, it is enough to make a projective measurement on the basis composed of the desired state and its orthogonal subspace (See Ch. 2). The detection stage is composed of six in-fiber beam splitters, one for each output, and twelve single-photon avalanche photodiodes that implement a probabilistic photon-number resolving detector used for the tomographic measurement and to estimate the success probability of the Bernoulli factory itself.

9.4 Experimental results

9.4.1 Experimental test of the operations

In the first part of the experiment, we characterize separately the set-ups implementing each field operation. To this end, we tune the internal phases of the chip implementing the desired operation. This is performed by controlling the current inside the heaters placed on the surface of the chip. In Fig. 9.4 a we show the complete process of a Bernoulli factory starting from the "state preparation" up to the "state tomography" process which is required for the final certification. By directly reconfiguring the circuit operation, it is possible to implement and characterize single building block operations. Fig. 9.4 b shows the internal configuration of the chip to characterize the product operation for which the input state is controlled by BS2 and BS3, and in which one photon each is placed, while for the addition building block depicted in Fig. 9.4 c the involved beam splitters are BS1 and BS2.
To test the single operations we generate a set of random states $(|z_1\rangle, |z_2\rangle)$ sampled by a uniform distribution on the Bloch's sphere. Each pair of states is generated in the state preparation stage by setting the phase and the reflectivity of the first layer of the interferometer. Then, the output is validated by measuring the success probability and the fidelity compared to the expected output state. The figure of merit in this case is provided by the mean fidelity over the set of sampled states. All results are summarized in Table 9.1 and Fig. 9.5.

9.4.2 Experimental concatenation of the operations

In the second part of the experiment, we demonstrate the modularity of our scheme by showing the possibility of concatenating single operations. This aspect is necessary to fulfil all requirements for the implementation of a complete Bernoulli

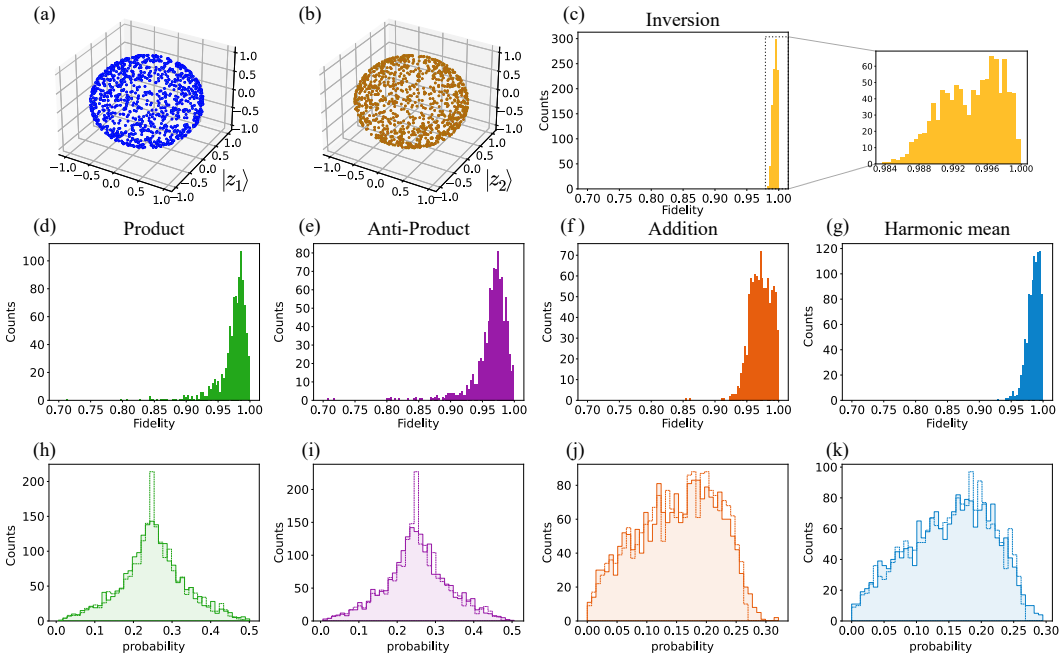

Figure 9.5. Experimental Results. Characterization of the building blocks is performed by generating a set of 1000 pairs of random state (z_1, z_2) sampled uniformly from the Bloch sphere. (a) Sampled states $|z_1\rangle$ and in (b) sample states for $|z_2\rangle$. The fidelity of the output state after the evolution is measured by projection with the target state. In panels (c-g) we report the distribution of the measured fidelities for each operation. Conversely, in panels (h-k) we compare the distribution of the success probability for each operation (solid lines) with the corresponding theoretical expectations (dashed lines).

Operation	Measured mean Fidelity	Corrected mean Fidelity
Inversion	0.989 ± 0.003	1.000 ± 0.003
Product	0.95 ± 0.02	0.99 ± 0.02
Anti-Product	0.95 ± 0.03	0.99 ± 0.02
Sum	0.90 ± 0.05	0.99 ± 0.02
Harmonic mean	0.92 ± 0.05	0.99 ± 0.02

Table 9.1. Results of the characterization for the two-photon operations. The mean fidelity is estimated by taking an average over an ensemble of 1000 pairs of state sampled uniformly from the Block sphere. The Measured mean fidelity is estimated directly from the data. Instead, the Corrected one takes into account the contribution from dark counts and accidental coincidences subtracting them from the measured coincidence.

factory. To test the concatenation we tune the internal phases of the chip in order to implement the desired sequence of operations, as shown in Fig. 9.4 (a). In this case, three photons are required to perform the sequence of two operations, i.e., addition followed by a product. The first two photons, impinging respectively in BS1 and BS2, are prepared to act as the input of the addition. The third photon impinging on BS3, together with the output one from the first operation, is the input of the product operation. Finally, the output is validated by direct projection over the target state in the final stage of the device, in order to measure the output fidelity. To test the correctness of the concatenation, we measure the output fidelity for a particular set of input states. All the results are summarized in Table 9.2a where F_C is fidelity measured experimentally when dark count and spurious coincidence are subtracted, and F_D is the theoretical fidelity calculated taking into account the partial distinguishability between the input photons. Additionally, by exchanging the order of the operations (sum and product) and by properly tuning the phase shifters a different circuit can be obtained. All the results are summarized in Table 9.2b.

9.5 Conclusive remarks

In this chapter, we analyse the Quantum to Quantum Bernoulli factory problem from a photonic point of view. In particular, it was shown that the use of photons and linear optics to transport and manipulate quantum information presents no limitations to the implementation of a QQBF protocol. To do so, three interferometers implementing the operations of sum, product and multiplicative inverse have been proposed which, combined with the field structure of the set of simulable functions, prove the possibility of implementing a generic Quantum to Quantum Bernoulli factory in the photonic paradigm. We built and analysed the interferometers for both polarization encoding (more suitable for implementation with bulk optics) and dual-rail encoding (more suitable for implementation with integrated photonics). In addition, the proposed interferometers were implemented and tested in a reconfigurable integrated photonic device, showing the correctness of the theoretical analysis and the possibility that they can be combined to create more complex functions. These results thus highlight that the photonic quantum to quantum

Input (z_1, z_2, z_3)	**Output** $z_1 z_2 + z_3$	**Corrected Fidelity** F_C	**Theoretical Fidelity** F_D
$(0, 0, 0)$	0	0.993 ± 0.005	1
$(\infty, \infty, 0)$	∞	0.993 ± 0.005	1
$(1, 1, 0)$	1	0.95 ± 0.02	0.96 ± 0.01
$(0, 0, 1)$	1	0.80 ± 0.02	0.79 ± 0.05
$(1, 1, 1)$	2	0.93 ± 0.01	0.92 ± 0.03

(a) product-sum

Input (z_1, z_2, z_3)	**Output** $(z_1 + z_2) z_3$	**Corrected Fidelity** F_C	**Theoretical Fidelity** F_D
$(0, 0, 1)$	0	0.98 ± 0.01	1
$(\infty, 0, 1)$	∞	1 ± 0.01	1
$(1, 0, 1)$	1	0.87 ± 0.02	0.88 ± 0.02
$(0, 1, 1)$	1	0.88 ± 0.02	0.88 ± 0.02
$(1, 1, 1)$	2	0.85 ± 0.02	0.88 ± 0.02

(b) sum-product

Table 9.2. Concatenation characterization. F_C is the fidelity measured at the output of the chip when the dark counts and the spurious coincidences are subtracted; F_D is the theoretical fidelity calculated by taking into account the partial distinguishability of the input photons.

Bernoulli factories can become a promising tool for new quantum protocols [299].

Statement of Work

The theoretical work presented in the chapter was developed by myself with a correctness revision by L. Castello and E. Galvão. The experimental realization, data taking and analysis were carried out by myself with the help of T. Giordani. The photonic chip used was realized in the laboratories of Professor R. Osellame with the help of A. Crespi.

Part V

Quantum Metrology

Chapter 10

Quantum metrology

One of the fundamental pillars of science is the measurement process. The objective of a measurement is to assign a value to a physical quantity by providing an estimate of it. Each experimentally measured value has an uncertainty which, according to the ISO definition, is the "parameter, associated with the result of a measurement that characterizes the dispersion of the values that could reasonably be attributed to the measured quantity" [300]. The causes of such uncertainty can be either technical or intrinsic. Errors of a technical nature are related to the experimental realization of the measurement and the uncontrollable imperfections of the apparatus involved. On the contrary, there are fundamental limits to uncertainty, such as those due to Heisenberg inequality, imposed by physical laws.

Metrology is that branch of science that studies, on the one hand, the application of statistics to give a mathematical foundation to the concept of error in measurement and, on the other hand, the techniques and technologies required to achieve the most accurate measurement possible. In this field, it has been demonstrated how the use of quantum systems leads to an advantage in terms of the precision of the measurements that can be made over an agent that only has access to classical resources. This consideration has led to the development of a new branch called *Quantum Metrology*, which aims to study how some features of quantum mechanics, e.g. entanglement, allow to reach an actual metrological advantage and the limits imposed by the theory itself on the precision of the measurements that can be done.

In this chapter, we are going to present the main concepts and theoretical results of quantum metrology theory. In particular, in the first part, we are going to describe the main characteristics of a generic measurement process and the associated theoretical results. Then, we will describe the quantum generalization of the classical results with emphasis on the application of the theory to the phase estimation problem. Finally, we will present two of the main estimation techniques used in both classical and quantum metrology and which are the foundation of most of the measurement protocols in the literature.

10.1 Estimation process

Given a physical system parametrized by a parameter λ, an estimation process aims to reconstruct the actual value of the parameter implemented by the physical

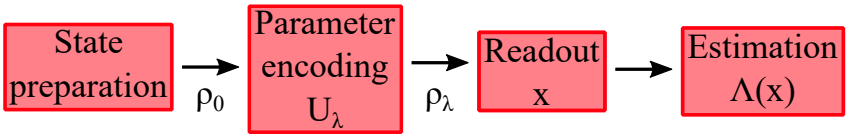

Figure 10.1. Schematic representation of an estimation process. A probe is prepared in the state ρ_0. An interaction is made with the system under investigation mediated by a unitary matrix U_λ. The resulting state ρ_λ is measured generating the outcome x. Finally an estimator $\Lambda(\vec{x})$ is applied to the results of the measurement providing an estimate of the value of the parameter λ.

apparatus under investigation. A generic estimation process can be schematized and divided into four steps (as represented in Fig. 10.1):

I) *Probe preparation*: A probe system is prepared in the state ρ_0 normally chosen to extract as much information as possible from the system.

II) *Encoding*: The prepared state is made to interact with the system under consideration through a unitary evolution U_λ so that in the resulting state $\rho_\lambda = U_\lambda \rho_0 U_\lambda^\dagger$ is encoded the information about the parameter λ. More generally, it is possible to consider the interaction through a non-unitary channel but the results do not change.

III) *Readout*: To extract the information encoded in the state ρ_λ a measurement is performed on the state. As done for the probe state, the measurement can be optimized to extract the maximum information about the parameter to be estimated.

IV) *Estimation*: An estimator $\Lambda(\vec{x})$, i.e. a function of measurement results $\vec{x}$, is used to reconstruct the value of the variable under consideration.

To increase the accuracy of the measurement the previous procedure described above is repeated ν times and an appropriate estimator that takes into account all results is employed.

Now we are going to present some definitions taken from statistics that are particularly useful in metrology. An estimator is defined *consistent* if it converges to the true value as the number of measurements made increases.

$$\lim_{\nu\to\infty} \Lambda(\vec{x}) = \lambda \qquad \forall\lambda \tag{10.1}$$

Moreover, an estimator is *unbiased* if its mean coincides with the true value for all possible values of the parameter

$$\bar{\Lambda} := \sum_{\vec{x}} P(\vec{x}|\lambda)\Lambda(\vec{x}) = \lambda \qquad \forall\lambda \tag{10.2}$$

where $P(\vec{x}|\lambda)$ is the conditional probability to obtain a list of measurement outcomes $\vec{x}$ given a certain value of the parameter of interest λ. This probability is also called *likelihood* and depends on both the probe state and the measurement. If we assume that the considered system does not have memory and therefore the ν measurements are independent, then the likelihood can be decomposed as $P(\vec{x}|\lambda) =$

$\prod_{i=1}^{\nu} P(x_i|\lambda)$. Although it is always desirable to find an unbiased estimator this is not always possible, to remedy the problem we will go on to define two other possible properties that are less stringent. An estimator is called *locally unbiased* if it is unbiased only for certain ranges of parameter values. Furthermore, an estimator is asymptotically unbiased if the mean converges to the true value for an infinite number of measurements $\lim_{\nu\to\infty} \bar{\Lambda} = \lambda \quad \forall\lambda$.

One of the most widely used estimators is the *maximum likelihood estimator* (MLE) [301] which is the parameter value that maximizes the likelihood probability for a certain list of experimental results:

$$\Lambda_{\text{MLE}}(\vec{x}) = \arg\max_{\lambda} P(\vec{x}|\lambda) \tag{10.3}$$

The MLE is a consistent asymptotically unbiased estimator and saturates the ultimate precision limit we see in the next section. Other estimators can be used like the Method of moments [302] (that do not require the knowledge of the likelihood) or the Bayesian estimator.

Given a particular estimation process, we want to quantify its accuracy. To do so, we define the *mean square error* as

$$\text{MSE}(\lambda) = \sum_{\vec{x}} P(\vec{x}|\lambda)(\Lambda(\vec{x}) - \lambda)^2 \tag{10.4}$$

Since normally this quantity is experimentally inaccessible we define a similar quantity called *variance* as

$$\Delta\lambda^2 = \sum_{\vec{x}} P(\vec{x}|\lambda)(\Lambda(\vec{x}) - \bar{\Lambda})^2 \tag{10.5}$$

that for unbiased estimators is equal to the mean square error.

10.1.1 Classical bounds

In the estimation scenario described above, we can consider the first case of classical resources. Since no quantum operations are allowed we can suppose that both the probe state and the measurements are fixed. To study the bounds of the estimation uncertainty we need to introduce a fundamental quantity F called *Fisher Information*. This quantity makes it possible to assess the amount of information encoded in the likelihood of the estimation process and it is defined as:

$$F(\lambda) = \sum_{\vec{x}} P(\vec{x}|\lambda)\left(\frac{\partial \ln(P(\vec{x}|\lambda))}{\partial\lambda}\right)^2 = \sum_{\vec{x}} \frac{1}{P(\vec{x}|\lambda)}\left(\frac{\partial P(\vec{x}|\lambda)}{\partial\lambda}\right)^2 \tag{10.6}$$

The fisher information is related to the probe state and the measure by the relation

$$F(\lambda) = \sum_{x} \frac{\text{Re}\{\text{Tr}[\rho_\lambda \Pi_x L_{\rho_\lambda}]\}^2}{\text{Tr}\{\Pi_x \rho_\lambda\}} \tag{10.7}$$

Where Π_x is the projector associated with the measurement result x and L_{ρ_λ} is a self-adjoint operator called *symmetric logarithmic derivative* (SLD) operator that is defined as the operator with the property

$$\frac{\partial\rho_\lambda}{\partial\lambda} = \frac{\rho_\lambda L_{\rho_\lambda} + L_{\rho_\lambda}\rho_\lambda}{2} \tag{10.8}$$

The Fisher information has the following properties [302, 303]: *Additivity*, given ν independent estimation processes applied on the same system, the total Fisher information $F_{\text{tot}}(\lambda)$ is the sum of the Fisher information of the individual processes $F_i(\lambda)$, i.e. $F_{\text{tot}}(\lambda) = \sum_i F_i(\lambda)$; *Convexity*, given as probe state a convex combination of density matrices $\rho_0 = \sum_j c_j \rho_j$ with $\sum_j c_j = 1$ and a constant measure than the Fisher information is less than the convex sum of those of the individual density matrices, i.e. $F_{\rho_0}(\lambda) \leq \sum_j c_j F_{\rho_j}(\lambda)$.

The Fisher information is related to the amount of information that can be extracted from a system by a fundamental inequality called *Cramér-Rao bound* (CRB). This result provides a lower bound on the variance of any arbitrary estimator with fixed measurements and a constant number of probes ν [304, 305]. Mathematically can be expressed as

$$\Delta\lambda^2 \geq \frac{1}{F(\lambda)} \frac{\partial \bar{\Lambda}}{\partial \lambda} \tag{10.9}$$

which restricted to unbiased estimators becomes

$$\Delta\lambda^2 \geq \frac{1}{F(\lambda)} \tag{10.10}$$

An estimator is defined *efficient* if it saturates such an inequality. Asymptotically the maximum likelihood estimator is efficient [306]. In the case of a limited number of measurements, the saturation of the bound is no more guaranteed and we enter in the so-called *limited data regime*.

10.1.2 Quantum Fisher information and quantum Cramér-Rao bound

Until now we have considered the scenario where both the probe state and the measurements are fixed and we saw the bounds on the variance optimized for the best possible estimator. Now, we will also admit the possibility of changing the measures made on the system as well. Given a fixed probe state ρ_0 and therefore an evolved state ρ_λ one can maximize the Fisher information over all the possible measurements performed on the state ρ_λ. We define this maximum as the *Quantum Fisher Information* (QFI) $F_Q(\lambda)$.

$$F_Q(\lambda) = \max_{\{\Pi_x\}} F(\lambda) \tag{10.11}$$

Like the classical version, the Quantum Fisher Information follows as well the property of additivity and convexity. By definition $F(\lambda) \leq F_Q(\lambda)$ and the CRB can be also extended to its quantum version i.e. the quantum Cramér-Rao bound (CRB):

$$\Delta\lambda^2 \geq \frac{1}{\nu F_Q(\lambda)} \tag{10.12}$$

The QCRB represents the ultimate bound on the variance that can be achieved by using a particular probe state as an input.

As done previously for the Fisher information we can associate the QFI to the SLD operator L_{ρ_λ} by the following relation [307–309]

$$F_Q(\lambda) = (\Delta L_{\rho_\lambda})^2 = \text{Tr}\left(\rho_\lambda L_{\rho_\lambda}^2\right) \tag{10.13}$$

where $(\Delta L_{\rho_\lambda})^2$ is the variance of the SLD operator over the state ρ_λ. Writing the state in the diagonal basis $\rho_\lambda = \sum_j p_j \, |\psi_j\rangle\langle\psi_j|$ then the QFI can be explicitly written as [310]

$$F_Q(\lambda) = 2\sum_{j,k} \frac{|\langle\psi_j|\partial_\lambda \rho_\lambda|\psi_k\rangle|^2}{p_j + p_k} = \sum_j \frac{(\partial_\lambda p_i)^2}{p_i} + 2\sum_{j\neq k} \frac{(p_j - p_k)^2}{p_j + p_k} |\langle\psi_j|\partial_\lambda \psi_k\rangle|^2 \quad (10.14)$$

In many scenarios, the parameter we want to estimate is the strength of the interaction term between the probe and the system under investigation or equivalently the interaction time. We can write the evolved state as $\rho_\lambda = e^{-i\lambda H}\rho_0 e^{i\lambda H}$, or equivalently $\partial_\lambda \rho_\lambda = i[\rho_\lambda, H]$, where H is the Hamiltonian of the interaction. In this particular case, the QFI does not depend on the unknown parameter and can be expressed as a function of the initial state ρ_0 and the Hamiltonian H. Given $\rho_0 = \sum_j p_j \, |\xi_j\rangle\langle\xi_j|$ then the F_Q is

$$F_Q = 2\sum_{j,k} \frac{(p_j - p_k)^2}{p_j + p_k} |\langle\xi_j|H|\xi_k\rangle|^2 \quad (10.15)$$

If the probe state is pure $\rho_0 = |\xi_0\rangle\langle\xi_0|$ is further simplified and becomes four times the variance of the hamiltonian computed on the initial state [45]:

$$F_Q = 4\Delta^2 H \quad (10.16)$$

To better understand the meaning of the Quantum Fisher information we want to show that it is related to how much the states are distinguishable as the parameter λ varies [311]. We can quantify the distance between two states ρ_1 and ρ_2 with the Bures distance defined as $D(\rho_1, \rho_2) = \sqrt{1 - \tilde{F}(\rho_1, \rho_2)}$ where $\tilde{F}(\rho_1, \rho_2)$ is the Uhlmann's fidelity defined in Eq. 1.45. Given the state ρ_λ and a small change in the parameter $\delta \ll 1$ then the distance between the perturbed state $\rho_{\lambda+\delta}$ and the original one ρ_λ is proportional to $F_Q(\lambda)$ [312].

$$D(\rho_\lambda, \rho_{\lambda+\delta}) = \frac{1}{8} F_Q(\lambda)\delta^2 \quad (10.17)$$

This relation tells us that the more the stats $\rho_{\lambda+\delta}$ and ρ_λ are distinguishable the greater is the QFI.

To complete the discussion, it is necessary to find the measure saturating the QCRB for a given probe state. This involves finding the measure for which the classical Fisher information and quantum one coincide. Due to the additivity property, to saturate the bound we can use local measurements for each probe without the need of resorting to entangling measurements [313–317]. It can be shown [310] how the optimal measure it is always a projective measure and is given by the observable

$$\hat{O}_\lambda = \lambda \mathbb{I} + \frac{L_{\rho_\lambda}}{F_Q(\lambda)} \quad (10.18)$$

this means that the best measure is performed on the eigenbasis of the SLD operator. By putting together the observable $\hat{O}$ with the estimators found in the previous paragraph, it is possible to create an estimation process that saturates the QCRB.

In general, the optimal operator depends on the parameter under consideration. This dependence is a major problem since it is necessary to know the value of the parameter in advance in order to estimate it. This issue means that it is generally not possible to saturate the limit. However, it is possible to reach the bound in the asymptotic limit through the use of adaptive algorithms as described below.

10.1.3 Standard quantum limit and Heisenberg limit

As a final step, we analyze the optimization of the estimation process over the possible input states. This optimization can be done by maximizing the QFI over all the initial probe states. In contrast to the previous results without knowing exactly the nature of the interaction, it is not possible to optimize the Fisher information on the input state. However, for the convexity property of the Fisher information, the maximum is reached always for probs in a pure state.

For the estimation of the time interaction generated by the unitary evolution $U_\lambda = e^{i\lambda H}$ the Quantum fisher information is maximized by a probe in the state

$$|\xi_S\rangle = \frac{|h_M\rangle + e^{i\chi}|h_m\rangle}{\sqrt{2}} \tag{10.19}$$

where $|h_M\rangle$ and $|h_m\rangle$ are the eigenstates of the hamiltonian with respectively maximum and minimum eigenvalues h_M and h_M. The corresponding QFI is

$$F_Q = (h_M - h_m)^2 \tag{10.20}$$

In general, indicating the optimal Quantum Fisher information as F_Q^{max} the related CRB is:

$$\Delta^2\lambda \geq \frac{1}{\nu F_Q^{max}} \tag{10.21}$$

As we can see until now, the variance scales as $1/\nu$, where ν is the number of probes used for the estimation. This scaling is called *Standard Quantum Limit* (SQL) or also *Shot Noise Limit*.

The estimation strategies analyzed so far are not the most general possible ones that a quantum agent can perform. Fig. 10.2 shows a so-called parallel strategy in which probes are grouped into clusters of m elements and a global state is prepared. After the interaction of each probe with the system under test, they are measured separately and the results are used to estimate the parameter under test. If the input state is entangled then it is possible to overcome the SQL [45, 313, 318–321].

If as before we consider the interaction time estimation problem where instead of using the input state $|\xi_S\rangle$ we replace it with the state of m probes

$$|\xi_E\rangle = \frac{|h_M\rangle^{\otimes m} + e^{i\chi}|h_m\rangle^{\otimes m}}{\sqrt{2}} \tag{10.22}$$

that is a maximally entangled state in the NOON form. For such state $\Delta^2 H = m^2(h_M - h_m)^2/4$ and so the corresponding Fisher information is $F = m^2(h_M - h_m)^2$. For ν indipendent set the CRB became

$$\Delta^2\lambda \geq \frac{1}{\nu m^2(h_M - h_m)^2} \tag{10.23}$$

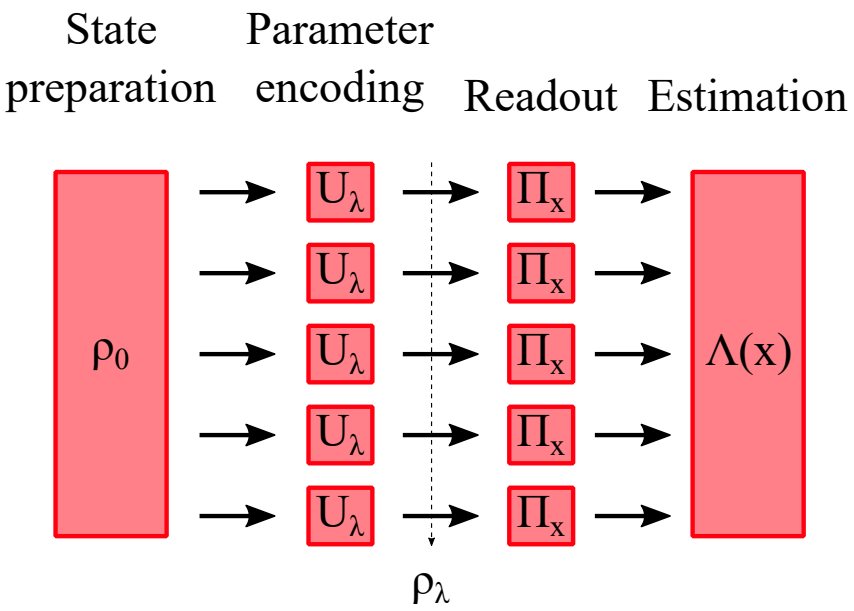

Figure 10.2. Conceptual scheme of a parallel estimation process. A parallel estimation process groups the probes into clusters of m elemnts (in figure five) and with each of them creates a global state, eventually entangled. Then each probe is made to interact independently with the system under test through the same evolution U_λ. Finally, each probe is measured and the results are used to estimate the parameter through an appropriate estimator. In this representation, only separable measurements are considered because it can be shown that entangled measurements do not perform better than separable ones.

As can be seen, there is a quadratic improvement in the scaling of the variance as a function of the number of probes used (which is νm). This improvement is called the *Heisemberg limit* (HL) and is the ultimate limit that can be reached by the variance while remaining within the limits of quantum mechanics. The fundamental role of entanglement for quantum gain is evidenced by the fact that the SQL violation is a sufficient condition for certifying the presence of entanglement in the probe state [322, 323].

It is important to note that we derived HL scaling and its relationship to entanglement for the case of the parallel estimation strategy with a linear interaction and where the number of probes in the system was used as a resource. For example, it is possible to achieve the HL without the use of entangled states through the use of multi-pass protocols, i.e. protocols in which the probe state is made to interact several times with the system under investigation [324–326].

10.2 Multiparameter quantum metrology

More generally, a physical system can have more than one parameter to measure. One may ask whether, as in the single-parameter case, the use of quantum resources improves the performance of an estimation process on a system with more than one parameter. This and other questions opened the way for the field of *quantum multi-parameter metrology* [327]. The generalization of quantum metrology to the multi-

parameter case results in a more complicated field and adherence to experimental reality [328–333]. A first approach to multi-parameter metrology is to estimate each variable separately, but sometimes a simultaneous measurement is necessary. The main reasons for using multi-parameter metrology are that: simultaneous parameter estimation can be more efficient in terms of resources used compared to the separate estimation case. Furthermore, in certain cases, even if there is a single parameter to be estimated, it is also necessary to measure other related ones such as experimental noise or possible imperfections in the apparatus.

We can consider a multiparameter estimation process where a set of d unknown parameters $\vec{\lambda} = (\lambda_1, \lambda_2, \ldots, \lambda_d)$ are estimated through as many estimators $\vec{\Lambda} = (\Lambda_1, \Lambda_2, \ldots, \Lambda_d)$. In this scenario, the Fisher information is generalized through the use of a Fisher Information matrix $\mathbb{F}$:

$$\mathbb{F}(\vec{\lambda})_{ij} = \sum_{\vec{x}} \frac{1}{P(\vec{x}|\vec{\lambda})} \frac{\partial P(\vec{x}|\vec{\lambda})}{\partial \lambda_i} \frac{\partial P(\vec{x}|\vec{\lambda})}{\partial \lambda_j} \tag{10.24}$$

Also, the sensitivity of the set of estimators is evaluated with the covariance matrix defined as:

$$C(\vec{\lambda})_{ij} = \sum_{\vec{x}} [\vec{\Lambda}(\vec{x}) - \vec{\lambda}]_i \, [\vec{\Lambda}(\vec{x}) - \vec{\lambda}]_j \, P(\vec{x}|\vec{\lambda}) \tag{10.25}$$

For unbiased estimators, the CRB becomes a matrix inequality in the form: [1]

$$C(\vec{\lambda}) \geq \frac{\mathbb{F}(\vec{\lambda})^{-1}}{\nu} \tag{10.26}$$

with ν the number of measures performed. The CRB is well-defined only when the Fisher information $\mathbb{F}$ is invertible. In that case, the CRB can always be saturated by the maximum likelihood estimator in the limit of large ν.

As done previously, it is possible to define a Quantum Fisher information matrix $(\mathbb{F}_Q(\vec{\lambda}))$ where one has optimized the Fisher information matrix over the possible measurements made on the probe state. The resulting expression is in the form:

$$\mathbb{F}_Q(\vec{\lambda})_{ij} = \mathrm{Tr}\left[\rho_{\vec{\lambda}} \frac{L_i L_j + L_j L_i}{2}\right] \tag{10.27}$$

where L_i is the symmetric logarithmic derivative operator of $\rho_{\vec{\lambda}}$ related to the parameter λ_i, defined by the property

$$\frac{\partial \rho_{\vec{\lambda}}}{\partial \lambda_i} = \frac{L_i \rho_{\vec{\lambda}} + \rho_{\vec{\lambda}} L_i}{2} \tag{10.28}$$

The corresponding QCRB is

$$C(\vec{\lambda}) \geq \frac{\mathbb{F}_Q(\vec{\lambda})^{-1}}{\nu} \tag{10.29}$$

To evaluate the precision of a multiparameter estimation process we can use the trace of the covariance matrix

$$\sum_j \Delta^2 \Lambda_j = \mathrm{Tr}[C(\lambda)] \geq \frac{Tr[\mathbb{F}_Q(\vec{\lambda})^{-1}]}{\nu} \tag{10.30}$$

[1] Given two positive semidefinite matrices A and B we say that $A \geq B$ if $A - B$ is a positive semi-definite matrix.

If we consider a pure state as a probe $\rho_{\vec{\lambda}} = \left|\psi_{\vec{\lambda}}\right\rangle\!\left\langle\psi_{\vec{\lambda}}\right|$, then the Quantum Fisher information can be expressed as

$$\mathbb{F}_Q(\vec{\lambda})_{ij} = 4\,\mathrm{Re}[\left\langle\partial_{\lambda_i}\psi_{\vec{\lambda}}\middle|\partial_{\lambda_j}\psi_{\vec{\lambda}}\right\rangle] + 4\left\langle\partial_{\lambda_i}\psi_{\vec{\lambda}}\middle|\psi_{\vec{\lambda}}\right\rangle\left\langle\partial_{\lambda_j}\psi_{\vec{\lambda}}\middle|\psi_{\vec{\lambda}}\right\rangle \tag{10.31}$$

In order to find the best possible accuracy on the estimation it is necessary to find necessary and sufficient conditions to saturate the QCRB but for the multiparameter case is not guaranteed that those conditions can be satisfied [334, 335]. A necessary condition for the saturability of the CRB is the condition

$$\forall i,j \quad Tr[\rho_{\vec{\lambda}}\,[L_i, L_j]] = 0 \tag{10.32}$$

which corresponds to saying that the optimal measurements for each parameter taken individually are compatible with each other. In the case of pure states, the symmetric logarithmic derivative operators can be expressed as

$$L_i = 2\left(\left|\partial_{\lambda_i}\psi_{\vec{\lambda}}\right\rangle\!\left\langle\psi_{\vec{\lambda}}\right| + \left|\psi_{\vec{\lambda}}\right\rangle\!\left\langle\partial_{\lambda_i}\psi_{\vec{\lambda}}\right|\right) \tag{10.33}$$

and, if the Quantum Fisher information is invertible, a necessary and sufficient condition for the saturation of the CRB is

$$\forall i,j \quad \mathrm{Im}[\,\langle L_i L_j|\psi_{\vec{\lambda}}|L_i L_j\rangle] = 0 \tag{10.34}$$

As in the case of single-parameter estimation, the Quantum Fisher information matrix is correlated with the state distance for small variations in the parameters considered. Indeed, the following inequality is valid

$$D(\rho_{\vec{\lambda}}, \rho_{\vec{\lambda}+\vec{\delta}}) = \frac{1}{8}\sum_{i,j}\mathbb{F}_Q(\vec{\lambda})_{ij}\delta_i\delta_j \tag{10.35}$$

where D is the Bures distance defined previously.

10.3 Phase estimation problem

One of the most studied applications of quantum metrology is the problem of phase estimation since many quantum parameter estimation problems can be traced back to this type of problem. A non-exhaustive list of such applications includes sensing on biological systems [336], atomic properties [337, 338], atomic clocks [339, 340], measurements of forces [341–343] and imaging [344–346].

The problem consists in estimating a phase difference φ between two different modes of the degree of freedom under consideration such as polarization, or paths. The unitary evolution associated with a phase shift can be written as

$$U_{ps} = e^{i\varphi H_{ps}} = e^{i\varphi\hat{n}} \tag{10.36}$$

Where $\hat{n}$ is the number operator associated with the degree of freedom under consideration and is the Hamiltonian that mediates the evolution. The maximum difference between the eigenvalues for a single probe is $h_M - h_m = 1$ so the Quantum fisher information is $F_Q = 1$.

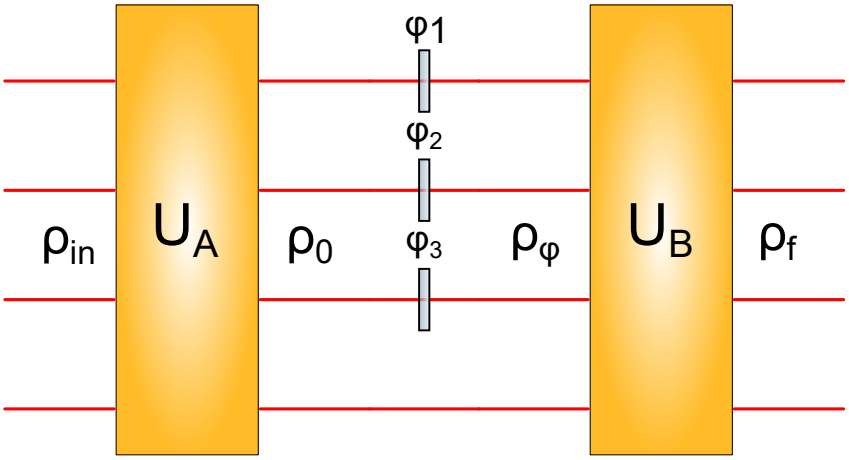

Figure 10.3. Multiphase estimation Interferometer. General scheme for the Multiphase estimation of d phases (in this example 3). A state ρ_{in}, typically a Fock state, is placed at the input of an interferometer with $d+1$ modes. A first interferometer that implements the unitary transformation U_A is used to generate the probe state ρ_0. After the encoding of the phases $\vec{\varphi}$ a second interferometer implementing a unitary transformation, U_B is applied to generate the final state ρ_f. This state is measured, typically on the Fock basis, and the result is used for the estimation of the phases $\vec{\varphi}$.

Since a definition of an observable associated with a phase still remain an open problem [347, 348] a direct measure is infeasible. However, it is possible to measure a phase difference through other observables that depend on it. In optics, a phase shift is measured through interferometric measurements. The most simple two-mode interferometer is the Mach-Zehnder interferometer (described in Chapter 2) thus representing the most common test platform used to test quantum metrology algorithms proposed in the literature.

10.3.1 Multiphase estimation problem

The multiphase estimation problem is the multiparameter extension of the phase estimation problem and consists of the evaluation of d different phases $\vec{\varphi} = (\varphi_1, \varphi_2, \dots \varphi_d)$ using an interferometer with $d+1$ modes. The typical structure of the interferometer used is shown in Fig. 10.3. A photonic state ρ_{in}, typically in a Fock state, is placed at the input of an interferometer implementing a unitary transformation U_A resulting in the creation of the probe state ρ_0. After the encoding of the phases in the state a second interferometer is applied, implementing the unitary evolution U_B, to generate the final state ρ_f which will subsequently be measured in the Fock basis.

In the case of multiphase estimation with pure states the evolved state can be written as $|\psi_{\vec{\varphi}}\rangle = U_{\vec{\varphi}}|\psi_0\rangle$ with $U_{\vec{\varphi}} = e^{i\sum_j \varphi_j \hat{n}_j}$. since the number operators on different modes commute $[\hat{n}_i, \hat{n}_j] = 0$, the QFI takes the form

$$\mathbb{F}_Q(\vec{\varphi})_{ij} = 4(\langle \hat{n}_i \hat{n}_j \rangle - \langle \hat{n}_i \rangle \langle \hat{n}_j \rangle) \tag{10.37}$$

where the expectation value is computed on to the state $|\psi_{\vec{\varphi}}\rangle$. If we compute the component of the Quantum Fisher information matrix related to a particular phase

we retrieve the same results as for the single-parameter case.

$$\mathbb{F}_Q(\varphi_i) = \mathbb{F}_Q(\vec{\varphi})_{ii} = 4\left\langle \Delta^2 \hat{n} \right\rangle \tag{10.38}$$

One of the first studies on multiphase estimation was provided in Ref. [349]. The authors consider probe states with a fixed number of photons N and show that the simultaneous estimation of the phases provides an improvement of a d factor in the scaling of the variance compared to the best quantum strategy that estimates the phases individually. They found that the optimal probe state with N photons is

$$|\psi_0\rangle_{opt} = \frac{|N0\ldots00\rangle + |0N\ldots00\rangle + \cdots + |00\ldots N0\rangle}{\sqrt{d+\sqrt{d}}} + \sqrt{\frac{\sqrt{d}}{d+\sqrt{d}}}\,|00\ldots0N\rangle \tag{10.39}$$

such an optimal state gives us a total variance of

$$\mathrm{Tr}\left[\mathbb{F}_Q(\vec{\varphi})^{-1}\right] = \frac{(1+\sqrt{d})^2 d}{4N^2} \tag{10.40}$$

instead, the best single-stage strategy returns a total variance of

$$\mathrm{Tr}\left[\mathbb{F}_Q(\vec{\varphi})^{-1}\right] = \frac{d^3}{4N^2} \tag{10.41}$$

Similar improvements were also found in the case of simultaneous phase estimation with non-commuting generators, for example in the simultaneous estimation of the components of a magnetic field [350], or in the presence of moderate amounts of noise [334].

10.4 Estimation protocols

In both classical and quantum metrology, there are various estimation protocols that can be applied. Below we report two protocols that are commonly used and form the basis of most of the approaches used in the literature.

10.4.1 Bayesian estimation

The Bayesian approach is a natural paradigm for implementing an estimation protocol [351,352]. In this framework, the unknown parameter λ and the experimental results x are treated as random variables and the degree of knowledge of the parameter is updated according to the measurement results. Formally the degree of knowledge on the parameter is encoded in a probability distribution $P(\lambda)$ called *prior distribution*. The experimental setup performing the measure on the system under examination is described by the likelihood distribution $P(x|\lambda)$. Once a measurement result x is recorded, the prior distribution is updated in the *positrior ditribution* $P(\lambda|x)$ according the Bayes' rule:

$$P(\lambda|x) = \frac{P(\lambda)P(x|\lambda)}{\int \mathrm{d}\lambda\, P(\lambda)P(x|\lambda)} \tag{10.42}$$

The posterior distribution contains the updated information from which all the interested quantities can be calculated. For example the mean square error of an estimator $\Lambda(x)$ averaged over the parameter λ is

$$\left\langle \Delta^2 \Lambda \right\rangle = \int \mathrm{d}\lambda \mathrm{d}x \, P(\lambda) P(x|\lambda) (\Lambda(x) - \lambda)^2 \tag{10.43}$$

and minimizing the expression over all the possible estimators we can find the optimal one Λ_{opt} which turns out to be the mean value of the variable calculated on the posterior distribution

$$\Lambda_{opt} = \int \mathrm{d}\lambda \, \lambda P(\lambda|x) \tag{10.44}$$

That optimal estimator is called *bayesian estimator* and is an unbiased asymptotically efficient estimator [353].

If we consider the case where the variables to be estimated are phases, then it is necessary to implement some modifications to account for their periodicity ($\varphi \simeq \varphi + 2k\pi \quad k \in \mathbb{Z}$). For this parameter, the canonical means is replaced by the circular mean defined as

$$\langle \varphi \rangle = \arg \left[\int \mathrm{d}\varphi \, e^{i\varphi} P(\varphi|x) \right] \tag{10.45}$$

In addition, the canonical variance expression is also replaced with the circular counterpart called *Holevo variance* V_H defined from the quantity S called *Sharpness* [354].

$$V_H = S^{-2} - 1 \qquad S = \left| \left\langle e^{i\varphi} \right\rangle \right| \tag{10.46}$$

The Holevo variance can describe the variance of an unbiased phase estimator and coincide with the standard variance for distribution sufficiently picked. Instead for biased estimators, the variance needs to be calculated as

$$V_B = S_b^{-2} - 1 \qquad S_b = |\langle \cos(\Phi - \varphi) \rangle| \tag{10.47}$$

One of the fundamental features of the bayesian approach is the possibility to be easily incorporated into adaptive protocols as we will see in the next section.

10.4.2 Adaptive protocols

Previously, it was seen that the optimal measure to saturate the CRB typically depends on the real value of the variable we are trying to estimate. Various adaptive protocols have been proposed in the literature that attempts to circumvent this problem [355–359]. In a non-adaptive protocol, the probes are sent through a fixed apparatus, and after collecting all the measurement results, an estimation of the unknown parameter λ is obtained. In contrast, adaptive protocols exploit additional controls on the experimental system, through a set of control parameters $\vec{\theta}$ that can be adjusted during the estimation process.

An adaptive protocol can be schematized as in Fig. 10.4 and consists of a four-step cycle repeated until the desired number of probes is reached. As a starting point a state $\rho_0(\theta)$ is generated through the parameter θ computed from the results of the previous cycle, if it is the first one then the starting state is ρ_{in}. After that,

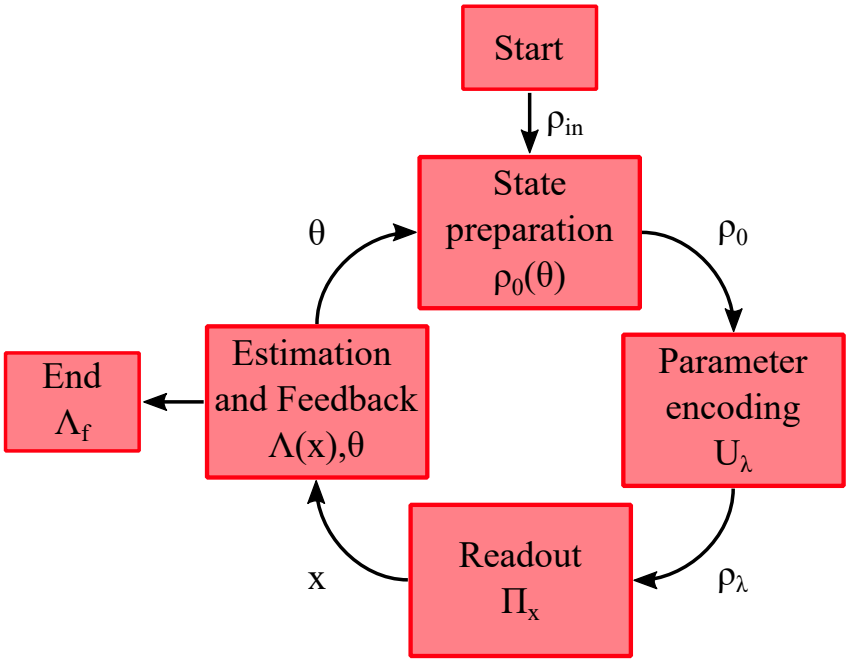

Figure 10.4. Conceptual scheme of an adaptive estimation protocol. The cycle of a general adaptive estimation protocol starts from an initial state ρ_{in} that is prepared in a state $\rho_0(\theta)$. Such a state interacts with the unknown parameter λ, and then the output state ρ_λ undergoes an appropriately chosen measurement Π_x. After such measurement, the results x are used to generate an estimation $\Lambda(x)$ and to define a suitable control parameter setting θ, employed to prepare the initial state of the next probe. In this way, the cycle is repeated for all the probes. At the end of the process, an estimator provides the final estimate of the parameter Λ_f.

the probe interacts with the system under exam through the unitary evolution U_λ. The resulting state ρ_λ is measured and the outcome x is recorded. The final step is the processing of the measure and the calculation of the control parameter θ to be used in the next iteration. The cycle continues until the number of desired probes is reached, and finally, an estimator of all the results is applied to generate the final estimation of the parameter Λ_f.

Adaptive protocols are useful to overcome different issues of the theory and they were initially proposed in [355]. As mentioned above, the first application is the possibility of saturating the CRB. Since in general, to implement the optimal measurement, it is necessary to know a priori the value of the variable to be estimated, a saturation of the bound with a non-adaptive algorithm is impossible. On the contrary, with an adaptive algorithm, it is possible to adjust the measurement according to the parameter estimate made from time to time thus saturating the CRB asymptotically [360]. A different problem is that in some cases, even if the optimal measurement does not depend on the value of the parameter to be estimated, it is computationally infeasible to implement. In these cases, the adaptive approach makes it possible to construct approximations of the measurement that solve the problem [361]. Also, for some likelihood, the same probability distribution of the result can be associated with different values of the parameter. For example in a

Mach-Zehnder interferometer probed with a single photon the output probability $P = \cos^2(\phi)$ is associated with two different values of the parameter. In those cases, it is impossible to discern the ambiguity. Conversely, if the measurement is allowed to be adapted, in the case of the Mach-Zehnder by adding a second controllable phase within the interferometer, the ambiguity can be overcome. A final application of adaptive strategies is the possibility of making the estimation procedure more resilient to noise or changes over time of the variable under investigation [362, 363].

To finish the discussion on adaptive estimation protocols, it is necessary to mention that they can be classified into two large families. *Online scheme:* At each step of the estimation the feedback parameters θ are calculated according to a heuristic and the results of the previous measurements. In this class, we can mention the Bayesian adaptive protocols, indeed the Bayesian estimation naturally fits in the adaptivity strategy since the posterior distribution is updated at each cycle. Also, the information in the posterior can be used to compute the optimal control parameters. *Offline scheme:* In this approach the feedback values to be used during the experiment are pre-calculated. The aim is then to optimize this sequence of feedback values. Various optimization techniques based on trial-and-error approaches can be exploited, such as those based on Particle Swarm Optimisation [364] and Differential Evolution [365–367].

Chapter 11

Experimental quantum metrology with integrated devices

In the previous chapter, we presented the theory of quantum metrology by showing the main concepts with a focus on describing the advantages of using quantum resources over classical ones. Furthermore, it was seen that one of the most relevant problems for the theory is the estimation of one or more phases implemented by a physical system.

In the following, we present two experimental applications of quantum metrology theory carried out during my PhD. In particular, in the first part, a multiphase estimation experiment was performed in an integrated photonic device using indistinguishable photon pairs as probe states. The correct functioning of the adaptive estimation protocol was demonstrated, and how the use of indistinguishable photons leads to a precision improvement copared to both the single-photon case and the case with distinguishable photon pairs. In the second part of the chapter, we study the possibility of reaching the ultimate limit on the sensitivity of a phase measurement given by the Heisenberg scaling. In particular, we experimentally demonstrate this advantage when measuring a rotation angle between two reference systems using single-photon states with high-order orbital angular momentum. Moreover, we employ an offline adaptive algorithm optimized over the available resources to fit the capabilities of the experimental apparatus. We verify performance overcoming the standard quantum limit for a considerable range of resources $\nu \sim 30.000$ by obtaining an improvement of the precision, in terms of variance, of more than 10 dB. All the results presented in this chapter represent the findings in the works:

Experimental multiparameter quantum metrology in adaptive regime. Mauro Valeri, Valeria Cimini, Simone Piacentini, Francesco Ceccarelli, Emanuele Polino, Francesco Hoch, Gabriele Bizzarri, Giacomo Corrielli, Nicolò Spagnolo, Roberto Osellame, Fabio Sciarrino. Phys. Rev. Research 5, 013138, February 2023 [4].

Non-asymptotic Heisenberg scaling: experimental metrology for a wide resources range. Valeria Cimini, Emanuele Polino, Federico Belliardo, Francesco Hoch, Bruno Piccirillo, Nicolò Spagnolo, Vittorio Giovannetti, Fabio

Sciarrino. arXiv:2110.02908 Oct 2021 [5].

11.1 Experimental multiparameter quantum metrology in a photonic chip

In this section, we present the experimental implementation of a quantum-enhanced multiphase estimation protocol in an integrated photonic chip showing the saturation of the quantum Cramér-Rao bound in the limited resource regime. In particular, we experimentally demonstrate the simultaneous estimation of 3 optical phases, showing the capability to overcome the optimal separable sensitivity limit, exploiting a two-photon input state distributed in a 4 mode interferometer. This is done by employing a Bayesian adaptive protocol that allows to efficiently allocate the number of resources for each estimation while ensuring an optimized convergence to the ultimate bound in the limited resource regime. Indeed, the application of real-time adaptive feedback enables approaching such bound already after only ~ 50 probes. This procedure is shown to provide performances that are independent of the particular value of the unknown parameters.

Differently from the works already present in the literature [157,368] we implement an adaptive protocol capable to achieve approaching the QCRB in a limited data regime. This kind of protocol has been previously investigated only in classical regime [369] or for quantum single-parameter estimation [370–372].

11.1.1 Experimental apparatus

Our photonic platform consists of an actively tunable integrated 4 mode interferometer realized through femtosecond laser waveguide writing in glass [373,374]. In particular, the internal geometry consists of two quarters in cascade, which are 4 mode generalizations of the beam splitter and for each input it split the optical power equally in all output modes. Each quarter is composed of four directional couplers arranged in a two-layers configuration and a three-dimensional waveguide crossing, as depicted in the inset of Fig. 11.1. Moreover, each quarter is equipped with two thermal phase shifters (R_{1-4}), which allow active control of the internal optical phase between the directional coupler layers (ϕ_{1-4}), and select a specific equivalence class of the quarter transformations [375]. Between the two quarters, the interferometric region is composed of four straight waveguide segments whose optical phases ϕ_{A-D} can be controlled by means of 8 thermal phase shifters (R_{a-d} and R_{A-D}). All thermal shifters have been fabricated by femtosecond laser micromachining and include laser-ablated isolation trenches around each microheater [376]. This configuration allows both to reduce the power consumption and greatly reduce the thermal cross-talk between adjacent shifters but at the cost of increasing the thermalization time of the device.

On the basis of the presented scheme, the transformation performed by the phase shifters fabricated on the internal waveguides of the interferometer can be expressed

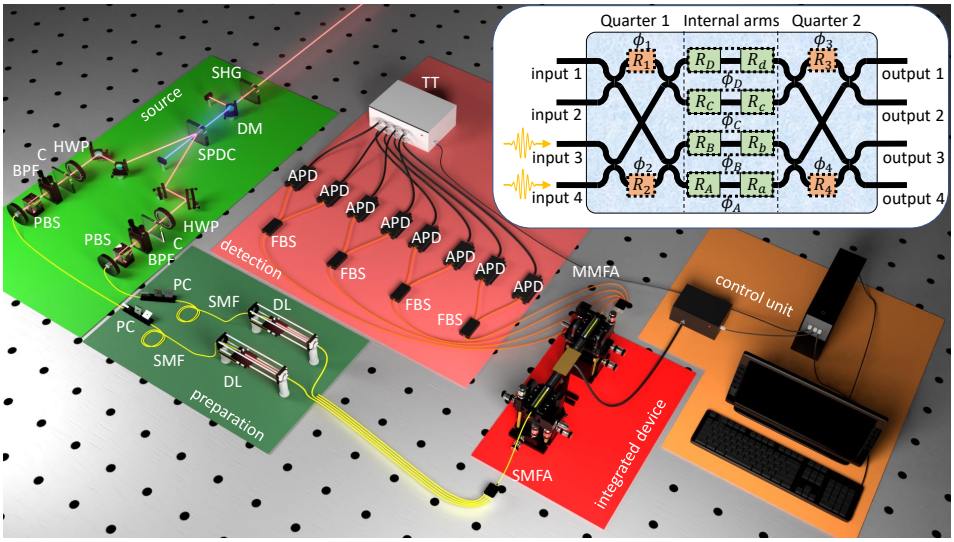

Figure 11.1. Experimental setup employed for the experiments of multiphase estimation in a photonic integrated interferometer. (i) Source. Two-photon states are generated via parametric-down-conversion in a BBO (β-Barium Borate) crystal. (ii) Preparation. Photons are made indistinguishable in time via delay lines, and in the polarization degree of freedom via a fiber polarization controller. (iii) Integrated device. Photons are injected into the integrated interferometer, and collected at the output, via fiber arrays. (iv) Detection. Two-photon events are collected via a probabilistic photon-counting scheme. (v) Control unit. Measurement outcomes are processed by the control unit and are used to drive the thermal shifter operation. Inset: Scheme of the integrated circuit. Each thermal shifter R_i is able to control a specific optical phase of the device. In particular, with regard to the internal waveguides of the interferometer, we identify the three independent internal phase-shifts $(\varphi_A, \varphi_B, \varphi_D) := (\phi_A - \phi_C, \phi_B - \phi_C, \phi_D - \phi_C)$ by setting C as reference mode. Instead, ϕ_{1-4} defines the equivalence class of each quarter transformation. **Legend.** SHG: second harmonic generation. DM: dichroic mirror. SPDC: spontaneous parametric down-conversion. HWP: half-wave plate. C: walk-off compensation. BPF: band-pass filter. PBS: polarizing beam-splitter. PC: polarization compensation. SMF: single-mode fiber. DL: delay line. SMFA: single-mode fiber array. MMFA: multi-mode fiber array. FBS: fiber beam-splitter. APD: avalanche photodiode. TT: time-tagger.

by the unitary matrix:

$$U_\phi = \begin{bmatrix} e^{i\phi_D} & 0 & 0 & 0 \\ 0 & e^{i\phi_C} & 0 & 0 \\ 0 & 0 & e^{i\phi_B} & 0 \\ 0 & 0 & 0 & e^{i\phi_A} \end{bmatrix}, \tag{11.1}$$

The interferometer is able to perform the simultaneous estimation of three independent phase shifts $\vec{\varphi}$ between three modes and the one used as a reference. In the following, we choose C as a reference, thus defining the triple of phases to be estimated as

$$\vec{\varphi} = (\varphi_A, \varphi_B, \varphi_D) \coloneqq (\phi_A - \phi_C, \phi_B - \phi_C, \phi_D - \phi_C) \tag{11.2}$$

The transformation induced by the actual device will also depend on the effective transmissivities and reflectivities of the 8 directional couplers.

11.1.2 Characterisation of device reachable bounds

We start by theoretically studying the operation and the bounds relative to the ideal device, i.e. when the reflectivities of all the directional couplers are equal to the nominal value of 1/2. The QFI depends only on the prepared probe state, therefore it is a function of the input modes of the injected photons and of the phases ϕ_1 and ϕ_2 of the first quarter whose unitary transformation is given by:

$$U_Q = \frac{1}{2}\begin{bmatrix} e^{i\phi_1} & ie^{i\phi_1} & i & -1 \\ ie^{i\phi_1} & -e^{i\phi_1} & 1 & i \\ i & 1 & -e^{i\phi_2} & ie^{i\phi_2} \\ -1 & i & ie^{i\phi_2} & e^{i\phi_2} \end{bmatrix}. \tag{11.3}$$

Depending on the specific input the dependence on these two phases can vanish. More specifically this condition is verified when the two photons are placed either in the first two modes ($|1100\rangle$) or in the last two ($|0011\rangle$). choosing the second possibility we generates, after the first quarter, the multiphoton entangled probe state:

$$|\psi_0\rangle = \frac{i}{2\sqrt{2}}(|2000\rangle - |0200\rangle + e^{-2i\phi_2}|0020\rangle - e^{-2i\phi_2}|0002\rangle) - \frac{1}{2}(|1100\rangle + e^{-2i\phi_2}|0011\rangle) \tag{11.4}$$

For our device, the use of two-photon quantum probes ensures to approach of the ultimate asymptotic quantum limit for the 3−phase estimation represented by the relative QCRB which results to be equal to $2.5/\nu$ (where ν is the number of two-photon probe states used) with associated Quantum Fisher information matrix:

$$\mathrm{QFI} = \begin{pmatrix} 2 & 0 & -1 \\ 0 & 2 & -1 \\ -1 & -1 & 2 \end{pmatrix} \qquad \mathrm{QFI}^{-1} = \begin{pmatrix} 0.75 & 0.25 & 0.5 \\ 0.25 & 0.75 & 0.5 \\ 0.5 & 0.5 & 1 \end{pmatrix}. \tag{11.5}$$

The computed bound represents the ultimate quantum limit achievable in the estimation precision for the considered input. The overall amount of resources is 2ν single photons. More specifically, we count as resources only the effective number of detected photon pairs thus working in a post-selection configuration.

The optimality of the full scheme is therefore demonstrated when the CRB, obtained after the measurement process is also considered, reaches the QCRB. Therefore, when studying the CRB also the characteristics of the second quarter must be considered in the model. The state generated at the output after injecting into the device two photons in the third and fourth input is a coherent superposition of 2 photons in the 4 output modes of the device:

$$\begin{aligned} |\psi\rangle_{out} =& a_{11}|2000\rangle + a_{22}|0200\rangle + a_{33}|0020\rangle + a_{44}|0002\rangle + a_{12}|1100\rangle + \\ &+ a_{13}|1010\rangle + a_{14}|1001\rangle + a_{23}|0110\rangle + a_{24}|0101\rangle + a_{34}|0011\rangle \end{aligned} \tag{11.6}$$

with $a_{11} = a_{22}$, $a_{33} = a_{44}$, $a_{13} = a_{24}$ and $a_{23} = a_{14}$ where all the coefficients now depend on the parameters imposed by U_Q transformation and on the particular

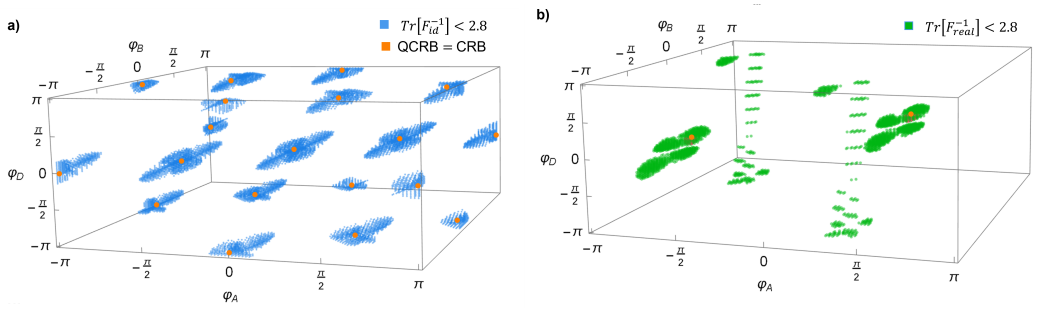

Figure 11.2. Theoretical Cramér-Rao Bound regions. Points corresponding to a value of the CRB $< 2.8/\nu$. The orange points correspond to the minimum where the QCRB is saturated. **a)** Bound relative to the ideal device. **b)** Bound for the real device whose minimum is $2.53/\nu$.

settings of ϕ_1, ϕ_2, ϕ_3 and ϕ_4. The CRB, given such a state, can indeed saturate the ultimate limit of $2.5/\nu$, satisfying the general necessary conditions for the saturation of QCRB of multiphase estimation in interferometric setups [377]. It is fundamental to notice that indistinguishability between the two input photons is a necessary condition to reach such a bound. The minimum of the CRB in the scenario of indistinguishable photons ensures the saturation of the QCRB and the achievement of a quantum-enhanced estimation over 3 parameters. Indeed, the use of completely distinguishable photons allows for achieving a minimum of the CRB equal to $3/\nu$.

To demonstrate the capability of reaching an estimation enhancement, we compare our result also with the optimal estimation obtained through single-photon states [349]. In order to make a fair comparison it is important to consider the same number of photons for classical strategies. In this case, the trace of the inverse Fisher information matrix is 5.6 for a single-photon prepared in the optimal state. Therefore, the preparation of two independent photons in such a state corresponds to a value of 2.8 for the trace of the inverse Fisher information matrix. Hence, a strategy employing 2ν independent optimal single-photon states are associated with an achievable bound of QCRB $= 2.8/\nu$. Consequently, the saturation of $2.5/\nu$ demonstrates quantum-enhanced measurement sensitivity reachable with indistinguishable two-photon states compared to any sequence of classical single-photon probes and independent measurement, even including the optimal single-photon state.

The parameter (phases) regions showing such an advantage where the achieved CRB, for the ideal device, is lower than 2.8 are limited and are reported in Fig. 11.2a. However, thanks to the implementation of an adaptive protocol we are able to demonstrate the sensitivity enhancement independently of the values of the estimated triplet of optical phase shifts in the limited resources regime.

In order to investigate the actual capabilities of the employed device with two-photon input states, it is necessary to reconstruct its likelihood function through a calibration procedure (See Chapter 4). This step is necessary to derive the achievable CRB with the actual device.

We reconstruct the 10 two-photon output probabilities by fitting the measured data for different values of voltages applied to the resistors of the device. In particular,

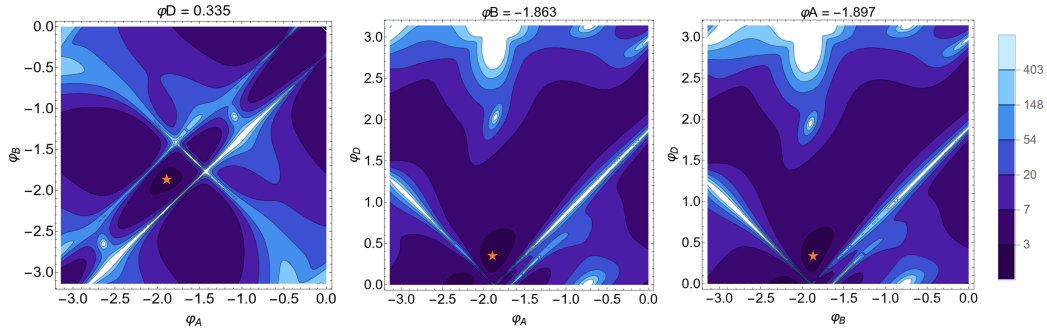

Figure 11.3. Slices of Fisher Information matrix. Three cuts of $\mathrm{Tr}[F^{-1}]$ obtained fixing, from left to right, respectively the values of φ_D, φ_B and φ_A. The plot shows the sensitivity of different regions of the parameters space. The orange star represents the minimum of the variance where the CRB is equal to $2.53/\nu$ which indeed coincides with the orange point of Fig. 11.2b. The color legend has been chosen logarithmic in order to highlight the regions associated with the minimum uncertainty

.

we collect measurements studying the device response as a function of the power dissipated on the three thermal shifters, i.e. R_a, R_b, R_d, allowing the complete tuning of the internal phases. More specifically, we measure the coincidence events registered at the output of the integrated circuit by dissipating through each selected resistor 10 different power values, which are equally spaced over the allowed range.

Finally, the output probabilities reconstructed from experimental data can be used to compute the FI matrix and retrieve the experimental CRB. In Fig. 11.2b we report the regions showing a bound lower than the minimum one achievable with the best classical states for such measurement. To highlight the regions of minimum uncertainty, we report three cuts of the inverse of the trace of the FI in Fig. 11.3, where the explicit two-variable function is plotted. From this plot, it is evident that the estimation uncertainty is highly related to the particular value of the triplet of phases under study. In order to perform the estimation in the point of minimum uncertainty independently from the particular value of the triplet investigated it is therefore necessary to implement an adaptive strategy which sets the device always in its more informative point. For the actual device, considering all the experimental imperfections, the minimum which corresponds to the achievable bound is $2.53/\nu$ and it is achieved in two different points of the space (see Fig. 11.2b). Note that this bound has been obtained considering all the main sources of imperfections affecting the experimental setup. More specifically, we consider the partial distinguishability of the two input photons and deviations from the ideal behaviour of the transformations performed by the optical elements in the integrated device, including transmissivities of the directional couplers and different detection efficiencies. This value is very close to the ideal one of $2.5/\nu$ and it is still below the critical threshold of 2.8. This means that our device allows us to demonstrate quantum enhancement in the simultaneous estimation of three optical phases, experimentally approaching the QCRB in a post-selected configuration.

We can also study the sensitivity performances obtained when estimating a linear combination of the parameters under study. Distributed sensing [378–382] represents

indeed a field that is increasingly being investigated lately. However, instead of looking at any generic combination of parameters $\vec{\nu}\cdot\vec{\varphi}=\sum_{i=1}^{d}\nu_i\varphi_i$, here, following [383], we can study the achieved performances over the optimal combination of phases to show quantum-enhanced sensitivity. Therefore, we compare for our setup the sensitivities reached with the simultaneous multiparameter estimation with respect to sequential strategies where the different parameters are all estimated independently. In particular, the optimal vector $\vec{\nu}$ for our setup is the eigenvector of the QFI matrix associated with the largest eigenvalue f_{max} i.e $\vec{\nu}_{max}=(1/2,1/2,-1/\sqrt{2})$. It follows that the optimal linear combination of optical phases that we can estimate is: $(\phi_A-\phi_D)/2+(\phi_B-\phi_D)/2-(\phi_C-\phi_D)/\sqrt{2}$. The study of this figure of merit allows us to consider also the off-diagonal terms of the QFI that in general depend on mode entanglement in the probe state. It is then possible to compute the sensitivity bound on the estimate of the linear combination, achieved when using the employed entangled input states, which is given in [383] and results to be:

$$\Delta^2(\vec{\nu}_{max}\cdot\vec{\varphi})=\vec{\nu}_{max}\mathcal{F}_Q\vec{\nu}_{max}^T=0.292. \tag{11.7}$$

The comparison can be done with the optimal separable strategy achieved using coherent states with an average number of photons $\langle\bar{n}\rangle=2$ to estimate sequentially three optical phases embedded in a network of Mach-Zehnder interferometers. In such a setting, the QCRB is:

$$\Delta^2(\vec{\nu}_{max}\cdot\vec{\varphi})_{\text{seq}}=\sum_{i=1}^{3}\frac{\nu_i^2}{\mathcal{F}_i}. \tag{11.8}$$

Here, $\mathcal{F}_i$ is the single-parameter QFI for coherent states injected into a Mach-Zehnder interferometer, i.e. $\mathcal{F}_i=\bar{n}_i$ [384]. By numerical optimization, we obtain the minimum of $\Delta^2(\vec{\nu}_{max}\cdot\vec{\varphi})_{\text{seq}}=1.45$, corresponding to the bound achievable with sequential classical measurements. Consequently, sensitivity on the estimation of the optimal linear combination below this separable bound is a demonstration of the enhancement achieved using entangled probes [383].

11.1.3 Experimental results with an adaptive strategy

Experimentally, we study the performances achieved when implementing adaptive strategies, able to set the device in the optimal working point for the estimation [324, 355, 369, 385, 386]. This optimization can be done before each probe and it is independent of the specific unknown values. It is based on controlling additional parameters, used as feedback during the estimation cycle. The capability of asymptotic saturation of lower bounds is not sufficient when an optimal estimation in a few probes is required. Moreover, the computation of which optimal feedbacks have to be applied is in general non-trivial, especially when the complexity of the system increases. For this reason, machine learning techniques are often adopted, able to tackle this hard computational task and in general to enhance sensing protocols [387–394].

Here, we employ a Bayesian framework (see Chapter 10) for the adaptive protocol, which represents a powerful tool for multiphase estimation [395, 396]. In particular, we use the Bayesian multiparameter estimation protocol employed in [369, 396, 397].

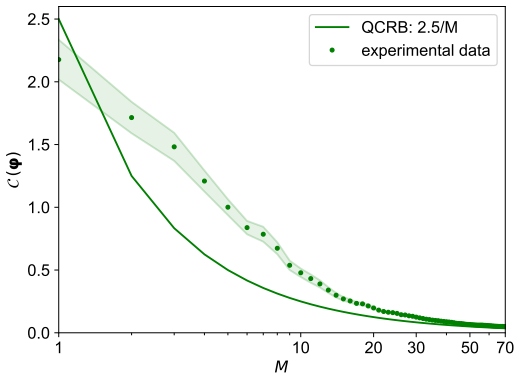

Figure 11.4. Experimental adaptive 3-phase estimation. Quadratic loss $\mathcal{C}(\vec{\varphi})$ is plotted as a function of the number ν of injected two-photon input states $|0011\rangle$. Green dots show the performance averaged on 12 different triple phases, estimated using the online Bayesian adaptive technique described in the main text. The experiment for each phase triplet is repeated 30 times and the final performance is characterized by the mean estimator, the shaded green area is the one standard deviation region. The line represents the ultimate precision bound, i.e. the QCRB $(2.5/\nu)$ for the ideal device when injected with indistinguishable photons.

Simultaneous adaptive two-phase estimation experiments have been demonstrated without quantum enhancement, injecting a three-mode interferometer with single-photon states [369]. Thus, we select such an approach for our multiphase estimation problem demonstrating the saturation of the ultimate precision bounds.

The realization of adaptive multiphase estimation requires the identification of unknown and control parameters. The structure of our platform allows us to handle independently two layers of internal phases by simply acting on different resistors: the phases to be estimated $\vec{\varphi}^{(X)}$ and the phases to be tuned for adaptive estimation $\vec{\varphi}^{(C)}$, such that $\vec{\varphi} = \vec{\varphi}^{(X)} + \vec{\varphi}^{(C)}$. In our case, the triplet of unknown parameters $\vec{\varphi}^{(X)}$ are set using the thermal shifters R_A, R_B, R_D, while the control parameters $\vec{\varphi}^{(C)}$ are tuned using R_a, R_b, R_d.

The adopted algorithm is based on a particle filtering sequential Monte Carlo technique [398] that guarantees high performances in computing integrals (replaced by sums) also when the dimensions of the space increase. The algorithm allows the computation of the control parameters to be applied during the adaptive estimation. Such optimal values are those which maximize the expected overall variance after measurement of the subsequent probe. Here, the expectation value is computed using the SMC approach.

In order to identify appropriate values of the algorithm parameters for the experiment, we simulated adaptive multiphase estimations for different configurations of such parameters. A set of phase triplets $\{\vec{\varphi}^{(X)}\}$ is uniformly selected in $[0, 2\pi] \times [0, 2\pi] \times [0, 2\pi]$ and estimated by a series of two-photon states. The estimation of each triplet is repeated 30 times. The output probability distribution of our device, given the considered entangled input state, can estimate unambiguously each of the three phases in a π range. For this reason, we set the a-priori Bayesian distribution equal to a uniform distribution with a π width. Note that, by repeating the estimation procedure several times, we obtain the mean of the Bayesian posterior distribution,

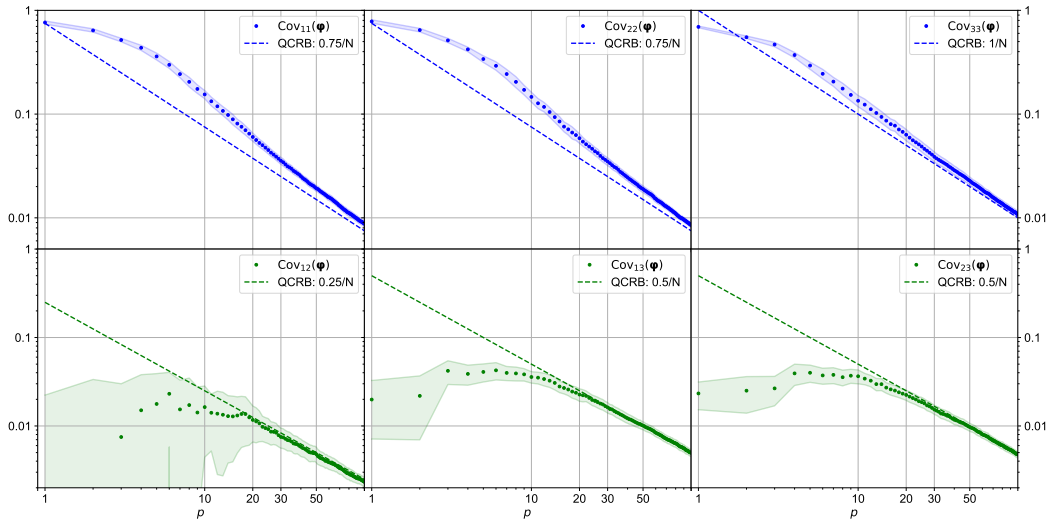

Figure 11.5. Experimental adaptive 3-phase estimation Quantum Fisher information Matrix. Comparison between the ideal QCRB and the measured covariance matrix during the adaptive three-phase estimation. Dots result from the median average on 12 uniformly distributed phases which are estimated 30 independent times, starting with uniform a-priori knowledge of π.

from which we retrieve the achieved sensitivity for all the performed repetitions, allowing us to compare our results with the bounds of the frequentist scenario.

The accuracy of the estimation can be computed by looking at different figures of merit. We start investigating a commonly employed one in the first studies of multiphase estimation [349] by firstly considering a figure of merit that takes into account the trace of the covariance matrix. Then, we generalize the discussion by considering also the off-diagonal terms of the covariance matrix, when demonstrating quantum-enhanced sensitivity for the estimate of a linear combination of the considered parameters. The covariance of the posterior distribution $\Sigma(\vec{\hat{\varphi}})$ represents the confidence interval of the estimate and thus the actual error of the quantum sensor employed. In parallel, the quadratic error distance $\mathcal{C}(\vec{\varphi})$, between the estimated parameters and their true values, provides a reliable evaluation of both the estimation uncertainty and the presence of possible biases. Such quantity is obtained as follows: $\mathcal{C}(\vec{\varphi}) = \int \mathrm{d}\varphi(\varphi - \hat{\varphi})^2 p(\varphi|x)$, here $p(\varphi|x)$ represents the posterior probability which is updated through the Bayesian procedure after each measurement result x has been registered. In the asymptotic regime the average of both the covariance and the quadratic error $\mathcal{C}(\vec{\varphi})$ must saturate the CRB. Conversely, this does not represent a stringent bound in the low number of probes regime due to the a-priori knowledge retained on the parameter values as discussed more in detail in [399]. Here, we employ the adaptive technique in order to approach the ultimate precision bound with the minimum number of probes, reporting the experimentally attained quadratic loss function averaged over 12 different triplets of phases. As shown in Fig. 11.4 we are able to reach performances close to the asymptotic limit already after sending around 50 probes. In Fig. 11.5 we also see that each component of the covariance matrix has similar behavior.

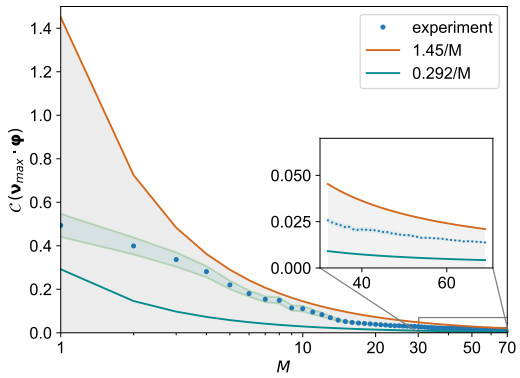

Figure 11.6. Experimental adaptive performances. Estimation performances as a function of the employed resources are reported in terms of $\mathcal{C}(\vec{\nu}_{max}\cdot\vec{\varphi})$. The experimental data with the relative standard deviation (shaded blue region) are averaged over 12 phases estimated 30 independent times. For comparison, both the separable (orange line) and parallel (cyan line) bounds are provided. The shaded grey area represents the region showing enhanced sensitivity compared to sequential strategies. The inset shows a zoom of the behavior for a number of two-photon probes in the range $M = 30 - 70$.

As done theoretically, we further use the adaptive approach to study the estimation of the optimal linear combination of the three parameters discussed in the previous section. The results of the experimental estimates are reported in Fig.11.6. Here, we manage to outperform classical separable strategies, by showing that the average over multiple repetitions of the estimation protocol performed on different triplets of phases is found to be below the sequential bound. Note that, with this work, we demonstrate experimentally the violation of the sequential bound, assuring the convenience of adopting parallel strategies in multiphase estimation problems.

11.2 Quantum metrology for a wide resources range

In the previous chapter, it was seen that the ultimate quantum limit on the accuracy attainable for a phase measurement scales with the number of the employed resources as Heisenberg Scaling, however, this result has problems at both conceptual and practical levels. From an experimental point of view, the biggest problem in implementing a parallel measurement process (as we see in the previous chapter) is the need to generate high-dimensional $NOON$ entangled states, which are difficult to implement and particularly sensitive to experimental imperfections. From a theoretical point of view, the biggest problem is that a phase measurement with a $NOON$ state at m qubits is periodic with period $2\pi/m$ so a phase estimate with such states needs to know in advance the value to be measured such that the periodicity can be disambiguated. This issue can be solved through the use of an adaptive approach that during the estimation process uses a series of entangled states with increasing dimensions m_j. In Ref. [400, 401] an offline adaptive algorithm that uses states with increasing dimensionality as the power of two $m_j = 2^j$. In particular, they show how to group a given number of total qubits ν in the various entangled states to achieve the highest possible accuracy and reach the Heisenberg scaling.

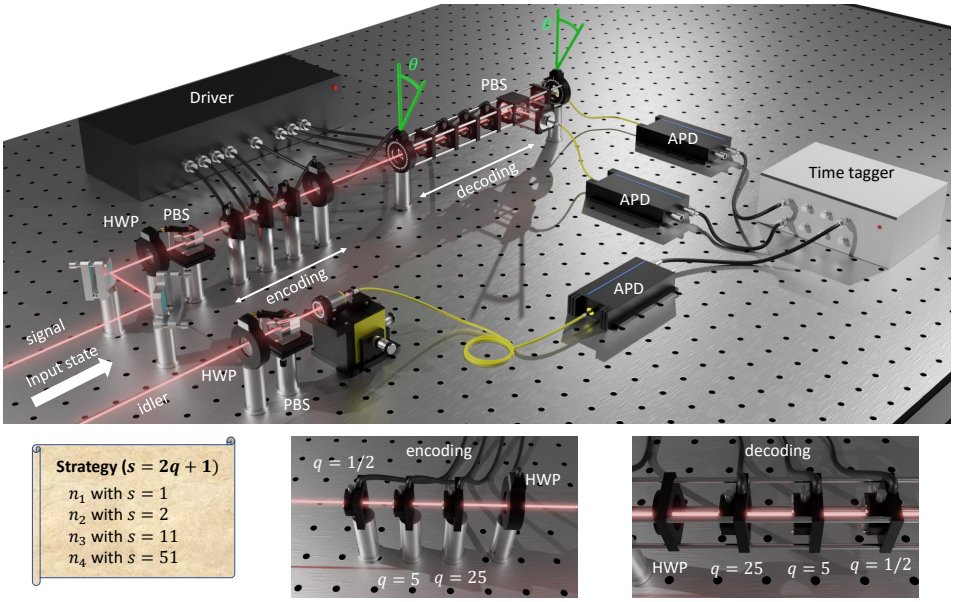

Figure 11.7. Experimental setup. Single photons pairs are generated by a degenerate type-II SPDC process inside a ppKTP pumped by a 404 nm cw laser. The idler photon is measured by a single photon avalanche photodiode (APD) and acts as a trigger for the signal that enters the apparatus. This consists of an encoding stage which is composed of a first polarizing beam splitter (PBS) and three q-plates with different topological charges $q = 1/2, 5, 25$, respectively, followed by a motorized half-waveplate (HWP). The decoding stage is composed of the same elements of the preparation mounted, in the reverse order, in a compact and motorized cage that can be freely rotated around the light propagation axis of an angle θ. After the final PBS, the photons are measured through a set of two APDs. Coincidences with the trigger photon are measured, analyzed via a time-tagger, and sent to a computing unit. The latter, according to the pre-calculated optimal strategy, controls all the voltages applied to the q-plates and the angle of rotation of the measurement stage.

From an experimental point of view, it is possible to replace entangled states and parallel estimation with a multi-step process where the phase to be measured is applied several times to the probe state. It is shown that by appropriately choosing the probe state and final measurements, it is possible to formally replicate the parallel approach but without the need to use entangled states.

In the following, we present a method that generalizes the algorithm presented in Ref. [401] and suitably allocates the available resources reaching Heisenberg scaling precision without any prior information on the parameter. We demonstrate experimentally such an advantage in measuring a rotation angle between two reference systems by using single-photon states with high-order orbital angular momentum (OAM). We quantitatively verify sub-SQL performances for a considerable range of resources $\nu \sim 30,000$ by achieving an error reduction, in terms of the obtained variance, greater than 10 dB below the standard quantum limit.

11.2.1 Experimental apparatus

In our experiment, we employ the total angular momentum of single photons as a tool to measure the rotation angle θ between two reference frames associated with two physical platforms [402]. The full apparatus is shown in Fig. 11.7. The key elements for the generation and measurement of OAM states are provided by q-plates (QPs) devices, able to modify the photons' OAM conditionally to the value of their polarization. A q-plate is a topologically charged half-wave plate that imprints an OAM $2\hbar\, q$ to an impinging photon and flips its polarization [403] (see Chapter 2).

In the preparation stage, single photon pairs at 808nm are generated by a $20mm$-long periodically poled titanyl phosphate (ppKTP) crystal pumped by a continuous laser with a wavelength equal to $404nm$. One of the two photons, the signal, is sent along the apparatus, while the other is measured by a single photon detector and acts as a trigger for the experiment. The probe state is prepared by initializing the single-photon polarization in the linear horizontal state $|H\rangle$, through a polarizing beam splitter (PBS). After the PBS, the photon passes through a QP with a topological charge q and a half-wave plate (HWP) which inverts its polarization, generating the following superposition:

$$|\psi_0\rangle = \frac{1}{\sqrt{2}}\big(\,|R\rangle\,|+l\rangle + |L\rangle\,|-l\rangle\,\big), \tag{11.9}$$

where $l = 2q$ is the value, in modulus, of the OAM carried by the photon. In this way, considering also the spin angular momentum carried by the polarization, the total angular momenta of the two components of the superposition are $\pm|l+1|$.

After the probe preparation, the generated state propagates and reaches the receiving station, where it enters a measurement apparatus rotated by an angle θ. Such a rotation is encoded in the photon state by means of a relative phase shift with a value $2|l+1|\,\theta$ between the two components of the superposition:

$$|\psi_\theta\rangle = \frac{1}{\sqrt{2}}\big(e^{i\,(l+1)\theta}\,|R\rangle\,|+l\rangle + e^{-i\,(l+1)\theta}\,|L\rangle\,|-l\rangle\,\big)\ . \tag{11.10}$$

To measure and retrieve efficiently the information on θ, such a vector vortex state is then reconverted into a polarization state with zero OAM. This is achieved by means of a second HWP and a QP with the same topological charge as the first one, oriented as the rotated measurement station:

$$|\psi_f\rangle = \frac{1}{\sqrt{2}}\big(\,|R\rangle + e^{-i\,2(l+1)\theta}\,|L\rangle\,\big)\ , \tag{11.11}$$

where the zero OAM state factories and is thus omitted.

In this way, the relative rotation between the two apparatuses is embedded in the polarization of the photon that is finally measured with a PBS (concordant with the rotated station) followed by single photon detectors. Note that an HWP is inserted just after the preparation PBS and before the first three QPs. Such an HWP is rotated by 0° and 22.5° during the measurements to obtain the projections in the $|H\rangle$, $|V\rangle$ basis and in the diagonal one ($|D\rangle$, $|A\rangle$). In each stage, half of the photons are measured on the former basis and half on the latter. To guarantee the alinement the entire measurement station is mounted on a single motorized rotation

cage. The interference fringes at the output of such a setup oscillate with an output transmission probability $P = \cos^2[(l+1)\theta]$ with a periodicity that is $\pi/(l+1)$. Hence, the maximum periodicity is π at $l = 0$ and, consequently, one can unambiguously estimate at most all the rotations in the range $[0, \pi)$.

The limit of the error on the estimation $\hat{\theta}$ of the rotation θ is:

$$\Delta^2\hat{\theta} \geq \frac{1}{4\,(l+1)^2\nu}\,, \tag{11.12}$$

where ν is the number of employed single photons carrying a total angular momentum $l+1$ times the number of repetitions of the measurement. Such a scaling is Heisenberg-like in the angular momentum resource $l+1$ and can be associated with the Heisenberg scaling achievable by multi-pass protocols for phase estimation, using non-entangled states [324]. This kind of protocol can overcome the SQL scaling, that in our case reads $1/(4\nu)$, corresponding to the limit calculated considering single-photon probes with zero OAM. Here, we investigate both the non-asymptotic and near-asymptotic regimes using non-adaptive protocols. Our apparatus is an all-automatized toolbox generalizing the photonic gear presented in [402]. In our case, six QPs are simultaneously aligned in a cascaded configuration and actively participate in the estimation process. The first three QPs, each with a different topological charge q, lie in the preparation stage, while the other three, each having respectively the same q as the first three, are in the measurement stage. All the QPs are mounted inside the same robust and compact rotation stage, able to rotate around the photon propagation direction. Notably, the whole apparatus is completely motorized and automated. Indeed, both the rotation stage and the voltages applied to the q-plates are driven by a computing unit that fully controls the measurement process.

During the estimation protocol of a rotation angle, only one pair of QPs with the same charge, one in the preparation and the other in the measurement stage, is simultaneously turned on. For a fixed value of the rotation angle, representing the parameter to measure, pairs of QPs with the same charge are turned on, while keeping the other pairs turned off. Data are then collected for each of the four possible configurations, namely all the q-plates turned off, i.e. $m = 1$, and the three settings producing $m = 2, 11, 51$, respectively. Finally, the measured events are divided among different estimation strategies and exploited for post-processing analysis.

11.2.2 Experimental result

The optimization of the uncertainty on the estimated rotation angle is obtained by employing the protocol described above. In particular, such an approach determines the use of the resources of each estimation stage. In this experiment, we have access to two different kinds of resources, namely the number of photon-pairs ν employed in the measurement and the value of their total angular momentum m. Therefore, the total number of employed resources is $N = \sum_{i=1}^{K} \nu_i m_i$, where ν_i is the number of photons with total angular momentum m_i, and $K = 4$. According to the above procedure, for every N we determine the sequence of the multiplicative factors m_i and ν_i associated with the optimal resource distribution. Note that, in the same

spirit of multi-pass protocols, where the resources invested for the estimation are given by the number of interactions of the probe with the sample, it is natural to consider the total angular momentum as a resource in the estimation protocol. Indeed, generating, propagating, and measuring higher-order OAM states of light require more effort, due to the necessity of using higher topological charge q-plates, of facing their divergence and challenging measurements, respectively.

The distance between the true value, θ, and the one obtained with the estimation protocol, $\hat{\theta}$, in the system periodicity $[0, \pi)$, is obtained computing the circular error as follows:

$$D_c(\hat{\theta}, \theta) = \frac{\pi}{2} - \left| (\theta - \hat{\theta}) \bmod \pi - \frac{\pi}{2} \right| . \tag{11.13}$$

Repeating the procedure for $r = 1, \ldots, R$ different runs of the protocol with $R = 200$, we retrieve, for each estimation strategy, the corresponding mean-square error (MSE):

$$\Delta^2 \hat{\theta} = \sum_{r=1}^{R} \frac{|\hat{\theta}_r - \theta|^2}{R}. \tag{11.14}$$

We remark that R in Eq. (11.14) and ν in Eq. (11.12) do not have the same interpretation. Indeed R is not a part of the protocol, but is merely the number of times we repeat it in order to get a reliable estimate of its precision. We then averaged such quantity over 17 different rotations with values between 0 and π, leading to $\overline{\Delta\hat{\theta}}$. In such a way, we investigate the uncertainty independently on the particular rotation angle inspected.

To show the improvement in the measurement sensitivity by exploiting strategies that have access to states with an increasing value of the total angular momentum we first consider the scenario where only photon states with $m = 1$ are generated. In this case, the MSE follows as expected, the SQL scaling as a function of the number of total resources. The obtained estimation error for the strategies constrained by such condition is represented by the blue points in Fig. 11.8a. Running the estimation protocol and exploiting also states with $m > 1$ it is possible to surpass the SQL and progressively approach performances following the same power law of Heisenberg scaling, for high values of m. In particular, we demonstrate such improvement by progressively adding to the estimation process a new step with a higher OAM value. We run the protocol limiting first the estimation strategy to states with $m = 1; 2$ (green points), then to $m = 1; 2; 11$ (cyan points) and finally to $m = 1; 2; 11; 51$ (magenta points). For each scenario, the number of photons ν per step is optimized accordingly. Performing the estimation with all the 4 available values of OAM allows us to achieve an error reduction, in terms of the obtained variance, up to 10.7 dB below the SQL. Note that the achievement of the Heisenberg scaling is obtained by progressively increasing the order of the OAM states employed in the probing process, mimicking the increase of N when using N00N-like states in multi-pass protocols. This is highlighted by a further analysis performed in Fig. 11.8b and Fig. 11.8c. More specifically, if beyond a certain value of N the OAM value is kept fixed, the estimation process will soon return to scale as the SQL power law.

To certify the quantum-inspired enhancement of the sensitivity scaling, we performed a first global analysis on the uncertainty scaling, considering the full range of N. This is performed by fitting the obtained experimental results with the function

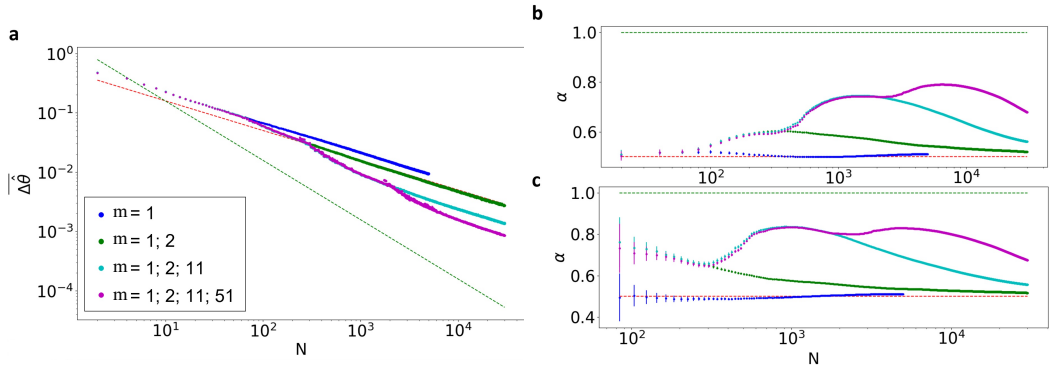

Figure 11.8. Approaching Heisenberg scaling with higher-order OAM states. a) Averaged measurement uncertainty over $R = 200$ repetitions of the algorithm and over 17 different angle measurements, in the interval $[0, \pi)$, as a function of the total amount of resources N. The adoption of single-photon states with progressively higher-order total angular momentum allows to progressively approach Heisenberg scaling. The red dashed line is the standard quantum limit for this system $1/(4N)$, while the green dashed line is the HL $\pi^2/(4N^2)$. **b)** Value of the coefficient α and its standard deviation obtained by fitting the points from $N = 2$ to the value reported on the $x-$axis with the curve $C/N^{2\alpha}$. **c)** Value of the coefficient α and its standard deviation obtained by fitting the points from $N = N_0$ to the value reported on the $x-$axis with the curve $C/N^{2\alpha}$. Purple points: estimation process with the full strategy. Blue points: estimation process by using only $m = 1$. Green points: estimation process by using only $m = 1; 2$. Cyan points: estimation by using only $m = 1; 2; 11$.

$C/N^{2\alpha}$. In particular, such a fitting procedure is performed considering batches of increasing size of the overall data. This choice permits investigating how the overall scaling of the measurement uncertainty, quantified by the coefficient α, changes as a function of N. Starting from the point $N = 2$, we performed the fit considering each time the subsequent 10 experimental averaged angle estimations (reported in Fig.11.8a) and evaluated the scaling coefficient α with its corresponding confidence interval for each data batch. The results of this analysis are reported in Fig. 11.8b. As shown in the plot, α is compatible with the SQL, i.e. $\alpha = 0.5$, when the protocol employs only states with $m = 1$. Sub-SQL performance is conversely achieved when states with $m > 1$ are introduced in the estimation protocol. The scaling coefficient of the best fit on the experimental data collected when exploiting all the available QPs (magenta points) achieves a maximum value of $\alpha = 0.7910 \pm 0.0002$, corresponding to the use of $6,460$ resources. The enhancement is still verified when the fit is performed considering the full set of $30,000$ resources. Indeed, the scaling coefficient value in this scenario still remains well above the SQL, reaching a value of $\alpha = 0.6786 \pm 0.0001$. Given that the data sets corresponding to $m = 1$ inherently follow the SQL, we now focus on those protocols with $m > 1$, thus taking into account only points starting from $N_0 = 62$. This value coincides with the first strategy exploiting states with $m = 2$. Fitting only such region, the maximum value of the obtained coefficient increases to $\alpha = 0.8301 \pm 0.0003$ for $N = 4,764$. Note that, as higher resource values m are introduced, the overall scaling coefficient of the estimation process, taking into account the full data set, progressively approaches

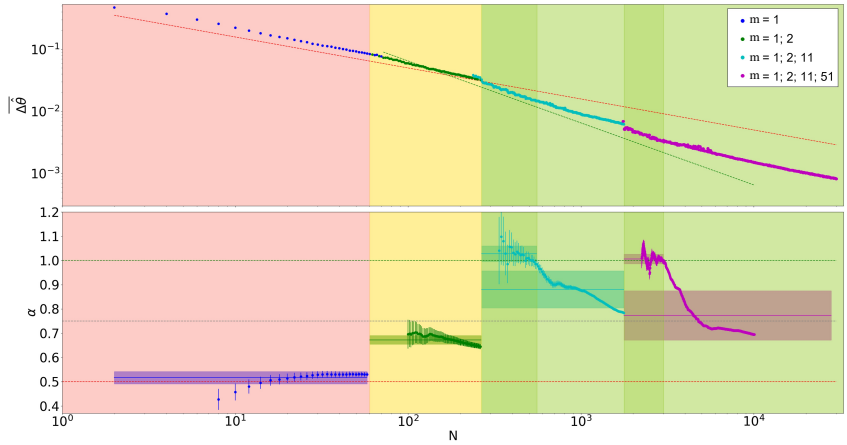

Figure 11.9. Certification of the Heisenberg scaling in the local scenario. Upper panel: measurement uncertainty averaged over 17 different angle values in the interval $[0, \pi)$ as a function of the number of resources N. We highlight the points with the color code associated with the maximum value of m exploited in each strategy. Blue points: strategies with $m = 1$. Green points: strategies relative to $m = 1; 2$. Cyan points: strategies relative to $m = 1; 2; 11$. Purple points: strategies for $m = 1; 2; 11; 51$. Error bars are smaller than the size of each point. Lower panel: the value of the coefficient α and the relative confidence interval for the four inspected regions. Such a confidence interval consists of a 3σ region, obtained for the best fit with function C/N^{α}. The fit is done on batches of data as described in the main text. The continuous lines show the average value of α in the respective region, while the shaded area is its standard deviation. The last reported point of α corresponds to the maximum batch of data which we can fit all together with the function $C/N^{2\alpha}$, without taking into account other sources of noise. In both the plots the salmon, yellow and green colored areas represent respectively regions with SQL scaling ($\alpha = 0.5$), sub-SQL scaling ($0.5 < \alpha \leq 0.75$), and a scaling approaching the Heisenberg-limit ($0.75 < \alpha \leq 1$). The red dotted line represents the SQL $= 1/(4N)$ ($\alpha = 0.5$) while the green one is the limit $= C/(4N^2)$ (obtained fixing $\alpha = 1$ and $C = 6$ which has been arbitrarily chosen in order to have the Heisenberg scaling comparison close to the experimental data in the regions of interest). The gray dotted line is the threshold $\alpha = 0.75$.

the same power law of Heisenberg scaling.

Then, we focus on the protocols which have access to the full set of states with $m = 1; 2; 11; 51$, and we perform a local analysis of the scaling, studying individually the regions defined by the order of OAM used, and characterized by different colors of the data points in the top panel of Fig. 11.9. This is performed by fitting the scaling coefficient with a batch procedure (as described previously) within each region. We first report in the top panel of Fig. 11.9 the obtained uncertainty $\overline{\Delta\hat{\theta}}$. Then, we study the overall uncertainty scaling, which shows a different trend depending on the maximum m value we have access to. To certify locally the achieved scaling, we study the obtained coefficient for the four different regions sharing strategies requiring states with the same maximum value of m. In the first region ($2 \leq N \leq 60$), since $m = 1$ no advantage can be obtained compared to the SQL. This can be quantitatively demonstrated by studying the compatibility, in 3σ, of the best-fit coefficient α with 0.5. Each of the blue points in the lower panel of Fig. 11.9 is

indeed compatible with the red dashed line. In the second region ($62 \leq N \leq 264$), since states with $m = 2$ are also introduced, it is possible to achieve a sub-SQL scaling. When states with up to $m = 11$ and $m = 51$ are also employed ($N > 264$) we observe that the scaling coefficient $\alpha > 0.75$ is well above the value obtained for the SQL. Finally, we can identify two regions ($266 \leq N \leq 554$ and $1,772 \leq N \leq 2,996$) where the scaling coefficient α obtained from a local fit is compatible, within 3σ, with the value $\alpha = 1$ corresponding to the same power law of the Heisenberg scaling. This holds for extended resource regions of size ~ 300 and $\sim 1,000$, respectively, and provides a quantitative certification of the achievement of Heisenberg scaling performances. Notably, such performances are achieved for values of m_i which are different from the optimal ones according to the method of [401], i.e. $m_i = 2^{i-1}$, showing the versatility of the approach that can be effectively adapted depending on the employed resources.

11.3 Conclusion

This chapter shows the experimental application of quantum metrology algorithms both with reconfigurable integrated photonic devices and bulk architectures. In particular, we demonstrated how the use of quantum probes increased the sensitivities of the estimation protocols, exceeding the SQL and approaching the QCRB. These experiments pave the way for new types of quantum sensors that are more precise. Indeed, our platform allows the integration of different optical elements, e.g. microfluidic channels [404] that enable the study of fluid solutions by exploiting the full potential of the quantum protocols shown above. In addition, the use of low-photon probe states allows the described techniques to be applied to the analysis of sensitive substances that would deteriorate if irradiated with light or other measurement methods.

Statement of Work

The work presented in this chapter was published in Valeri et. al. Phys. Rev. Research 5, 013138, February 2023 [4] and Cimini et. al. arXiv:2110.02908 Oct 2021 [5]. The realization of the experimental apparatus and data-taking was carried out by myself, M. Valeri and V. Cimini. The characterization of the chip and the data analysis were carried out by M. Valeri and V. Cimini. The photonic chip used was realized in the laboratories of Professor R. Osellame with the help of A. Crespi.

Conclusions and perspectives

This thesis presents the development and use of integrated photonic chips for quantum computing applications. After a brief introduction, the basic concepts of quantum information theory and quantum photonics were explained. Subsequently, two new protocols were proposed and tested for the characterization of linear interferometers in terms of implemented unitary matrix and device imperfections. The first applies a black-box approach using second-order correlation measurements implemented with coherent light. This approach allows an interferometer to be characterized even in the presence of phase fluctuations at the input and output of the device, without having to use indistinguishable photons as in other protocols proposed in the literature. This is a considerable advantage in cases where it is difficult to find a source of indistinguishable photons. The second algorithm is specific to integrated devices implementing a universal geometry according to Clements' configuration since despite the diffusion of this geometry an algorithm to characterize it had not yet been presented. The proposed algorithm attempts to reconcile the number of measurements required with the final accuracy by using, where possible, an analytical approach based on parameters derived from fits made on redundant measurements.

We then demonstrated the fabrication of the first reconfigurable 32-mode chip with three-dimensional continuous coupled geometry, testing its performance in terms of reconfigurability and performing a bosonic sampling experiment with it. The effectiveness of the approach for constructing compact reconfigurable interferometers with a high number of modes has been demonstrated, but the points regarding the possibility of constructing random unitary Haar arrays remain to be clarified. In fact, it has been seen how the device, despite being highly reconfigurable, does not generate a uniform type distribution. This may be due to two causes, the first being that there are indeed unreachable matrices and the second being that the distributions of the values of the control parameters used to drive the device are by no means trivial. To try to solve this problem, one proposal would be to use the characterization algorithms described above, combined with machine learning algorithms, to model the device and try to derive the distributions of the control parameters needed to generate random Haar units.

In the fourth part, we theoretically analyzed the Bernoulli quantum-to-quantum factory problem, providing a computational characterization in terms of the number of qubits used and the maximum achievable success probability. Furthermore, a procedure for constructing the optimal quantum circuit associated with a desired function was provided. In addition, two new variants of the problem, named respectively, were proposed and analyzed, which further extend the capabilities of

the original problem in future applications. Moreover, the possibility of implementing a photonic version of the algorithm was demonstrated by presenting three interferometers that, when chained together, allow a generic quantum-to-quantum Bernoulli factory to be realized and its capabilities and resilience to noise to be tested experimentally. The next step would be to be able to perform a computational complexity analysis similar to that done previously for the qubit paradigm.

Finally, in the last part, we show the experimental realization of a multi-parameter quantum metrology protocol applied to the estimation of three phases of an integrated chip. We show how the use of pairs of indistinguishable photons increases the sensitivity of the device compared to the use of single photons and also the attainment of the theoretical ultimate limit achievable with such a device. A development of this experiment is the integration of the presented measuring device with a sensor, e.g. of fluids, for the application of the presented algorithms to a real case.

This work paves the way for new technological applications of integrated photonic circuits for information and quantum computation applications.

Part VI

Appendices

Appendix A

Appendix to chapter 2: Hong-Ou-Mandel effect probability

In this appendix, we show the calculation of the Hong-Ou-Mandel effect for a general unitary transformation. First, we calculate the states at the outputs i and j when two photons, respectively in the state $|\phi\rangle$ e $|\psi\rangle$, are injected in the input modes h and k of a linear optical network implementing a unitary transformation U. We first choose an orthonormal basis to express the states on the two input modes:

$$|\phi\rangle_h = \sum_l \alpha_l a_{lh}^\dagger |0\rangle \quad \sum_l |\alpha_l|^2 = 1 \qquad |\psi\rangle_k = \sum_m \beta_m a_{mk}^\dagger |0\rangle \quad \sum_m |\beta_m|^2 = 1 \tag{A.1}$$

Then, the two-photon states is expanded as:

$$|\phi\rangle_h \otimes |\psi\rangle_k = \sum_{l,m} \alpha_l \beta_m a_{lh}^\dagger a_{mk}^\dagger |0\rangle \tag{A.2}$$

The state after the unitary evolution is:

$$\begin{aligned} \tilde{U} |\phi\rangle_h \otimes |\psi\rangle_k &= \sum_{l,m} \alpha_l \beta_m \hat{U} a_{lh}^\dagger \hat{U}^\dagger \hat{U} a_{mk}^\dagger \hat{U}^\dagger |0\rangle \\ &= \sum_{l,m} \alpha_l \beta_m \left(\sum_r U_{rh} a_{lr}^\dagger \right) \left(\sum_s U_{sk} a_{ms}^\dagger \right) |0\rangle \end{aligned} \tag{A.3}$$

since we are interested only when the photons come out in the outputs i or j we can see only the component where $r, s \in \{i, j\}$

$$\begin{aligned} &\sum_{l,m} \alpha_l \beta_m (U_{ih} a_{li}^\dagger + U_{jh} a_{lj}^\dagger)(U_{ik} a_{mi}^\dagger + U_{jk} a_{mj}^\dagger) |0\rangle \\ &= \sum_{l,m} \alpha_l \beta_m (U_{ih} U_{jk} a_{li}^\dagger a_{mj}^\dagger + U_{jh} U_{ik} a_{lj}^\dagger a_{mi}^\dagger + U_{ih} U_{ik} a_{li}^\dagger a_{mi}^\dagger + U_{jh} U_{jk} a_{lj}^\dagger a_{mj}^\dagger) |0\rangle \\ &= \sum_{l,m} \underbrace{(U_{ih} U_{jk} \alpha_l \beta_m + U_{jh} U_{ik} \alpha_m \beta_l) a_{li}^\dagger a_{mj}^\dagger}_{\text{non-collisional term}} + \underbrace{\alpha_l \beta_m (U_{ih} U_{ik} a_{il}^\dagger a_{im}^\dagger + U_{jh} U_{jk} a_{jl}^\dagger a_{jm}^\dagger)}_{\text{colisional term}} |0\rangle \end{aligned} \tag{A.4}$$

In the final expression, we can recognize two terms: the first one is the non-collisional therm which is when the two photons exit from different outputs of the interferometer; the second one is the collisional therm which is when the two photons exit from the same output of the interferometer. Since are interested in the probability of measuring two photons in two different output ports $i \neq j$, we calculate the probability that the output state is in the non-collisional term

$$\begin{aligned} P_{ij}^{hk} &= \sum_{l,m} (U_{ih}U_{jk}\alpha_l\beta_m + U_{jh}U_{ik}\alpha_m\beta_l)(U_{ih}U_{jk}\alpha_l\beta_m + U_{jh}U_{ik}\alpha_m\beta_l)^* \\ &= |U_{ih}|^2|U_{jk}|^2 + |U_{jh}|^2|U_{ik}|^2 + (U_{ih}U_{jk}U_{jh}^*U_{ik}^* + U_{jh}U_{ik}U_{ih}^*U_{jk}^*)|\langle\phi|\psi\rangle|^2 \end{aligned} \tag{A.5}$$

In this expression, we observe that the indistinguishable photons scenario is obtained for $|\langle\phi|\psi\rangle|^2 = 1$, while the distinguishable particle case corresponds to $|\langle\phi|\psi\rangle|^2 = 0$. Using the definition of the HOM visibility, we find Eq. (2) of the main text.

$$\mathcal{V}_{ij}^{hk} = 1 - \frac{(P_{ij}^{hk})^{\mathrm{I}}}{(P_{ij}^{hk})^{\mathrm{D}}} = -\frac{U_{ih}U_{jk}U_{jh}^*U_{ik}^* + U_{jh}U_{ik}U_{ih}^*U_{jk}^*}{|U_{ih}|^2|U_{jk}|^2 + |U_{jh}|^2|U_{ik}|^2} \tag{A.6}$$

When residual distinguishability is present the measured visibility follows the following equation:

$$\mathcal{V}_{ij}^{hk} = -\frac{U_{ih}U_{jk}U_{jh}^*U_{ik}^* + U_{jh}U_{ik}U_{ih}^*U_{jk}^*}{|U_{ih}|^2|U_{jk}|^2 + |U_{jh}|^2|U_{ik}|^2}|\langle\phi|\psi\rangle|^2 \tag{A.7}$$

Appendix B

Appendix to chapter 7: 3D chip validation

In the experiment we benchmarked the integrated device by performing several Boson Sampling experiments with three- and four-photon states. We repeated the measurements for ten different configurations of the optical circuits for the three-photon case, and further three configurations for the four-photon state

$$\rho^{4-\text{photon}} \sim \frac{1}{\alpha+\beta+\gamma}\left(\alpha\,|1111\rangle\langle 1111| + \beta\,|2002\rangle\langle 2002| + \gamma\,|0220\rangle\langle 0220|\right), \quad \text{(B.1)}$$

We adopted the likelihood ratio tests to assign the data to a given hypothesis. First, the data were validated against the uniform sampler [284]. This algorithm requires the estimation of the quantifier $\mathcal{P} = \prod_i \sum_j |U_{ij}|^2$ where the index i labels the modes in which photons are detected, the index j the input modes and U the unitary matrix representing the circuit. The counter W initialized to zero is updated after the measurement k according to the following rule

$$W_k = \begin{cases} W_{k-1} + 1 & \text{if } \mathcal{P} \geq \left(\frac{n}{m}\right)^n \\ W_{k-1} - 1 & \text{if } \mathcal{P} < \left(\frac{n}{m}\right)^n, \end{cases} \quad \text{(B.2)}$$

where n and m are the numbers of photons and modes in the optical circuit. The intuition behind this method is that the quantifier $\mathcal{P}$ reflects somehow the probability to observe the outcome k. If this quantity is greater than the uniform probability it is plausible that the event was sampled from a non-trivial distribution. The second test applied to the Boson Sampling data regards the validation against the distinguishable particles [223]. In this case, the quantifier is the ratio between the probability $q = |\text{Per}\, U_{(ij)}|^2$ to detect indistinguishable particles, and the probability $d = \text{Per}\,|U_{(ij)}|^2$ to detect distinguishable particles in the set of output modes j given the input modes labelled by i. $U_{(ij)}$ stands for the sub-matrix identified by the input labels i and output labels j and Per is the matrix permanent. By defining $\mathcal{L} = \frac{q}{d}$, the counter C is updated after each outcome k from the Boson Sampling as

$$C_k = \begin{cases} C_{k-1} + 1 & \text{if } \mathcal{L} \geq 1 \\ C_{k-1} - 1 & \text{if } \mathcal{L} < 1, \end{cases} \quad \text{(B.3)}$$

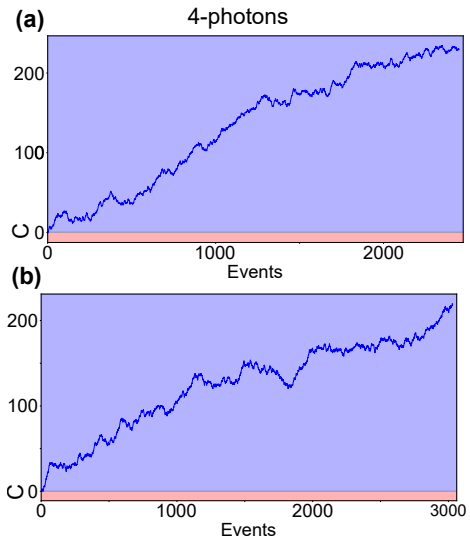

Figure B.1. 4-photon experiments validation. We report the validations against the distinguishable particle hypothesis for the state in Eq. (B.1). These further 4-photon experiments were not reported in the main chapter.

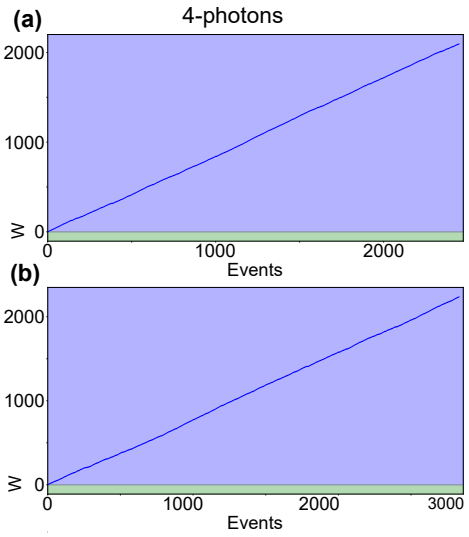

Figure B.2. 4-photon experiments validation. We report the validations against the uniform hypothesis for the state in Eq. (B.1). These further 4-photon experiments were not reported in the main chapter.

Note that the expressions of p and q are related to the collision-free subspace accessible in the reported experiment. Furthermore, both quantifiers $\mathcal{P}$ and $\mathcal{L}$ depend on the element of the matrix U representing the interferometer.

In Fig. B.1-B.2 we report the validation tests performed for the two four-photon experiments not included in the main chapter. In Fig. B.3-B.4 we have reported the nine three-photon Boson Sampling validations whose slope values are reported in Fig. 7.6.

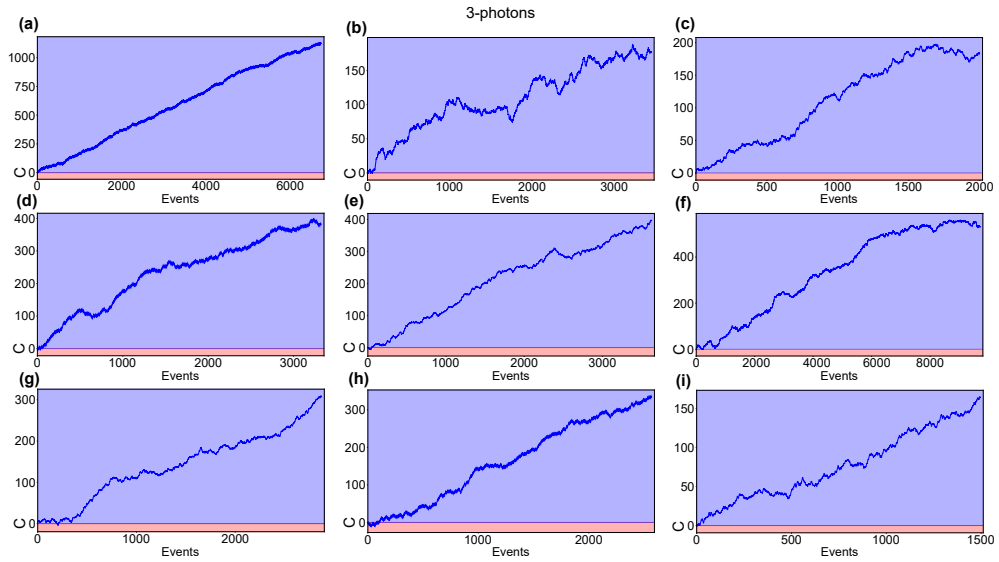

Figure B.3. 3-photon Boson Sampling validations against the distinguishable particle sampler. We report the complete set of Boson Sampling experiments for the 3-photon case states. The plots report the validation against the distinguishable samplers for different settings of the optical circuits. The validation is successful in all nine cases.

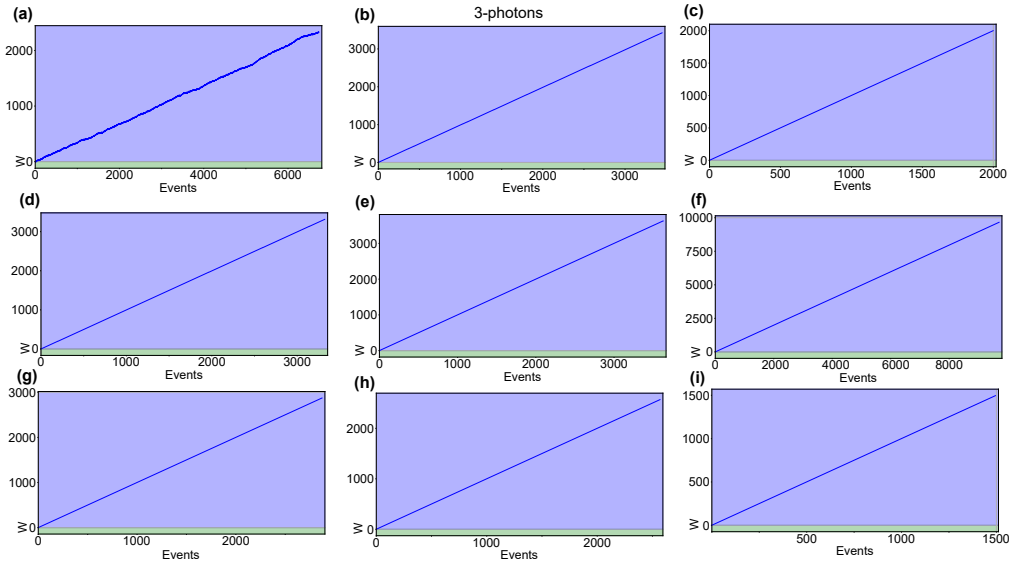

Figure B.4. 3-photon Boson Sampling validations against the uniform distribution. We report the complete set of Boson Sampling experiments for the 3-photon case states. The plots report the validation against the uniform sampler for different settings of the optical circuits. The validation is successful in all nine cases.

Appendix C

Appendix to chapter 8: Succes probability of $g(z) = 2z^2 + z$

In this appendix, we prove the equations (8.23) and (8.24) for the success probability of the function $g(z) = 2z^2 + z$ as a function of the number of qubits used in the implementation of the Quantum Bernoulli Factory. Starting from the general equation (8.22) it is possible to replace the coefficients p_j and q_j with those of our polynomial and obtain the equation

$$P_n(z) = \frac{2(\left|2z^2+z\right|^2+1)}{(1+|z|^2)^n\left(\left|\frac{n+7}{n(n-1)}-1\right|+\frac{n+7}{n(n-1)}+1\right)} = \frac{\left|2z^2+z\right|^2+1}{(1+|z|^2)^n\max\{1,\frac{n+7}{n(n-1)}\}} \tag{C.1}$$

Now we have to integrate the success probability over the distribution of states that can be presented to the circuit. For the Eq (8.23) we have to integrate the success probability over the distribution of all the states uniformly. Using the Eq (1.30) we can writhe the equation

$$< P_n >= \frac{1}{4\pi}\int_{-1}^{1} \mathrm{d}h \int_0^{2\pi} \mathrm{d}\phi\, P_n\left(\sqrt{\frac{1+h}{1-h}}e^{i\phi}\right) \tag{C.2}$$

$$< P_n >= \frac{1}{2^{n+1}\max\{1,\frac{n+7}{n(n-1)}\}}\int_{-1}^{1} \mathrm{d}h\, 4(1+h)^{n-2}(1+h)^2+(1-h)^{n-1}(1+h)+(1-h)^n \tag{C.3}$$

$$< P_n >= \frac{1}{2^{n+1}\max\{1,\frac{n+7}{n(n-1)}\}}\left(4\frac{2^{n+2}}{(n+1)n(n-1)}+\frac{2^{n+1}}{(n+1)n}+\frac{2^{n+1}}{(n+1)}\right) \tag{C.4}$$

$$< P_n >= \frac{n^2+7}{(n-1)n(n+1)\max\{1,\frac{n+7}{n(n-1)}\}} \tag{C.5}$$

For the Eq (8.24) the procedure is similar but the set of equatorial state (state in the form $(e^{i\phi}|0\rangle + |1\rangle)/\sqrt{2}$) we can write the equation as

$$< P_n >= \frac{1}{2\pi}\int_0^{2\pi} \mathrm{d}\phi\, P_n\left(e^{i\phi}\right) \tag{C.6}$$

that explicitly became

$$< P_n >= \frac{1}{2^{n+1}\pi \max\{1, \frac{n+7}{n(n-1)}\}} \int_0^{2\pi} \mathrm{d}\phi \; 6 + 4\cos(3\phi) \tag{C.7}$$

$$< P_n >= \frac{6}{2^n \max\{1, \frac{n+7}{n(n-1)}\}} \tag{C.8}$$

Acronym

BBO	Beta-Barium Borat
BS	Beam splitter
CRB	Cramér-Rao bound
ECCT	Extended Church-Turing thesis
FI	Fisher Information
HL	Heisemberg limit
HOM	Hong-Ou-Mandel
KTP	Potassium titanyl phosphate
MLE	Maximum likelihood estimator
MSE	Mean-square error
OAM	Orbital angular momentum
QCRB	Quantum Cramér-Rao bound
QFI	Quantum Fisher Information
QP	Q-plate
QQBF	Quantum to Quantum Bernoulli factory
SFWM	Spontaneous four-wave mixing
SQL	Standard Quantum Limit
SLD	Symmetric logarithmic derivative
SPAD	Single-photon avalanche photodiodes
SPDC	Spontaneous parametric down-conversion

Bibliography

[1] Taira Giordani, Chiara Esposito, Francesco Hoch, Gonzalo Carvacho, Daniel J. Brod, Ernesto F. Galvão, Nicolò Spagnolo, and Fabio Sciarrino. Witnesses of coherence and dimension from multiphoton indistinguishability tests. *Physical Review Research*, 3(2), April 2021.

[2] Francesco Hoch, Simone Piacentini, Taira Giordani, Zhen-Nan Tian, Mariagrazia Iuliano, Chiara Esposito, Anita Camillini, Gonzalo Carvacho, Francesco Ceccarelli, Nicolò Spagnolo, Andrea Crespi, Fabio Sciarrino, and Roberto Osellame. Reconfigurable continuously-coupled 3d photonic circuit for boson sampling experiments. *npj Quantum Information*, 8(1), May 2022.

[3] Francesco Hoch, Taira Giordani, Nicolò Spagnolo, Andrea Crespi, Roberto Osellame, and Fabio Sciarrino. Characterization of multimode linear optical networks. *Advanced Photonics Nexus*, 2(01), January 2023.

[4] Mauro Valeri, Valeria Cimini, Simone Piacentini, Francesco Ceccarelli, Emanuele Polino, Francesco Hoch, Gabriele Bizzarri, Giacomo Corrielli, Nicolò Spagnolo, Roberto Osellame, and Fabio Sciarrino. Experimental multiparameter quantum metrology in adaptive regime, Feb 2023.

[5] Valeria Cimini, Emanuele Polino, Federico Belliardo, Francesco Hoch, Bruno Piccirillo, Nicolò Spagnolo, Vittorio Giovannetti, and Fabio Sciarrino. Non-asymptotic heisenberg scaling: experimental metrology for a wide resources range, 2021.

[6] Federico Belliardo, Valeria Cimini, Emanuele Polino, Francesco Hoch, Bruno Piccirillo, Nicolò Spagnolo, Vittorio Giovannetti, and Fabio Sciarrino. Optimizing quantum-enhanced bayesian multiparameter estimation in noisy apparata, 2022.

[7] Han-Sen Zhong, Yu-Hao Deng, Jian Qin, Hui Wang, Ming-Cheng Chen, Li-Chao Peng, Yi-Han Luo, Dian Wu, Si-Qiu Gong, Hao Su, Yi Hu, Peng Hu, Xiao-Yan Yang, Wei-Jun Zhang, Hao Li, Yuxuan Li, Xiao Jiang, Lin Gan, Guangwen Yang, Lixing You, Zhen Wang, Li Li, Nai-Le Liu, Jelmer J. Renema, Chao-Yang Lu, and Jian-Wei Pan. Phase-programmable gaussian boson sampling using stimulated squeezed light. *Phys. Rev. Lett.*, 127:180502, Oct 2021.

[8] Lars S. Madsen, Fabian Laudenbach, Mohsen Falamarzi. Askarani, Fabien Rortais, Trevor Vincent, Jacob F. F. Bulmer, Filippo M. Miatto, Leonhard

Neuhaus, Lukas G. Helt, Matthew J. Collins, Adriana E. Lita, Thomas Gerrits, Sae Woo Nam, Varun D. Vaidya, Matteo Menotti, Ish Dhand, Zachary Vernon, Nicolás Quesada, and Jonathan Lavoie. Quantum computational advantage with a programmable photonic processor. *Nature*, 606(7912):75–81, June 2022.

[9] William R. Clements, Peter C. Humphreys, Benjamin J. Metcalf, W. Steven Kolthammer, and Ian A. Walmsley. Optimal design for universal multiport interferometers. *Optica*, 3(12):1460–1465, Dec 2016.

[10] Fulvio Flamini, Lorenzo Magrini, Adil S Rab, Nicolò Spagnolo, Vincenzo D'Ambrosio, Paolo Mataloni, Fabio Sciarrino, Tommaso Zandrini, Andrea Crespi, Roberta Ramponi, and Roberto Osellame. Thermally reconfigurable quantum photonic circuits at telecom wavelength by femtosecond laser micromachining. *Light: Science & Applications*, 4(11):e354–e354, November 2015.

[11] Nicolò Spagnolo, Lorenzo Aparo, Chiara Vitelli, Andrea Crespi, Roberta Ramponi, Roberto Osellame, Paolo Mataloni, and Fabio Sciarrino. Quantum interferometry with three-dimensional geometry. *Scientific Reports*, 2(1), November 2012.

[12] M. S. Keane and George L. O'Brien. A bernoulli factory. *ACM Trans. Model. Comput. Simul.*, 4(2):213–219, April 1994.

[13] A. C. Thomas and Jose H. Blanchet. A practical implementation of the bernoulli factory, 2011.

[14] MARK HUBER. Nearly optimal bernoulli factories for linear functions. *Combinatorics, Probability and Computing*, 25(4):577–591, 2016.

[15] Elchanan Mossel and Yuval Peres. New coins from old: Computing with unknown bias, December 2005.

[16] Luis Mendo. An asymptotically optimal bernoulli factory for certain functions that can be expressed as power series. *Stochastic Processes and their Applications*, 129(11):4366–4384, November 2019.

[17] Howard Dale, David Jennings, and Terry Rudolph. Provable quantum advantage in randomness processing. *Nature Communications*, 6(1), September 2015.

[18] Jiaqing Jiang, Jialin Zhang, and Xiaoming Sun. Quantum-to-quantum bernoulli factory problem. *Physical Review A*, 97(3), March 2018.

[19] Howard Dale. Quantum coins and quantum sampling, 2016.

[20] Yong Liu, Jiaqing Jiang, Pingyu Zhu, Dongyang Wang, Jiangfang Ding, Xiaogang Qiang, Anqi Huang, Ping Xu, Jialin Zhang, Guojing Tian, Xiang Fu, Mingtang Deng, Chunqing Wu, Xiaoming Sun, Xuejun Yang, and Junjie Wu. General quantum bernoulli factory: framework analysis and experiments. *Quantum Science and Technology*, 6(4):045025, sep 2021.

[21] Xiao Yuan, Ke Liu, Yuan Xu, Weiting Wang, Yuwei Ma, Fang Zhang, Zhaopeng Yan, R. Vijay, Luyan Sun, and Xiongfeng Ma. Experimental quantum randomness processing using superconducting qubits. *Physical Review Letters*, 117(1), June 2016.

[22] Raj B. Patel, Terry Rudolph, and Geoff J. Pryde. An experimental quantum bernoulli factory. *Science Advances*, 5(1):eaau6668, January 2019.

[23] Xiang Zhan, Kunkun Wang, Lei Xiao, Zhihao Bian, and Peng Xue. Experimental demonstration of quantum-to-quantum bernoulli factory. *Physical Review A*, 102(1), July 2020.

[24] https://www.phoqusing.eu.

[25] Anthony Laing and Jeremy L. O'Brien. Super-stable tomography of any linear optical device, 2012.

[26] Michael A. Nielsen and Isaac L. Chuang. *Quantum Computation and Quantum Information*. Cambridge University Press, 2009.

[27] Aram W. Harrow and Ashley Montanaro. Quantum computational supremacy. *Nature*, 549(7671):203–209, September 2017.

[28] Frank Arute, Kunal Arya, Ryan Babbush, Dave Bacon, Joseph Bardin, Rami Barends, Rupak Biswas, Sergio Boixo, Fernando Brandao, David Buell, Brian Burkett, Yu Chen, Jimmy Chen, Ben Chiaro, Roberto Collins, William Courtney, Andrew Dunsworth, Edward Farhi, Brooks Foxen, Austin Fowler, Craig Michael Gidney, Marissa Giustina, Rob Graff, Keith Guerin, Steve Habegger, Matthew Harrigan, Michael Hartmann, Alan Ho, Markus Rudolf Hoffmann, Trent Huang, Travis Humble, Sergei Isakov, Evan Jeffrey, Zhang Jiang, Dvir Kafri, Kostyantyn Kechedzhi, Julian Kelly, Paul Klimov, Sergey Knysh, Alexander Korotkov, Fedor Kostritsa, Dave Landhuis, Mike Lindmark, Erik Lucero, Dmitry Lyakh, Salvatore Mandrà, Jarrod Ryan McClean, Matthew McEwen, Anthony Megrant, Xiao Mi, Kristel Michielsen, Masoud Mohseni, Josh Mutus, Ofer Naaman, Matthew Neeley, Charles Neill, Murphy Yuezhen Niu, Eric Ostby, Andre Petukhov, John Platt, Chris Quintana, Eleanor G. Rieffel, Pedram Roushan, Nicholas Rubin, Daniel Sank, Kevin J. Satzinger, Vadim Smelyanskiy, Kevin Jeffery Sung, Matt Trevithick, Amit Vainsencher, Benjamin Villalonga, Ted White, Z. Jamie Yao, Ping Yeh, Adam Zalcman, Hartmut Neven, and John Martinis. Quantum supremacy using a programmable superconducting processor. *Nature*, 574:505–510, 2019.

[29] Yulin Wu, Wan-Su Bao, Sirui Cao, Fusheng Chen, Ming-Cheng Chen, Xiawei Chen, Tung-Hsun Chung, Hui Deng, Yajie Du, Daojin Fan, Ming Gong, Cheng Guo, Chu Guo, Shaojun Guo, Lianchen Han, Linyin Hong, He-Liang Huang, Yong-Heng Huo, Liping Li, Na Li, Shaowei Li, Yuan Li, Futian Liang, Chun Lin, Jin Lin, Haoran Qian, Dan Qiao, Hao Rong, Hong Su, Lihua Sun, Liangyuan Wang, Shiyu Wang, Dachao Wu, Yu Xu, Kai Yan, Weifeng Yang, Yang Yang, Yangsen Ye, Jianghan Yin, Chong Ying, Jiale Yu, Chen Zha, Cha Zhang, Haibin Zhang, Kaili Zhang, Yiming Zhang, Han Zhao, Youwei Zhao, Liang

Zhou, Qingling Zhu, Chao-Yang Lu, Cheng-Zhi Peng, Xiaobo Zhu, and Jian-Wei Pan. Strong quantum computational advantage using a superconducting quantum processor. *Phys. Rev. Lett.*, 127:180501, Oct 2021.

[30] Feng Pan, Keyang Chen, and Pan Zhang. Solving the sampling problem of the sycamore quantum circuits. *Phys. Rev. Lett.*, 129:090502, Aug 2022.

[31] Bureau international des poids et mesures, editor. *General Conference on Weights and Measures Proceedings of the 26th meeting of the CGPM*. Imprimerie Agate, November 2018.

[32] W. Heisenberg. *Über den anschaulichen Inhalt der quantentheoretischen Kinematik und Mechanik*, pages 478–504. Springer Berlin Heidelberg, Berlin, Heidelberg, 1985.

[33] Charles H. Bennett and Stephen J. Wiesner. Communication via one- and two-particle operators on einstein-podolsky-rosen states. *Phys. Rev. Lett.*, 69:2881–2884, Nov 1992.

[34] Charles H. Bennett, Gilles Brassard, Claude Crépeau, Richard Jozsa, Asher Peres, and William K. Wootters. Teleporting an unknown quantum state via dual classical and einstein-podolsky-rosen channels. *Phys. Rev. Lett.*, 70:1895–1899, Mar 1993.

[35] Artur K. Ekert. Quantum cryptography based on bell's theorem. *Phys. Rev. Lett.*, 67:661–663, Aug 1991.

[36] David Deutsch and Richard Jozsa. Rapid solution of problems by quantum computation. *Proceedings of the Royal Society of London. Series A: Mathematical and Physical Sciences*, 439(1907):553–558, December 1992.

[37] Serge Lang. *Complex Analysis*. Graduate Texts in Mathematics. Springer, New York, NY, 4 edition, December 1998.

[38] Helle Bechmann-Pasquinucci and Asher Peres. Quantum cryptography with 3-state systems. *Phys. Rev. Lett.*, 85:3313–3316, Oct 2000.

[39] Matthias Fitzi, Nicolas Gisin, and Ueli Maurer. Quantum solution to the byzantine agreement problem. *Phys. Rev. Lett.*, 87:217901, Nov 2001.

[40] Nicolas J. Cerf, Mohamed Bourennane, Anders Karlsson, and Nicolas Gisin. Security of quantum key distribution using d-level systems. *Phys. Rev. Lett.*, 88:127902, Mar 2002.

[41] D. Bruß and C. Macchiavello. Optimal eavesdropping in cryptography with three-dimensional quantum states. *Phys. Rev. Lett.*, 88:127901, Mar 2002.

[42] Dagmar Bruß. Optimal eavesdropping in quantum cryptography with six states. *Phys. Rev. Lett.*, 81:3018–3021, Oct 1998.

[43] N. K. Langford, R. B. Dalton, M. D. Harvey, J. L. O'Brien, G. J. Pryde, A. Gilchrist, S. D. Bartlett, and A. G. White. Measuring entangled qutrits and their use for quantum bit commitment. *Phys. Rev. Lett.*, 93:053601, Jul 2004.

[44] Daniel M. Greenberger, Michael A. Horne, and Anton Zeilinger. Going beyond bell's theorem, 2007.

[45] Vittorio Giovannetti, Seth Lloyd, and Lorenzo Maccone. Advances in quantum metrology. *Nature Photonics*, 5(4):222–229, March 2011.

[46] Mark Hillery, Vladimír Bužek, and André Berthiaume. Quantum secret sharing. *Physical Review A*, 59(3):1829–1834, March 1999.

[47] W. K. Wootters and W. H. Zurek. A single quantum cannot be cloned. *Nature*, 299(5886):802–803, October 1982.

[48] Yuri Gurevich and Andreas Blass. Quantum circuits with classical channels and the principle of deferred measurements, 2021.

[49] Sanjeev Arora and Boaz Barak. *Computational complexity*. Cambridge University Press, Cambridge, England, April 2009.

[50] Peter W. Shor. Polynomial-time algorithms for prime factorization and discrete logarithms on a quantum computer. *SIAM Journal on Computing*, 26(5):1484–1509, 1997.

[51] Scott Aaronson and Alex Arkhipov. The computational complexity of linear optics. In *Proceedings of the 43rd annual ACM symposium on Theory of computing - STOC '11*. ACM Press, 2011.

[52] Fulvio Flamini, Nicolò Spagnolo, and Fabio Sciarrino. Photonic quantum information processing: a review. *Reports on Progress in Physics*, 82(1):016001, November 2018.

[53] Marlan O. Scully and M. Suhail Zubairy. *Quantum Optics*. Cambridge University Press, September 1997.

[54] Rodney Loudon. *The quantum theory of light*. Oxford University Press, London, England, 3 edition, September 2000.

[55] Alessandro Rossi, Giuseppe Vallone, Andrea Chiuri, Francesco De Martini, and Paolo Mataloni. Multipath entanglement of two photons. *Physical Review Letters*, 102(15), April 2009.

[56] P. J. Shadbolt, M. R. Verde, A. Peruzzo, A. Politi, A. Laing, M. Lobino, J. C. F. Matthews, M. G. Thompson, and J. L. O'Brien. Generating, manipulating and measuring entanglement and mixture with a reconfigurable photonic circuit. *Nature Photonics*, 6(1):45–49, December 2011.

[57] Michael Reck, Anton Zeilinger, Herbert J. Bernstein, and Philip Bertani. Experimental realization of any discrete unitary operator. *Phys. Rev. Lett.*, 73:58–61, Jul 1994.

[58] B. Neethi Simon, C. M. Chandrashekar, and Sudhavathani Simon. Hamilton's turns as a visual tool kit for designing single-qubit unitary gates. *Physical Review A*, 85(2), February 2012.

[59] Bahaa E. A. Saleh. *Fundamentals of Photonics*. Wiley-Interscience, 2007.

[60] Filippo Cardano, Ebrahim Karimi, Sergei Slussarenko, Lorenzo Marrucci, Corrado de Lisio, and Enrico Santamato. Polarization pattern of vector vortex beams generated by q-plates with different topological charges. *Applied Optics*, 51(10):C1, March 2012.

[61] Filippo Cardano, Alessio D'Errico, Alexandre Dauphin, Maria Maffei, Bruno Piccirillo, Corrado de Lisio, Giulio De Filippis, Vittorio Cataudella, Enrico Santamato, Lorenzo Marrucci, Maciej Lewenstein, and Pietro Massignan. Detection of zak phases and topological invariants in a chiral quantum walk of twisted photons. *Nature Communications*, 8(1), June 2017.

[62] Manuel Erhard, Mehul Malik, and Anton Zeilinger. A quantum router for high-dimensional entanglement. *Quantum Science and Technology*, 2(1):014001, March 2017.

[63] Chong-Ki Hong, Zhe-Yu Ou, and Leonard Mandel. Measurement of subpicosecond time intervals between two photons by interference. *Phys. Rev. Lett.*, 59(18):2044, 1987.

[64] Bryan T. Gard, Keith R. Motes, Jonathan P. Olson, Peter P. Rohde, and Jonathan P. Dowling. An introduction to boson-sampling, 2014.

[65] Jian-Wei Pan, Christoph Simon, Časlav Brukner, and Anton Zeilinger. Entanglement purification for quantum communication. *Nature*, 410(6832):1067–1070, April 2001.

[66] Jian-Wei Pan, Sara Gasparoni, Rupert Ursin, Gregor Weihs, and Anton Zeilinger. Experimental entanglement purification of arbitrary unknown states. *Nature*, 423(6938):417–422, May 2003.

[67] Dik Bouwmeester, Jian-Wei Pan, Klaus Mattle, Manfred Eibl, Harald Weinfurter, and Anton Zeilinger. Experimental quantum teleportation. *Nature*, 390(6660):575–579, December 1997.

[68] D. Boschi, S. Branca, F. De Martini, L. Hardy, and S. Popescu. Experimental realization of teleporting an unknown pure quantum state via dual classical and einstein-podolsky-rosen channels. *Physical Review Letters*, 80(6):1121–1125, February 1998.

[69] Jian-Wei Pan, Dik Bouwmeester, Harald Weinfurter, and Anton Zeilinger. Experimental entanglement swapping: Entangling photons that never interacted. *Physical Review Letters*, 80(18):3891–3894, May 1998.

[70] G. Molina-Terriza, A. Vaziri, R. Ursin, and A. Zeilinger. Experimental quantum coin tossing. *Physical Review Letters*, 94(4), January 2005.

[71] Christian Schimpf, Marcus Reindl, Francesco Basso Basset, Klaus D. Jöns, Rinaldo Trotta, and Armando Rastelli. Quantum dots as potential sources of strongly entangled photons: Perspectives and challenges for applications in quantum networks. *Applied Physics Letters*, 118(10):100502, mar 2021.

[72] J. C. Loredo, C. Antón, B. Reznychenko, P. Hilaire, A. Harouri, C. Millet, H. Ollivier, N. Somaschi, L. De Santis, A. Lemaître, I. Sagnes, L. Lanco, A. Auffèves, O. Krebs, and P. Senellart. Generation of non-classical light in a photon-number superposition. *Nature Photonics*, 13(11):803–808, August 2019.

[73] Panagiotis Vergyris, Thomas Meany, Tommaso Lunghi, Gregory Sauder, James Downes, M. J. Steel, Michael J. Withford, Olivier Alibart, and Sébastien Tanzilli. On-chip generation of heralded photon-number states. *Scientific Reports*, 6(1), October 2016.

[74] Simone Atzeni, Adil S. Rab, Giacomo Corrielli, Emanuele Polino, Mauro Valeri, Paolo Mataloni, Nicolò Spagnolo, Andrea Crespi, Fabio Sciarrino, and Roberto Osellame. Integrated sources of entangled photons at the telecom wavelength in femtosecond-laser-written circuits. *Optica*, 5(3):311, March 2018.

[75] Stephan Krapick, Benjamin Brecht, Harald Herrmann, Viktor Quiring, and Christine Silberhorn. On-chip generation of photon-triplet states. *Opt. Express*, 24(3):2836–2849, Feb 2016.

[76] Claire Autebert, Natalia Bruno, Anthony Martin, Aristide Lemaitre, Carmen Gomez Carbonell, Ivan Favero, Giuseppe Leo, Hugo Zbinden, and Sara Ducci. Integrated algaas source of highly indistinguishable and energy-time entangled photons. *Optica*, 3(2):143–146, Feb 2016.

[77] Xiang Guo, Chang ling Zou, Carsten Schuck, Hojoong Jung, Risheng Cheng, and Hong X Tang. Parametric down-conversion photon-pair source on a nanophotonic chip. *Light: Science & Applications*, 6(5):e16249–e16249, November 2016.

[78] Zhizhong Yan, Yuwen Duan, L. G. Helt, Martin Ams, Michael J. Withford, and M. J. Steel. Generation of heralded single photons beyond 1100 nm by spontaneous four-wave mixing in a side-stressed femtosecond laser-written waveguide. *Applied Physics Letters*, 107(23):231106, December 2015.

[79] Justin B. Spring, Paolo L. Mennea, Benjamin J. Metcalf, Peter C. Humphreys, James C. Gates, Helen L. Rogers, Christoph Söller, Brian J. Smith, W. Steven Kolthammer, Peter G. R. Smith, and Ian A. Walmsley. Chip-based array of near-identical, pure, heralded single-photon sources. *Optica*, 4(1):90–96, Jan 2017.

[80] J. W. Silverstone, D. Bonneau, K. Ohira, N. Suzuki, H. Yoshida, N. Iizuka, M. Ezaki, C. M. Natarajan, M. G. Tanner, R. H. Hadfield, V. Zwiller, G. D. Marshall, J. G. Rarity, J. L. O'Brien, and M. G. Thompson. On-chip quantum interference between silicon photon-pair sources. *Nature Photonics*, 8:104 EP –, Dec 2013.

[81] S. Paesani, M. Borghi, S. Signorini, A. Maïnos, L. Pavesi, and A. Laing. Near-ideal spontaneous photon sources in silicon quantum photonics. *Nature Communications*, 11(1):2505, May 2020.

[82] S. Signorini, M. Sanna, S. Piccione, M. Ghulinyan, P. Tidemand-Lichtenberg, C. Pedersen, and L. Pavesi. A silicon source of heralded single photons at 2 μm. *APL Photonics*, 6(12):126103, December 2021.

[83] Pisek Kultavewuti, Eric Y. Zhu, Xingxing Xing, Li Qian, Vincenzo Pusino, Marc Sorel, and J. Stewart Aitchison. Polarization-entangled photon pair sources based on spontaneous four wave mixing assisted by polarization mode dispersion. *Scientific Reports*, 7(1), July 2017.

[84] C. Xiong, X. Zhang, A. Mahendra, J. He, D.-Y. Choi, C. J. Chae, D. Marpaung, A. Leinse, R. G. Heideman, M. Hoekman, C. G. H. Roeloffzen, R. M. Oldenbeuving, P. W. L. van Dijk, C. Taddei, P. H. W. Leong, and B. J. Eggleton. Compact and reconfigurable silicon nitride time-bin entanglement circuit. *Optica*, 2(8):724–727, Aug 2015.

[85] J. M. Arrazola, V. Bergholm, K. Brádler, T. R. Bromley, M. J. Collins, I. Dhand, A. Fumagalli, T. Gerrits, A. Goussev, L. G. Helt, J. Hundal, T. Isacsson, R. B. Israel, J. Izaac, S. Jahangiri, R. Janik, N. Killoran, S. P. Kumar, J. Lavoie, A. E. Lita, D. H. Mahler, M. Menotti, B. Morrison, S. W. Nam, L. Neuhaus, H. Y. Qi, N. Quesada, A. Repingon, K. K. Sabapathy, M. Schuld, D. Su, J. Swinarton, A. Száva, K. Tan, P. Tan, V. D. Vaidya, Z. Vernon, Z. Zabaneh, and Y. Zhang. Quantum circuits with many photons on a programmable nanophotonic chip. *Nature*, 591(7848):54–60, March 2021.

[86] Kaiyi Wu, Qianni Zhang, and Andrew W. Poon. Integrated si3n4 microresonator-based quantum light sources with high brightness using a subtractive wafer-scale platform. *Opt. Express*, 29(16):24750–24764, Aug 2021.

[87] M Borghi, C Castellan, S Signorini, A Trenti, and L Pavesi. Nonlinear silicon photonics. *Journal of Optics*, 19(9):093002, aug 2017.

[88] S. Signorini and L. Pavesi. On-chip heralded single photon sources. *AVS Quantum Science*, 2(4):041701, 2020.

[89] J. Wang, S. Paesani, Y. Ding, R. Santagati, P. Skrzypczyk, A. Salavrakos, J. Tura, R. Augusiak, L. Mančinska, D. Bacco, D. Bonneau, J. W. Silverstone, Q. Gong, A. Acín, K. Rottwitt, L. K. Oxenløwe, J. L. O'Brien1, A. Laing, and M. G. Thompson. Multidimensional quantum entanglement with large-scale integrated optics. *Science*, 2018.

[90] Xiaogang Qiang, Xiaoqi Zhou, Jianwei Wang, Callum M. Wilkes, Thomas Loke, Sean O'Gara, Laurent Kling, Graham D. Marshall, Raffaele Santagati, Timothy C. Ralph, Jingbo B. Wang, Jeremy L. O'Brien, Mark G. Thompson, and Jonathan C. F. Matthews. Large-scale silicon quantum photonics implementing arbitrary two-qubit processing. *Nature Photonics*, 12(9):534–539, Sep 2018.

[91] Yulin Chi, Jieshan Huang, Zhanchuan Zhang, Jun Mao, Zinan Zhou, Xiaojiong Chen, Chonghao Zhai, Jueming Bao, Tianxiang Dai, Huihong Yuan, Ming Zhang, Daoxin Dai, Bo Tang, Yan Yang, Zhihua Li, Yunhong Ding, Leif K. Oxenløwe, Mark G. Thompson, Jeremy L. O'Brien, Yan Li, Qihuang Gong, and Jianwei Wang. A programmable qudit-based quantum processor. *Nature Communications*, 13(1):1166, Mar 2022.

[92] F. Kaneda and P. G. Kwiat. High-efficiency single-photon generation via large-scale active time multiplexing. *Science Advances*, 5(10):eaaw8586, 2019.

[93] N. Somaschi, V. Giesz, L. De Santis, J. C. Loredo, M. P. Almeida, G. Hornecker, S. L. Portalupi, T. Grange, C. Antón, J. Demory, C. Gómez, I. Sagnes, N. D. Lanzillotti-Kimura, A. Lemaítre, A. Auffeves, A. G. White, L. Lanco, and P. Senellart. Near-optimal single-photon sources in the solid state. *Nature Photonics*, 10(5):340–345, March 2016.

[94] Fabian Olbrich, Jonatan Höschele, Markus Müller, Jan Kettler, Simone Luca Portalupi, Matthias Paul, Michael Jetter, and Peter Michler. Polarization-entangled photons from an InGaAs-based quantum dot emitting in the telecom c-band. *Applied Physics Letters*, 111(13):133106, September 2017.

[95] Gabija Kiršansk, Henri Thyrrestrup, Raphaël S. Daveau, Chris L. Dreeßen, Tommaso Pregnolato, Leonardo Midolo, Petru Tighineanu, Alisa Javadi, Søren Stobbe, Rüdiger Schott, Arne Ludwig, Andreas D. Wieck, Suk In Park, Jin D. Song, Andreas V. Kuhlmann, Immo Söllner, Matthias C. Löbl, Richard J. Warburton, and Peter Lodahl. Indistinguishable and efficient single photons from a quantum dot in a planar nanobeam waveguide. *Phys. Rev. B*, 96:165306, Oct 2017.

[96] Alexander Schlehahn, Sarah Fischbach, Ronny Schmidt, Arsenty Kaganskiy, André Strittmatter, Sven Rodt, Tobias Heindel, and Stephan Reitzenstein. A stand-alone fiber-coupled single-photon source. *Scientific Reports*, 8(1), January 2018.

[97] H. Snijders, J. A. Frey, J. Norman, V. P. Post, A. C. Gossard, J. E. Bowers, M. P. van Exter, W. Löffler, and D. Bouwmeester. Fiber-coupled cavity-qed source of identical single photons. *Phys. Rev. Applied*, 9:031002, Mar 2018.

[98] Francesco Lenzini, Ben Haylock, Juan C. Loredo, Raphael A. Abrahão, Nor A. Zakaria, Sachin Kasture, Isabelle Sagnes, Aristide Lemaitre, Hoang-Phuong Phan, Dzung Viet Dao, Pascale Senellart, Marcelo P. Almeida, Andrew G. White, and Mirko Lobino. Active demultiplexing of single photons from a solid-state source. *Laser & Photonics Reviews*, 11(3):1600297, April 2017.

[99] C. Antón, J. C. Loredo, G. Coppola, H. Ollivier, N. Viggianiello, A. Harouri, N. Somaschi, A. Crespi, I. Sagnes, A. Lemaître, L. Lanco, R. Osellame, F. Sciarrino, and P. Senellart. Interfacing scalable photonic platforms: solid-state based multi-photon interference in a reconfigurable glass chip. *Optica*, 6(12):1471–1477, Dec 2019.

[100] Stephen C. Wein, Juan C. Loredo, Maria Maffei, Paul Hilaire, Abdelmounaim Harouri, Niccolo Somaschi, Aristide Lemaître, Isabelle Sagnes, Loïc Lanco, Olivier Krebs, Alexia Auffèves, Christoph Simon, Pascale Senellart, and Carlos Antón-Solanas. Photon-number entanglement generated by sequential excitation of a two-level atom. *Nature Photonics*, 16(5):374–379, April 2022.

[101] Robert W Boyd. *Nonlinear Optics*. Academic Press, San Diego, CA, 3 edition, March 2008.

[102] Christophe Couteau. Spontaneous parametric down-conversion. *Contemporary Physics*, 59(3):291–304, July 2018.

[103] Osung Kwon, Young-Wook Cho, and Yoon-Ho Kim. Single-mode coupling efficiencies of type-II spontaneous parametric down-conversion: Collinear, noncollinear, and beamlike phase matching. *Physical Review A*, 78(5), November 2008.

[104] N. Boeuf. Calculating characteristics of noncollinear phase matching in uniaxial and biaxial crystals. *Optical Engineering*, 39(4):1016, April 2000.

[105] Han-Sen Zhong, Yuan Li, Wei Li, Li-Chao Peng, Zu-En Su, Yi Hu, Yu-Ming He, Xing Ding, Weijun Zhang, Hao Li, Lu Zhang, Zhen Wang, Lixing You, Xi-Lin Wang, Xiao Jiang, Li Li, Yu-Ao Chen, Nai-Le Liu, Chao-Yang Lu, and Jian-Wei Pan. 12-photon entanglement and scalable scattershot boson sampling with optimal entangled-photon pairs from parametric down-conversion. *Physical Review Letters*, 121(25), December 2018.

[106] Álvaro Cuevas, Andrea Geraldi, Carlo Liorni, Luís Diego Bonavena, Antonella De Pasquale, Fabio Sciarrino, Vittorio Giovannetti, and Paolo Mataloni. All-optical implementation of collision-based evolutions of open quantum systems. *Scientific Reports*, 9(1), March 2019.

[107] Hui Wang, Yu He, Yu-Huai Li, Zu-En Su, Bo Li, He-Liang Huang, Xing Ding, Ming-Cheng Chen, Chang Liu, Jian Qin, Jin-Peng Li, Yu-Ming He, Christian Schneider, Martin Kamp, Cheng-Zhi Peng, Sven Höfling, Chao-Yang Lu, and Jian-Wei Pan. High-efficiency multiphoton boson sampling. *Nature Photonics*, 11(6):361–365, May 2017.

[108] Yu He, X. Ding, Z.-E. Su, H.-L. Huang, J. Qin, C. Wang, S. Unsleber, C. Chen, H. Wang, Y.-M. He, X.-L. Wang, W.-J. Zhang, S.-J. Chen, C. Schneider, M. Kamp, L.-X. You, Z. Wang, S. Höfling, Chao-Yang Lu, and Jian-Wei Pan. Time-bin-encoded boson sampling with a single-photon device. *Physical Review Letters*, 118(19), May 2017.

[109] M. V. Chekhova and Z. Y. Ou. Nonlinear interferometers in quantum optics. *Advances in Optics and Photonics*, 8(1):104, March 2016.

[110] Hui Wang, Wei Li, Xiao Jiang, Y.-M. He, Y.-H. Li, X. Ding, M.-C. Chen, J. Qin, C.-Z. Peng, C. Schneider, M. Kamp, W.-J. Zhang, H. Li, L.-X. You, Z. Wang, J. P. Dowling, S. Höfling, Chao-Yang Lu, and Jian-Wei Pan. Toward

scalable boson sampling with photon loss. *Physical Review Letters*, 120(23), June 2018.

[111] L. Vivien and L. Pavesi. *Handbook of Silicon Photonics*. CRC press, 2013.

[112] Menno Poot, Carsten Schuck, Xiao song Ma, Xiang Guo, and Hong X. Tang. Design and characterization of integrated components for sin photonic quantum circuits. *Opt. Express*, 24(7):6843–6860, Apr 2016.

[113] Daniel Llewellyn, Yunhong Ding, Imad I. Faruque, Stefano Paesani, Davide Bacco, Raffaele Santagati, Yan-Jun Qian, Yan Li, Yun-Feng Xiao, Marcus Huber, Mehul Malik, Gary F. Sinclair, Xiaoqi Zhou, Karsten Rottwitt, Jeremy L. O'Brien, John G. Rarity, Qihuang Gong, Leif K. Oxenlowe, Jianwei Wang, and Mark G. Thompson. Chip-to-chip quantum teleportation and multi-photon entanglement in silicon. *Nature Physics*, 16(2):148–153, Feb 2020.

[114] Carlos Abellan, Waldimar Amaya, David Domenech, Pascual Mu noz, Jose Capmany, Stefano Longhi, Morgan W. Mitchell, and Valerio Pruneri. Quantum entropy source on an inp photonic integrated circuit for random number generation. *Optica*, 3(9):989–994, Sep 2016.

[115] Stefano Paesani, Yunhong Ding, Raffaele Santagati, Levon Chakhmakhchyan, Caterina Vigliar, Karsten Rottwitt, Leif K. Oxenløwe, Jianwei Wang, Mark G. Thompson, and Anthony Laing. Generation and sampling of quantum states of light in a silicon chip. *Nature Physics*, 15(9):925–929, 2019.

[116] Jianwei Wang, Stefano Paesani, Raffaele Santagati, Sebastian Knauer, Antonio A Gentile, Nathan Wiebe, Maurangelo Petruzzella, Jeremy L O'Brien, John G Rarity, Anthony Laing, et al. Experimental quantum hamiltonian learning. *Nat. Phys.*, 13(6):551, 2017.

[117] Raffaele Santagati, Jianwei Wang, Antonio A. Gentile, Stefano Paesani, Nathan Wiebe, Jarrod R. McClean, Sam Morley-Short, Peter J. Shadbolt, Damien Bonneau, Joshua W. Silverstone, David P. Tew, Xiaoqi Zhou, Jeremy L. O'Brien, and Mark G. Thompson. Witnessing eigenstates for quantum simulation of hamiltonian spectra. *Science Advances*, 4(1), 2018.

[118] Jeremy C. Adcock, Caterina Vigliar, Raffaele Santagati, Joshua W. Silverstone, and Mark G. Thompson. Programmable four-photon graph states on a silicon chip. *Nature Communications*, 10(1):3528, Aug 2019.

[119] Caterina Vigliar, Stefano Paesani, Yunhong Ding, Jeremy C. Adcock, Jianwei Wang, Sam Morley-Short, Davide Bacco, Leif K. Oxenløwe, Mark G. Thompson, John G. Rarity, and Anthony Laing. Error-protected qubits in a silicon photonic chip. *Nature Physics*, 17(10):1137–1143, Oct 2021.

[120] Caterina Taballione, Reinier van der Meer, Henk J Snijders, Peter Hooijschuur, Jörn P Epping, Michiel de Goede, Ben Kassenberg, Pim Venderbosch, Chris Toebes, Hans van den Vlekkert, Pepijn W H Pinkse, and Jelmer J Renema. A universal fully reconfigurable 12-mode quantum photonic processor. *Materials for Quantum Technology*, 1(3):035002, August 2021.

[121] Caterina Taballione, Malaquias Correa Anguita, Michiel de Goede, Pim Venderbosch, Ben Kassenberg, Henk Snijders, Narasimhan Kannan, Devin Smith, Jörn P. Epping, Reinier van der Meer, Pepijn W. H. Pinkse, Hans van den Vlekkert, and Jelmer J. Renema. 20-mode universal quantum photonic processor, 2022.

[122] Andreas Boes, Bill Corcoran, Lin Chang, John Bowers, and Arnan Mitchell. Status and potential of lithium niobate on insulator (lnoi) for photonic integrated circuits. *Laser & Photonics Reviews*, 12(4):1700256, 2018.

[123] Yuechen Jia, Lei Wang, and Feng Chen. Ion-cut lithium niobate on insulator technology: Recent advances and perspectives. *Applied Physics Reviews*, 8(1):011307, 2021.

[124] Christof P. Dietrich, Andrea Fiore, Mark G. Thompson, Martin Kamp, and Sven Höfling. Gaas integrated quantum photonics: Towards compact and multi-functional quantum photonic integrated circuits. *Laser & Photonics Reviews*, 10(6):870–894, 2016.

[125] Meint Smit, Kevin Williams, and Jos van der Tol. Past, present, and future of inp-based photonic integration. *APL Photonics*, 4(5):050901, 2019.

[126] Emanuele Pelucchi, Giorgos Fagas, Igor Aharonovich, Dirk Englund, Eden Figueroa, Qihuang Gong, Hübel Hannes, Jin Liu, Chao-Yang Lu, Nobuyuki Matsuda, Jian-Wei Pan, Florian Schreck, Fabio Sciarrino, Christine Silberhorn, Jianwei Wang, and Klaus D. Jöns. The potential and global outlook of integrated photonics for quantum technologies. *Nature Reviews Physics*, 4(3):194–208, Mar 2022.

[127] Alberto Politi, Martin J. Cryan, John G. Rarity, Siyuan Yu, and Jeremy L. O'Brien. Silica-on-silicon waveguide quantum circuits. *Science*, 320(5876):646–649, 2008.

[128] Alberto Politi, Jonathan C. F. Matthews, and Jeremy L. O'Brien. Shor’s quantum factoring algorithm on a photonic chip. *Science*, 325(5945):1221–1221, 2009.

[129] P. J. Shadbolt, M. R. Verde, A. Peruzzo, A. Politi, A. Laing, M. Lobino, J. C. F. Matthews, M. G. Thompson, and J. L. O'Brien. Generating, manipulating and measuring entanglement and mixture with a reconfigurable photonic circuit. *Nature Photonics*, 6(1):45–49, Jan 2012.

[130] Alberto Peruzzo, Jarrod McClean, Peter Shadbolt, Man-Hong Yung, Xiao-Qi Zhou, Peter J. Love, Alán Aspuru-Guzik, and Jeremy L. O'Brien. A variational eigenvalue solver on a photonic quantum processor. *Nature Communications*, 5(1):4213, Jul 2014.

[131] Jacques Carolan, Christopher Harrold, Chris Sparrow, Enrique Martín-López, Nicholas J. Russell, Joshua W. Silverstone, Peter J. Shadbolt, Nobuyuki Matsuda, Manabu Oguma, Mikitaka Itoh, Graham D. Marshall, Mark G. Thomp-

son, Jonathan C. F. Matthews, Toshikazu Hashimoto, Jeremy L. O'Brien, and Anthony Laing. Universal linear optics. *Science*, 349(6249):711–716, 2015.

[132] M Svalgaard, CV Poulsen, A Bjarklev, and Ole Poulsen. Direct uv writing of buried singlemode channel waveguides in ge-doped silica films. *Electronics Letters*, 30(17):1401–1403, 1994.

[133] Justin B Spring, Benjamin J Metcalf, Peter C Humphreys, W Steven Kolthammer, Xian-Min Jin, Marco Barbieri, Animesh Datta, Nicholas Thomas-Peter, Nathan K Langford, Dmytro Kundys, J. C. Gates, B. J. Smith, P. G. R. Smith, and I. A. Walmsley. Boson sampling on a photonic chip. *Science*, 339(6121):798–801, 2013.

[134] Benjamin J Metcalf, Justin B Spring, Peter C Humphreys, Nicholas Thomas-Peter, Marco Barbieri, W Steven Kolthammer, Xian-Min Jin, Nathan K Langford, Dmytro Kundys, James C Gates, et al. Quantum teleportation on a photonic chip. *Nature Photonics*, 8(10):770, 2014.

[135] Paolo L. Mennea, William R. Clements, Devin H. Smith, James C. Gates, Benjamin J. Metcalf, Rex H. S. Bannerman, Roel Burgwal, Jelmer J. Renema, W. Steven Kolthammer, Ian A. Walmsley, and Peter G. R. Smith. Modular linear optical circuits. *Optica*, 5(9):1087–1090, Sep 2018.

[136] Matthew T. Posner, T. Hiemstra, Paolo L. Mennea, Rex H. S. Bannerman, Ulrich B. Hoff, Andreas Eckstein, W. Steven Kolthammer, Ian A. Walmsley, Devin H. Smith, James C. Gates, and Peter G. R. Smith. High-birefringence direct uv-written waveguides for use as heralded single-photon sources at telecommunication wavelengths. *Opt. Express*, 26(19):24678–24686, Sep 2018.

[137] Michael Kues, Christian Reimer, Piotr Roztocki, Luis Romero Cortés, Stefania Sciara, Benjamin Wetzel, Yanbing Zhang, Alfonso Cino, Sai T. Chu, Brent E. Little, David J. Moss, Lucia Caspani, José Azaña, and Roberto Morandotti. On-chip generation of high-dimensional entangled quantum states and their coherent control. *Nature*, 546(7660):622–626, Jun 2017.

[138] Christian Reimer, Michael Kues, Piotr Roztocki, Benjamin Wetzel, Fabio Grazioso, Brent E. Little, Sai T. Chu, Tudor Johnston, Yaron Bromberg, Lucia Caspani, David J. Moss, and Roberto Morandotti. Generation of multiphoton entangled quantum states by means of integrated frequency combs. *Science*, 351(6278):1176–1180, 2016.

[139] Christian Reimer, Stefania Sciara, Piotr Roztocki, Mehedi Islam, Luis Romero Cortés, Yanbing Zhang, Bennet Fischer, Sébastien Loranger, Raman Kashyap, Alfonso Cino, Sai T. Chu, Brent E. Little, David J. Moss, Lucia Caspani, William J. Munro, José Azaña, Michael Kues, and Roberto Morandotti. High-dimensional one-way quantum processing implemented on d-level cluster states. *Nature Physics*, 15(2):148–153, Feb 2019.

[140] Rafael R. Gattass and Eric Mazur. Femtosecond laser micromachining in transparent materials. *Nature Photonics*, 2(4):219–225, April 2008.

[141] Linda Sansoni, Fabio Sciarrino, Giuseppe Vallone, Paolo Mataloni, Andrea Crespi, Roberta Ramponi, and Roberto Osellame. Two-particle bosonic-fermionic quantum walk via integrated photonics. *Phys. Rev. Lett.*, 108(1):010502, 12 2012.

[142] Andrea Crespi, Roberto Osellame, Roberta Ramponi, Vittorio Giovannetti, Rosario Fazio, Linda Sansoni, Francesco De Nicola, Fabio Sciarrino, and Paolo Mataloni. Anderson localization of entangled photons in an integrated quantum walk. *Nature Photonics*, 7:322–328, 2013.

[143] Ioannis Pitsios, Leonardo Banchi, Adil S. Rab, Marco Bentivegna, Debora Caprara, Andrea Crespi, Nicolò Spagnolo, Sougato Bose, Paolo Mataloni, Roberto Osellame, and Fabio Sciarrino. Photonic simulation of entanglement growth and engineering after a spin chain quench. *Nature Communications*, 8(1):1569, 2017.

[144] Andrea Crespi, Roberta Ramponi, Roberto Osellame, Linda Sansoni, Irene Bongioanni, Fabio Sciarrino, Giuseppe Vallone, and Paolo Mataloni. Integrated photonic quantum gates for polarization qubits. *Nature Communications*, 2(1):566, 2011.

[145] Giacomo Corrielli, Andrea Crespi, Riccardo Geremia, Roberta Ramponi, Linda Sansoni, Andrea Santinelli, Paolo Mataloni, Fabio Sciarrino, and Roberto Osellame. Rotated waveplates in integrated waveguide optics. *Nature Communications*, 5(1):4249, 2014.

[146] Max Tillmann, Borivoje Dakić, René Heilmann, Stefan Nolte, Alexander Szameit, and Philip Walther. Experimental boson sampling. *Nature Photon.*, 7(7):540–544, 2013.

[147] Andrea Crespi, Roberto Osellame, Roberta Ramponi, Daniel J Brod, Ernesto F Galvão, Nicolo Spagnolo, Chiara Vitelli, Enrico Maiorino, Paolo Mataloni, and Fabio Sciarrino. Integrated multimode interferometers with arbitrary designs for photonic boson sampling. *Nature Photon.*, 7(7):545–548, 2013.

[148] Marco Bentivegna, Nicolò Spagnolo, Chiara Vitelli, Fulvio Flamini, Niko Viggianiello, Ludovico Latmiral, Paolo Mataloni, Daniel J Brod, Ernesto F Galvão, Andrea Crespi, Roberta Ramponi, Roberto Osellame, and Fabio Sciarrino. Experimental scattershot boson sampling. *Sci. Adv.*, 1(3):e1400255, 2015.

[149] N. Spagnolo, C. Vitelli, L. Aparo, P. Mataloni, F. Sciarrino, A. Crespi, Ramponi. R., and R. Osellame. Three-photon bosonic coalescence in an integrated tritter. *Nature Commun.*, 4:1606, 2013.

[150] Andrea Crespi, Roberto Osellame, Roberta Ramponi, Marco Bentivegna, Fulvio Flamini, Nicolò Spagnolo, Niko Viggianiello, Luca Innocenti, Paolo Mataloni, and Fabio Sciarrino. Suppression law of quantum states in a 3d photonic fast fourier transform chip. *Nature Communications*, 7(1):10469, Feb 2016.

[151] Niko Viggianiello, Fulvio Flamini, Luca Innocenti, Daniele Cozzolino, Marco Bentivegna, Nicolò Spagnolo, Andrea Crespi, Daniel J Brod, Ernesto F Galvão, Roberto Osellame, and Fabio Sciarrino. Experimental generalized quantum suppression law in sylvester interferometers. *New J. Phys.*, 20(3):033017, mar 2018.

[152] Konstantinos Poulios, Robert Keil, Daniel Fry, Jasmin D. A. Meinecke, Jonathan C. F. Matthews, Alberto Politi, Mirko Lobino, Markus Gräfe, Matthias Heinrich, Stefan Nolte, Alexander Szameit, and Jeremy L. O'Brien. Quantum walks of correlated photon pairs in two-dimensional waveguide arrays. *Phys. Rev. Lett.*, 112:143604, Apr 2014.

[153] Philipp M. Preiss, Ruichao Ma, M. Eric Tai, Alexander Lukin, Matthew Rispoli, Philip Zupancic, Yoav Lahini, Rajibul Islam, and Markus Greiner. Strongly correlated quantum walks in optical lattices. *Science*, 347(6227):1229–1233, 2015.

[154] Filippo Caruso, Andrea Crespi, Anna Gabriella Ciriolo, Fabio Sciarrino, and Roberto Osellame. Fast escape of a quantum walker from an integrated photonic maze. *Nature Communications*, 7:11682, 2016.

[155] Zhi-Qiang Jiao, Jun Gao, Wen-Hao Zhou, Xiao-Wei Wang, Ruo-Jing Ren, Xiao-Yun Xu, Lu-Feng Qiao, and Xian-Min Jin. Two-dimensional quantum walk of correlated photons, 2020.

[156] Hao Tang, Leonardo Banchi, Tian-Yu Wang, Xiao-Wen Shang, Xi Tan, Wen-Hao Zhou, Zhen Feng, Anurag Pal, Hang Li, Cheng-Qiu Hu, M. S. Kim, and Xian-Min Jin. Generating haar-uniform randomness using stochastic quantum walks on a photonic chip. *Phys. Rev. Lett.*, 128:050503, Feb 2022.

[157] Emanuele Polino, Martina Riva, Mauro Valeri, Raffaele Silvestri, Giacomo Corrielli, Andrea Crespi, Nicolò Spagnolo, Roberto Osellame, and Fabio Sciarrino. Experimental multiphase estimation on a chip. *Optica*, 6(3):288–295, Mar 2019.

[158] Mathias Pont, Riccardo Albiero, Sarah E. Thomas, Nicolò Spagnolo, Francesco Ceccarelli, Giacomo Corrielli, Alexandre Brieussel, Niccolo Somaschi, Hêlio Huet, Abdelmounaim Harouri, Aristide Lemaître, Isabelle Sagnes, Nadia Belabas, Fabio Sciarrino, Roberto Osellame, Pascale Senellart, and Andrea Crespi. Quantifying n-photon indistinguishability with a cyclic integrated interferometer. *Phys. Rev. X*, 12:031033, Sep 2022.

[159] G. Corrielli, S. Atzeni, S. Piacentini, I. Pitsios, A. Crespi, and R. Osellame. Symmetric polarization-insensitive directional couplers fabricated by femtosecond laser writing. *Opt. Express*, 26(12):15101, jun 2018.

[160] F. Ceccarelli, S. Atzeni, A. Prencipe, R. Farinaro, and R. Osellame. Thermal Phase Shifters for Femtosecond Laser Written Photonic Integrated Circuits. *J. Light. Technol.*, 37(17):4275–4281, 2019.

[161] Jun Zhang, Mark A Itzler, Hugo Zbinden, and Jian-Wei Pan. Advances in InGaAs/InP single-photon detector systems for quantum communication. *Light: Science & Applications*, 4(5):e286–e286, May 2015.

[162] L. C. Comandar, B. Fröhlich, J. F. Dynes, A. W. Sharpe, M. Lucamarini, Z. L. Yuan, R. V. Penty, and A. J. Shields. Gigahertz-gated InGaAs/InP single-photon detector with detection efficiency exceeding 55% at 1550 nm. *Journal of Applied Physics*, 117(8):083109, February 2015.

[163] Nicholas J. D. Martinez, Michael Gehl, Christopher T. Derose, Andrew L. Starbuck, Andrew T. Pomerene, Anthony L. Lentine, Douglas C. Trotter, and Paul S. Davids. Single photon detection in a waveguide-coupled ge-on-si lateral avalanche photodiode. *Optics Express*, 25(14):16130, June 2017.

[164] Ryan E. Warburton, Giuseppe Intermite, Maksym Myronov, Phil Allred, David R. Leadley, Kevin Gallacher, Douglas J. Paul, Neil J. Pilgrim, Leon J. M. Lever, Zoran Ikonic, Robert W. Kelsall, Edgar Huante-Ceron, Andrew P. Knights, and Gerald S. Buller. Ge-on-si single-photon avalanche diode detectors: Design, modeling, fabrication, and characterization at wavelengths 1310 and 1550 nm. *IEEE Transactions on Electron Devices*, 60(11):3807–3813, November 2013.

[165] B. Korzh, N. Walenta, T. Lunghi, N. Gisin, and H. Zbinden. Free-running InGaAs single photon detector with 1 dark count per second at 10% efficiency. *Applied Physics Letters*, 104(8):081108, February 2014.

[166] M. Covi, B. Pressl, T. Günthner, K. Laiho, S. Krapick, C. Silberhorn, and G. Weihs. Liquid-nitrogen cooled, free-running single-photon sensitive detector at telecommunication wavelengths. *Applied Physics B*, 118(3):489–495, February 2015.

[167] Andreas Pfenning, Fabian Hartmann, Fabian Langer, Martin Kamp, Sven Höfling, and Lukas Worschech. Sensitivity of resonant tunneling diode photodetectors. *Nanotechnology*, 27(35):355202, July 2016.

[168] Kunihiro Inomata, Zhirong Lin, Kazuki Koshino, William D. Oliver, Jaw-Shen Tsai, Tsuyoshi Yamamoto, and Yasunobu Nakamura. Single microwave-photon detector using an artificial

Λ

-type three-level system. *Nature Communications*, 7(1), July 2016.

[169] J. S. Pelc, L. Ma, C. R. Phillips, Q. Zhang, C. Langrock, O. Slattery, X. Tang, and M. M. Fejer. Long-wavelength-pumped upconversion single-photon detector at 1550 nm: performance and noise analysis. *Optics Express*, 19(22):21445, October 2011.

[170] Qi Hu, Jeppe Seidelin Dam, Christian Pedersen, and Peter Tidemand-Lichtenberg. High-resolution mid-IR spectrometer based on frequency upconversion. *Optics Letters*, 37(24):5232, December 2012.

[171] J. S. Pelc, Paulina S. Kuo, Oliver Slattery, Lijun Ma, Xiao Tang, and M. M. Fejer. Dual-channel, single-photon upconversion detector at 13 μm. *Optics Express*, 20(17):19075, August 2012.

[172] Enrico Pomarico, Bruno Sanguinetti, Rob Thew, and Hugo Zbinden. Room temperature photon number resolving detector for infared wavelengths. *Optics Express*, 18(10):10750, May 2010.

[173] Fei Ma, Ming-Yang Zheng, Quan Yao, Xiu-Ping Xie, Qiang Zhang, and Jian-Wei Pan. 1064-μm-band up-conversion single-photon detector. *Optics Express*, 25(13):14558, June 2017.

[174] Hao Li, Lu Zhang, Lixing You, Xiaoyan Yang, Weijun Zhang, Xiaoyu Liu, Sijing Chen, Zhen Wang, and Xiaoming Xie. Large-sensitive-area superconducting nanowire single-photon detector at 850 nm with high detection efficiency. *Optics Express*, 23(13):17301, June 2015.

[175] W. J. Zhang, H. Li, L. X. You, Y. H. He, L. Zhang, X.Y. Liu, X. Y. Yang, J. J. Wu, Q. Guo, S. J. Chen, Z. Wang, and X. M. Xie. Superconducting nanowire single-photon detectors at a wavelength of 940 nm. *AIP Advances*, 5(6):067129, June 2015.

[176] Taro Yamashita, Kentaro Waki, Shigehito Miki, Robert A. Kirkwood, Robert H. Hadfield, and Hirotaka Terai. Superconducting nanowire single-photon detectors with non-periodic dielectric multilayers. *Scientific Reports*, 6(1), October 2016.

[177] Haig A. Atikian, Pawel Latawiec, Michael J. Burek, Young-Ik Sohn, Srujan Meesala, Normand Gravel, Ammar B. Kouki, and Marko Lončar. Freestanding nanostructures via reactive ion beam angled etching. *APL Photonics*, 2(5):051301, May 2017.

[178] Nicola A. Tyler, Jorge Barreto, Gerardo E. Villarreal-Garcia, Damien Bonneau, Döndü Sahin, Jeremy L. O'Brien, and Mark G. Thompson. Modelling superconducting nanowire single photon detectors in a waveguide cavity. *Optics Express*, 24(8):8797, April 2016.

[179] R. Arpaia, M. Ejrnaes, L. Parlato, F. Tafuri, R. Cristiano, D. Golubev, Roman Sobolewski, T. Bauch, F. Lombardi, and G.P. Pepe. High-temperature superconducting nanowires for photon detection. *Physica C: Superconductivity and its Applications*, 509:16–21, February 2015.

[180] Hiroki Takesue, Shellee D. Dyer, Martin J. Stevens, Varun Verma, Richard P. Mirin, and Sae Woo Nam. Quantum teleportation over 100 km of fiber using highly efficient superconducting nanowire single-photon detectors. *Optica*, 2(10):832, September 2015.

[181] Hanna Le Jeannic, Varun B. Verma, Adrien Cavaillès, Francesco Marsili, Matthew D. Shaw, Kun Huang, Olivier Morin, Sae Woo Nam, and Julien Laurat. High-efficiency WSi superconducting nanowire single-photon detectors

for quantum state engineering in the near infrared. *Optics Letters*, 41(22):5341, November 2016.

[182] WeiJun Zhang, LiXing You, Hao Li, Jia Huang, ChaoLin Lv, Lu Zhang, XiaoYu Liu, JunJie Wu, Zhen Wang, and XiaoMing Xie. NbN superconducting nanowire single photon detector with efficiency over 90% at 1550 nm wavelength operational at compact cryocooler temperature. *Science China Physics, Mechanics & Astronomy*, 60(12), October 2017.

[183] Iman Esmaeil Zadeh, Johannes W. N. Los, Ronan B. M. Gourgues, Violette Steinmetz, Gabriele Bulgarini, Sergiy M. Dobrovolskiy, Val Zwiller, and Sander N. Dorenbos. Single-photon detectors combining high efficiency, high detection rates, and ultra-high timing resolution. *APL Photonics*, 2(11):111301, November 2017.

[184] Vadim V. Vorobyov, Alexander Yu. Kazakov, Vladimir V. Soshenko, Alexander A. Korneev, Mikhail Y. Shalaginov, Stepan V. Bolshedvorskii, Vadim N. Sorokin, Alexander V. Divochiy, Yury B. Vakhtomin, Konstantin V. Smirnov, Boris M. Voronov, Vladimir M. Shalaev, Alexey V. Akimov, and Gregory N. Goltsman. Superconducting detector for visible and near-infrared quantum emitters [invited]. *Optical Materials Express*, 7(2):513, January 2017.

[185] Shigehito Miki, Masahiro Yabuno, Taro Yamashita, and Hirotaka Terai. Stable, high-performance operation of a fiber-coupled superconducting nanowire avalanche photon detector. *Optics Express*, 25(6):6796, March 2017.

[186] Aaron J. Miller, Adriana E. Lita, Brice Calkins, Igor Vayshenker, Steven M. Gruber, and Sae Woo Nam. Compact cryogenic self-aligning fiber-to-detector coupling with losses below one percent. *Optics Express*, 19(10):9102, April 2011.

[187] Brice Calkins, Paolo L. Mennea, Adriana E. Lita, Benjamin J. Metcalf, W. Steven Kolthammer, Antia Lamas-Linares, Justin B. Spring, Peter C. Humphreys, Richard P. Mirin, James C. Gates, Peter G. R. Smith, Ian A. Walmsley, Thomas Gerrits, and Sae Woo Nam. High quantum-efficiency photon-number-resolving detector for photonic on-chip information processing. *Optics Express*, 21(19):22657, September 2013.

[188] Rajveer Nehra, Chun-Hung Chang, Qianhuan Yu, Andreas Beling, and Olivier Pfister. Photon-number-resolving segmented detectors based on single-photon avalanche-photodiodes. *Optics Express*, 28(3):3660, January 2020.

[189] Antia Lamas-Linares, Brice Calkins, Nathan A. Tomlin, Thomas Gerrits, Adriana E. Lita, Jörn Beyer, Richard P. Mirin, and Sae Woo Nam. Nanosecond-scale timing jitter for single photon detection in transition edge sensors. *Applied Physics Letters*, 102(23):231117, June 2013.

[190] Yongbo Yuan, Qingfeng Dong, Bin Yang, Fawen Guo, Qi Zhang, Ming Han, and Jinsong Huang. Solution-processed nanoparticle super-float-gated organic field-effect transistor as un-cooled ultraviolet and infrared photon counter. *Scientific Reports*, 3(1), September 2013.

[191] F. Najafi, F. Marsili, E. Dauler, R. J. Molnar, and K. K. Berggren. Timing performance of 30-nm-wide superconducting nanowire avalanche photodetectors. *Applied Physics Letters*, 100(15):152602, April 2012.

[192] Robert M. Heath, Michael G. Tanner, Alessandro Casaburi, Mark G. Webster, Lara San Emeterio Alvarez, Weitao Jiang, Zoe H. Barber, Richard J. Warburton, and Robert H. Hadfield. Nano-optical observation of cascade switching in a parallel superconducting nanowire single photon detector. *Applied Physics Letters*, 104(6):063503, February 2014.

[193] M. Avenhaus, K. Laiho, M. V. Chekhova, and C. Silberhorn. Accessing higher order correlations in quantum optical states by time multiplexing. *Physical Review Letters*, 104(6), February 2010.

[194] O. Thomas, Z.L. Yuan, and A.J. Shields. Practical photon number detection with electric field-modulated silicon avalanche photodiodes. *Nature Communications*, 3(1), January 2012.

[195] C. Schuck, X. Guo, L. Fan, X. Ma, M. Poot, and H. X. Tang. Quantum interference in heterogeneous superconducting-photonic circuits on a silicon chip. *Nature Communications*, 7(1):10352, Jan 2016.

[196] J. P. Sprengers, A. Gaggero, D. Sahin, S. Jahanmirinejad, G. Frucci, F. Mattioli, R. Leoni, J. Beetz, M. Lermer, M. Kamp, S. Höfling, R. Sanjines, and A. Fiore. Waveguide superconducting single-photon detectors for integrated quantum photonic circuits. *Applied Physics Letters*, 99(18):181110, 2011.

[197] D. Sahin, A. Gaggero, Z. Zhou, S. Jahanmirinejad, F. Mattioli, R. Leoni, J. Beetz, M. Lermer, M. Kamp, S. Höfling, and A. Fiore. Waveguide photon-number-resolving detectors for quantum photonic integrated circuits. *Applied Physics Letters*, 103(11):111116, 2013.

[198] W. H. P. Pernice, C. Schuck, O. Minaeva, M. Li, G. N. Goltsman, A. V. Sergienko, and H. X. Tang. High-speed and high-efficiency travelling wave single-photon detectors embedded in nanophotonic circuits. *Nature Communications*, 3(1):1325, Dec 2012.

[199] Di Zhu, Marco Colangelo, Changchen Chen, Boris A. Korzh, Franco N. C. Wong, Matthew D. Shaw, and Karl K. Berggren. Resolving photon numbers using a superconducting nanowire with impedance-matching taper. *Nano Letters*, 20(5):3858–3863, May 2020.

[200] Max Tillmann, Christian Schmidt, and Philip Walther. On unitary reconstruction of linear optical networks. *Journal of Optics*, 18(11):114002, sep 2016.

[201] Nicolò Spagnolo, Enrico Maiorino, Chiara Vitelli, Marco Bentivegna, Andrea Crespi, Roberta Ramponi, Paolo Mataloni, Roberto Osellame, and Fabio Sciarrino. Learning an unknown transformation via a genetic approach. *Scientific Reports*, 7(1):14316, Oct 2017.

[202] Ish Dhand, Abdullah Khalid, He Lu, and Barry C Sanders. Accurate and precise characterization of linear optical interferometers. *Journal of Optics*, 18(3):035204, feb 2016.

[203] Saleh Rahimi-Keshari, Matthew A. Broome, Robert Fickler, Alessandro Fedrizzi, Timothy C. Ralph, and Andrew G. White. Direct characterization of linear-optical networks. *Opt. Express*, 21(11):13450–13458, Jun 2013.

[204] S. M. Popoff, G. Lerosey, R. Carminati, M. Fink, A. C. Boccara, and S. Gigan. Measuring the transmission matrix in optics: An approach to the study and control of light propagation in disordered media. *Phys. Rev. Lett.*, 104:100601, Mar 2010.

[205] S M Popoff, G Lerosey, M Fink, A C Boccara, and S Gigan. Controlling light through optical disordered media: transmission matrix approach. *New Journal of Physics*, 13(12):123021, dec 2011.

[206] Daniel Suess, Nicola Maraviglia, Richard Kueng, Alexandre Maïnos, Chris Sparrow, Toshikazu Hashimoto, Nobuyuki Matsuda, David Gross, and Anthony Laing. Rapid characterisation of linear-optical networks via phaselift, 2020.

[207] Valeria Cimini, Emanuele Polino, Mauro Valeri, Ilaria Gianani, Nicolò Spagnolo, Giacomo Corrielli, Andrea Crespi, Roberto Osellame, Marco Barbieri, and Fabio Sciarrino. Calibration of multiparameter sensors via machine learning at the single-photon level. *Phys. Rev. Applied*, 15:044003, Apr 2021.

[208] Alessia Suprano, Danilo Zia, Emanuele Polino, Taira Giordani, Luca Innocenti, Alessandro Ferraro, Mauro Paternostro, Nicolò Spagnolo, and Fabio Sciarrino. Dynamical learning of a photonics quantum-state engineering process. *Advanced Photonics*, 3(6):1 – 11, 2021.

[209] Sergei Kuzmin, Ivan Dyakonov, and Sergei Kulik. Architecture agnostic algorithm for reconfigurable optical interferometer programming. *Opt. Express*, 29(23):38429–38440, Nov 2021.

[210] Robert Keil, Alexander Szameit, Felix Dreisow, Matthias Heinrich, Stefan Nolte, and Andreas Tünnermann. Photon correlations in two-dimensional waveguide arrays and their classical estimate. *Phys. Rev. A*, 81:023834, Feb 2010.

[211] R. Hanbury Brown and R. Q. Twiss. A test of a new type of stellar interferometer on sirius. *Nature*, 178(4541):1046–1048, Nov 1956.

[212] Michał Oszmaniec and Daniel J Brod. Classical simulation of photonic linear optics with lost particles. *New Journal of Physics*, 20(9):092002, sep 2018.

[213] Richard Sinkhorn and Paul Knopp. Concerning nonnegative matrices and doubly stochastic matrices. *Pacific Journal of Mathematics*, 21:343–348, 1967.

[214] Richard Sinkhorn. Continuous dependence on A in the D_1AD_2 theorems. *Proceedings of the American Mathematical Society*, 32(2):395–398, 1972.

[215] Martin Idel. A review of matrix scaling and sinkhorn's normal form for matrices and positive maps, 2016.

[216] Nicolò Spagnolo, Chiara Vitelli, Linda Sansoni, Enrico Maiorino, Paolo Mataloni, Fabio Sciarrino, Daniel J. Brod, Ernesto F. Galvão, Andrea Crespi, Roberta Ramponi, and Roberto Osellame. General rules for bosonic bunching in multimode interferometers. *Physical Review Letters*, 111(13), September 2013.

[217] A. P. Lund, A. Laing, S. Rahimi-Keshari, T. Rudolph, J. L. O'Brien, and T. C. Ralph. Boson sampling from a gaussian state. *Phys. Rev. Lett.*, 113:100502, Sep 2014.

[218] Craig S. Hamilton, Regina Kruse, Linda Sansoni, Sonja Barkhofen, Christine Silberhorn, and Igor Jex. Gaussian boson sampling. *Phys. Rev. Lett.*, 119:170501, Oct 2017.

[219] M. A. Broome, A. Fedrizzi, S. Rahimi-Keshari, J. Dove, S. Aaronson, T. C. Ralph, and A. G. White. Photonic boson sampling in a tunable circuit. *Science*, 339(6121):794–798, December 2012.

[220] J. B. Spring, B. J. Metcalf, P. C. Humphreys, W. S. Kolthammer, X.-M. Jin, M. Barbieri, A. Datta, N. Thomas-Peter, N. K. Langford, D. Kundys, J. C. Gates, B. J. Smith, P. G. R. Smith, and I. A. Walmsley. Boson sampling on a photonic chip. *Science*, 339(6121):798–801, December 2012.

[221] Max Tillmann, Borivoje Dakić, René Heilmann, Stefan Nolte, Alexander Szameit, and Philip Walther. Experimental boson sampling. *Nature Photonics*, 7(7):540–544, May 2013.

[222] Andrea Crespi, Roberto Osellame, Roberta Ramponi, Daniel J. Brod, Ernesto F. Galvão, Nicolò Spagnolo, Chiara Vitelli, Enrico Maiorino, Paolo Mataloni, and Fabio Sciarrino. Integrated multimode interferometers with arbitrary designs for photonic boson sampling. *Nature Photonics*, 7(7):545–549, May 2013.

[223] Nicolò Spagnolo, Chiara Vitelli, Marco Bentivegna, Daniel J. Brod, Andrea Crespi, Fulvio Flamini, Sandro Giacomini, Giorgio Milani, Roberta Ramponi, Paolo Mataloni, Roberto Osellame, Ernesto F. Galvão, and Fabio Sciarrino. Experimental validation of photonic boson sampling. *Nature Photonics*, 8(8):615–620, June 2014.

[224] Jacques Carolan, Jasmin D. A. Meinecke, Peter J. Shadbolt, Nicholas J. Russell, Nur Ismail, Kerstin Wörhoff, Terry Rudolph, Mark G. Thompson, Jeremy L. O'Brien, Jonathan C. F. Matthews, and Anthony Laing. On the experimental verification of quantum complexity in linear optics. *Nature Photonics*, 8(8):621–626, July 2014.

[225] Mark Rudelson, Alex Samorodnitsky, and Ofer Zeitouni. Hafnians, perfect matchings and gaussian matrices. *The Annals of Probability*, 44(4), July 2016.

[226] David A. Plaisted and Samuel Zaks. An NP-complete matching problem. *Discrete Applied Mathematics*, 2(1):65–72, April 1980.

[227] Kaushik P. Seshadreesan, Jonathan P. Olson, Keith R. Motes, Peter P. Rohde, and Jonathan P. Dowling. Boson sampling with displaced single-photon fock states versus single-photon-added coherent states: The quantum-classical divide and computational-complexity transitions in linear optics. *Physical Review A*, 91(2), February 2015.

[228] Jonathan P. Olson, Kaushik P. Seshadreesan, Keith R. Motes, Peter P. Rohde, and Jonathan P. Dowling. Sampling arbitrary photon-added or photon-subtracted squeezed states is in the same complexity class as boson sampling. *Physical Review A*, 91(2), February 2015.

[229] Jelmer J. Renema. Simulability of partially distinguishable superposition and gaussian boson sampling. *Physical Review A*, 101(6), June 2020.

[230] Jun Gao, Xiao-Wei Wang, Wen-Hao Zhou, Zhi-Qiang Jiao, Ruo-Jing Ren, Yu-Xuan Fu, Lu-Feng Qiao, Xiao-Yun Xu, Chao-Ni Zhang, Xiao-Ling Pang, Hang Li, Yao Wang, and Xian-Min Jin. Quantum advantage with membosonsampling. *Chip*, 1(2):100007, June 2022.

[231] Nicolò Spagnolo, Daniel J. Brod, Ernesto F. Galvão, and Fabio Sciarrino. Non-linear boson sampling, 2021.

[232] Seinosuke Toda. PP is as hard as the polynomial-time hierarchy. *SIAM Journal on Computing*, 20(5):865–877, October 1991.

[233] L.G. Valiant. The complexity of computing the permanent. *Theoretical Computer Science*, 8(2):189–201, 1979.

[234] Herbert Ryser. *Combinatorial Mathematics*. American Mathematical Society, 1963.

[235] Lidror Troyansky. Permanent uncertainty: on the quantum evaluation of the determinant and the permanent of a matrix, 1996.

[236] Larry Stockmeyer. On approximation algorithms for # p. *SIAM Journal on Computing*, 14(4):849–861, November 1985.

[237] Herbert J Ryser. *Combinatorial Mathematics*. Carus Monograph. Mathematical Association of America, Washington, D.C., DC, August 1978.

[238] Alex Neville, Chris Sparrow, Raphaël Clifford, Eric Johnston, Patrick M. Birchall, Ashley Montanaro, and Anthony Laing. Classical boson sampling algorithms with superior performance to near-term experiments. *Nature Physics*, 13(12):1153–1157, October 2017.

[239] W. K. Hastings. Monte carlo sampling methods using markov chains and their applications. *Biometrika*, 57(1):97–109, April 1970.

[240] Peter Clifford and Raphaël Clifford. The classical complexity of boson sampling. In *Proceedings of the Twenty-Ninth Annual ACM-SIAM Symposium on Discrete Algorithms*, SODA '18, page 146–155, USA, 2018. Society for Industrial and Applied Mathematics.

[241] Nicolás Quesada and Juan Miguel Arrazola. Exact simulation of gaussian boson sampling in polynomial space and exponential time. *Physical Review Research*, 2(2), April 2020.

[242] Andreas Björklund. Counting perfect matchings as fast as ryser. In *Proceedings of the Twenty-Third Annual ACM-SIAM Symposium on Discrete Algorithms*, SODA '12, page 914–921, USA, 2012. Society for Industrial and Applied Mathematics.

[243] Saleh Rahimi-Keshari, Timothy C. Ralph, and Carlton M. Caves. Sufficient conditions for efficient classical simulation of quantum optics. *Physical Review X*, 6(2), June 2016.

[244] Scott Aaronson and Daniel J. Brod. BosonSampling with lost photons. *Physical Review A*, 93(1), January 2016.

[245] Gil Kalai and Guy Kindler. Gaussian noise sensitivity and bosonsampling, 2014.

[246] Xun Gao and Luming Duan. Efficient classical simulation of noisy quantum computation, 2018.

[247] Daniel J. Brod, Ernesto F. Galvão, Andrea Crespi, Roberto Osellame, Nicolò Spagnolo, and Fabio Sciarrino. Photonic implementation of boson sampling: a review. *Advanced Photonics*, 1(3):034001, 2019.

[248] C. Gogolin, M. Kliesch, L. Aolita, and J. Eisert. Boson-sampling in the light of sample complexity, 2013.

[249] Scott Aaronson and Alex Arkhipov. Bosonsampling is far from uniform, 2013.

[250] Marco Bentivegna, Nicolò Spagnolo, Chiara Vitelli, Daniel J. Brod, Andrea Crespi, Fulvio Flamini, Roberta Ramponi, Paolo Mataloni, Roberto Osellame, Ernesto F. Galvão, and Fabio Sciarrino. Bayesian approach to boson sampling validation. *International Journal of Quantum Information*, 12(07n08):1560028, November 2014.

[251] Marco Bentivegna, Nicolò Spagnolo, Chiara Vitelli, Fulvio Flamini, Niko Viggianiello, Ludovico Latmiral, Paolo Mataloni, Daniel J. Brod, Ernesto F. Galvão, Andrea Crespi, Roberta Ramponi, Roberto Osellame, and Fabio Sciarrino. Experimental scattershot boson sampling. *Science Advances*, 1(3), April 2015.

[252] Benoit Seron, Leonardo Novo, Alex Arkhipov, and Nicolas J. Cerf. Efficient validation of boson sampling from binned photon-number distributions, 2022.

[253] Valery Shchesnovich. Distinguishing noisy boson sampling from classical simulations. *Quantum*, 5:423, March 2021.

[254] Malte C. Tichy, Klaus Mayer, Andreas Buchleitner, and Klaus Mølmer. Stringent and efficient assessment of boson-sampling devices. *Physical Review Letters*, 113(2), July 2014.

[255] Malte Christopher Tichy, Markus Tiersch, Fernando de Melo, Florian Mintert, and Andreas Buchleitner. Zero-transmission law for multiport beam splitters. *Physical Review Letters*, 104(22), June 2010.

[256] Iris Agresti, Niko Viggianiello, Fulvio Flamini, Nicolò Spagnolo, Andrea Crespi, Roberto Osellame, Nathan Wiebe, and Fabio Sciarrino. Pattern recognition techniques for boson sampling validation. *Physical Review X*, 9(1), January 2019.

[257] Mattia Walschaers, Jack Kuipers, Juan-Diego Urbina, Klaus Mayer, Malte Christopher Tichy, Klaus Richter, and Andreas Buchleitner. Statistical benchmark for BosonSampling. *New Journal of Physics*, 18(3):032001, March 2016.

[258] Leandro Aolita, Christian Gogolin, Martin Kliesch, and Jens Eisert. Reliable quantum certification of photonic state preparations. *Nature Communications*, 6(1), November 2015.

[259] Kai Liu, Austin Peter Lund, Yong-Jian Gu, and Timothy Cameron Ralph. A certification scheme for the boson sampler. *Journal of the Optical Society of America B*, 33(9):1835, August 2016.

[260] V. S. Shchesnovich. Universality of generalized bunching and efficient assessment of boson sampling. *Physical Review Letters*, 116(12), March 2016.

[261] Hui Wang, Jian Qin, Xing Ding, Ming-Cheng Chen, Si Chen, Xiang You, Yu-Ming He, Xiao Jiang, L. You, Z. Wang, C. Schneider, Jelmer J. Renema, Sven Höfling, Chao-Yang Lu, and Jian-Wei Pan. Boson sampling with 20 input photons and a 60-mode interferometer in a 10^{14}-dimensional hilbert space. *Phys. Rev. Lett.*, 123:250503, Dec 2019.

[262] Han-Sen Zhong, Hui Wang, Yu-Hao Deng, Ming-Cheng Chen, Li-Chao Peng, Yi-Han Luo, Jian Qin, Dian Wu, Xing Ding, Yi Hu, Peng Hu, Xiao-Yan Yang, Wei-Jun Zhang, Hao Li, Yuxuan Li, Xiao Jiang, Lin Gan, Guangwen Yang, Lixing You, Zhen Wang, Li Li, Nai-Le Liu, Chao-Yang Lu, and Jian-Wei Pan. Quantum computational advantage using photons. *Science*, 370(6523):1460–1463, December 2020.

[263] Jacques Carolan, Christopher Harrold, Chris Sparrow, Enrique Martín-López, Nicholas J. Russell, Joshua W. Silverstone, Peter J. Shadbolt, Nobuyuki Matsuda, Manabu Oguma, Mikitaka Itoh, Graham D. Marshall, Mark G. Thompson, Jonathan C. F. Matthews, Toshikazu Hashimoto, Jeremy L. O'Brien, and Anthony Laing. Universal linear optics. *Science*, 349(6249):711–716, August 2015.

[264] Max Tillmann, Si-Hui Tan, Sarah E. Stoeckl, Barry C. Sanders, Hubert de Guise, René Heilmann, Stefan Nolte, Alexander Szameit, and Philip Walther. Generalized multiphoton quantum interference. *Physical Review X*, 5(4), October 2015.

[265] Andrea Crespi, Roberto Osellame, Roberta Ramponi, Marco Bentivegna, Fulvio Flamini, Nicolò Spagnolo, Niko Viggianiello, Luca Innocenti, Paolo Mataloni, and Fabio Sciarrino. Suppression law of quantum states in a 3d photonic fast fourier transform chip. *Nature Communications*, 7(1), February 2016.

[266] J. C. Loredo, M. A. Broome, P. Hilaire, O. Gazzano, I. Sagnes, A. Lemaitre, M. P. Almeida, P. Senellart, and A. G. White. Boson sampling with single-photon fock states from a bright solid-state source. *Physical Review Letters*, 118(13), March 2017.

[267] Jianwei Wang, Stefano Paesani, Raffaele Santagati, Sebastian Knauer, Antonio A. Gentile, Nathan Wiebe, Maurangelo Petruzzella, Jeremy L. O'Brien, John G. Rarity, Anthony Laing, and Mark G. Thompson. Experimental quantum hamiltonian learning. *Nature Physics*, 13(6):551–555, March 2017.

[268] Niko Viggianiello, Fulvio Flamini, Luca Innocenti, Daniele Cozzolino, Marco Bentivegna, Nicolò Spagnolo, Andrea Crespi, Daniel J Brod, Ernesto F Galvão, Roberto Osellame, and Fabio Sciarrino. Experimental generalized quantum suppression law in sylvester interferometers. *New Journal of Physics*, 20(3):033017, March 2018.

[269] Han-Sen Zhong, Li-Chao Peng, Yuan Li, Yi Hu, Wei Li, Jian Qin, Dian Wu, Weijun Zhang, Hao Li, Lu Zhang, Zhen Wang, Lixing You, Xiao Jiang, Li Li, Nai-Le Liu, Jonathan P. Dowling, Chao-Yang Lu, and Jian-Wei Pan. Experimental gaussian boson sampling. *Science Bulletin*, 64(8):511–515, April 2019.

[270] Caterina Taballione, Tom A. W. Wolterink, Jasleen Lugani, Andreas Eckstein, Bryn A. Bell, Robert Grootjans, Ilka Visscher, Dimitri Geskus, Chris G. H. Roeloffzen, Jelmer J. Renema, Ian A. Walmsley, Pepijn W. H. Pinkse, and Klaus-J. Boller. 8×8 reconfigurable quantum photonic processor based on silicon nitride waveguides. *Optics Express*, 27(19):26842, September 2019.

[271] Richard P. Feynman. Simulating physics with computers. *International Journal of Theoretical Physics*, 21(6-7):467–488, June 1982.

[272] David P. DiVincenzo. The physical implementation of quantum computation. *Fortschritte der Physik*, 48(9-11):771–783, September 2000.

[273] Regina Kruse, Craig S. Hamilton, Linda Sansoni, Sonja Barkhofen, Christine Silberhorn, and Igor Jex. Detailed study of gaussian boson sampling. *Phys. Rev. A*, 100:032326, Sep 2019.

[274] Haoyu Qi, Daniel J. Brod, Nicolás Quesada, and Raúl García-Patrón. Regimes of classical simulability for noisy gaussian boson sampling. *Phys. Rev. Lett.*, 124:100502, Mar 2020.

[275] Raúl García-Patrón, Jelmer J. Renema, and Valery Shchesnovich. Simulating boson sampling in lossy architectures. *Quantum*, 3:169, August 2019.

[276] Han-Sen Zhong, Yu-Hao Deng, Jian Qin, Hui Wang, Ming-Cheng Chen, Li-Chao Peng, Yi-Han Luo, Dian Wu, Si-Qiu Gong, Hao Su, Yi Hu, Peng Hu, Xiao-Yan Yang, Wei-Jun Zhang, Hao Li, Yuxuan Li, Xiao Jiang, Lin Gan, Guangwen Yang, Lixing You, Zhen Wang, Li Li, Nai-Le Liu, Jelmer J. Renema, Chao-Yang Lu, and Jian-Wei Pan. Phase-programmable gaussian boson sampling using stimulated squeezed light. *Phys. Rev. Lett.*, 127:180502, Oct 2021.

[277] Jianwei Wang, Fabio Sciarrino, Anthony Laing, and Mark G. Thompson. Integrated photonic quantum technologies. *Nature Photonics*, 14(5):273–284, October 2019.

[278] Zhi-Qiang Jiao, Jun Gao, Wen-Hao Zhou, Xiao-Wei Wang, Ruo-Jing Ren, Xiao-Yun Xu, Lu-Feng Qiao, Yao Wang, and Xian-Min Jin. Two-dimensional quantum walks of correlated photons. *Optica*, 8(9):1129–1135, Sep 2021.

[279] Jun Gao, Zhi-Qiang Jiao, Ruo-Jing Ren, Xiao-Wei Wang, Xiao-Yun Xu, Wen-Hao Zhou, Lu-Feng Qiao, and Xian-Min Jin. Experimental collision-free dominant boson sampling, 2019.

[280] Alexander Arriola, Simon Gross, Nemanja Jovanovic, Ned Charles, Peter G. Tuthill, Santiago M. Olaizola, Alexander Fuerbach, and Michael J. Withford. Low bend loss waveguides enable compact, efficient 3d photonic chips. *Optics Express*, 21(3):2978, January 2013.

[281] Ciro Pentangelo, Simone Atzeni, Francesco Ceccarelli, Roberto Osellame, and Andrea Crespi. Analytical modeling of the static and dynamic response of thermally actuated optical waveguide circuits. *Physical Review Research*, 3(2), May 2021.

[282] Nicholas J Russell, Levon Chakhmakhchyan, Jeremy L O'Brien, and Anthony Laing. Direct dialling of haar random unitary matrices. *New Journal of Physics*, 19(3):033007, March 2017.

[283] Roel Burgwal, William R. Clements, Devin H. Smith, James C. Gates, W. Steven Kolthammer, Jelmer J. Renema, and Ian A. Walmsley. Using an imperfect photonic network to implement random unitaries. *Optics Express*, 25(23):28236, October 2017.

[284] Scott Aaronson and Alex Arkhipov. Bosonsampling is far from uniform. *Quantum Info. Comput.*, 14(15–16):1383–1423, nov 2014.

[285] Taira Giordani, Fulvio Flamini, Matteo Pompili, Niko Viggianiello, Nicolò Spagnolo, Andrea Crespi, Roberto Osellame, Nathan Wiebe, Mattia Walschaers,

Andreas Buchleitner, and Fabio Sciarrino. Experimental statistical signature of many-body quantum interference. *Nature Photonics*, 12(3):173–178, February 2018.

[286] Fulvio Flamini, Nicolò Spagnolo, and Fabio Sciarrino. Visual assessment of multi-photon interference. *Quantum Science and Technology*, 4(2):024008, March 2019.

[287] Xiang Zhan, Lei Xiao, Zhihao Bian, Kunkun Wang, Xingze Qiu, Barry C. Sanders, Wei Yi, and Peng Xue. Detecting topological invariants in nonunitary discrete-time quantum walks. *Physical Review Letters*, 119(13), September 2017.

[288] C. Antón, J. C. Loredo, G. Coppola, H. Ollivier, N. Viggianiello, A. Harouri, N. Somaschi, A. Crespi, I. Sagnes, A. Lemaître, L. Lanco, R. Osellame, F. Sciarrino, and P. Senellart. Interfacing scalable photonic platforms: solid-state based multi-photon interference in a reconfigurable glass chip. *Optica*, 6(12):1471, November 2019.

[289] J. Von Neumann. Various techniques used in connection with random digits. *Applied Math Series*, 12(36-38), 1951.

[290] Philippe Flajolet, Maryse Pelletier, and Michele Soria. On buffon machines and numbers, 2009.

[291] Krzysztof Latuszynski, Ioannis Kosmidis, Omiros Papaspiliopoulos, and Gareth O. Roberts. Simulating events of unknown probabilities via reverse time martingales, 2009.

[292] Şerban Nacu and Yuval Peres. Fast simulation of new coins from old. *The Annals of Applied Probability*, 15(1A), February 2005.

[293] Vineet Goyal and Karl Sigman. On simulating a class of bernstein polynomials. *ACM Transactions on Modeling and Computer Simulation*, 22(2):1–5, March 2012.

[294] Mark Huber. Optimal linear bernoulli factories for small mean problems, 2015.

[295] Peter Occil. Bernoulli factory algorithms. https://peteroupc.github.io/bernoulli.html, Jun 2022.

[296] Renato Paes Leme and Jon Schneider. Multiparameter bernoulli factories, 2022.

[297] Giulio Morina, Krzysztof Łatuszyński, Piotr Nayar, and Alex Wendland. From the bernoulli factory to a dice enterprise via perfect sampling of markov chains. *The Annals of Applied Probability*, 32(1), February 2022.

[298] Theodore J Yoder. Building and bounding quantum bernoulli factories. *Unpublished dissertation. Massachussets Institute of Technology*, 2015.

[299] Elham Kashefi and Anna Pappa. Multiparty delegated quantum computing. *Cryptography*, 1(2):12, July 2017.

[300] ISO/TMBG Technical Management Board. Uncertainty of measurement. Standard, International Organization for Standardization, Geneva, CH, oct 2008.

[301] R. A. Fisher. On the mathematical foundations of theoretical statistics. *Philosophical Transactions of the Royal Society of London. Series A, Containing Papers of a Mathematical or Physical Character*, 222(594-604):309–368, January 1922.

[302] Luca Pezze' and Augusto Smerzi. Quantum theory of phase estimation, 2014.

[303] M. Cohen. The fisher information and convexity (corresp.). *IEEE Transactions on Information Theory*, 14(4):591–592, July 1968.

[304] Harald Cramer. *Mathematical methods of statistics (PMS-9), volume 9*. Princeton Landmarks in Mathematics and Physics. Princeton University Press, Princeton, NJ, March 1999.

[305] C. Radhakrishna Rao. Information and the accuracy attainable in the estimation of statistical parameters. In *Springer Series in Statistics*, pages 235–247. Springer New York, 1992.

[306] E L Lehmann and George Casella. *Theory of Point Estimation*. Springer Texts in Statistics. Springer, New York, NY, 2 edition, December 1998.

[307] Carl W. Helstrom. Quantum detection and estimation theory. *Journal of Statistical Physics*, 1(2):231–252, 1969.

[308] Samuel L. Braunstein and Carlton M. Caves. Statistical distance and the geometry of quantum states. *Physical Review Letters*, 72(22):3439–3443, May 1994.

[309] Alexander S Holevo. *Probabilistic and statistical aspects of quantum theory*. Monographs (Scuola Normale Superiore). Edizioni della Normale, Pisa, Switzerland, 1 edition, May 2011.

[310] Matteo G. A. Paris. QUANTUM ESTIMATION FOR QUANTUM TECHNOLOGY. *International Journal of Quantum Information*, 07(supp01):125–137, January 2009.

[311] Jasminder S. Sidhu and Pieter Kok. Geometric perspective on quantum parameter estimation. *AVS Quantum Science*, 2(1):014701, February 2020.

[312] Hans-J rgen Sommers and Karol Zyczkowski. Bures volume of the set of mixed quantum states. *Journal of Physics A: Mathematical and General*, 36(39):10083–10100, September 2003.

[313] Vittorio Giovannetti, Seth Lloyd, and Lorenzo Maccone. Quantum metrology. *Physical Review Letters*, 96(1), January 2006.

[314] Richard D. Gill and Serge Massar. State estimation for large ensembles. *Physical Review A*, 61(4), March 2000.

[315] Akio Fujiwara. Strong consistency and asymptotic efficiency for adaptive quantum estimation problems. *Journal of Physics A: Mathematical and General*, 39(40):12489–12504, September 2006.

[316] Masahito Hayashi and Keiji Matsumoto. Asymptotic performance of optimal state estimation in qubit system. *Journal of Mathematical Physics*, 49(10):102101, October 2008.

[317] Hiroshi Nagaoka. On the parameter estimation problem for quantum statistical models. In *Asymptotic Theory of Quantum Statistical Inference*, pages 125–132. WORLD SCIENTIFIC, February 2005.

[318] Carlton M. Caves. Quantum-mechanical noise in an interferometer. *Physical Review D*, 23(8):1693–1708, April 1981.

[319] Samuel L. Braunstein. Quantum limits on precision measurements of phase. *Physical Review Letters*, 69(25):3598–3601, December 1992.

[320] Hwang Lee, Pieter Kok, and Jonathan P. Dowling. A quantum rosetta stone for interferometry. *Journal of Modern Optics*, 49(14-15):2325–2338, November 2002.

[321] Vittorio Giovannetti, Seth Lloyd, and Lorenzo Maccone. Quantum-enhanced measurements: Beating the standard quantum limit. *Science*, 306(5700):1330–1336, November 2004.

[322] Roland Krischek, Christian Schwemmer, Witlef Wieczorek, Harald Weinfurter, Philipp Hyllus, Luca Pezzé, and Augusto Smerzi. Useful multiparticle entanglement and sub-shot-noise sensitivity in experimental phase estimation. *Physical Review Letters*, 107(8), August 2011.

[323] Philipp Hyllus, Wiesław Laskowski, Roland Krischek, Christian Schwemmer, Witlef Wieczorek, Harald Weinfurter, Luca Pezzé, and Augusto Smerzi. Fisher information and multiparticle entanglement. *Physical Review A*, 85(2), February 2012.

[324] B. L. Higgins, D. W. Berry, S. D. Bartlett, H. M. Wiseman, and G. J. Pryde. Entanglement-free heisenberg-limited phase estimation. *Nature*, 450(7168):393–396, November 2007.

[325] D. W. Berry, B. L. Higgins, S. D. Bartlett, M. W. Mitchell, G. J. Pryde, and H. M. Wiseman. How to perform the most accurate possible phase measurements. *Physical Review A*, 80(5), November 2009.

[326] I. Afek, O. Ambar, and Y. Silberberg. Classical bound for mach-zehnder superresolution. *Physical Review Letters*, 104(12), March 2010.

[327] Magdalena Szczykulska, Tillmann Baumgratz, and Animesh Datta. Multi-parameter quantum metrology. *Advances in Physics: X*, 1(4):621–639, July 2016.

[328] Sanah Altenburg and Sabine Wölk. Multi-parameter estimation: global, local and sequential strategies. *Physica Scripta*, 94(1):014001, November 2018.

[329] Jesús Rubio and Jacob Dunningham. Bayesian multiparameter quantum metrology with limited data. *Physical Review A*, 101(3), March 2020.

[330] Chiara Macchiavello. Optimal estimation of multiple phases. *Physical Review A*, 67(6), June 2003.

[331] Emanuele Roccia, Valeria Cimini, Marco Sbroscia, Ilaria Gianani, Ludovica Ruggiero, Luca Mancino, Marco G. Genoni, Maria Antonietta Ricci, and Marco Barbieri. Multiparameter approach to quantum phase estimation with limited visibility. *Optica*, 5(10):1171, September 2018.

[332] Jing Yang, Shengshi Pang, Yiyu Zhou, and Andrew N. Jordan. Optimal measurements for quantum multiparameter estimation with general states. *Physical Review A*, 100(3), September 2019.

[333] Sammy Ragy, Marcin Jarzyna, and Rafał Demkowicz-Dobrzański. Compatibility in multiparameter quantum metrology. *Physical Review A*, 94(5), November 2016.

[334] H. Yuen and M. Lax. Multiple-parameter quantum estimation and measurement of nonselfadjoint observables. *IEEE Transactions on Information Theory*, 19(6):740–750, November 1973.

[335] K Matsumoto. A new approach to the cramér-rao-type bound of the pure-state model. *Journal of Physics A: Mathematical and General*, 35(13):3111–3123, March 2002.

[336] Michael A. Taylor and Warwick P. Bowen. Quantum metrology and its application in biology. *Physics Reports*, 615:1–59, February 2016.

[337] Christopher R. Ekstrom, Jörg Schmiedmayer, Michael S. Chapman, Troy D. Hammond, and David E. Pritchard. Measurement of the electric polarizability of sodium with an atom interferometer. *Physical Review A*, 51(5):3883–3888, May 1995.

[338] Rym Bouchendira, Pierre Cladé, Saïda Guellati-Khélifa, François Nez, and François Biraben. New determination of the fine structure constant and test of the quantum electrodynamics. *Physical Review Letters*, 106(8), February 2011.

[339] S. A. Diddams, J. C. Bergquist, S. R. Jefferts, and C. W. Oates. Standards of time and frequency at the outset of the 21st century. *Science*, 306(5700):1318–1324, November 2004.

[340] Andrew D. Ludlow, Martin M. Boyd, Jun Ye, E. Peik, and P. O. Schmidt. Optical atomic clocks. *Reviews of Modern Physics*, 87(2):637–701, June 2015.

[341] Achim Peters, Keng Yeow Chung, and Steven Chu. Measurement of gravitational acceleration by dropping atoms. *Nature*, 400(6747):849–852, August 1999.

[342] T. L. Gustavson, P. Bouyer, and M. A. Kasevich. Precision rotation measurements with an atom interferometer gyroscope. *Physical Review Letters*, 78(11):2046–2049, March 1997.

[343] Karol Gietka, Farokh Mivehvar, and Helmut Ritsch. Supersolid-based gravimeter in a ring cavity. *Physical Review Letters*, 122(19), May 2019.

[344] L A Lugiato, A Gatti, and E Brambilla. Quantum imaging. *Journal of Optics B: Quantum and Semiclassical Optics*, 4(3):S176–S183, April 2002.

[345] Vittorio Giovannetti, Seth Lloyd, Lorenzo Maccone, and Jeffrey H. Shapiro. Sub-rayleigh-diffraction-bound quantum imaging. *Physical Review A*, 79(1), January 2009.

[346] Marco Genovese. Real applications of quantum imaging. *Journal of Optics*, 18(7):073002, June 2016.

[347] R Lynch. The quantum phase problem: a critical review. *Physics Reports*, 256(6):367–436, May 1995.

[348] Stephen M. Barnett and David T. Pegg. Quantum optical phase. In *Quantum Communication, Computing, and Measurement*, pages 415–422. Springer US, 1997.

[349] Peter C. Humphreys, Marco Barbieri, Animesh Datta, and Ian A. Walmsley. Quantum enhanced multiple phase estimation. *Physical Review Letters*, 111(7), August 2013.

[350] Tillmann Baumgratz and Animesh Datta. Quantum enhanced estimation of a multidimensional field. *Physical Review Letters*, 116(3), January 2016.

[351] Steven M Kay. *Fundamentals of statistical processing, volume I.* Prentice Hall, Philadelphia, PA, March 1993.

[352] George E P Box and George C Tiao. *Bayesian inference in statistical analysis.* Wiley Classics Library. Wiley-Interscience, Newy York, January 2011.

[353] Lucien Le Cam. *Asymptotic methods in statistical decision theory.* Springer series in statistics. Springer, New York, NY, 1986 edition, December 2012.

[354] L Accardi, A Frigerio, and V Gorini, editors. *Quantum probability and applications to the quantum theory of irreversible processes.* Lecture Notes in Mathematics. Springer, Berlin, Germany, 1984 edition, April 1984.

[355] H. M. Wiseman. Adaptive phase measurements of optical modes: Going beyond the marginal q distribution. *Physical Review Letters*, 75(25):4587–4590, December 1995.

[356] D. W. Berry and H. M. Wiseman. Optimal states and almost optimal adaptive measurements for quantum interferometry. *Physical Review Letters*, 85(24):5098–5101, December 2000.

[357] Andrew C. Doherty, Salman Habib, Kurt Jacobs, Hideo Mabuchi, and Sze M. Tan. Quantum feedback control and classical control theory. *Physical Review A*, 62(1), June 2000.

[358] Jing Zhang, Yu xi Liu, Re-Bing Wu, Kurt Jacobs, and Franco Nori. Quantum feedback: Theory, experiments, and applications. *Physics Reports*, 679:1–60, March 2017.

[359] G. Y. Xiang, B. L. Higgins, D. W. Berry, H. M. Wiseman, and G. J. Pryde. Entanglement-enhanced measurement of a completely unknown optical phase. *Nature Photonics*, 5(1):43–47, December 2010.

[360] O E Barndorff-Nielsen and R D Gill. Fisher information in quantum statistics. *Journal of Physics A: Mathematical and General*, 33(24):4481–4490, June 2000.

[361] H.M. Wiseman, D.W. Berry, S.D. Bartlett, B.L. Higgins, and G.J. Pryde. Adaptive measurements in the optical quantum information laboratory. *IEEE Journal of Selected Topics in Quantum Electronics*, 15(6):1661–1672, 2009.

[362] Hidehiro Yonezawa, Daisuke Nakane, Trevor A. Wheatley, Kohjiro Iwasawa, Shuntaro Takeda, Hajime Arao, Kentaro Ohki, Koji Tsumura, Dominic W. Berry, Timothy C. Ralph, Howard M. Wiseman, Elanor H. Huntington, and Akira Furusawa. Quantum-enhanced optical-phase tracking. *Science*, 337(6101):1514–1517, September 2012.

[363] Lidan Zhang, Kaimin Zheng, Fang Liu, Wei Zhao, Lei Tang, Hidehiro Yonezawa, Lijian Zhang, Yong Zhang, and Min Xiao. Quantum-limited fiber-optic phase tracking beyond π range. *Optics Express*, 27(3):2327, January 2019.

[364] Alexander Hentschel and Barry C. Sanders. Machine learning for precise quantum measurement. *Physical Review Letters*, 104(6), February 2010.

[365] Neil B. Lovett, Cécile Crosnier, Martí Perarnau-Llobet, and Barry C. Sanders. Differential evolution for many-particle adaptive quantum metrology. *Physical Review Letters*, 110(22), May 2013.

[366] Pantita Palittapongarnpim, Peter Wittek, Ehsan Zahedinejad, Shakib Vedaie, and Barry C. Sanders. Learning in quantum control: High-dimensional global optimization for noisy quantum dynamics. *Neurocomputing*, 268:116–126, December 2017.

[367] Pantita Palittapongarnpim and Barry C. Sanders. Robustness of quantum-enhanced adaptive phase estimation. *Physical Review A*, 100(1), July 2019.

[368] Seongjin Hong, Yong-Su Kim, Young-Wook Cho, Seung-Woo Lee, Hojoong Jung, Sung Moon, Sang-Wook Han, Hyang-Tag Lim, et al. Quantum enhanced multiple-phase estimation with multi-mode n00n states. *Nature communications*, 12(1):1–8, 2021.

[369] Mauro Valeri, Emanuele Polino, Davide Poderini, Ilaria Gianani, Giacomo Corrielli, Andrea Crespi, Roberto Osellame, Nicolò Spagnolo, and Fabio Sciarrino. Experimental adaptive bayesian estimation of multiple phases with limited data. *npj Quantum Information*, 6:92, Dec 2020.

[370] Guo-Yong Xiang, Brendon Lloyd Higgins, DW Berry, Howard Mark Wiseman, and GJ Pryde. Entanglement-enhanced measurement of a completely unknown optical phase. *Nature Photonics*, 5(1):43–47, 2011.

[371] Adriano A Berni, Tobias Gehring, Bo M Nielsen, Vitus Händchen, Matteo GA Paris, and Ulrik L Andersen. Ab initio quantum-enhanced optical phase estimation using real-time feedback control. *Nature Photonics*, 9(9):577, 2015.

[372] Shakib Daryanoosh, Sergei Slussarenko, Dominic W Berry, Howard M Wiseman, and Geoff J Pryde. Experimental optical phase measurement approaching the exact heisenberg limit. *Nature communications*, 9(1):1–6, 2018.

[373] Giacomo Corrielli, Andrea Crespi, and Roberto Osellame. Femtosecond laser micromachining for integrated quantum photonics. *Nanophotonics*, 10(15):3789–3812, 2021.

[374] Thomas Meany, Markus Gräfe, René Heilmann, Armando Perez-Leija, Simon Gross, Michael J Steel, Michael J Withford, and Alexander Szameit. Laser written circuits for quantum photonics. *Laser & Photonics Reviews*, 9(4):363–384, 2015.

[375] Marek Żukowski, Anton Zeilinger, and Michael A Horne. Realizable higher-dimensional two-particle entanglements via multiport beam splitters. *Physical Review A*, 55(4):2564, 1997.

[376] Francesco Ceccarelli, Simone Atzeni, Ciro Pentangelo, Francesco Pellegatta, Andrea Crespi, and Roberto Osellame. Low power reconfigurability and reduced crosstalk in integrated photonic circuits fabricated by femtosecond laser micromachining. *Laser & Photonics Reviews*, 14(10):2000024, 2020.

[377] Luca Pezzè, Mario A Ciampini, Nicolò Spagnolo, Peter C Humphreys, Animesh Datta, Ian A Walmsley, Marco Barbieri, Fabio Sciarrino, and Augusto Smerzi. Optimal measurements for simultaneous quantum estimation of multiple phases. *Physical Review Letters*, 119(13):130504, 2017.

[378] Si-Ran Zhao, Yu-Zhe Zhang, Wen-Zhao Liu, Jian-Yu Guan, Weijun Zhang, Cheng-Long Li, Bing Bai, Ming-Han Li, Yang Liu, Lixing You, et al. Field demonstration of distributed quantum sensing without post-selection. *Physical Review X*, 11(3):031009, 2021.

[379] Timothy J Proctor, Paul A Knott, and Jacob A Dunningham. Multiparameter estimation in networked quantum sensors. *Physical review letters*, 120(8):080501, 2018.

[380] Li-Zheng Liu, Yu-Zhe Zhang, Zheng-Da Li, Rui Zhang, Xu-Fei Yin, Yue-Yang Fei, Li Li, Nai-Le Liu, Feihu Xu, Yu-Ao Chen, et al. Distributed quantum phase estimation with entangled photons. *Nature Photonics*, 15(2):137–142, 2021.

[381] Xueshi Guo, Casper R Breum, Johannes Borregaard, Shuro Izumi, Mikkel V Larsen, Tobias Gehring, Matthias Christandl, Jonas S Neergaard-Nielsen, and Ulrik L Andersen. Distributed quantum sensing in a continuous-variable entangled network. *Nature Physics*, 16(3):281–284, 2020.

[382] Wenchao Ge, Kurt Jacobs, Zachary Eldredge, Alexey V Gorshkov, and Michael Foss-Feig. Distributed quantum metrology with linear networks and separable inputs. *Physical review letters*, 121(4):043604, 2018.

[383] Marco Malitesta, Augusto Smerzi, and Luca Pezzè. Distributed quantum sensing with squeezed-vacuum light in a configurable network of mach-zehnder interferometers. *arXiv preprint arXiv:2109.09178*, 2021.

[384] Luca Pezzé and Augusto Smerzi. Mach-zehnder interferometry at the heisenberg limit with coherent and squeezed-vacuum light. *Physical review letters*, 100(7):073601, 2008.

[385] Saikat Guha Kwan Kit Lee, Christos Gagatsos and Amit Ashok. Quantum multi-parameter adaptive bayesian estimation and application to super-resolution imaging. *arXiv preprint arXiv:2202.09980*, 2022.

[386] Valeria Cimini, Marta Mellini, Giordano Rampioni, Marco Sbroscia, Emanuele Roccia, Livia Leoni, Marco Barbieri, and Ilaria Gianani. Adaptive tracking of enzymatic reactions with quantum light. *Optics Express*, 27(24):35245–35256, 2019.

[387] Emanuele Polino, Mauro Valeri, Nicolò Spagnolo, and Fabio Sciarrino. Photonic quantum metrology. *AVS Quantum Science*, 2(2):024703, 2020.

[388] Federico Vernuccio, Arianna Bresci, Valeria Cimini, Alessandro Giuseppi, Giulio Cerullo, Dario Polli, and Carlo Michele Valensise. Artificial intelligence in classical and quantum photonics. *Laser & Photonics Reviews*, page 2100399, 2022.

[389] Samuel Nolan, Augusto Smerzi, and Luca Pezzè. A machine learning approach to bayesian parameter estimation. *npj Quantum Information*, 7(1):1–8, 2021.

[390] Lukas J Fiderer, Jonas Schuff, and Daniel Braun. Neural-network heuristics for adaptive bayesian quantum estimation. *PRX Quantum*, 2(2):020303, 2021.

[391] Valeria Cimini, Ilaria Gianani, Nicolò Spagnolo, Fabio Leccese, Fabio Sciarrino, and Marco Barbieri. Calibration of quantum sensors by neural networks. *Physical Review Letters*, 123(23):230502, 2019.

[392] Valeria Cimini, Emanuele Polino, Mauro Valeri, Ilaria Gianani, Nicolò Spagnolo, Giacomo Corrielli, Andrea Crespi, Roberto Osellame, Marco Barbieri, and Fabio Sciarrino. Calibration of multiparameter sensors via machine learning at the single-photon level. *Physical Review Applied*, 15(4):044003, 2021.

[393] Tailong Xiao, Jianping Fan, and Guihua Zeng. Parameter estimation in quantum sensing based on deep reinforcement learning. *npj Quantum Information*, 8(1):1–12, 2022.

[394] Valeria Cimini, Mauro Valeri, Emanuele Polino, Simone Piacentini, Francesco Ceccarelli, Giacomo Corrielli, Nicolò Spagnolo, Roberto Osellame, and Fabio Sciarrino. Deep reinforcement learning for quantum multiparameter estimation. *arXiv preprint arXiv:2209.00671*, 2022.

[395] Valentin Gebhart, Augusto Smerzi, and Luca Pezzè. Bayesian quantum multiphase estimation algorithm. *Physical Review Applied*, 16(1):014035, 2021.

[396] Christopher E. Granade, Christopher Ferrie, Nathan Wiebe, and D. G. Cory. Robust online hamiltonian learning. *New Journal of Physics*, 14:103013, 2012.

[397] Nathan Wiebe and Christopher E. Granade. Efficient bayesian phase estimation. *Physical Review Letters*, 117:010503, 2016.

[398] Christopher Granade, Christopher Ferrie, Ian Hincks, Steven Casagrande, Thomas Alexander, Jonathan Gross, Michal Kononenko, and Yuval Sanders. QInfer: Statistical inference software for quantum applications. *Quantum*, 1:5, April 2017.

[399] Simone Evaldo D'Aurelio, Mauro Valeri, Emanuele Polino, Valeria Cimini, Ilaria Gianani, Marco Barbieri, Giacomo Corrielli, Andrea Crespi, Roberto Osellame, Fabio Sciarrino, et al. Experimental investigation of bayesian bounds in multiparameter estimation. *Quantum Science and Technology*, 2022.

[400] A Yu Kitaev. Quantum measurements and the abelian stabilizer problem. *arXiv preprint quant-ph/9511026*, 1995.

[401] Federico Belliardo and Vittorio Giovannetti. Achieving Heisenberg scaling with maximally entangled states: An analytic upper bound for the attainable root-mean-square error. *Phys. Rev. A*, 102(4):042613, October 2020. Publisher: American Physical Society.

[402] Vincenzo D'Ambrosio, Nicolo' Spagnolo, Lorenzo Del Re, Sergei Slussarenko, Ying Li, Leong Chuan Kwek, Lorenzo Marrucci, Stephen P. Walborn, Leandro Aolita, and Fabio Sciarrino. Photonic polarization gears for ultra-sensitive angular measurements. *Nat. Comm.*, 4:2432, 2013.

[403] L. Marrucci, C. Manzo, and D. Paparo. Optical spin-to-orbital angular momentum conversion in inhomogeneous anisotropic media. *Phys. Rev. Lett.*, 96:163905, 2006.

[404] Andrea Crespi, Mirko Lobino, Jonathan C. F. Matthews, Alberto Politi, Chris R. Neal, Roberta Ramponi, Roberto Osellame, and Jeremy L. O'Brien. Measuring protein concentration with entangled photons. *Applied Physics Letters*, 100(23):233704, June 2012.